TECHNISCHE UNIVERSITÄT MÜNCHEN
Lehrstuhl für Baumechanik

Output-only measurement-based parameter identification of dynamic systems subjected to random load processes

Katrin S. Runtemund

Vollständiger Abdruck der von der Ingenieurfakultät Bau Geo Umwelt der Technischen Universität München zur Erlangung des akademischen Grades eines

Doktor-Ingenieurs

genehmigten Dissertation.

Vorsitzender: Univ.-Prof. Dr. sc. techn. (ETH) Daniel Straub

Prüfer der Dissertation:

1. Univ.-Prof. Dr.-Ing. habil. Gerhard Müller
2. Prof. Pol D. Spanos, Ph.D.
   Rice University, Houston/USA

Die Dissertation wurde am 24.04.2013 bei der Technischen Universität München eingereicht und durch die Ingenieurfakultät Bau Geo Umwelt am 13.09.2013 angenommen.

Abstract

In the present work a new output-only measurement based method is proposed which allows identifying the modal parameters of structures subjected to natural loads such as wind, ocean waves, traffic or human walk. The focus lies on the dynamic excitation of structures by wind turbulences and wind-induced ocean waves modeled as stationary Gaussian random process. In contrast to the existing output-only identification techniques which model the unmeasured load as white noise process, statistical information about the dynamic excitation, e.g. obtained by measurements of the wind fluctuations in the vicinity of the structure, are taken into account which improve the identification results as well as allow identifying the unmeasured load process exciting the structure.

The identification problem is solved on basis of a recently developed method called *H-fractional spectral moment (H-FSM) decomposition* of the transfer function $H(\omega)$ which allows representing Gaussian random processes with known power spectral density (PSD) function as output of a linear fractional differential equation with white noise input.

In the present work (i) the efficiency and accuracy of this method is improved by the use of an alternative fractional operator and (ii) a modification is proposed which makes it applicable to short as well as long memory processes. (iii) The most widely used wind and ocean wave model spectra are compared and discussed, and the corresponding H-FSMs are provided in closed form allowing to simulate realization of the processes in a straight forward manner. (iv) Based on the FSM decomposition a state space representation of arbitrarily correlated Gaussian processes is developed in closed form which neither requires the factorization of the PSD function nor any optimization procedure. Combined with the state space model of the structure, it leads to an overall model with white noise input, (v) which can be efficiently combined with any state-space model-based parameter identification algorithms such as the well known (weighted) extended Kalman filter algorithm used here. (vi) The method is successfully applied for the stiffness and damping estimation of single and multi-degree of freedom systems subjected to wind and wind-wave turbulences as well as for the estimation of the unmeasured load process. vii) Finally, a sensitivity analysis of the filter accuracy is conducted in order to improve the accuracy and efficiency of the method.

Zusammenfassung

In der vorliegenden Arbeit wird eine neue Methode zur Identifikation modaler Parameter dynamischer Systeme entwickelt, die auf (Output-only) Messungen der Systemantwort infolge der natürlichen Anregung durch Lasten wie z.B. Wind, Wellen, Verkehr oder Personen basiert. Der Fokus der Arbeit liegt hierbei auf der stochastischen Anregung durch Windturbulenzen und windinduzierten Wellen, welche als Realisation stationärer Gaußscher Prozesse modelliert werden. Im Gegensatz zu bestehenden Output-only Identifikationsverfahren, die die unbekannten Lasten vereinfacht als weiße Rauschprozesse beschreiben, werden hier zusätzliche statistische Informationen, die beispielsweise durch Windmessung in der Nähe der Struktur gewonnen werden, berücksichtigt. Dies führt nicht nur zu einer Verbesserung der Parameterschätzung, sondern ermöglicht auch die gleichzeitige Lastidentifikation .
Das entwickelte Identifikationsverfahren basiert auf einer kürzlich entwickelten Methode, der sogenannten „*H-fractional spectral moment (H-FSM) decomposition*“, d.h. der Zerlegung der Überragungsfunktion $H(\omega)$ mit Hilfe von spektralen Momenten fraktionaler Ordnung. Die Methode erlaubt einen Gaußschen Prozess mit gegebener Leistungsspektraldichte (PSD) als Output einer linearen fraktionalen Differentialgleichung mit weißem Rauschen als Input zu simulieren.
Im Rahmen dieser Arbeit wird (i) die Effizienz und die Genauigkeit dieser Methode durch die Verwendung eines alternativen fraktionalen Integraloperators verbessert und (ii) die Definition der H-FSMs derart modifiziert, dass die Methode nicht nur für sogenannte „Short Memory“ Prozesse mit exponentiell abklingender Autokorrelation, sondern auch für langkorrelierte („Long Memory“) Prozesse anwendbar ist. iii) Die gebräuchlichsten Wind und Windwellen charakterisierenden Modell–Spektren werden diskutiert und die zugehörigen H-FSMs in analytischer Form zur Verfügung gestellt, mit Hilfe derer, Realisationen der Prozesse in einfacher Weise generiert werden können. (iv) Auf der H-FSM Zerlegung aufbauend, wird ein für beliebig korrelierte Lastprozesse gültiges lineares Zustandsraummodel in analytischer Form hergeleitet, das im Gegensatz zu gebräuchlichen Methoden weder die spektrale Faktorisierung der Leistungsspektraldichte noch die Anwendung eines Optimierungsverfahrens erfordert. (v) Es erlaubt die Lasten in die Systemgleichungen zu integrieren, so dass das System mit korrelierten Lasten auf ein Gesamtsystem höherer Ordnung mit weißem

Rauschen als Input zurückgeführt werden kann, dessen Parameter dann mit einem beliebigen Zustandsraum-basierten Verfahren, wie z.B. das hier verwendete Erweiterte Kalman Filter, identifiziert werden können. (vi) Die Methode wird für die Schätzung der Steifigkeits- und Dämpfungsparameter von Ein- und Mehrfreiheitsgradsystemen unter wind- und welleninduzierten Lasten sowie für die Schätzung des unbekannten Lastprozesses verwendet. (vii) Schließlich wird eine Sensitivitätsanalyse durchgeführt, mit dem Ziel, die Genauigkeit und die Effizienz des Algorithmus weiter zu verbessern.

Acknowledgments

It has been a great privilege to spend several years as research assistant at the Chair of Structural Mechanics of the Faculty of Civil, Geo and Environmental Engineering at Technische Universität München.

I would like to express my sincere gratitude to my supervisor Prof. Gerhard Müller for his guidance, patience and unconditional trust, that encouraged me to follow my own ideas and research interests. I greatly appreciated the familiar atmosphere at the chair and my colleges will always remain dear to me.

Besides my supervisor, I would like to thank Prof. Pol Spanos for agreeing to be co-examiner of my thesis and for his encouraging and insightful comments.

I owe my deepest gratitude to my mentor Giulio Cottone for many valuable discussions that helped me to understand my research area better. Without his continuous optimism concerning this work, enthusiasm, encouragement and support this study would hardly have been completed.

Foremost, I would like to thank my family and friends for having been a constant source of moral and spiritual support, concern and strength all these years.

Contents

Abstract III

Zusammenfassung IV

Acknowledgments VI

List of Symbols and Acronyms X

1 Introduction 1
- 1.1 Motivation . . . 1
- 1.2 Outline . . . 3

2 Stochastic Models of Dynamic Excitations 6
- 2.1 A brief review on probability and stochastic process . . . 6
  - 2.1.1 Second-order characterization . . . 8
  - 2.1.2 Important processes . . . 10
    - 2.1.2.1 White noise process . . . 10
    - 2.1.2.2 Gaussian process . . . 11
- 2.2 Aerodynamic Wind Excitation . . . 13
  - 2.2.1 Mean wind velocity profile . . . 15
  - 2.2.2 Turbulence . . . 17
    - 2.2.2.1 Turbulence intensity . . . 18
    - 2.2.2.2 Integral scales of turbulence . . . 18
    - 2.2.2.3 Asymptotic properties of the turbulence spectra . . . 20
    - 2.2.2.4 Turbulence model spectra . . . 26
  - 2.2.3 Models for wind loads on structures . . . 29
- 2.3 Wind wave excitation . . . 32
  - 2.3.1 Ocean wave spectra . . . 33
  - 2.3.2 Sea states . . . 34
  - 2.3.3 Generation of wind waves . . . 35
  - 2.3.4 Linear wave model . . . 37
  - 2.3.5 Model spectra of the fully developed sea . . . 39
  - 2.3.6 Wind-induced wave forces . . . 45

3 State-of-the-Art on Digital Simulation of Ambient Loads - Traditional Methods 49
- 3.1 Wave superposition-based methods . . . 50
- 3.2 Digital filter schemes . . . 54
  - 3.2.1 Parametric time series-based methods . . . 54

3.2.2 Shaping filters . . . 59
3.2.2.1 The spectral factorization theorem . . . 60

4 State Space (Markovian) Modeling of Ambient Loads 64
4.1 Definition . . . 64
4.2 State space model of AR and MA series . . . 66
4.3 State space model of an ARMA series . . . 68
4.4 Relation between state space model and transfer function . . . 69
4.5 State space augmentation . . . 73
4.5.1 Numerical example . . . 75

5 Fractional Representation of Stationary Gaussian Processes 77
5.1 A short historical overview . . . 78
5.2 Grünwald - Letnikov fractional integral . . . 79
5.3 Reconstruction of AC and PSD function by fractional spectral moment decomposition . . . 81
5.4 Reconstruction of impulse response and transfer function by H-FSM decomposition . . . 83
5.4.1 Numerical examples . . . 85
5.4.1.1 Exponentially autocorrelated wind gusts . . . 85
5.4.1.2 Wind gusts with von Kármán velocity PSD . . . 86
5.4.1.3 Wind waves with Pierson Moskowitz PSD . . . 87
5.5 Digital simulation of Gaussian random processes with target PSD function . . . 88
5.5.1 Short memory principle . . . 90
5.5.2 Numerical examples . . . 92
5.5.3 Investigation of the simulation accuracy: discretization and truncation errors . . . 93
5.6 Long-memory processes . . . 100
5.6.1 Properties . . . 100
5.6.2 Proposed modification of the H-FSM decomposition for the representation of Gaussian processes with power-law decay . . . 103
5.6.2.1 Numerical example . . . 104
5.6.3 Digital simulation of a Gaussian random process with power-law decay by H-FSM decomposition . . . 104
5.6.3.1 Numerical example . . . 105
5.7 Summary of the main findings . . . 106

6 Structural Parameter Identification by Kalman Filter Approaches 109
6.1 Kalman filter . . . 110
6.1.1 Model assumptions . . . 112
6.1.2 Bayesian approach to the Kalman filter . . . 114
6.1.2.1 Recursive Bayesian filtering . . . 116
6.1.3 Nonlinear state estimation . . . 120
6.1.3.1 Derivation of the extended Kalman filter for adaptive estimation . . . 121
6.1.3.2 Initialization of the Kalman filter algorithm . . . 125

6.1.3.3 The weighted extended Kalman filter algorithm (W-EKF) . . 126
6.1.4 Application to a three story shear building 128

7 A New Parameter Identification Method of Structures Excited by Random Loads 142
7.1 Proposed modification of the EKF algorithm 142
7.1.1 Generalized state space representation of colored random processes . . 143
7.1.2 Generalized state space model of structures subjected to random loads 145
7.1.3 Parameter identification of a SDOF dynamical structure 146
7.1.3.1 Case study 1: Exponentially correlated wind gusts 146
7.1.3.2 Case Study 2: Wind gusts with von Kármán velocity PSD 154
7.1.3.3 Case Study 3: Wind waves with Pierson-Moskowitz PSD . 154
7.1.4 Enhancing the method's efficiency by the weighted H-fractional extended Kalman filter 154
7.1.5 Parameter identification of a three story shear building 155
7.1.5.1 Case Study 1: Exponentially correlated wind gusts 156
7.1.5.1.1 Influence of the sampling interval on the filter convergence 158
7.1.5.1.2 Influence of the accuracy of the load modeling on the filter performance 159
7.1.5.2 Case Study 2: Wind gusts with von Kármán velocity PSD 164

8 Conclusions and Outlook 169

Annexe 176
A.1 Definitions 176
A.1.1 Characteristic function 176
A.1.2 Stationarity 177
A.1.3 Ergodicity 177
A.1.4 Selected processes 178
B.1 Digital Simulation of Ambient Loads 184
B.1.1 Iterative derivation of the ARMA coefficients 184
B.1.2 Fractional spectral moments 186
C.1 Kalman Filter 193
C.1.1 Least square approach to the Kalman filter 193
C.1.2 Partial derivative matrices 198
D.1 State-of-the-art on System Identification Techniques for Operational Modal Analysis 200
D.1.1 NExT-type methods 201
D.1.2 ARMA-type methods 203
D.1.3 Stochastic realization-based methods 209
D.1.4 Stochastic subspace-based methods 213

Bibliography 220

List of Symbols and Acronyms

Typical units are given in square brackets.

Subscripts

a	[–]	augmented
c	[–]	continuous-time
d	[–]	discrete-time
k	[–]	time step k at time $t = k\tau$, where τ is the sampling interval
Exp	[–]	Exponential
Kar	[–]	von Kármán
PM	[–]	Pierson Moskowitz

Superscripts

A^{-1}	[–]	inverse of A (matrix)
A^T	[–]	transpose of A (matrix)
X^*	[–]	complex conjugate of X
$\hat{X}$	[–]	estimate of X
$\bar{X}$	[–]	mean value of X
$\tilde{X}$	[–]	true (undisturbed) value of X

Greek letters

α	[–]	Power exponent of the wind profile
$\alpha_k(\gamma)$, $\alpha_{c,k}(\gamma)$	[–]	Coefficients of the (centered) GL discretization
$\eta = Im\gamma$	[–]	Imaginary part of the complex number $\gamma \in \mathbb{C}$
$\Delta\eta$	[–]	Discretization step width along the imaginary axix
$\eta(t,x)$	[m]	Sea surface profile at time t and location x
γ_i	[m^2,$(m/s)^2$]	Mean square of the ith element of the posterior error $d_{i,k\|k}$; s. Eq. (6.42a)
γ_i^N	[–]	Mean square of the ith element of the posterior error $d_{i,k\|k}$ normalized with respect to the undisturbed system response; s. Eq. (6.43a)
$\hat{\gamma}_i^N$	[–]	Normalized mean square of the ith element of the posterior error $d_{i,k\|k}$ normalized with respect to the noisy system response; s. Eq. (6.42b)
κ	[–]	Surface drag coefficient
λ	[m]	Wavelength
$\lambda_X(\gamma)$	[N^2/s^γ]	Spectral moments of the PSD function of the load process $\{X(t)\}$ of order $\gamma \in \mathbb{N}_0$
$\Lambda_X(\gamma)$	[N^2/s^γ]	Fractional spectral moments of the PSD function of the process $\{X(t)\}$ of order $\gamma \in \mathbb{C}$
$\mu(t)$	[m, N]	Mean value at time t, e.g. of displacement or force
$\phi(t)$	[rad]	Phase angle at time t
$\Pi_H(\gamma)$	[$s^{-(1/2+\gamma)}$]	H-fractional spectral moments of the transfer function $H(\omega)$ of order $\gamma \in \mathbb{C}$
ω	[rad/s]	Angular frequency
ω_i	[–]	Sample point
Ω	[–]	Sample space
$\psi_a(z;f)$	[Ns/m]	Aerodynamic admittance function relating wind force and wind velocity
$\rho = Re\gamma$	[–]	Real part of the complex number $\gamma \in \mathbb{C}$
ρ_a, ρ_w	[kg/m^3]	Air, water density
$\rho_u(x,y,z;\tau)$	[–]	Normalized AC function of the longitudinal wind velocity fluctuations
σ	[m, N]	Standard deviation, e.g. displacement, force
σ^2	[m^2, N^2]	Variance, e.g. displacement, force
σ_η	[m]	Standard deviation of the surface evaluation

σ_F	[N]	Standard deviation of the dynamic drag force $F'_D(z;t)$
σ_u, σ_v, σ_w	[m/s]	Standard deviation of the longitudinal, lateral and vertical wind fluctuations
σ_y	[m]	Standard deviation of the floor displacements
$\sigma_{\dot{y}}$	[m/s]	Standard deviation of the floor velocities
σ_k	[N/m, Ns/m]	Standard deviation of estimated stiffness and damping parameters
$\mathbf{\Sigma}_{yy,k}$	[m^2]	Covariance matrix of the floor displacements
$\mathbf{\Sigma}_{\dot{y}\dot{y},k}$	[(m/s)^2]	Covariance matrix of the floor velocities
$\mathbf{\Sigma}_{pp,k}$	[(N/m)^2, (Ns/m)^2]	Covariance matrix of the unknown stiffness and damping parameters
$\mathbf{\Sigma}_{xx,k}$	[m^2]	Covariance matrix of the state estimates
θ^j	[m^2,(m/s)^2]	Objective function, i.e. the average of all measurement square errors at the end of the jth iteration 6.30a
θ^j_{min}	[–]	Minimum of the objective function
θ^N_{min}	[–]	Minimum of the objective function normalized with respect to the undisturbed system response, s. Eq. (6.42c)
$\hat{\theta}^N_{min}$	[–]	Minimum of the objective function normalized with respect to the noisy system response, s. Eq. (6.43b)
τ	[s]	Time shift/lag, sampling interval

Latin letters

$a(x,z;t)$	[m/s^2]	Horizontal water particle acceleration
a_0,...a_p	[–]	Coefficients of the autoregressive model $AR(p)$ of order p
$d\beta(t) = W(t)dt$		Increment of the Brownian motion process
A	[m^2]	Surface area of the structure in the wind flow
$\mathbf{A}$	[–]	State transition coefficient matrix
AR(p)	[–]	Autoregressive model of order p
ARV(n,p)	[–]	n-dimensional vector AR model of order p
ARMA(p,q)	[–]	Autoregressive moving average model of order p,q
ARMA(n,p,q)	[–]	n-dimensional ARMA model of order p,q
b_0,...b_q	[–]	Coefficients of the moving average model
B	[m]	Characteristic length of an object in the wind flow
$B(t)$	[N]	Brownian motion process
ΔB	[N]	Increments of the Brownian motion process

$\mathbf{B}$	[–]	Force transition matrix
c	[m/s]	Propagation velocity of the sea wave
c	[Ns/m]	Viscous damping coefficient
c_1, c_2, c_3	[Ns/m]	Viscous damping coefficients of the three story shear building (s. Fig. 6.6a)
$c_0, c_1, ...$	[–]	Coefficients of the infinite moving average model $MA(\infty)$
C_d	[–]	Dimensionless drag coefficient
C_F	[–]	Dimensionless force coefficient
C_m	[–]	Dimensionless inertia coefficient
$C_X(t_1,t_2)$	[N^2]	Autocovariance function of the process $\{X(t)\}$
$\mathbf{C}$	[–]	Observation transition matrix
d_0,d_1,...	[–]	Coefficients of the infinite autoregressive model $AR(\infty)$
d	[m]	Height above the ground where the mean wind velocity is zero
$\mathbf{d}_k$	[m, m/s]	Innovation: Discrepancy between actual measurement and prediction
$\mathbf{d}_{k\|k}$	[m, m/s]	Posterior innovation: Discrepancy between actual measurement and optimal estimate
D	[m]	Diameter of a cylinder
D	[–]	Ratio of critical damping
$\mathbf{D}$	[–]	Measurement noise transition matrix
$e_{c,0}$	[–]	Initial relative error of the damping estimates
$e_{k,0}$	[–]	Initial relative error of the stiffness estimates
$\mathbf{e}_{x,k}$	[m, m/s]	Posterior error at time k
$\mathbf{e}_{x,k+1\|k}$	[m, m/s]	Prior prediction error at time $k+1$ including all information up to time k
f	[Hz]	Frequency
F, F_{min}	[m]	Storm fetch, minimum fetch
$F_d(x,z;t)$	[N]	Horizontal drag force of the sea wave
$F_D(z;t)$	[N]	Aerodynamic drag (or along wind) force
$\bar{F}_D(z;t)$	[N]	Mean value of the aerodynamic drag force
$F'_D(z;t)$	[N]	Dynamic time-dependent part of the aerodynamic drag force
$F_m(x,z;t)$	[N]	Horizontal inertia force of the sea wave
$g = 9.81$	[m/s^2]	Gravitational acceleration
$G_X(\omega)$, $G_X(f)$	[N^{2}s]	One-sided PSD function of the load process $\{X(t)\}$

$\mathbf{G}$	[–]	Process noise transition matrix
$h(t)$	[s/kg]	Impulse response function
H	[m]	Wave height (measured from wave crest to trough)
H_0	[m]	Most probable wave height
$\bar{H}$	[m]	Mean probable wave height
H_{rms}	[m]	Root-mean-square wave height
H_s	[m]	Significant wave height
$H(\omega,z)$	[rad/s]	Transfer function relating sea surface evaluation, velocity and acceleration
$H(\omega)$, $\mathbf{H}(\omega)$	[$s^{1/2}$]	Transfer function and transfer matrix relating white noise input and colored load process
$H(\gamma)$	[s/kg]	Matrix transfer function obtained by FSM decomposition, s. Eq. (5.31)
I_u, I_v, I_w	[–]	Turbulence intensities of the fluctuation components u_D, v_D and w_D
I_F	[–]	Intensity of the dynamic drag force fluctuations $F'_D(z;t)$
$\mathbf{I}_{n\times n}$	[–]	Identity matrix of order $n \times n$
KC	[–]	Keulegan-Carpenter number
$k = \frac{2\pi}{\lambda}$	[–]	Wavenumber
k	[N/m]	Stiffness coefficient
k_1, k_2, k_3	[N/m]	Stiffness coefficients of the three story shear building (s. Fig. 6.6a)
L	[–]	Backshift operator
$L_{C,u}(z)$	[m]	Longitudinal integral length scale of wind eddies proposed by Couninhan
$L_u(z)$	[m]	Longitudinal integral length scale of wind eddies
$L_i^j(z)$	[m]	Longitudinal, lateral and vertical integral length scale of eddies at height z in $j = x,y,z$ direction
m	[kg]	Mass
m	[–]	Number of considered fractional spectral moments
m_1, m_2, m_3	[kg]	Mass coefficients of the three story shear building (s. Fig. 6.6a)
$M = p\tau$	[s]	Considered process memory (s. Eq. 5.5.1)
MA(q)	[–]	Moving average model of order p
MA(n,q)	[–]	n-dimensional MA model of order p
$n = \frac{fL_u}{\bar{U}_z}$	[–]	Dimensionless (reduced) frequency

$n_z = \frac{fz}{U_z}$	[–]	Monin similarity coordinate (dimensionless frequency)
$\{N(t)\}$	[N]	Autocorrelated random process
p	[–]	Number of load coefficients
$p_v(z;t)$	[N/m²]	Velocity pressure
$p(X)$	[–]	Probability density function of the random number X
$\mathbf{p}_k$	[–]	parameter vector
q_W	[N²]	Intensity of the white noise process
Q_k, $\mathbf{Q}_k$	[N²]	Process noise covariance (matrix) at time k
R_k, $\mathbf{R}_k$	[m², (m/s)²]	Measurement noise covariance (matrix) at time k
$R_X(t)$	[N²]	AC function of the stationary process $\{X(t)\}$
$R_X(t_1,t_2)$	[N²]	AC function of the non-stationary process $\{X(t)\}$
$R_{XY}(t)$	[N²]	Cross correlation function of the stationary processes $\{X(t)\}$ and $\{Y(t)\}$
$R_{XY}(t_1,t_2)$	[N²]	Cross correlation function of the non-stationary processes $\{X(t)\}$ and $\{Y(t)\}$
s	[–]	Complex frequency of the Laplace domain
$S_X(\omega)$, $S_X(f)$	[N²s]	two-sided PSD function of the load process $\{X(t)\}$
t	[s]	Time
t_s	[s]	Sampling interval
T	[s]	(Averaging) time period
T_p	[s]	Wave period
$T_u(z)$	[s]	Heights dependent integral time scale of the longitudinal wind fluctuations
u_D, v_D, w_D	[m/s]	Longitudinal (along wind), lateral and vertical component of the dynamic wind velocity fluctuations
U_*	[m/s]	Friction velocity
U_g	[m/s]	Gradient wind velocity
$\bar{U}(z)$, $\bar{U}_z$	[m/s]	Longitudinal mean wind speed
$U(\omega)$	[–]	Unit step function
$\mathbf{U}_D(x,y,z;t)$	[m/s]	Random vector process of the dynamic wind velocity fluctuation at location x, y, z in space and at time t
$v(x,z;t)$	[m/s]	Horizontal water particle velocity
$W(t)$, W_k	[N]	Elements of the white noise process $\{W(t)\}$, $\{W_t\}$
$\{W(t)\}$,$\{\mathbf{W}(t)\}$	[N]	White noise (vector) process
x, y, z	[–]	Coordinates of the Cartesian coordinate system
$\mathbf{x}_{k\|k}$	[m, m/s]	Posterior state estimate at time k including all measurements up to time k

$\mathbf{x}_{k+1\|k}$	[m, m/s]	Prior state estimate at time $k+1$ including all measurements up to time k
X	[–]	Random variable
X_{ref}	[m, m/s]	Reference sensor
$X(t)$, X_k	[N]	Elements of the random process $\{X(t)\}$, $\{X_t\}$
$\{X(t)\}$, $\{\mathbf{X}(t)\}$	[N]	Continuous-time random (vector) process
$\{X_t\}$, $\{\mathbf{X}_t\}$	[N]	Discrete-time (vector) random process
$\mathbf{x}_k$	[–]	State vector
V_k	[m, m/s]	Measurement noise
z	[m]	Height over ground
$z = e^s$	[–]	Complex parameter in the z-domain
z_0	[m]	Roughness length
z_g	[m]	Gradient height
z_{ref}	[m]	Reference height
$\mathbf{z}_k$	[–]	Measurement vector

Mathematical symbols

$\{\cdot\}$	[–]	Random Process
$\binom{n}{k} = \frac{n!}{k!(n-k)!}$	[–]	Binomial coefficient
$\mathbb{C}$	[–]	Set of complex numbers
$\mathcal{C}_q$	[–]	Controllability Matrix of order q
$\delta(t-t_0)$	[–]	Dirac delta function at point t_0
δ_{kj}	[–]	Kronecker delta function
$(D^\gamma f)(t)$	[–]	(Fractional) derivative of order $\gamma \in \mathbb{C}$
$(D_c^\gamma f)(t)$	[–]	Centered Grünwald-Letnikov fractional derivative of order $\gamma \in \mathbb{C}$
$(D_+^\gamma f)(t)$, $(D_-^\gamma f)(t)$	[–]	Right- and left-sided fractional derivative operator of order $\gamma \in \mathbb{C}$
$E[\cdot]$	[–]	Expectation operator
$F_n(x_1,..,x_n;t_1..,t_n)$	[–]	n-th dimensional probability distribution function of a random process
${}_pF_q[a_1,...a_p;b_1,...b_q;z]$	[–]	Generalized hypergeometric function of order p,q
$\mathcal{F}\{\omega;t\}$	[–]	Fourier transform
$\mathcal{F}^{-1}\{t;\omega\}$	[–]	Inverse Fourier transform
$\Gamma(\cdot)$	[–]	Gamma function

$\mathcal{H}_{p,q}$	[–]	Hankel matrix of order p,q
$(I^{\gamma} f)(t)$	[–]	(Fractional) derivative of order $\gamma \in \mathbb{C}$
$(I_c^{\gamma} f)(t)$	[–]	Centered Grünwald-Letnikov fractional integral of order $\gamma \in \mathbb{C}$
$(I_+^{\gamma} f)(t)$, $(I_-^{\gamma} f)(t)$	[–]	Right- and left-sided fractional integral operator of order $\gamma \in \mathbb{C}$
$\{k;\, k = 0,1,2,...\}$	[–]	Discrete index set
$\ln(\cdot)$	[–]	Natural logarithm
$\mathcal{L}(\cdot)$	[–]	Linear differential operator
$\circ\!\!-\!\!\bullet$	[–]	Transform from time to Laplace domain
$\mathcal{M}\{t;\gamma\}$	[–]	Mellin transform
$\mathcal{M}^{-1}\{\gamma,t\}$	[–]	Inverse Mellin transform
$p(x_1,..,x_n;t_1,..,t_n)$	[–]	n-th dimensional probability density function of a random process
$\mathbb{N} = \{1,2,3,...\}$	[–]	Set of positive integer number
$\mathbb{N}_0 = \{0,1,2,...\}$	[–]	Set of non-negative integer numbers
$\mathcal{O}_p$	[–]	Observability Matrix of order p
$\mathbb{R}^{n\times n}$	[–]	$n \times n$-dimensional set of real numbers
$\{X(t_i;\cdot)\}$	[–]	Family of random variables characterizing the random process
$\{X(\cdot;\omega_i)\}$	[–]	Realization of a random process

Acronyms

AC	Autocorrelation function
AIC	Akaike's Information Theoretic Criterion
AvTs	Ambient vibrations Tests
AR	Autoregressive model
ARMA	Autoregressive Moving Average
BR	Balanced Realization Method
CVA	Canonical Variant Analysis
CF	Characteristic Function
EMA	Experimental Modal Analysis
FPE	Akaike's Final Prediction Error Criterion
FRF	Frequency Response Functions
GL	Grünwald-Letnikov

G-EKF	Gaussian Extended Kalman Filter
DC	Data Correlation
DOF	Degree of Freedom
DSS	Data-Driven Stochastic Subspace Method
ERA	Eigensystem Realization Algorithm
EKF	Extended Kalman filter
EMA	Experimental Modal Analysis
FFT	Fast Fourier Transform
FSM	Fractional Spectral Moment
H-EKF	H-fractional Extended Kalman Filter
H-WEKF	Weighted H-fractional Extended Kalman Filter
ITD	Ibrahim Time Domain
IRF	Impulse Response Functions
JONSWAP	Joint North Sea Wave Project
KC	Keulegan-Carpenter Number
KF	Kalman Filter
LS	Least Squares
MA	Moving Average Model
MDOF	Multi Degree of Freedom
MS	Mean Square
MSE	Mean Square Error
MWL	Mean Water Level
PEM	Prediction Error Method
NExT	Natural Excitation Technique
OMA	Operational Modal Analysis
PC	Principal Component Method
PM, P-M	Pierson Moskowitz
PSD	Power Spectral Density
PDF	Probability Density Function
SDOF	Single Degree of Freedom
S-EKF	Spectral Extended Kalman Filter
SISO	Single Input Single Output
SM	Spectral Moments
SSI	Stochastic Subspace Identification Method
SSI-COV	Covariance-Driven SSI Method
SWL	Still Water Level

SVD	Singular Value Decomposition
UPC	Un-Weighted Principal Component Method

1 Introduction

Ambient vibration identification techniques, that is methods, which are based on the measurement of the system-response only, have attracted great interest in engineering in recent years. In the present work a new output-only measurement based method is proposed which allows identifying the modal parameters of structures subjected to autocorrelated loads. The focus lies on the dynamic excitation of structures by wind turbulences and wind-induced ocean waves. In contrast to the classical ambient vibration approaches, statistical information about the dynamic excitation, e.g. obtained by measurement of the wind fluctuations in the vicinity of the structure, are taken into account which improve the identification results as well as allow identifying the unmeasured load process exciting the structure.

1.1 Motivation

Forced vibration tests on structures of civil engineering interest are expensive and time consuming as they are performed using impact hammers or heavy shakers, needed to excite the modes of interest with sufficient energy. Moreover, they often require temporary out of service state of the structure which causes increments of costs. Conversely, ambient vibration tests can be conducted continuously in time measuring the structural response for large time intervals using the excitation of both natural and/or service loads such as wind, traffic, seismic ground motions or human walk. Such loads are caused by the superposition of multiple inputs and thus lead to a broad-band excitation of a significant number of vibration modes [Yuen and Katafygiotis 2001; Cunha and Caetano 2006].
The first use of the ambient vibration technique for the dynamic characterization of full-scale structures is reported in the seventies. Since then, ambient vibration tests gained great attention in civil engineering in the scope of parameter identification (eigenfrequencies, damping ratios and modal shapes) [James et al 1993; Peeters et al 1995, 1998; De Roeck et al 2000; Brownjohn 2003; Ren and Zong 2004; Gentile and Saisi 2007], model updating

[Jaishi and Ren 2005; Gentile and Saisi 2007] as well as damage detection and health monitoring [Doebling and Farrar 1996; Peeters et al 2001; Lee et al 2002] of slender structures such as pedestrian bridges, chimneys, long-span frame structures or high-rise buildings.
In case that the unmeasured system's excitation can be modeled as a stochastic white noise process, various experimental modal identification methods for output-only measurements are available. Whiteness implies that the process is uncorrelated and its power spectral density (PSD) function is constant over all frequencies. From a physical point of view, the white noise process cannot exist in nature as the constant PSD leads to a process with infinite variance corresponding to an unbounded, infinite fast varying signal. However, the white noise assumption is justified, if the PSD function of the input process is flat within the system bandpass, that is within the frequency range in which the system is vibrating predominately. The comparison and discussion of existing ambient vibration identification techniques is beyond this work, but for completeness' sake a conceptional description of the most important time-domain methods can be found in the annexe D.1.
In case of non-white excitations, the parameter identification problem is more complex and classical ambient vibration techniques lead to poor identification results. In this case, the parameter identification problem to be solved consists of two subparts, namely: i) the digital simulation of the random load process; and ii) the estimation of the structural response to the random load using output-only model identification techniques. In case that both parts are handled individually, numerous methods for the system identification as well as for the simulation of stochastic processes are available, but for the solution of the combined problem few techniques appeared in literature (s. chapter 3).
This leads to the motivation to address the identification problem of structures subjected to arbitrarily correlated load processes in this work. Similar to the classical ambient vibration identification techniques, the proposed method is based on output-only measurements of the system response, while the actual load process exciting the structure remains unmeasured. Though, in order to include the load process in the identification algorithm, it is assumed that information about the statistics of the process are available, e.g. from additional measurements in the vicinity of the structure.
The focus of this work lies on the stochastic excitation by wind velocity fluctuations and the random nature of the surface evaluation of the fully developed sea. A large number of actual measured data indicates that such processes can be modeled as stationary Gaussian random processes and thus are completely characterized by the second order statistics, namely mean value and autocorrelation and PSD function, respectively. The assumption of Gaussianity can be justified mathematically by the central limit theorem which states that the sum of a large number of independent identical distributed random variables follows approximately a Gaussian distribution [Maybeck 1979, p. 8, 109].

The solution of the identification problem under correlated loads is based on a concept found in [Lewis et al 2008] which allows introducing colored processes in the Kalman filter algorithm. As many of the classical time-domain ambient vibration identification techniques, the Kalman filter is based on a linear(ized) state space model where random inputs are introduced as Gaussian white noises. In case the white noise assumption is inadequate and autocorrelations in the ambient loads or measurements must be considered, in [Lewis et al 2008] a procedure called state space augmentation is proposed: It is based on the spectral factorization theorem which allows modeling a wide sense stationary random process with given rational PSD function as an output of a linear system with white noise input. This system can then be added to the original system by augmenting the state space representation leading to an overall linear system driven by white noise once again to which standard tools as the Kalman filter based on linear system theory for response analysis, optimization, and design of active control devices can be applied [Chen and Kareem 2001].
Though, difficulties arise if the PSD function is of non-rational form, as in this case, the spectral factorization is difficult and in general not possible in analytic form. In the present work, the problem is solved on basis of a recently developed method which allows representing PSD and autocorrelation (AC) function in closed form by means of a generalized Taylor expansion using fractional spectral moments (FSMs) [Cottone and Di Paola 2010c]. Based on this concept, a state space representation of arbitrarily correlated load processes is derived in analytic form which neither requires the factorization of the PSD nor any optimization procedure and which can be easily combined with common state space model based system identification methods such as the Kalman filter algorithm used here. Moreover, it shall be highlighted, that the method is i) applicable to a wide range of Gaussian processes of both, short and long memory[1]; ii) it allows the simultaneous estimation of the structural parameters and the unmeasured load process; and iii) due to its analytic form its implementation is straight forward.
The outline of the thesis is given in the following.

1.2 Outline

Chapter 2 deals with stochastic models for the description of the dynamic excitation of structures by wind and wind waves. To this aim, physical and phenomenological models of wind turbulences and sea waves are discussed. Emphasis is placed on the spectral representation of wind and wind wave turbulences. Varies model spectra, extensively used in wind

[1] A process with short memory exhibits an exponentially decaying autocorrelation function, while long memory processes are characterized by a much slower decaying autocorrelation function (s. section 5.6)

and ocean engineering are discussed and compared with respect to their applicability and theoretic basis. Furthermore, the equations for the calculation of the associated load spectra are summarized.

In **Chapter 3** a literature review on the state-of-the-art of classical approaches for the digital simulation of stationary Gaussian random processes with target PSD function is given, including the spectral representation methods as well as parametric time series models such as ARMA-based approaches and the spectral factorization theorem. The methods are described and critically discussed with respect to computational efficiency, applicability and restrictions.

Chapter 4 introduces the concept of state space modeling and states space augmentation needed for the derivation of the Kalman filter equations discussed in **Chapter 5** as well as for the development of the new identification algorithm proposed in **Chapter 6**. Furthermore, equivalent state space formulations of the discussed digital filter schemes are derived.

Chapter 5 starts with a brief historical overview of fractional calculus and its importance in engineering applications. In order to explain and clarify the idea of fractional calculus, the Grünwald-Letnikov form of fractional integral and derivative operators is derived which is commonly used for the discretization of such operators. Then the principles of the *fractional spectral moment (FSM) decomposition* proposed in [Cottone and Di Paola 2010c; Cottone et al 2010d] are summarized and verified by three load processes which are of great relevance in wind and ocean engineering. Furthermore, the accuracy and efficiency of the method is discussed. The use of an alternative discretization operator is proposed, which leads to a significant improvement of the accuracy and efficiency of the method. Finally, a modified form of the FSM decomposition is proposed and verified which makes the method applicable for the modeling of long memory processes with unbounded variance.

Chapter 6 recalls the principles of the Kalman filter algorithm in the scope of structural parameter identification under white noise excitation. After explaining the basic concept, the classical Kalman filter equations are derived by means of the Bayesian theorem. Then the theory of the extended Kalman filter (EKF) and the weighted iterated EKF is introduced which is used in the thesis for the solution of the nonlinear parameter identification problem. The method is applied for the identification of the stiffness and damping parameters of a three story shear building excited by Gaussian white noise. By means of a sensitivity analysis the dependence of the filter accuracy and convergence on the initializations of the filter is investigated.

In **Chapter 7** a new extended Kalman filter-based algorithm for the parameter identification of structures excited by correlated random loads is proposed. Focus lies on the stochastic excitation by wind turbulences and wind waves. In contrast to classical ambient vibration identification techniques, which model the unmeasured load process as white noise and thus

are not applicable in case of non-white excitations, the proposed method takes into account additional information about the second-order statistics of the load process, e.g. obtained from measurements in the vicinity of the structure, and thus allows estimating both, the unknown system parameters as well as the unmeasured load process.
The new filter is called *H-fractional (weighted) extended Kalman filter* as it combines the (weighted) extended Kalman filter algorithm with the H-fractional spectral moment decomposition needed for introducing the unmeasured load process into the filter equations. After deriving the latter, the method is applied to estimate the stiffness and damping parameters of single- and multi-degree of freedom systems as well as the unmeasured load process exciting the structure. Finally, a sensitivity analysis is undertaken, in order to investigate the dependence of the accuracy of the load and parameter identification on the chosen parameterization of the load process.
Chapter 8 summarized the results and provides conclusions.

2 Stochastic Models of Dynamic Excitations

The dynamic excitation of structures by natural and/or service loads, such as wind, ocean waves, traffic, seismic ground motion and human walk exhibits an obvious character of randomness and thus is termed stochastic excitation. Consequently, such loads are in general described stochastically in terms of probability and modeled as realizations of random processes. An excellent introduction to stochastic process models for typical dynamic excitations can be found in [Li and Chen 2009, ch. 3].
This chapter deals with the characterization of natural loads which are of great importance in wind and ocean engineering applications, in particular, loads caused by turbulences in the wind velocity flow and by the random nature of the surface evaluation of the ocean. A detailed comparison of the most important model spectra is given with the aim to evaluate their applicability for engineering problems. Restrictions in the applicability result from the fact, that the spectra are in general phenomenological models combining side-specific measurement data with fundamental theory, as will be discussed in the following.
The chapter starts with a brief review on the fundamental principles of random processes and introduces the notation conventions, that will be used throughout the thesis.

2.1 A brief review on probability and stochastic process

A stochastic process (random process or random function) $\{X(t)\}$, denoted in the following by the symbol $\{\cdot\}$, can be represented as a set of random variables $X(t)$ ordered by an index set $t \in T$. If the index set $T = \{t; 0 < t < \infty\}$ is continuous and interpreted as time, then the process is referred to as a continuous time process, while if the random variables X_0,X_1,X_2,... are ordered by the discrete index set $\{k;\ k = 0,1,2,...\}$ the process is called a discrete time process and will be denoted as $\{X_k\}$.
In general, the stochastic process $\{X(t)\}$, $t \in T$ is defined as a function of two arguments

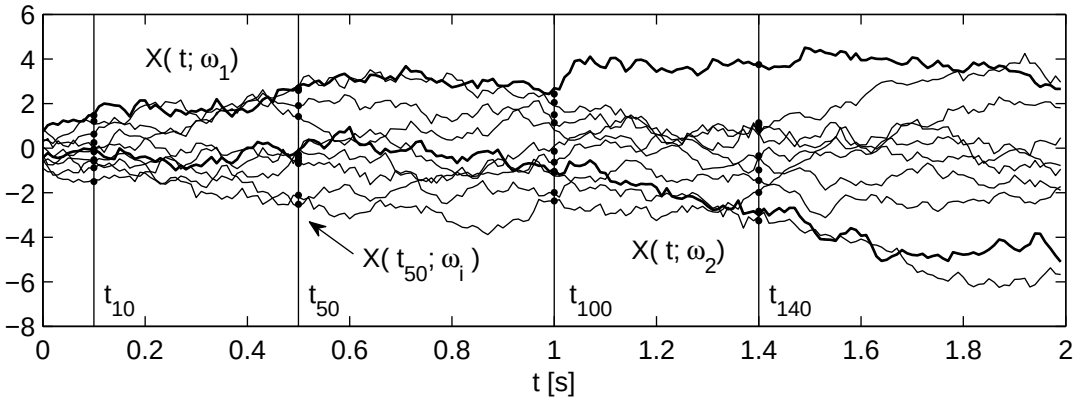

Figure 2.1: Realizations of a continuous-time stochastic process

$\{X(t;\omega); t \in T, \omega \in \Omega\}$ where Ω is called the sample space. If the first argument $t = t_i \in T$ is fixed (indicated as line in Fig. 2.1), then $\{X(t_i;\cdot)\}$ is a family of random variables depending upon the chosen parameter t_i. If instead the second argument $\omega_i \in \Omega$ is fixed, $\{X(\cdot;\omega_i)\}$ is a function of time, depending upon the chosen parameter ω_i[1]. That is, for each outcome ω_i a so-called realization of the process, sometimes also named sample function, trajectory or path [Åström 1970, p. 13-14], is obtained. In that way, a stochastic process can be regarded either as a family of realizations or as a family of random variables as illustrated in Fig. 2.1. In the former case, the process $\{X(t_1;\cdot), t_1 \in T\}$ is characterized by the marginal distribution

$$F(x_1;t_1) = P\{X(t_1;\cdot) \leq x_1\} \tag{2.1a}$$

and corresponding marginal probability density function

$$f(x_1;t_1) = \frac{\partial F(x_1;t_1)}{\partial x_1} \tag{2.1b}$$

Similarly, let $\{X(t;\cdot), t \in T\}$ be a stochastic process which is characterized by the multidimensional set of random variables $X(t_1;\cdot), X(t_2;\cdot), \ldots X(t_n;\cdot)$ defined for arbitrary distinct times $t_i \in T$, $i = 1, 2, \ldots, n$, then its finite dimensional probability distribution is of order n and given by

$$F_n(x_1, x_2, \ldots, x_n; t_1, t_2, \ldots, t_n) = P(X(t_1;\cdot) \leq x_1, X(t_2;\cdot) \leq x_2, \ldots, X(t_n;\cdot) \leq x_n) \tag{2.2a}$$

[1] Throughout this work, the second argument is omitted for sake of simplicity in notation, i.e. $\{X(\cdot;\omega_i)\} \equiv \{X(t)\}$

where $x_i \in \mathbb{R}$. The corresponding finite dimensional density function of $\{X(t)\}$ can be obtained by taking the derivative

$$p_n(x_1, x_2, \ldots, x_n; t_1, t_2, \ldots, t_n) = \frac{\partial^n}{\partial x_1 \partial x_2 \ldots \partial x_n} F_n(x_1, x_2, \ldots, x_n; t_1, t_2, \ldots, t_n) \tag{2.2b}$$

providing that these derivatives exists. However, in order to define a stochastic process by an arbitrary collection of distribution functions F_n, $n = 1, 2, \ldots$ the latter must satisfy the conditions of symmetry and consistency (Kolmogorov's theorem [Kolmogorov 1933]): The symmetry condition implies that F_n is symmetric in all pairs $(t_i; x_i)$ and the consistency condition states that any distribution function $F_m(x_1, x_2, \ldots, x_m; t_1, t_2, \ldots, t_m)$ of order $m < n$ can be derived from the distribution function $F_n(x_1, x_2, \ldots, x_n; t_1, t_2, \ldots, t_n)$ [Åström 1970, p. 14].

2.1.1 Second-order characterization

In order to have a complete probabilistic description of a stochastic process, the distribution function (2.2a) must be known for every set of random variables belonging to that process, that is for all possible choices of x_i, t_i and $n = 1, 2, \ldots$. Therefore, such a complete probabilistic process model is rarely used in engineering applications since it contains far too many parameters to be estimated from a finite measurement data set [Brockwell and Davis 2002, p. 7]. Instead, the random variables of the process are often characterized by certain averages, the so-called expected values. Assume a random variable X with probability density $p(X)$, then the expectation operator, denoted as $E[\cdot]$ is defined as

$$E[g(X)] = \int_{-\infty}^{\infty} g(x)p(x)dx \tag{2.3a}$$

which can be interpreted as the probability weighted average of all possible outcomes of the function $g(\cdot)$. Choosing $g(X) = X^j$, the formal definition of integer moments of order $j \in \mathbb{N}$ is obtained, i.e.

$$E\left[X^j\right] = \int_{-\infty}^{\infty} x^j p(x)dx \tag{2.3b}$$

In particular, the first order moment, i.e. $\mu = E[X]$, is commonly denoted as mean value of the random variable X, while the second order moment is related to the variance using the identity $\sigma^2 = E[X^2] - \mu^2$. Instead of calculating the moments of the random variable X by evaluating the integral, they can be also derived from the Fourier transform of the probability density function, the so-called characteristic function as shown in A.1.1 for completeness'

sake.

The concept can be extended for random vectors and used for the characterization of random processes. Let $X(t_1)$, $X(t_2)$, ... $X(t_n)$ denote a finite set of the random process $\{X(t;\cdot), t \in T\}$, then the joint moments of order $m = m_1 + \ldots + m_n$ are defined by the ensemble average

$$E\left[X(t_1)^{m_1}..X(t_n)^{m_n}\right] = \int_{-\infty}^{\infty}..\int_{-\infty}^{\infty} x_1^{m_1}\ldots x_n^{m_n} p(x_1,..,x_n;t_1,\ldots,t_n)dx_1..dx_n \tag{2.4}$$

In many applications the second order statistics, i.e. the first and second order moments, namely the mean $\mu(t)$ and AC function $R(t_1,t_2)$ are of particular interest and given by

$$\mu(t) = E\left[X(t)\right] = \int_{-\infty}^{\infty} xp(x,t)dx \tag{2.5a}$$

$$R_X(t_1,t_2) = E\left[X(t_1)X(t_2)\right] = \int_{-\infty}^{\infty}\int_{-\infty}^{\infty} x_1x_2p(x_1,x_2;t_1,t_2)dx_1dx_2 \tag{2.5b}$$

The AC function is related to the autocovariance function by

$$C_X(t_1,t_2) = R_X(t_1,t_2) - \mu_1(t)\mu_2(t) \tag{2.5c}$$

that is, in case the process is of zero mean AC and covariance function coincide.

In many cases, the second order statistics of the process are assumed to be time-invariant and ergodic (s. A.1.3). In this case, the time average over a single long time history $\{X(\cdot;\omega_i)\}$ of the process and the ensemble average of a large number of realizations $\{X(t_i;\cdot)\}$ coincide [Lutes and Sarkani 2004, p. 251]. Thus, instead of using Eqs. (2.5), the mean $\mu(t)$ and AC function $R(\tau)$ of an ergodic and stationary process can be expressed in the form

$$\mu(t) = E\left[X(t)\right] = \int_{-\infty}^{\infty} X(t)dt = const. \tag{2.6a}$$

$$R_X(\tau) = E\left[X(t)X(t+\tau)\right] = \int_{-\infty}^{\infty} X(t)X(t+\tau)dt \tag{2.6b}$$

where τ denotes an arbitrary time shift. Processes which satisfy the conditions (2.6) are said to be *stationary in the wide sense* [Priestley 1981, ch. 3]. Alternatively, they can be characterized in the frequency domain by its PSD function $S_X(\omega)$. The AC and the PSD are related by the Fourier transform pair

$$R_X(\tau) = \mathcal{F}\{S_X(\omega);t\} = \int_{-\infty}^{\infty} S_X(\omega)e^{i\omega\tau}d\omega \tag{2.7a}$$

$$S_X(\omega) = \mathcal{F}^{-1}\{R_X(\tau);\omega\} = \frac{1}{2\pi}\int_{-\infty}^{\infty} R_X(\tau)e^{-i\omega\tau}d\tau \tag{2.7b}$$

Clearly, the concept of stationarity can be extended to higher-order moments (s. A.4). The most rigorous definition of stationarity is the so-called strict stationarity, which says that the

joint finite dimensional distribution defined in (A.5) characterizing the process is invariant for an arbitrary time shift. It must be kept in mind, that in general case the knowledge of the time-invariance of the second order moments does not provide any information on the finite dimensional distribution, and thus, a stationary process in the wide sense may not be stationary in the strict sense.
Wide-sense stationary processes can be characterized by the so-called *spectral* moments (SMs) introduced by [Vanmarcke 2010]. They are the moments of the one-sided PSD $G_X(\omega)$

$$\lambda_X(\gamma) = \int_0^\infty 2U(\omega)S_X(\omega)\omega^\gamma d\omega = \int_0^\infty \omega^\gamma G_X(\omega)d\omega \tag{2.8}$$

where $U(\omega)$ is the unit step function and where $\gamma \in \mathbb{N}_0$. They represent important time-domain properties of the underlying process, in particular the zero-order SM $\lambda_X(\gamma = 0)$ corresponds to the variance of the process $\{X(t)\}$ and the second- and forth-order SMs $\lambda_X(\gamma = 2)$, $\lambda_X(\gamma = 4)$ give the variance of its derivatives $\{\dot{X}(t)\}$, $\{\ddot{X}(t)\}$, respectively. Higher order SMs are not of general interest, as they do not provide further information about the process and are often divergent.
Later in section 5 the classical SMs are generalized for complex orders, that is $j \in \mathbb{C}$ and denoted as $\Lambda_X(\gamma)$. They are called fractional spectral moments and will be essential for the development of the novel identification method proposed in chapter 7.

2.1.2 Important processes

In the following the properties of the Gaussian random process and the Gaussian white noise process are briefly reviewed. For completeness' sake, in annexe A.1.4 the Brownian motion process is discussed, which is of great importance for the solution of stochastic differential equations with white noise input as they are appear within the Kalman filter framework. Furthermore, the second order statistics of multivariate and multidimensional Gaussian random processes are summarized.

2.1.2.1 White noise process

A stationary random process with constant PSD function $S_W(\omega)$ is defined as white noise process $\{W(t)\}$. Whiteness implies that the process is uncorrelated, i.e. its AC function is described by the dirac delta function $\delta(t)$, being infinite at time lag $\tau = 0$ and zero elsewhere,

and the PSD function is constant over all frequencies, i.e.

$$\begin{aligned} S_W(\omega) &= \frac{q_W}{2\pi} \\ R_W(\tau) &= q_W \delta(\tau) \end{aligned} \tag{2.9}$$

where q_W is the intensity of the process. *Band limited white noise* denotes a process whose PSD function is flat over a finite range of frequencies and vanishes above a certain frequency ω_0. Its AC and PSD function is given by

$$\begin{aligned} S_{Wb}(\omega) &= \begin{cases} \frac{q_W}{2\pi}, & |\omega| \leq \omega_0 \\ 0, & \text{else} \end{cases} \\ R_{Wb}(\tau) &= \frac{q_W}{\pi\tau} \sin(\omega_0 \tau) \end{aligned} \tag{2.10}$$

The so-called *white noise sequence* refers to a discretized white noise process with zero mean and AC function

$$R_W(\tau) = E[W_k W_j] = q_W t_s \delta_{kj} \tag{2.11}$$

where δ_{kj} denotes the Kronecker delta function, q_W denotes the intensity and t_s the sampling interval. If the random variables W_k are assumed to be Gaussian distributed, the process is referred to as Gaussian white noise sequence and will be indicted as

$$\{W_t\} \sim \mathrm{WN}(0, \sigma_W^2) \tag{2.12}$$

where $\sigma_W = \sqrt{q_W t_s}$. In the multivariate case the zero mean white noise sequence is defined similarly

$$\mathbf{R}_W(\tau) = E[\mathbf{W}_k \mathbf{W}_j^T] = \mathbf{R}\delta_{kj} \qquad \text{indicated as} \qquad \{\mathbf{W}\} \sim \mathrm{WN}(\mathbf{0}, \mathbf{R}) \tag{2.13}$$

where $\mathbf{R} = \sigma_W^2 \mathbf{I} \in \mathbb{R}^{m \times m}$ denotes the autocovariance matrix of the vector process $\{\mathbf{W}\} \in \mathbb{R}^m$ and $\mathbf{I} \in \mathbb{R}^{m \times m}$ the identity matrix. In annexe A.1.4.3 more details about the white noise process and its applicability are given.

2.1.2.2 Gaussian process

In engineering, many physical phenomena are the result of the superposition of a large number of individual random processes. E.g. the randomness of wind turbulences is caused by

the superposition of eddies of different sizes and rotational velocity and the random pattern of the surface evaluation of the fully developed sea can be thought to be the result of the superposition of an infinite number of independent sinusoidal waves with random phase, height, wavelength and propagation direction. Short-term measurements of the wind fluctuations over homogeneous terrain[2] and the ocean indicate that such processes may be be modeled as stationary Gaussian process. The assumption of Gaussianity can be justified mathematically by the central limit theorem which states that the sum of independent identical distributed random variables follows approximately a Gaussian distribution [Maybeck 1979, p. 8, 109]. A process is said to be Gaussian, if the finite dimensional density function of the process $\{X(t)\}$ follows a normal distribution (see A.7). Thus, Gaussian processes are completely characterized by the statistics up to the second order. Hence, the existence of a time invariant mean $\mu(t)$ and autocorrelation function $R_X(\tau)$ defined in Eq. (2.6) ensures the stationarity of the Gaussian process. That is, in the Gaussian case, weak stationarity of the process also implies strict stationarity.

Another important property of the Gaussian process which makes it so interesting in many applications, is its invariance of linear transformation. That is, a stationary Gaussian process which undergoes a linear transformation such as integration, differentiation, linear filtering, sampling and summation with other Gaussian processes, remains Gaussian [Bendat and Piersol 2010, p. 147ff.]. This concept is extensively used for the modeling of random processes as discussed in chapter 3 as it allows generating a colored Gaussian process with target PSD function, by passing a Gaussian white noise through a linear system. Moreover, the property strongly contributed to the great success of the Kalman filter algorithm, used in chapter 6 to solve the parameter identification problem, as it allows performing the filter operations rapidly and efficiently.

The following two sections describe the second order statistics of loads caused by turbulences in the wind velocity flow and by the random nature of the sea surface evaluation. Focus lies on the spectral representation of such loads as it will be needed for the development of the proposed identification algorithm. To this aim a detailed comparison of the most important model spectra is given and their applicability and restrictions for the use in engineering applications is discussed.

[2] For the turbulence in complex terrain a skewness of about −0.1 is not uncommon, implying that the Gaussian model is not quire fulfilled [Det Norske Veritas 2010]

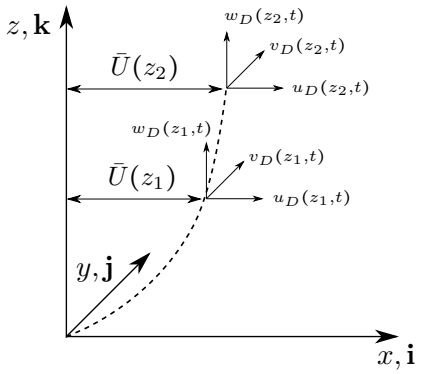

Figure 2.2: Velocity components of turbulent wind [Balendra 1993, p. 50]

2.2 Aerodynamic Wind Excitation

Wind is the result of moving air caused by varying thermal and pressure conditions in the atmosphere. The wind velocity at a given point in the space is usually modeled as a Gaussian stochastic process completely characterized by its mean value and its power spectral density function. Let x, y, z be a location in space, where z is the distance from the ground and x defines the along-wind direction, then the wind velocity field $U(x,y,z;t)$ can be decomposed into its time average $\bar{U}(z)$ of the main wind direction at height z and a zero mean random vector process $\mathbf{U}_D(x,y,z;t) = [u_D(x,y,z;t),v_D(x,y,z;t),w_D(x,y,z;t)]$, describing its dynamical fluctuations [Di Paola and Zingales 2008] as shown in Fig. 2.2. Hence, the velocity field is characterized in vector form by [Balendra 1993, p. 49]

$$U(x,y,z;t) = \bar{U}(z)\mathbf{i} + u_D(x,y,z;t)\mathbf{i} + v_D(x,y,z;t)\mathbf{j} + w_D(x,y,z;t)\mathbf{k} \tag{2.14}$$

If the averaging time is sufficient long, typically $T = [10,60]$ [min.], then the mean value $\bar{U}(z)$ is a time-invariant function of the height z. Due to the surface friction, the mean wind speed increases with height until it reaches a constant value at great distance where frictional effects are negligible. The so-called gradient wind velocity $U_g(t)$ results from pressure gradients in the atmosphere caused by the varying solar heating of the earth [Mendis et al 2007]. The region in which the friction forces influence the wind velocity is called *atmospheric boundary layer* whose thickness z_g (the gradient height) depends on the ground roughness. In Fig. 2.3 a typical measurement of wind speeds at three heights on a tall mast for a fully developed boundary-layer flow in the atmosphere is shown. The following properties can be observed [Holmes 2007, p. 55-56]:

(i) The average wind velocity increases with increasing height.

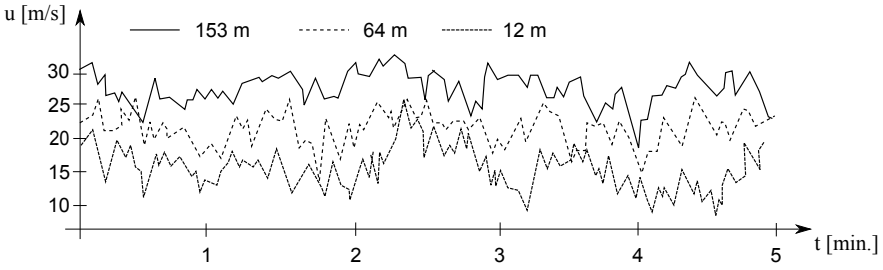

Figure 2.3: Typical measurement of wind speeds at three heights during gales on a tall mast for a fully developed boundary-layer flow in the atmosphere [Holmes 2007, p. 56]

(ii) Gusts/turbulences occur at all heights.

(iii) The gusts show a broad band frequency content, i.e. slowly changing gusts are superposed by high frequent variations in the wind flow.

(iv) In particular, the slow frequent variations seem to be similar at all heights.

Van der Hoven [Van der Hoven 1957] investigated the frequency dependency of the wind characteristics and weather systems in the atmospheric boundary layer based on long- and short term measurements of the wind velocity taken at 80 [m] height at the meteorological tower of the Brookhaven National Laboratory, New York. Fig. 2.4 shows the proposed wind spectrum over a wide range of frequencies, constructed by piercing together various portions of the spectrum. It indicates how the variance of the wind process is distributed with respect to frequency. As the frequency axis ranges over several decades, a logarithmic scale is used for the horizontal axis. In order to preserve that the area below the power spectral density function $S(f)$ is proportional to the energy per frequency, the vertical axis is multiplied by the frequency using the following identity

$$\sigma_u^2 = \int_0^\infty G_u(f)df = \int_0^\infty f \cdot G_u(f)d(\ln f) \tag{2.15}$$

where $G_u(f) = 2S(f)$ denotes the one-sided power spectral density function.
The wind spectrum is split into three domains, namely the *mesometeorological* and *micrometeorological* range describing wind speed fluctuations for periods longer and shorter than about one hour, respectively, and a *spectral gap* where the spectral energy is negligible. In the former the peaks result from seasonal and daily variations (seasonal, diurnal peak) as well as changes in the general weather patterns (synoptic peak) due to the passing of large pressure systems, occurring typically all four days [Burton et al 2001, p. 11ff]. The associated long term (i.e. low-frequency) variations of the wind velocity on a time-scale of one to several hours, can be considered constant if viewed at turbulence time scale, and thus are referred to as quasi-steady mean wind speed [Gavriluta et al 2012]. If the spectral gap in

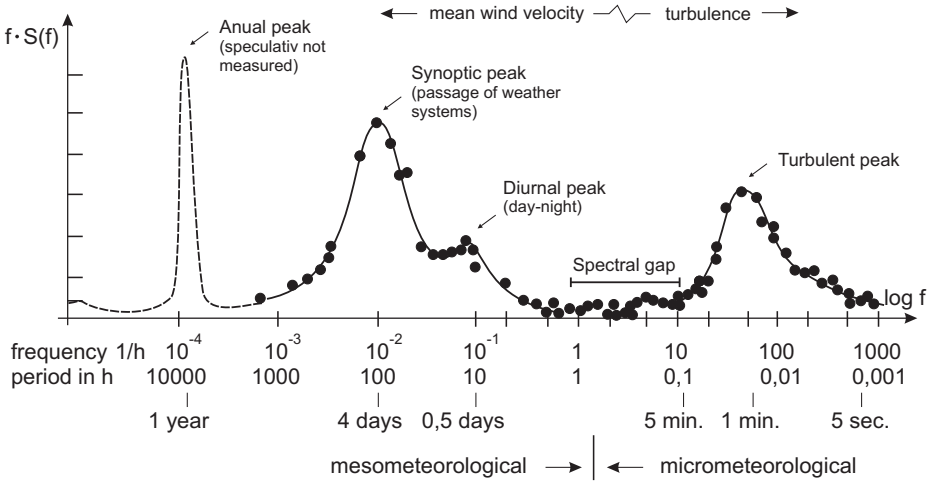

Figure 2.4: Broad band frequency spectrum of the horizontal wind velocity proposed by Van der Hoven (1957) based on measurements taken form the farm Brookhaven, New York [Burton et al 2001, p. 12], [Petersen 2000, p. 596]

the period from approximately one day to 10 minutes is reasonably distinct, then the long and short term variations, i.e. the mean velocity and the turbulent fluctuations, are mutually independent and can be treated separately by choosing an appropriate averaging time for the calculation of the power spectrum and superposed as in Eq. (2.14). In many wind engineering applications just the high frequency micrometeorological domain of the wind spectrum corresponding to the turbulences, i.e. wind fluctuation of typically 10 minutes time scale, of the boundary layer is of interest. Due to the spectral gap, the latter can be modeled as zero mean random process based on the micrometeorological power spectral density function, if averaging is performed on a 10 minutes time window [Burton et al 2001, p. 11ff].
The main properties of the wind mean velocity and the wind turbulences are discussed in the following.

2.2.1 Mean wind velocity profile

The mean wind velocity profile within the atmospheric boundary layer is depicted for different terrains in Fig. 2.5. It can either be described by a power law or logarithmic law. The latter can be derived analytically from the physics of the boundary layer (see for instance [Holmes 2007, p. 56ff.]) and is used by both engineers and meteorologists for modeling the strong wind conditions in the upper 20-30% of the atmospheric boundary layer near the surface [Stathopoulos and Baniotopoulos 2007, p. 2]. It is given by

$$\bar{U}(z) = \frac{1}{k} U_* \ln\left(\frac{z-d}{z_0}\right) \tag{2.16}$$

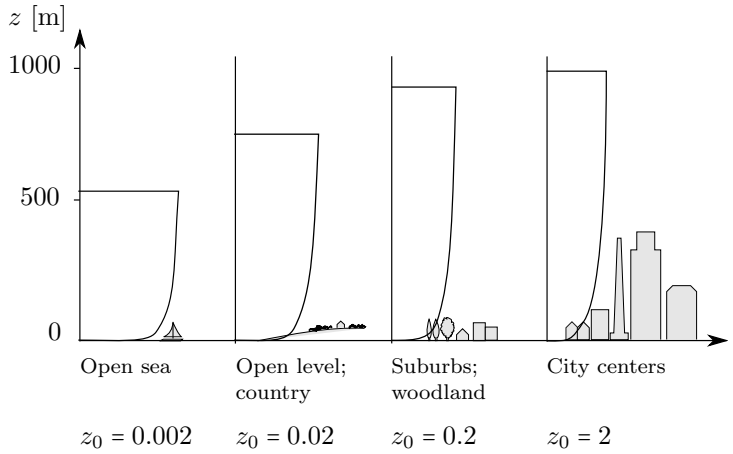

Figure 2.5: Mean wind profiles for different terrains [Mendis et al 2007]

where $k \approx 0.4$ is the exponentially found von Kármán's constant, U_* [m/s] denotes the friction velocity and z_0 [m] is the roughness length, related to the roughness of the ground surface. If the mean velocity is known for a given height above ground, then the friction velocity can be calculated from Eq. (2.16) by

$$U_* = k\bar{U}(z)\ln^{-1}\left(\frac{z-d}{z_0}\right) \tag{2.17}$$

Another measure for the surface roughness is the so-called dimensionless surface drag coefficient κ [-] which can be used to relate the friction velocity to the mean wind speed at 10 [m] above ground by $U_* = \sqrt{\kappa}\,\bar{U}(10)$. Both parameters are given in Tab. 2.1 for different terrain conditions [Holmes 2007, p. 55 ff]. The constant d [m] is the height above the ground where the velocity is zero. In the open terrain or sea d can be set to zero, while for very rough terrain, such as urban areas or forests, d is about one or two meters below the average height of trees and buildings, i.e. typically values in city centers are $d \approx 10-25$ [m] and in suburban terrain $d \approx 5-10$ [m] [Balendra 1993, p. 49]. Due to the mathematical properties of the logarithmic function, the mean velocity pursuant to Eq. 2.16 is not defined for $z < d$ and is negative in case $z - d < z_0$. Furthermore the logarithmic law was derived for fully developed wind flow over homogeneous terrain which is rarely the case in engineering applications [Holmes 2007, p. 55 ff]. Hence, the power law is preferred by some engineers and is defined empirically by

$$\bar{U}(z) = \bar{U}(z_{ref})\left(\frac{z}{z_{ref}}\right)^{\alpha} \tag{2.18}$$

Terrain type	roughness length z_0 [m]	surface drag coefficient κ [-]
Very flat terrain (snow, desert)	0.001 - 0.005	0.002 - 0.003
Open terrain (grassland, few trees)	0.01 - 0.05	0.003 - 0.006
Suburban terrain (buildings 3 - 5 m)	0.1 - 0.5	0.0075 - 0.02
Dense urban (buildings 10 - 30 m)	1 - 5	0.03 - 0.3

Table 2.1: Terrain types, roughness length and surface drag coefficient [Holmes 2007, p. 58]

where the reference height is in general set z_{ref} = 10 [m] and where α denotes the power exponent [Balendra 1993] which depends on the surface roughness and the height range of the trees and buildings. The main advantage of the power law towards the logarithmic law is related to the fact, that integrations of the power law needed in the response analysis can be performed much easier than in case of the logarithmic law. However, both profiles can be matched closely with respect to a chosen reference height z_{ref} by the relationship $\alpha = \ln(z_{ref}/z_0)^{-1}$ which relates the exponent α of the power law and the surface roughness length z_0 of the logarithmic law [Holmes 2007, p. 58-59].

2.2.2 Turbulence

The fluctuating components in Eq. (2.14) are known as turbulences which result either from convective movement, so-called meteorological turbulences, and/or ground roughness referred to as mechanical turbulences due to the retarding effect of obstacles (e.g. buildings), the terrain type (open field, forest, etc.) and general relief or topography. In engineering, in general just the mechanical turbulences are of interest, as they are predominant in the case of boundary layer flow at high wind speed.
The turbulence or gustiness is lower in smoother terrain (e.g. grass land) than in rougher terrain (e.g. urban with tall buildings) and decreases with increasing height above ground [Stathopoulos and Baniotopoulos 2007, p. 3-4]. The longitudinal component $u_D(x,y,z;t)$ of the wind fluctuations $\mathbf{U}_D(x,y,z;t)$ in Eq. (2.14) is the largest one and especially effects vertical structures such as high rise buildings which are flexible in the along-wind direction. The vertical component $w_D(x,y,z;t)$ is mainly relevant for horizontal, i.e. vertically flexible, structures such as long-span bridges [Balendra 1993, p. 49]. The turbulences are characterized by the turbulence intensity, the correlation lengths and the power spectral density functions: The former is a measure of the magnitude of the wind velocity fluctuations, the autocorrelation function is a measure of the wind field's memory and related to the eddy size and the power spectral density function gives information about the frequency content of the turbulence and is especially important for structural design. In the following sections, these properties will be discussed in detail.

2.2.2.1 Turbulence intensity

The turbulence intensity is a measure of the standard deviation σ of the turbulences which can be estimated either by calculating the root mean square (here given exemplarily for the longitudinal wind direction) of the velocity fluctuations or by integration of the PSD function of the wind turbulences, i.e.

$$\sigma_u = \sqrt{\frac{1}{T}\int_0^T u_D(x,y,z;t)^2 dt} = \sqrt{\int_0^\infty G_u(f)df} \tag{2.19}$$

where T is the averaging period. The turbulence intensities I_u, I_v, I_w are defined as the ratio of the standard deviation of the corresponding fluctuation component and the mean value of the predominant wind direction, i.e.

$$I_u = \frac{\sigma_u}{\bar{U}(z)}; \qquad I_v = \frac{\sigma_v}{\bar{U}(z)}; \qquad I_w = \frac{\sigma_w}{\bar{U}(z)} \tag{2.20}$$

2.2.2.2 Integral scales of turbulence

Wind turbulences can be decomposed into a mixture of eddies of different sizes and rotational characteristics which are transported by the mean wind $\bar{U}(z)$ [m/s] and which fluctuate with a certain frequency f [Hz]. Theoretically, spatial distribution, size and form of the eddies are irregular in space and subjected to permanent changes in time. Geoffrey I. Taylor (1939) suggested that under certain conditions, the turbulence statistics can be thought to be 'frozen' in time while the wind field propagates in space with mean velocity. That suggestion is also known as *Taylor's frozen-in turbulence hypothesis* ([Holm 2005]) and is based on the assumptions that the rate of change of the eddy size and distribution is small compared to the propagation velocity in space. Consequently, the time while the eddy passes the observer is too short for noticeable changes and hence can be considered as 'frozen' [Mur Amada 2009, p. 11]. Based on the Taylor's hypothesis, the size of the eddies can be related to the time scale, i.e. the eigenperiod or frequency of the fluctuations, respectively, by the wavelength $\lambda = \bar{U}(z)/f$ [m]. The average sizes of the eddies are measured by an integral length scale, sometimes also called correlation length of the turbulence, as it is based on the normalized autocorrelation function, here given for the longitudinal component by

$$\rho_u(x,y,z;\tau) = \frac{\int_0^T u(x,y,z;t)u(x,y,z;\tau+t)dt}{\int_0^T u(x,y,z;t)^2 dt} \tag{2.21}$$

If the velocity flow is horizontally homogeneous, i.e. independent of the location x, y and thus $u(x,y,z;t) = u(z;t)$ as assumed in the following, then the autocorrelation function depends only on the height z above the ground and the time shift τ of the velocity signal.
The integral time scale T_u given by

$$T_u(z) = \int_0^\infty \rho_u(z;\tau)d\tau \tag{2.22}$$

is a measure of the average period over which the wind velocity fluctuation are correlated. According to Taylor's hypothesis, $\rho_u(z;\tau) = \rho_u(z;r_x)$, where $r_x = \bar{U}_z\tau$ denotes the distance in along wind direction between two locations in space. Consequently, the longitudinal integral length scale of the eddies can by obtained simply by multiplication of the integral time length with the mean wind velocity, leading to [Dyrbye and Hansen 1997, p. 40]

$$L_u(z) = T_u(z)\bar{U}(z) \tag{2.23}$$

Each of the fluctuating velocity components $u_D(z;t)$, $v_D(z;t)$ and $w_D(z;t)$ is characterized by three integral scales $L_i^x(z)$, $L_i^y(z)$, $L_i^z(z)$ and $i = u, v, w$ in longitudinal, lateral and vertical directions corresponding to the three dimensions of the eddies in space leading altogether to nine integral scales of turbulence [Simiu and Scanlan 1996, p. 53ff]. If the size of the eddies and the dimensions of the structure are comparable so that the turbulences envelope the structure completely, then the correlation of the wind pressure might lead to a significant excitation of the structure. However, small eddies effect the structure just locally so that the pressure fluctuations can be considered to be uncorrelated with distance of separation and the overall effect of the longitudinal turbulence will be small [Mendis et al 2007]. In section 2.2.3 an aerodynamic admittance function is introduced, which takes this effect into account. The integral length scales can be estimated by full-scale measurements. Similar to the mean velocity, the eddy size depends mainly on the surface roughness z_0 of the terrain, the height over ground z and - at greater heights - on the wind speed. The quality of the estimates strongly depends on the degree of stationarity of the used wind records [Dyrbye and Hansen 1997, p. 41]. J. Counihan analyzed wind velocity data based on measurements in the period 1880 - 1972 and discussed various models of the integral length scale. He observed that the integral length scale increases with decreasing surface roughness z_0 and increases with the height. He suggested the following purely empirical expression for the longitudinal integral length scale [Counihan 1975]

$$L_{C,u} = Cz^m \tag{2.24}$$

at heights in the range of $z = 10 - 240$ [m] over ground. Values for the parameters C and m are given graphically as function of the surface roughness in [Counihan 1975]. Purely empirical formulations as the one proposed by Counihan are often based on records obtained at heights comparatively near the ground and at moderate hourly-mean reference wind speeds corresponding to $\bar{U}_{10} = 10$ [m/s] at heights $z = 10$ [m]. However, typical design wind speeds are of order $\bar{U}_{10} = 20 - 30$ [m/s] which leads to semi-theoretical models of the integral length scale by extrapolating the measured data obtained at moderate wind speeds and heights to the much higher design wind speed at heights corresponding to taller buildings. The model proposed by the Engineering Sciences Data Unit [ESDU-85020 1985] is based on a similarity theory approach and the observation, that the influence of the wind velocity on the eddy size is no longer negligible at greater height. It leads to fairly complicated expressions for the integral scale length depending on the ratios z/h, σ_u/U_* and the so-called Richardson number $U_*/(fz_0)$ obtained by spectral fitting of the von Kármán spectrum to measurement data [Burton et al 2001, p. 25] (compare Eq. 2.33-2.35).

2.2.2.3 Asymptotic properties of the turbulence spectra

As discussed in section 2.2, the frequency content of the gusts is characterized by the micrometeorological range of the PSD of the wind velocity. If measurement data is available, the site-specific spectral densities of the turbulence can be obtained by spectral fitting. Besides, there exists various model spectra, which were derived combining empirical observations and theoretic aspects. In section 2.2.2.4 some of the most widely used spectra will be discussed and compared. To this aim in the following, the asymptotic characteristics resulting from theory are defined.

According to the *Kolmogorov law*, the wind velocity spectrum decays proportionally with $f^{-5/3}$ at high frequencies [Burton et al 2001, p. 22]. As illustrated in Fig. 2.6, it is based on the observation that turbulent energy is generated in large eddies (low frequencies) either by shear wind or convection and dissipated by the decay of the eddies to higher and higher frequencies until a sufficiently small length scale is reached such that the viscosity of the fluid can effectively dissipate as heat [Dyrbye and Hansen 1997, p. 41-42]. According to Kolmogorov's second hypothesis, in the intermediate range, the so-called inertia subrange, the production and dissipation of turbulent energy is balanced and the eddy motion is assumed to be independent of the viscosity and solely determined by the energy transfer leading to a constant rate of energy dissipation ϵ. Kolmogorov showed that the following relation holds

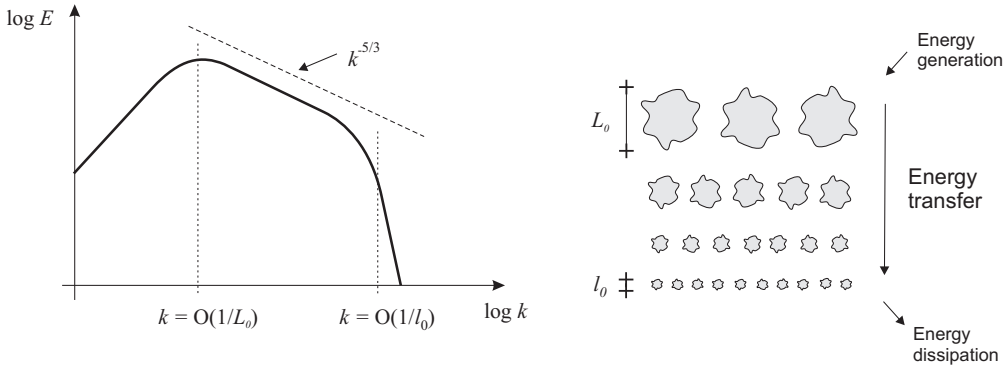

Figure 2.6: Left: Log-Log plot of the energy spectrum of turbulence where the power law $k^{-5/3}$ appears as straight line [Mathieu and Scott 2000, p. 242]; Right: Energy cascade theory, i.e. energy transfer by the continuous break up of the eddies into smaller eddies from a macroscale L_0 (outer scale of turbulence) to a microscale l_0 (inner scale of turbulence) [Andrews 2004, p. 6ff]

for high wavenumbers $k = 2\pi/\lambda$ [rad/m] [Simiu and Scanlan 1996, p. 55-56]

$$S_u(k) = a\epsilon^{2/3}k^{-5/3} \qquad \Leftrightarrow \qquad S_u(f) = a\epsilon^{2/3}\left(\frac{2\pi f}{\bar{U}_z}\right)^{-5/3} \tag{2.25}$$

where $a = 0.5$ has been found by measurements. The second relation is obtained, by substituting $k = 2\pi f/\bar{U}(z)$ using Taylor's hypothesis (2.2.2.2). Close to the ground, the integral length scale can be assumed to be of order z. For a given average velocity $\bar{U}_z$, height z and terrain roughness length z_0, Kolmogorov proposed the following normalized one-sided PSD function [Andersen and Enmark 2011, p. 397]

$$\text{Kolmogorov:} \quad \frac{fG_u(f)}{U_*^2} = 0.26n_z^{-2/3} \tag{2.26}$$

where U_* is the friction velocity defined in Eq. (2.17) and where the dimensionless frequency $n_z = fz/\bar{U}_z$ is also known as Monin similarity coordinate [Dyrbye and Hansen 1997, p. 42]. In general, Eq. (2.26) provides a very good approximation of spectra in the high frequency region[3] and may, for engineering purposes, be conservatively assumed to be valid for $n_z > 0.2$ [Simiu and Scanlan 1996, p. 59]. However, at greater heights, the turbulence scale cannot be assumed to be proportional to the height and hence z is in general replaced by the turbulence length scale defined in Eq. (2.23). Experimental measurements at different heights in the inertial subrange and dimensional analysis indicated that the non-dimensional half-power

[3] in the following the frequency band of the turbulence spectrum between $n, n_z = 0$ and the lower end of the inertia subrange is indicated as low frequency range and beyond as high frequency range.

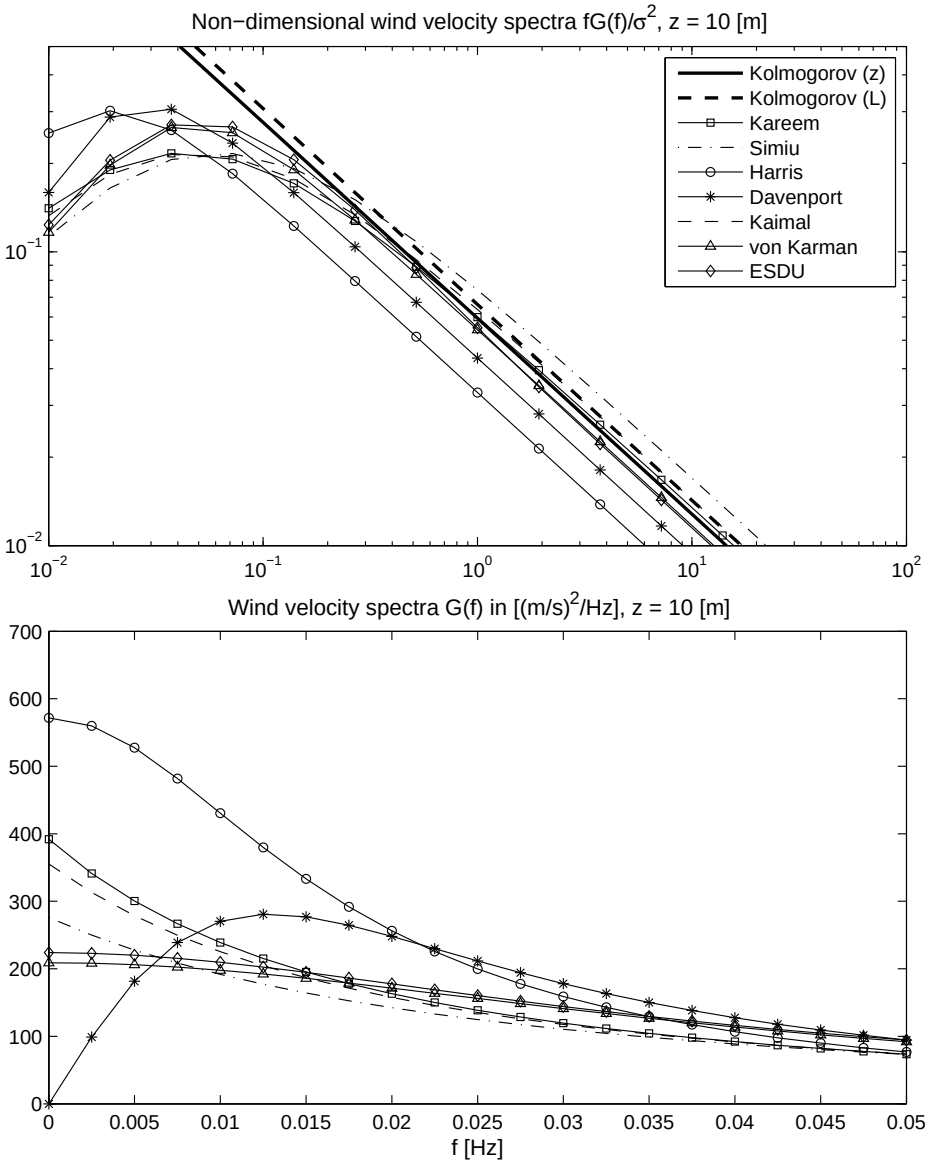

Figure 2.7: Chosen parameters: $z = 10$ [m], $\bar{U}_{10} = 20$ [m/s] , $L_u(z) = L_u^{EC}(z)$ [m] pursuant to Eq. (2.30), $z_0 = 0.05$ [-], $\kappa = 0.006$ [-] (open terrain, grassland); Top: Log-Log plot of the non-dimensional turbulence spectra; Bottom: Comparison of the spectra in the low-frequency range

spectrum, the so-called reduced PSD, approaches at high frequencies

$$\text{Kolmogorov } (L_u): \qquad \frac{fG_u(f)}{\sigma_u^2} \approx A(z) n^{-2/3} \tag{2.27}$$

using the dimensionless (or reduced) frequency $n = fL_u/\bar{U}_z$, and where $A(z)$ is typically of order $0.1 - 0.15$ [Mur Amada 2009, p. 13]. As it is closely related to the Kolmogorov form defined in Eq. (2.26) with the main difference, that the dimensionless frequency is depending on the integral scale length $L_u(z)$ instead of the height z, it is denoted as *Kolmogorov (L)*

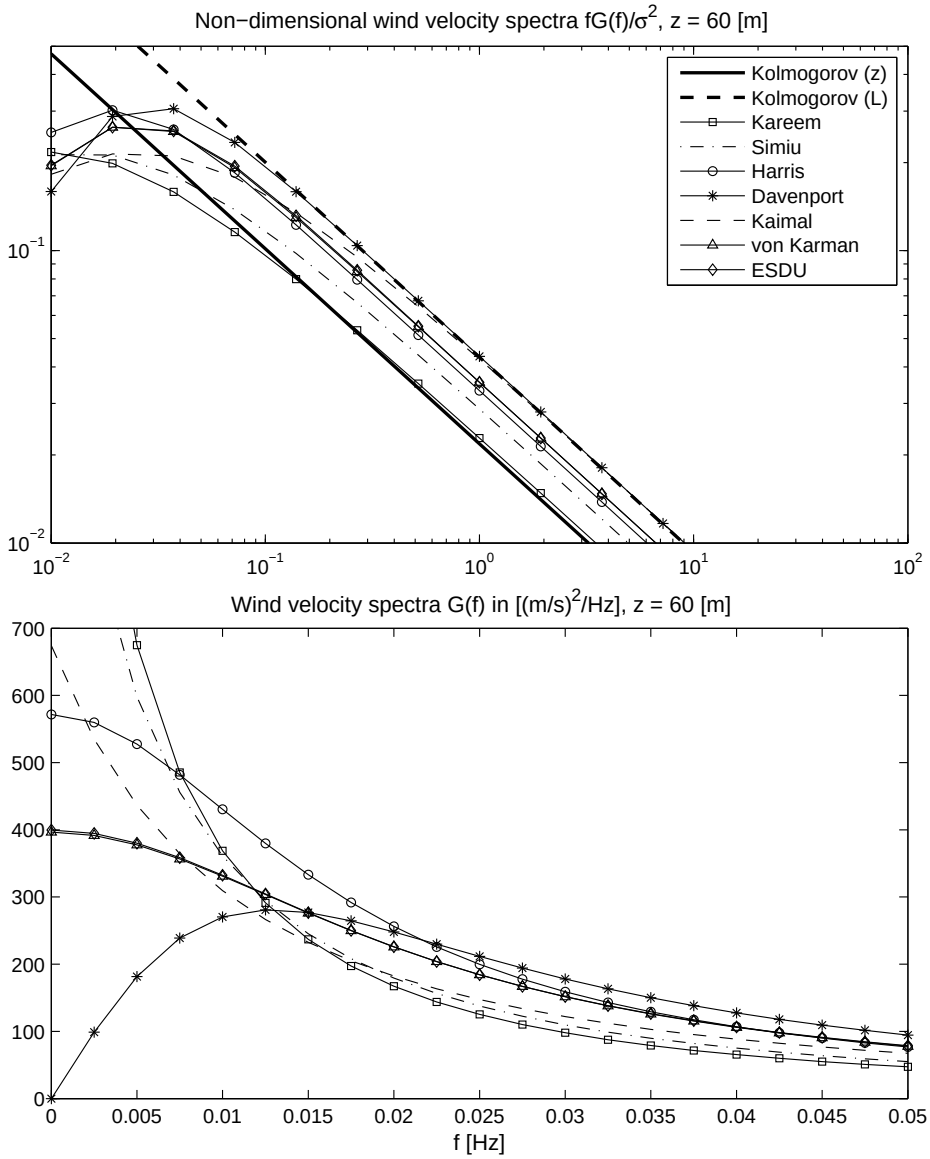

Figure 2.8: Chosen parameters: $z = 60$ [m], $\bar{U}_{10} = 20$ [m/s] , $L_u(z) = L_u^{EC}(z)$ [m] pursuant to Eq. (2.30), $z_0 = 0.05$ [-], $\kappa = 0.006$ [-] (open terrain, grassland); Top: Log-Log plot of the non-dimensional turbulence spectra; Bottom: Comparison of the spectra in the low-frequency range

in the following. According to [ESDU-85020 1985], the function $A(z)$ is slowly decreasing with height and approximated by $A(z) = 0.115\left[1 + 0.315(1 - \frac{z}{h})^6\right]^{2/3}$ where h is the gradient height. However, in [Dyrbye and Hansen 1997, p. 42] a constant value $A(z) = 0.14$ is proposed for structures up to $200 - 300$ [m] yielding an estimate of the PSD function within approximately 5 % accuracy.

Various model spectra for the characterization of the along wind velocity fluctuations exist, among them the spectrum proposed by von Kármán [Von Kármán 1948; Harris 1968], Davenport [Davenport 1961], Harris [Harris 1970], Kaimal [Kaimal et al 1972], Simiu [Simiu

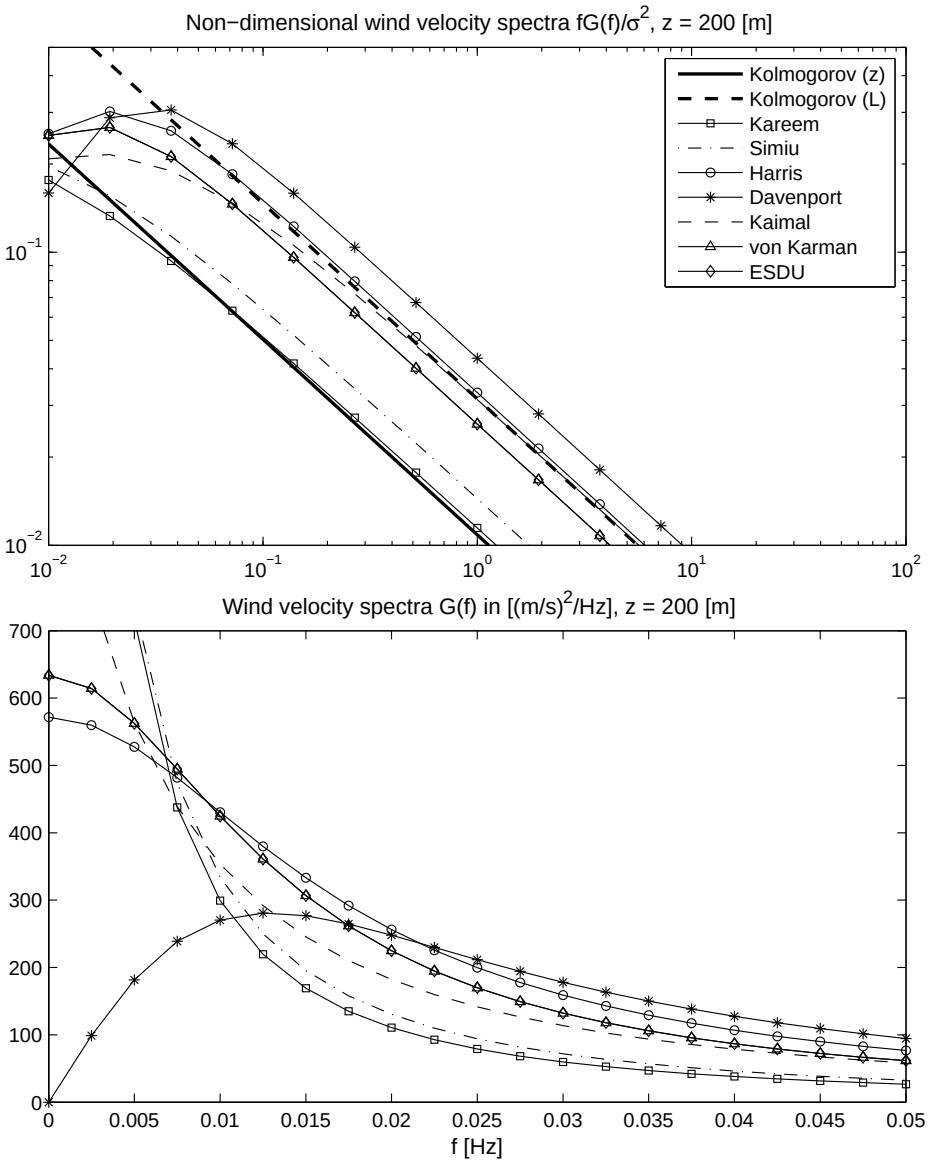

Figure 2.9: Chosen parameters: z = 200 [m], $\bar{U}_{10}$ = 20 [m/s], $L_u(z) = L_u^{EC}(z)$ [m] pursuant to Eq. (2.30), z_0 = 0.05 [-], κ = 0.006 [-] (open terrain, grassland); Top: Log-Log plot of the non-dimensional turbulence spectra; Bottom: Comparison of the spectra in the low-frequency range

1974], Kareem [Kareem 1985] and ESDU [ESDU-85020 1985]. The different spectra and their non-dimensional form $fG_u(z;f)/\sigma_u^2$ of the velocity fluctuations are depicted in Fig. 2.7 - 2.9, for different heights over ground, namely z = 10 [m], z = 60 [m] and z = 200 [m], respectively. The remaining parameters have been chosen as follows: $\bar{U}_{10}$ = 20 [m/s], $\bar{U}_z$ according to the logarithmic law in Eq. (2.16), $L_u(z) = L_u^{EC}(z)$ given in Eq. (2.30) and z_0 = 0.05, κ = 0.006 assuming open terrain, grassland according to Tab. 2.1. For comparison, additional the high-frequency approximations *Kolmogorov (z)* and *Kolmogorov (L)* proposed in Eq. (2.26), (2.27), valid within the inertia subrange (approx. $n_z, n > 0.2$), are illustrated. The corner

frequency ($f \approx 0.2$), where the spectra approaches the asymptotic limit, indicates the lower bound of the inertia subrange. As mentioned previously, the *Kolmogorov (z)* spectrum is appropriate as long as the integral scale length $L_u(z)$ is proportional to the height z. Examination of Fig. 2.7 - 2.9 reveals that for $z = 10$ [m] both limits agree, but with increasing height the energy is underestimated choosing $L_u(z) \sim z$.
At high frequencies ($f > 0.2$ [Hz]) the different models decrease proportionally to the Kolmogorov limits Fig. 2.7 - 2.9, Top) and thus show similar characteristics, but at low frequencies, they differ significantly (Fig. 2.7 - 2.9, Bottom). This is due to the fact, that the model parameters characterizing the low frequency range of the spectrum are difficult to obtain by measurements. The difficulties are caused by the required high frequency resolution of the experimental data which leads to long sampling times where the stationarity of the signal becomes questionable. However, for the structural design of land-based structures an accurate approximation of the high frequency band ($f > 0.2$) of the turbulence spectrum is in general sufficient, as the natural eigenfrequencies of such structures are relative high and thus the low frequency content of the excitation is of minor importance [Simiu and Scanlan 1996, p. 342]. In contrast, in the design of ocean based structures, such as tension leg platforms, which are much more flexible in the horizontal plane, the low frequency range can be significant for the structural response analysis and hence must be modeled adequately [Gurley and Kareem 1993].
The lower frequency range between zero and the lower bound of the inertia subrange, depends on the local atmospheric and topographic conditions and thus the spectrum lacks a universal description. However, the following property can be used to characterize and compare the low frequency region of the spectra [Simiu and Scanlan 1996]: Using the relation

$$G_u(z;f) = \frac{1}{2\pi}\int_0^\infty 4R(z;\tau)\cos(2\pi f t)d\tau \tag{2.28}$$

between the AC and the one-sided PSD function and substituting the definition for the integral scale length $L_u(z)$ according to Eq. (2.21), the power spectral density function should theoretically approach at $f = 0$ [Hz] the value

$$G_u(z;0) = \frac{4\sigma_u^2 L_u(z)}{2\pi\bar{U}_z} \tag{2.29}$$

It is important to note that due to the relation in Eq. (2.28), the existence of $G_u(z;0)$ requires, that its derivative $G'(z;0) = \partial G_u(z;f)/\partial f = 0$ vanishes for $f = 0$ [Hz], i.e. the spectrum approaches a horizontal asymptote at low frequencies.

2.2.2.4 Turbulence model spectra

Two spectra for isotropic along wind turbulences which tend to the asymptotic limit at high frequencies are the widely used Kaimal [Kaimal et al 1972] and the von Kármán velocity spectrum [Von Kármán 1948; Harris 1968], given by

$$\text{Kaimal:} \quad \frac{fG_u(z;f)}{\sigma_u^2} = \frac{6.8n}{(1+10.2n)^{5/3}}; \qquad L_u^{EC}(z) = 300\left(\frac{z}{200}\right)^{0.67+0.05\ln z_0} \tag{2.30}$$

$$\text{von Kármán:} \quad \frac{fG_u(z;f)}{\sigma_u^2} = \frac{4n}{(1+70.8n^2)^{5/6}}; \tag{2.31}$$

with the dimensionless frequency $n = fL_u(z)/\bar{U}_z$. The Kaimal spectrum is used in Eurocode 1 [EN 1991-1-4:2005 2010], where it is defined for the range $z_{min} < z < 200$ [m] using the given integral scale length $L_u^{EC}(z)$ unless measurement data indicates otherwise [Det Norske Veritas 2010]. For heights below $z < 50$ [m], Simiu [Simiu 1974] proposed the form

$$\text{Simiu:} \quad \frac{fG_u(z;f)}{\sigma_u^2} = \frac{2}{3}\frac{\lambda n_z}{(1+\lambda n_z)^{5/3}}; \qquad \lambda = 50; \tag{2.32}$$

where $n_z = fz/\bar{U}_z$. It must be stressed, that the form of the Kaimal and Simiu spectrum coincides, setting $\lambda = 10.2$. Comparing Fig. 2.7 - 2.9, it is evident that both spectra show a similar behavior for lower heights, but with increasing distance to the ground, the Kaimal spectrum approaches the *Kolmogorov (L)* limit 2.27 while the Simiu spectrum leads to an underestimation of the PSD at high frequencies. This is caused by the fact, that the Simiu spectrum assumes a proportional increase of the turbulence length scale with heights. To be precise the integral length has the form $L_u(z) = 1/(12\pi)\lambda z$ as can be shown by means of the low frequency relation $G_u(z;0)$ in Eq. (2.29). As mentioned previously, at greater height ($z \geq 50$ [m]) the proportional increase of the turbulence length scale with heights is not appropriate. Thus, in such cases z in Eq. (2.32) should be replaced by the estimated length scale $L_u(z)$ of the wind data using Eq. (2.23).

In comparison to the von Kármán spectrum, the one proposed by Kaimal agrees better with empirical observations of atmospheric turbulences and is characterized by a lower and broader peak [Burton et al 2001, p. 22ff]. It is fitted based on measurement data collected under strong wind conditions over flat homogeneous terrain in Kansas [Kaimal et al 1972]. Thus the spectrum implies a relative low terrain roughness and convection effects are not considered. These conditions are for instance met in offshore applications such as wind parks where the Kaimal spectrum is widely used also due to its simplicity [Mur Amada 2009]. It gives an accurate representation of the turbulent fluctuations in the high frequency range,

but it is not recommended for low frequent fluctuations [Dyrbye and Hansen 1997, p. 43]. The von Kármán representation is sometimes also called Kármán-Harris spectrum [Holmes 2007, p. 67] as it was analytically derived for laboratory turbulences in wind tunnels by von Kármán [Von Kármán 1948] and adapted later for wind engineering by Harris [Harris 1968]. It is suited for the representation of atmospheric turbulence above about $z = 150$ [m], but has some deficiencies at lower altitudes. Measurements have shown that the von Kármán spectrum underestimates the measured spectral density function at high frequencies [Lungu and van Gelder 1997]. In Harris [Harris 1990] the deficiencies of the Kármán spectrum in fitting data measured in the layer nearest to the ground are discussed. The model parameters ($a = 4$, $b = 70.8$) result directly from the integral scale length defined in Eq. (2.23) and the condition 2.15 calculated analytically from the spectrum itself and thus do not depend on the experimental data. Consequently, characteristic properties of the measured spectrum such as the position and heights of its maximum or the level of the spectrum at high frequencies cannot be included in the model. In [ESDU-85020 1985] the following more flexible form is recommended

$$\text{ESDU:} \quad \frac{fG_u(z;f)}{\sigma_u^2} = \beta_1 \frac{2.987n/\alpha}{[1+(2\pi n/\alpha)^2]^{5/6}} + \beta_2 \frac{1.294n/\alpha}{[1+(\pi n/\alpha)^2]^{5/6}} F_1 \tag{2.33}$$

where $h = U_*/(6f)$ is the gradient height of the boundary layer and

$$\begin{aligned} A &= 0.115[1+0.315(1-z/h)^6]^{2/3}; & \alpha &= 0.535 + 2.76(0.138-A)^{0.68} \\ \beta_1 &= 2.357\alpha - 0.761; & \beta_2 &= 1-\beta_1 \end{aligned} \tag{2.34}$$

The expression F_1 is based on particular orders of the Gauss Hypergeometric function and can be approximated by

$$F_1 = 1 + 0.455e^{-0.75n\alpha^{0.8}} \tag{2.35}$$

For $\beta_1 = 1$ and $\alpha = 0.747$, Eq. (2.33) reduces to the Kármán form (2.31). Moreover, the parameters β_1, β_2, α are derived in such a way that for high frequencies the spectrum agrees with the *Kolmogorov (L)* limit (2.25) choosing $A(z) = 0.115$. Furthermore, Fig. 2.7 - 2.9 shows, the von Kármán spectrum and its modified version proposed in [ESDU-85020 1985] are with increasing heights, where the side-specific characteristics are of less importance, almost identical.

The spectra proposed by Davenport and Harris are derived by averaging various wind speed measurements over land at different heights above the surface. Consequently, the dependency of the turbulence spectrum on the height is not reflected. They are given by the following

equations

$$\text{Davenport:} \quad \frac{fG_u(f)}{\sigma_u^2} = \frac{2}{3}\frac{n^2}{(1+n^2)^{4/3}}; \qquad L_{u,D} \approx 1200\ [m]; \qquad \bar{n} = \frac{fL_{u,D}}{\bar{U}_{10}} \tag{2.36}$$

$$\text{Harris:} \quad \frac{fG_u(f)}{\sigma_u^2} = \frac{2}{3}\frac{n}{(2+n^2)^{5/6}}; \qquad L_{u,H} \approx 1800\ [m]; \qquad \bar{n} = \frac{fL_{u,H}}{\bar{U}_{10}} \tag{2.37}$$

The Davenport spectrum approaches $G_u(z;0) = 0$ as $f \to 0$, implying that the integral length scale $L_u(z)$ is zero which is physically not possible. The resulting sharp drop in the frequency range close to zero leads to an underestimation of the energy of the wind velocity in the low frequency region while the energy at high frequencies is in general overestimate at greater hight[4] as illustrated by Fig. 2.7 - 2.9 [Simiu and Scanlan 1996, p. 61]. In contrast, the Harris spectrum approaches the *Kolmogorov (L)* limit (2.27) just for great heights (here for $z = 200$ [m]) and thus, in general, leads to an underestimation of the energy in the high frequency band. Both spectra are not recommended for the use in the low frequencies range below $f < 0.01$ [Hz] [Det Norske Veritas 2010].

While the spectra by Davenport and Harris are widely used to model the wind excitation of land-based structures, the Kareem spectrum is more appropriate for offshore applications [Li and Kareem 1990] and is given by

$$\text{Kareem:} \quad \frac{fG_u(z;f)}{\sigma_u^2} = \frac{Bn_z}{(1+Cn_z)^{5/3}}; \qquad n_z = \frac{fz}{\bar{U}_z} \tag{2.38}$$

where B and C are empirical constants to be determined from observed data by spectral fitting in order to satisfy the *Kolmogorov (z)* limit at high frequencies, the position of the peak value as well as the turbulence intensity [Kareem 1985]. E.g. for $\bar{U}(10) = 20$ [m/s] the parameters are computed as $B = 335$ and $C = 71$. Furthermore, it must be stressed, that for $B = 6.8$ and $C = 10.2$, the spectrum coincides with the one proposed by Kaimal (2.30). The development was motivated by the observation, that spectra over the sea seem to have relatively more energy at low frequencies than land-based spectra [Busch and Panofsky 1968]. Moreover, Kareem compared measured values of the variance of the longitudinal velocity fluctuations over sea based on observations conducted by Smith in the years 1976 - 1978 at an offshore stable platform installed at Sable Island (Novia Scotia, North Atlantic ocean) [Smith 1980] and the theoretic values resulting from the integration of three widely used standard turbulence spectra, namely the Kaimal, Harris and Davenport spectrum. He showed that especially at higher mean wind speeds of about $\bar{U}_{10} = 20 - 25$ [m/s], these standard models underestimate the true deviation of the fluctuations by 21 %, 6 % and 11%,

[4] for $z > 10$ [m] [Simiu and Scanlan 1996, p. 61]

	Applications	Restrictions	Kolmogorov Limit (2.26)	Foundation
Kaimal	off-shore structures; land-based structures with low terrain roughness	$z < 200$ [m]	agrees	empirical, strong wind conditions, flat homogeneous terrain
Kareem	off-shore structures	adjustable parameters		empirical
von Kármán	atmospheric turbulences (e.g. aircraft design), wind tunnel tests	$z \geq 200$ [m]	agrees	theoretically founded on the relation 2.23
ESDU	empirical modification of the von Kármán spectrum with adjustable parameters			
Simiu	off-shore structures; land-based structures with low terrain roughness	$z < 50$ [m]	under-estimated	empirical
Davenport	land-based structures	$f > 0.01$ [Hz]	over-estimated	empirical, averaging various measurements over land at different height
Harris	land-based structures		under-estimated	

Table 2.2: Comparison of wind velocity model spectra

respectively. In contrast, the greater flexibility of the Kareem spectrum allows describing the low frequency content of the wind velocity fluctuations accurately, by employing information derived from actual measurements and, at the same time, keeps the Kolmogorov limit at high frequencies [Kareem 1985]. Analysis of full-scale measurements from the Gulf of Mexico, North Sea, Pacific and Atlantic oceans confirms the adequacy of the proposed model for the description of ocean wind data [Gurley and Kareem 1993].
The main results of the comparison of the different wind velocity model spectra are summarized in Tab. 2.2.

2.2.3 Models for wind loads on structures

The gustiness of the wind might lead to a critical excitation of the structure immersed in the turbulent wind flow. For the structural design a relation between the pressure fluctuations over the surface or the equivalent resultant forces and moments and the wind velocity fluctuations is needed. As an analytical modeling of such wind flows is in general not possible, simplified empirical formulas based on wind tunnel tests are used.
Assuming that the structure is completely enveloped by the flow, the time-varying aerody-

namic force can be approximated by the formula

$$F_{tot}(z;t) = \frac{1}{2}\rho_a A C_F U^2(z;t) \tag{2.39}$$

where ρ_a is the air density and C_F denote the force coefficient. C_F strongly depends on the geometry of the body and is determined by wind tunnel tests as ratio of the wind load per unit of area A and the velocity pressure $p_v(z;t) = 1/2\rho_a U_{tot}^2(z;t)$. The area A is in general a characteristic size, e.g. the projected frontal area or in case of long or two-dimensional structures, A is replaced by a characteristic length B, which for instance describes the projected length normal to the flow or the length of the diagonal of a rectangular body. The squared wind velocity $U^2(z;t)$ results from Eq. (2.14) and is given by

$$U^2(z;t) = [\bar{U}(z) + u_D(z;t)]^2 + v_D^2(z,t) + w_D^2(z;t) \approx \bar{U}^2(z) + 2\bar{U}(z)u_D(z;t) \tag{2.40}$$

The last equality is based on the assumption that the mean wind velocity $\bar{U}(z)$ is much greater then the magnitude of the turbulence components $u_D(z;t)$, $v_D(z;t)$ and $w_D(z;t)$. To be precise, in wind engineering, the ratio $u_D(z;t)/\bar{U}(z)$ of the along wind component $u_D(z;t)$, which can be assumed to show the highest fluctuations, rarely exceeds a value of 0.2, and thus the squared values $u_D^2(z;t)$, $v_D^2(z;t)$, $w_D^2(z;t)$ are negligible. Furthermore, it must be stressed, that the spatial correlation of the velocity fluctuations is neglected, which allows reduce the velocity field $\mathbf{U}(x,y,z;t)$ (2.14) to the random vector process $\mathbf{U}(z;t)$ used in Eq. (2.40). This simplification is justified if the wind fluctuations are completely correlated over the surface, i.e. if the dimensions of the structure are sufficiently small compared to the spatial correlation length of the wind turbulences [Simiu and Scanlan 1996, p. 180-181].
Due to these assumptions the aerodynamic force defined in Eq. (2.39) reduces to the along wind component, the so-called drag force, which can be decomposed into its horizontal mean value $\bar{F}_D(z)$ and a dynamic time-dependent part $F'_D(z;t)$ [Dyrbye and Hansen 1997, p. 56]

$$F_D(z;t) = \bar{F}_D(z) + F'_D(z;t) \tag{2.41a}$$

where

$$\bar{F}_D(z) = \frac{1}{2}\rho_a A C_d \bar{U}^2(z) \tag{2.41b}$$

$$F'_D(z;t) = \rho_a A C_d \bar{U}(z) u_D(z;t) \tag{2.41c}$$

where C_d denotes the drag coefficient C_d, e.g. known from measurements. It must be noted, that in the general case the drag coefficient is a frequency dependent function of the wind

velocity fluctuations. Thus, setting it constant results in a further approximation [Simiu and Scanlan 1996, p. 181].
The statistics of the dynamic component are described by the one-sided PSD function which, introducing the relation (2.41b), is of form

$$G_F(f) = [\rho_a A C_d \bar{U}(z)]^2 G_u(f) = \frac{4\bar{F}_D^2(z)}{\bar{U}^2(z)} G_u(f) \tag{2.42}$$

The statistical properties of the force fluctuations, such as variance and intensity σ_F^2, I_F, respectively, follow directly from the corresponding properties of the wind speed fluctuations defined in Eq. (2.19-2.20) and are given by [Dyrbye and Hansen 1997, p. 57]

$$\sigma_F^2 = \int_0^\infty \frac{4\bar{F}_D^2(z)}{\bar{U}^2(z)} G_u(f) df = \frac{4\bar{F}_D^2(z)}{\bar{U}^2(z)} \sigma_u^2 \tag{2.43a}$$

$$I_F = \frac{\sigma_F}{\bar{F}_D(z)} = 2\frac{\sigma_u}{\bar{U}(z)} = 2I_u \tag{2.43b}$$

However, the magnitude of the dynamic response of the structure does not only depends on the turbulence intensity but also on the size of the eddies, i.e. the integral scale length of the turbulence defined in Eq. (2.23). If, as assumed here, the dimensions of the eddies are comparable with the dimensions of the structure, they envelope the structure completely and cause well correlated pressure fluctuations which might lead to a severe excitation of the structure. [Kareem and Dalton 1982].
For larger structures, the velocity fluctuations at different locations of the structure do not occur simultaneously and thus their correlation over the whole area A must be taken into account. The influence of the departure from perfectly correlated flow is introduced by multiplying the PSD function in Eq. (2.42) with a correction factor, the so-called aerodynamic admittance function $\chi_a^2(z,f)$ given here for a rectangular structure, yielding

$$G_F(f) = (\rho_a A C_d \bar{U}(z))^2 |\chi_a(z;f)|^2 G_u(f) \tag{2.44a}$$

where

$$\chi_a(z;f) = \left[1 + \left(\frac{2f\sqrt{A}}{\bar{U}(z)}\right)^{4/3}\right]^{-1} \tag{2.44b}$$

Fig. 2.10 depicts the function for various plates and prisms in turbulent flow with respect to the dimensionless frequency $n = f\sqrt{A}/\bar{U}(z)$ and shows a good agreement with experimental data. The argument n can be interpreted as ratio of the dimension of the structure $\sqrt{A}$ and the characteristic eddy size of natural wind $\bar{U}(z)/f$. At low frequencies or for small

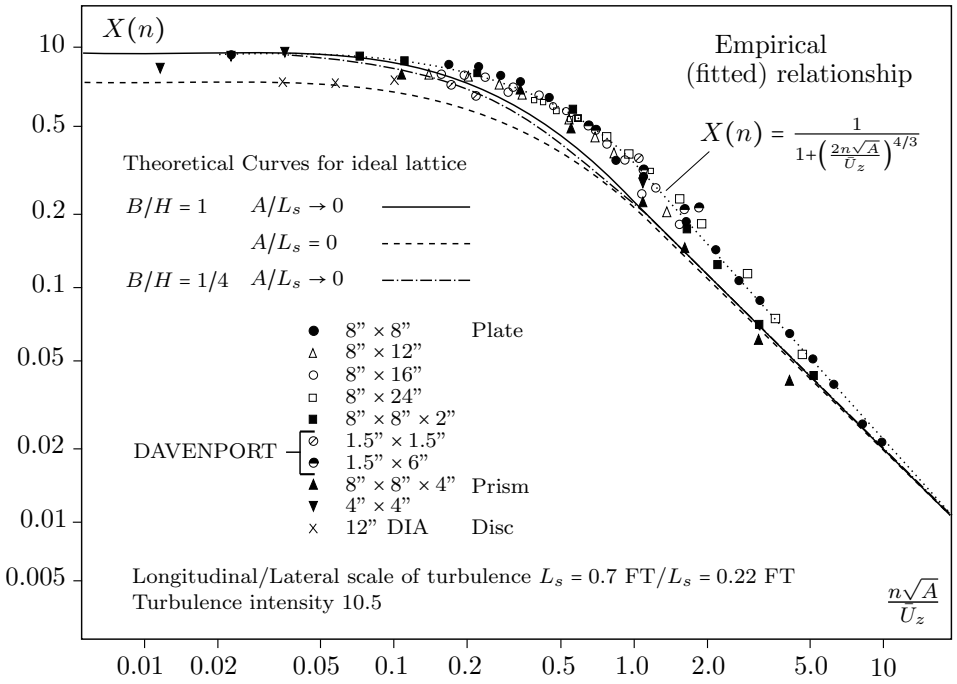

Figure 2.10: Experimental and theoretical aerodynamic admittance functions for flat plates and prisms perpendicular to the flow [Dyrbye and Hansen 1997, p. 60]

structures, i.e. $n << 1$, the turbulences can be considered to be fully correlated, and thus the aerodynamic admittance function tends towards 1.0. Conversely, at high frequencies or for very large bodies, that is $n >> 1$, the function tends towards zero as the gusts effect the structure just locally leading to small, nearly uncorrelated pressure fluctuations [Holmes 2007, p. 123].

2.3 Wind wave excitation

If natural forces such as wind, earthquakes, tidal forces (due to gravity between earth, moon and sun), the Coriolis force (due to the earth's rotation) or the surface tension are acting on the ocean, surface waves are caused [World Meteorological Organization 1988, p. 1]. In [Munk 1950] it is observed that the period (or the frequency) of the generated waves, describing the time in which two successive crests passes, is a characteristic measure which gives information about the nature of the causing force. Thus the location of the peaks in the wave spectrum can be used for the classification of the ocean waves as depicted in Fig. 2.11.

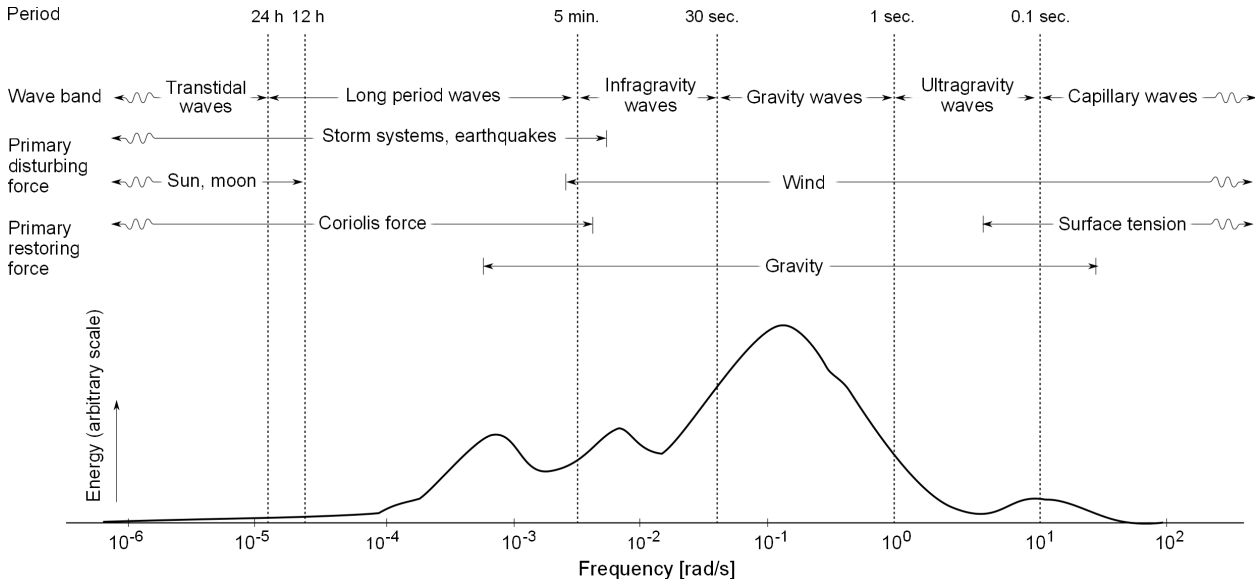

Figure 2.11: Idealized energy spectrum of surface ocean waves [Kinsman 2002]

2.3.1 Ocean wave spectra

The capillary waves are the smallest waves of period less than $T_p < 0.1$ [s] whose properties are strongly influenced by the surface tension of the water.

The ordinary gravity waves vary randomly in height and period over location and time, and thus have a probabilistic nature. They can be split into wind *sea* if the waves are directly generated and affected by the local winds and *swell*, if the waves have escaped the generating wind field, i.e. they have been generated elsewhere, or some time ago. Sea is of shorter period and in general of shorter wavelength, steeper and more confused than swell. As the frequency bands of sea and swell are overlapping and there's no gap in the wave spectrum, the separating period between sea and swell just can be estimated roughly and is about 10 [s] [Kinsman 2002, p. 22].

The ultra-gravity and ordinary-gravity waves are caused mainly by two mechanism, namely a horizontal pressure gradient in the air flow between the windward and leeward side of the wave and a tangential friction drag on the water surface leading to a mass transport according to the linear wave theory as discussed in [Munk 1950]. The infra-gravity waves describe surface waves at periods longer than the swell and wind-driven waves. In deep water the wave heights are in general small ($H \leq 1$ [cm]) and the period is of about 20-500 [s]. The waves causes pressure fluctuations at the deep sea bed and thus are greatly affected by the bottom topography. They are of greater importance for the modeling of harbor oscillations and near-shore processes such as sediment transport [Dolenc et al 2005].

The long-period band and the transtidal band of periods $T_p > 5$ [min.] are caused by large

scale atmospheric pressure systems, earthquakes, and tidal forces, respectively [Kinsman 2002, p. 24].
Most of the energy is introduced by the ordinary gravity waves and the tidal waves. In the following only the former class will be discussed in more detail as it is of great importance for the design of ocean and offshore engineering structures [World Meteorological Organization 1988, p. 1].

2.3.2 Sea states

The wind characteristics and the growth of the waves is not just influenced by the wind speed and the turbulence intensity in the lower boundary layer, but also by the water depth, the area over which the wind blows, the so-called fetch, and the duration the wind has blown. Hence, the generation of wind waves is characterized by three states:

a) *Developing sea*: In the first state the sea is said to be developing as the mean values of the statistical properties are increasing in along wind direction x as the sea becomes rougher and thus the wind energy is absorbed more effectively. The minimum fetch F_{min} describes the length of this region in wind direction, i.e. $x \leq F_{min}$ [McCormick 2009, p. 1ff]. The process which causes the waves to grow in heights and length is explained in more detail in section (2.3.3).

b) *Fully developed sea*: If the wind blows steadily for a long time over a large area, the waves reaches an equilibrium state and the sea is said to be fully developed. Thus the average wave height and wave period can be assumed to be stationary in time and constant over distance $F_{min} < x \leq F$, where F denotes the storm fetch.

c) *Decaying sea*: Finally, when the waves escape the wind field, the wave energy starts to decrease in the so-called decay region, i.e. $F < x < X_D$, where X_D represents the decay length and where the sea is referred to as decaying sea or swell.

It must be noted that the wave spectra of all three states show similar characteristics but are not identical. E.g. the peak energy value in the developing sea is lower than the one in the fully developed sea and the modal period, i.e. the period of maximum energy intensity, is shifted to lower periods (higher frequencies). Moreover in contrast to the time- and space-variant wave spectra of the developing and decaying sea, the spectrum of the fully developed sea can be assumed to be independent of both time and position within $F_{min} < x \leq F$. In the decaying sea, the modal period increases with x, whereas the overall energy intensity, corresponding to the area under the curve, decreases. The change of the frequency content of

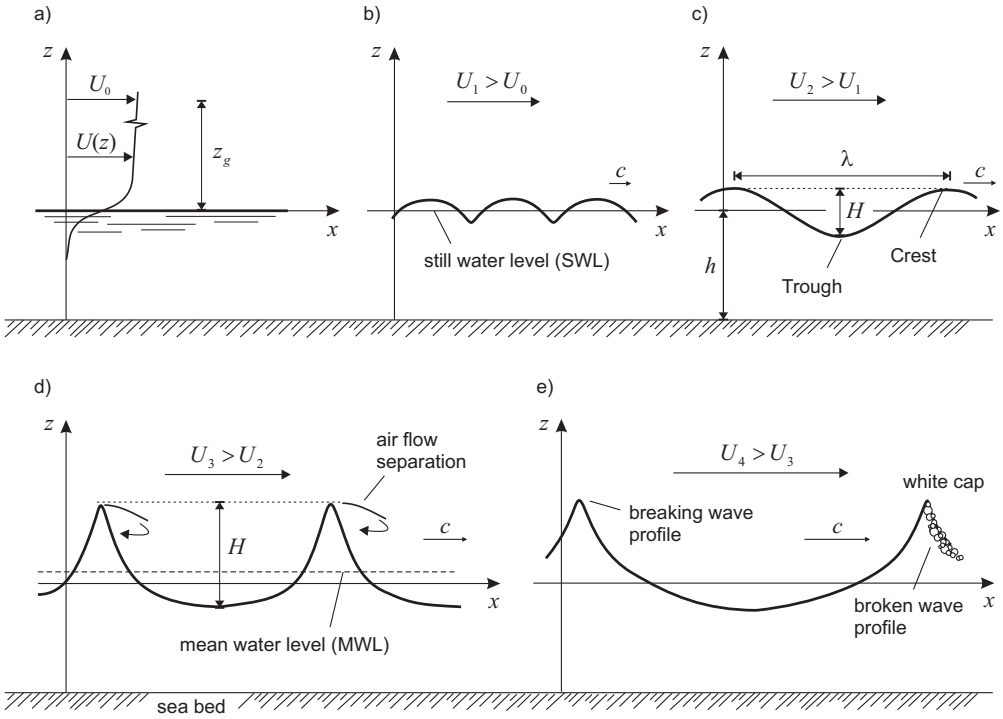

Figure 2.12: States of the sea: a) Calm sea; b) Capillary waves; c) Linear waves; d) Nonlinear waves; e) Breaking waves [McCormick 2009, p. 46]

the wave spectrum is caused by a phenomenon called dispersion describing the dependency of the propagation velocity c on the frequency. Thus the longer waves, or similarly the waves with greater period (smaller frequency), outrun the shorter waves of lesser period [McCormick 2009, p. 1ff].

In the following the discussion is restricted to deep water waves of the fully developed sea. They are modeled using the classical theory of linear wave analysis also known as Airy's wave theory suggested by George B. Airy in the middle of the nineteenth century (see [Coleridge 1845, p. 241-396]). Without going into details, solely the main results needed for a description of the wave loads are presented. A comprehensive derivation of the equations used in linear and nonlinear wave theory can be found e.g. in [McCormick 2009].

2.3.3 Generation of wind waves

In order to show under which conditions the linear wave assumption is adequate, the process which causes the waves to grow in both height and length is illustrated in Fig. (2.12) and summarized in the following [McCormick 2009, p. 45ff]:

a) If the free surface of the sea is effected by a slight breeze of relative small velocity U_0 [m/s], the air flow in the boundary layer can be assumed to be laminar, i.e. it flows in parallel

layers without lateral mixing and turbulences. The mean wind speed at different heights is characterized by a logarithmic profile as previously discussed. Due to the viscosity of the air, it adheres to the water particles on the free surface and drags them in flow direction. Due to the lack of turbulences the air flow does not cause waves and the sea remains calm as illustrated in Fig. 2.12a.

b) If the velocity increases $U_1 > U_0$, the lower part of the boundary layer becomes turbulent. Small ripples at the surface, so-called *capillary waves*, are created if the pressure fluctuations in the airflow above the water are sufficient to induce small deformation on the sea surface. The shape of the wave profile is predominantly influenced by the surface tension leading to broad chests and narrow troughs as depicted in Fig. 2.12b, whereas the shear stresses on the surface causes the propagation of the waves in air flow direction with velocity c [m/s]. They decay quickly as they are strongly damped by viscous forces, and for their generation wind velocities above 1-2 Beaufort are required. These waves are often studied visually by photographing the glitter of the sun on the sea surface. They increase the surface roughness, so that the wind can grip the water more effectively [Munk 1950]. However, the capillary waves are in general of minor importance in engineering applications as their energy is relative small.

c) The energy of the wind turbulences in the boundary layer as well as the shear stresses increase with growing wind velocity and the stronger air flow $U_2 > U_1$ is indicated as wind rather than as breeze. The energy exchange between the air and the water leads to the development of longer waves with sinusoidal shape as depicted in Fig. 2.12c. The so-called *linear waves* are characterized by a sinusoidal profile and thus can be described using linear wave theory by superposition of waves with different wavelength λ and altitude H.

d) A further increase of the wind velocity $U_3 > U_2$ results in an increase of the wave heights and length as well as the propagation velocity. The wind profile is non-symmetric showing a narrow crest and a broad trough, as illustrated in Fig. 2.12d, and as the water volume above and below the still water level (SWL) must be balanced, the mean water level (MWL) lies above the SWL. The air flow is blocked by the waves leading to a horizontal pressure gradient on the leeward (wind-averted) side of the waves so that the wind profile is no longer symmetric. The waves are called *nonlinear waves* as their properties cannot be described by linear equations.

e) If the wind speed further increases so that the propagation velocity equals the horizontal velocity of the water particles, the waves start to break and hence are called *breaking waves*. The shape of the waves is characterized by a broad trough and a peaked crest

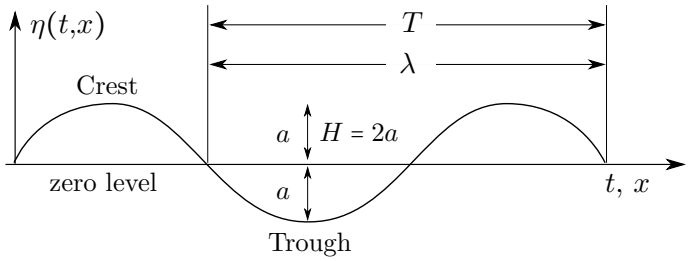

Figure 2.13: Idealized ocean wave due to linear wave theory [World Meteorological Organization 1988]

which shows a white cap if the water is sheared of the crest and spilled down the leeward side as white foam as sketched in Fig. 2.12e

2.3.4 Linear wave model

A large number of actual measured data indicates, that the free surface particle displacement of the ocean wave can be represented by a zero-mean stationary stochastic process [Li and Chen 2009, p. 68]. The simplest model is based on the linear wave analysis which is valid for non-breaking, deep water surface waves and which allows considering waves in a spectral sense. It is based on the assumption, that the amplitude of the waves H is small compared to the wavelength λ and the water depth h. The first assumption $H/\lambda << 1$ implies a small steepness of the waves, while the second assumptions $H/h << 1$ indicates that deep water waves are considered, i.e. $\lambda/h < 2$, which are unaffected by the sea bed topography. They allow the linearization of the boundary conditions at the water surface and an analytic solution of the underlying differential equation can be found (s. [McCormick 2009, p. 47ff.]) for further detail). Furthermore it is assumed that the water is incompressible, i.e. of constant density, and that the viscosity of the water flow can be disregarded, that is friction effects are ignored. The latter assumption is valid if the viscous forces are small in comparison to the inertial (gravity) forces and the pressure acting perpendicularly to the surface of the water particle. Furthermore, the water flow is assumed to be irrotational, i.e. the individual particle does not rotate and a group of water particles move around each other but without mixing effects [World Meteorological Organization 1988, p. 1].
Assuming linear wave theory, the wave has a sinusoidal form as illustrated in Fig. 2.13 and the free surface profile can be described as

$$\eta(t,x) = a\sin(kx - \omega) = a\sin(k[x - ct]) \tag{2.45}$$

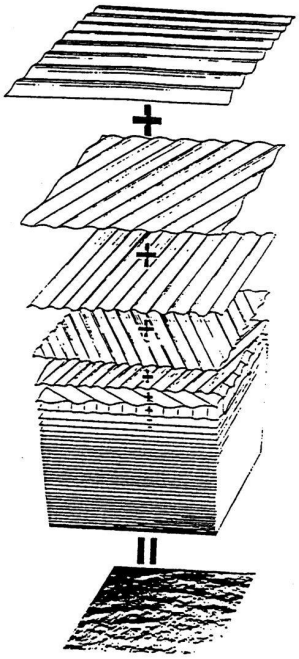

Figure 2.14: Sea generated by the superposition of many sine waves with random amplitude and phase [Pierson et al 1955]

where $a = H/2$ [m] denotes the amplitude of the wave measured with respect to the mean water level. The constants k [rad/m] and $\omega = 2\pi/T$ [rad/s] indicate the wave number and the angular frequency of the oscillating wave, respectively. The second equality in Eq. (2.45) can be interpreted as frozen wave profile with wavelength $\lambda = 2\pi/k$ [m] which moves in the direction of the horizontal x-axis with constant velocity $c = \omega/k$ [m/s] which is also known as phase velocity. Alternatively, the wave speed as well as the wave length can be expressed in terms of the wave period using the expressions $c = \lambda/T$ [m/s] and $\lambda = cT$ [m]. Thus, the wave is described in a two-dimensional coordinate system x,z in order to account for the wave propagation in x direction as well as its vertical oscillation in z direction [Chakrabarti 2005, p. 83ff]. However, the actual surface of the sea does not resemble the simple form depicted in Fig. 2.13, but has a more random nature. The waves appear in irregular, constantly changing shapes since they are continually being overtaken and crossed by others. Hence, the random pattern can be generated by superposing an infinite number of independent sinusoidal waves with random phase which differ from each other in height, wavelength and propagation direction as illustrated in Fig. 2.14 [World Meteorological Organization 1988, p. 7] leading to the following formula for the surface evaluation suggested in [Pierson et al 1955, p. 17ff]

$$\eta(t,x) = \lim_{N\to\infty} \sum_{j=1}^{N} a_j \sin(k_j x - \omega_j t + \theta_j) \tag{2.46}$$

2.3.5 Model spectra of the fully developed sea

A number of different procedures exist for the description of the sea surface [Bai 2003, p. 21-22]. In the frequency domain, the power spectral density function represents the distribution of the energy content of the sea over a range of measured wave frequencies (or periods). Various deep-water wave spectral models exist to characterize the fully developed sea, among them the spectra proposed by Neumann [Neumann 1953], Bretschneider [Bretschneider 1959] and Pierson and Moskowitz [Pierson and Moskowitz 1963] are the most widely used [Chakrabarti 2005, p. 106]. These spectra follow the generic equation [Li and Chen 2009, p. 68]

$$G(\omega) = \frac{A}{\omega^p} e^{-\frac{B}{\omega^q}} \tag{2.47}$$

where the parameters p and q are typically of order $p = 5-6$, $q = 2-4$ and result from curve-fitting of the measurement data while the coefficients A and B model the influence of the wind velocity, the wave height and other physical parameters such as the modal frequency (or period), the fetch length, the wind duration [McCormick 2009, p. 137]. The parameters of the three spectra are chosen as

$$\text{Neumann:} \qquad p = 6;\ q = 2;\ A = \frac{C\pi}{2};\qquad B = \frac{2g^2}{\bar{U}_{7.5}^2} \tag{2.48}$$

$$\text{Bretschneider:} \qquad p = 5;\ q = 4;\ A = 0.1687 H_s^2 \omega_s^4;\ B = 0.675\omega_s^4 \tag{2.49}$$

$$\text{Pierson-Moskowitz:} \qquad p = 5;\ q = 4;\ A = 0.0081 g^2;\qquad B = 0.74\left(\frac{g}{\bar{U}_{19.5}}\right)^4 \tag{2.50}$$

These spectra are derived by empirical fitting of various wave data sets in combination with dimensional and theoretical reasoning. Longuet-Higgins [Longuet-Higgins 1952] showed that for a narrow-banded wave spectrum, the surface evaluation can be assumed to be Gaussian distributed. As it is known, that the maximum values of a normally distributed random parameter follow a Rayleigh distribution[5] [World Meteorological Organization 1988, p. 10], Longuet-Higgins concluded that the wave heights, which corresponds to the maximum values of the sea state, are Rayleigh distributed. The latter was shown theoretically and verified by experimental data leading to the following probability density function for the wave height

$$p(H) = \frac{H}{4\sigma_\eta} e^{-\frac{H^2}{8\sigma_\eta}} = 2\frac{H}{H_{rms}^2} e^{-\frac{H^2}{H_{rms}^2}} \tag{2.51}$$

[5] The Rayleigh probability density function is: $p(x) = \frac{x}{\sigma^2} e^{-x^2/2\sigma^2}, \quad x \geq 0$ for $\sigma > 0$

where H is defined on the interval $[0,\infty]$, σ_η denotes the standard deviation of the surface evaluation and H_{rms} is the root-mean square of the wave heights defined as

$$H_{rms} = \sqrt{\int_0^\infty H^2 p(H) dH} \cong \sqrt{\frac{1}{N}\sum_{j=1}^{N} H_j^2} = \sqrt{8}\sigma_\eta \tag{2.52}$$

One interesting property of the Rayleigh distribution is, that all characteristic wave height parameters are interrelated and can be calculated once a single wave height parameter is determined. The most frequent wave height parameters are

a) the most probable wave height $H_0 = 2\sigma_\eta$, (2.53a)

b) the mean wave height $\bar{H} = \sqrt{2\pi}\sigma_\eta \approx 2.5\sigma_\eta$, (2.53b)

c) the root-mean-square wave height $H_{rms} = \sqrt{8}\sigma_\eta \approx 2.8\sigma_\eta$ and (2.53c)

d) the significant wave height $H_s = 4\sigma_\eta$ (2.53d)

The latter is also denoted as $H_{1/3}$, as it is defined by the average wave height considering the highest one-third of all waves, i.e.

$$H_s = \frac{1}{N/3}\sum_{j=1}^{N/3} H_j \tag{2.53e}$$

where N is the number of all individual wave heights and H_i are the wave heights ranked from highest to lowest, i.e. $H_1 > H_2 > \ldots > H_N$. Due to the dependency of the different wave heights $\bar{H}$, H_s and H_{rms}, respectively, on the variance of the surface evaluation σ_η, the relations in Eq. (2.53a-2.53d) can be used to scale the measured wave spectra. E.g. using Eq. (2.53d) the following relation between the significant wave height and the one-sided PSD function can be used

$$H_s = 4\sqrt{\int_0^\infty G(\omega) d\omega} = 4\sqrt{m_0} \tag{2.53f}$$

where $m_0 = \sigma_\eta^2$ is the zeros moment of the PSD function of the surface evaluation corresponding to the area below the PSD function.

The development of the Neumann spectrum was based on the characteristic wave heights H_c and period T_c obtained by visual observations (in literature often indicated by using the symbols $\tilde{T}$, $\tilde{H}$) of the apparent waves in the fully developed North Atlantic sea. By plotting the values H_c/T_c^2 versus the ratios $(T_c/\bar{U}_z)^2$ in a semi-logarithmic scale, as illustrated in Fig. 2.15, Neumann derived an empirical envelope curve in the form

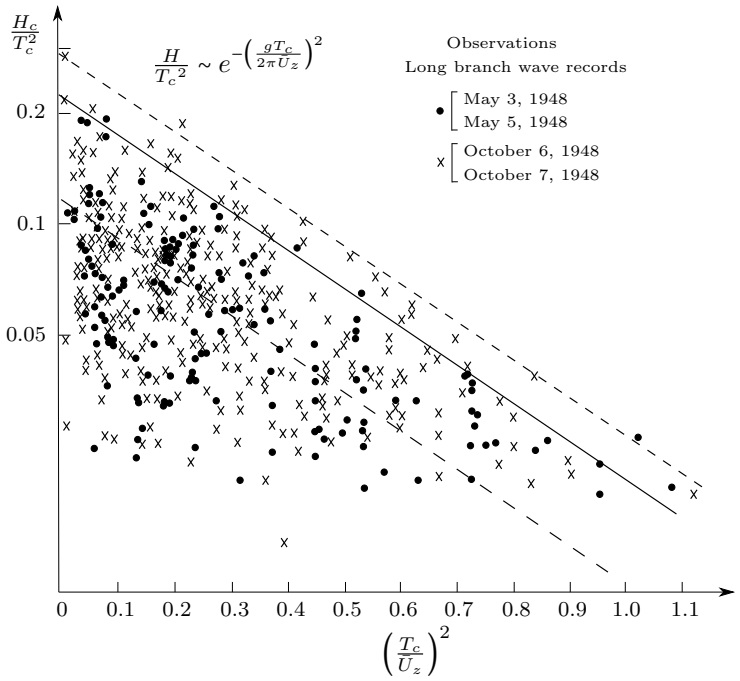

Figure 2.15: Ratio of the observed apparent wave heights to the wave period, H_c/T_c^2 versus different ratios of the wave period to the mean wind speed $(T_c/\bar{U}_z)^2$ plotted in semi-logarithmic scale for fully developed sea [Neumann 1953, p. 12]

$$\frac{H_c}{T_c^2} = Ce^{-\left(\frac{g}{2\pi}\cdot\frac{T_c}{\bar{U}_z}\right)^2} \tag{2.54}$$

where C [m/s^2] is a constant. He observed that the apparent waves may occur with any steepness but due to instabilities and breaking cannot exceed a certain maximum value. Below this envelope curve any value of the ratio H_c/T_c^2 may occur at a given ratio $T_c/\bar{U}_z$. Neumann concluded, that the observed apparent waves result from the superposition of a large number of individual wave trains with individual period T concentrated around the observed apparent wave period T_c. Thus the corresponding wave heights H_c at a given period T_c can be interpreted as spectral wave height for a certain spectral wave band $T_c \pm \Delta T/2$ of width ΔT [Neumann 1953, p. 9ff.]. Since the wave energy density E [J/m^2] per area equals $g\rho_w H^2/8$ is proportional to the squared wave heights (see for instance [McCormick 2009, p. 64-65] for further detail), Neumann assumed, that the wave spectrum is proportional to the squared apparent height H_c^2 obtained from Eq. 2.54 [Bretschneider 1959, p. 149]. The constant C is chosen in such a way that the variance of the process is equal to the so-called energy coefficient obtained by Longuet-Higgins [Longuet-Higgins 1952] given by $4/\pi\bar{H}^2$. The latter coincides with the mean square value of the wave height $H_{rsm}^2 = 4/\pi\bar{H}^2$ as can be shown by combining Eq. (2.53c) and Eq. (2.53b) assuming that the wave heights are Rayleigh distributed (s. Eq. 2.51). Using the relation defined in Eq. (2.53c) between the

variance of the surface evaluation and the mean square value of the wave height the following relation of the spectrum of the surface evaluation and the Neumann spectrum can be found

$$H_{rms}^2 = \int_0^\infty G_N(\omega)d\omega = 8\sigma_\eta^2 = 8\int_0^\infty G_\eta(\omega)d\omega \tag{2.55}$$

It is interesting to note, that the relation in Eq. (2.55) can also be derived analytically from the wave energy density $E = g\rho_w H^2/8$ without using the assumption that the wave height follow a Rayleigh distribution as shown in [McCormick 2009, p. 134-135]. In the Neumann spectrum defined in Eq. (2.48), $C = 3.05$ [m^2/s^5] and the mean wind velocity is chosen with respect to the height $z = 7.5$ [m] over the sea surface.

The wave spectrum for a given sea-state proposed by Bretschneider [Bretschneider 1959] depends on two parameters, namely the significant wave height H_s defined in Eq. (2.53e) and the modal angular wave frequency ω_s [Bai 2003, p. 22-23]. From statistical analysis of the wave data he noticed that the variability of both, the wave period as well as the wave height follow a Rayleigh distribution. Thus the Bretschneider spectrum was derived theoretically by squaring all components of H and summing according to the distribution function. The significant angular frequency $\omega_s = 2\pi/T_s$ in Eq. (2.49) describes the average angular frequency corresponding to the significant waves in the short-term record of period $T_s = 1/f_s$ and height H_s. The latter is given by the relation $T_s = (4/5)^{0.25}T_p$, where $T_p = 2\pi/\omega_p$ denotes the period corresponding to the angular wave frequency ω_p of the modal value. While the area under the Neumann spectrum was forced to be equal to the Longuet-Higgins energy coefficient $H_{rms}^2 = 4/\pi\bar{H}^2$, the Bretschneider spectrum satisfies this property automatically [Bretschneider 1959, p. 150].

The spectrum proposed by Pierson and Moskowitz [Pierson and Moskowitz 1963] is based on 460 spectra observed and recorded of the fully developed sea in the North Atlantic Ocean from 1955 to 1960 for wind speeds between 20 to 40 knots [Moskowitz 1964]. It has the same exponent values p, q as the Bretschneider spectrum, however, the derivation of the coefficients A and B in Eq. (2.47) does not make use of the assumption that the wave heights and wavelengths follow a Rayleigh distribution, but is based on the similarity hypothesis of Kitaigorodskii and on at-sea measurements of the wave properties. Kitaigorodskii assumed that the wave spectral density depends on four parameters, namely fetch F, gravity acceleration g [m/s^2], friction velocity of the wind U_* [m/s] and frequency f [Hz]. Instead of using the friction velocity as a parameter, the proposed spectrum in Eq. 2.50 is given with respect to the mean wind speed $\bar{U}_{19.5}$ [m/s] measured at $z = 19.5$ [m]. In order to refer the wind velocities measured at any z to the one needed in Eq. (2.50), Pierson suggested the following

relation for $U_{10} \approx 30$ [m/s]

$$\bar{U}_z = U_{10}\left[1 + \frac{\sqrt{0.80 + 0.114U_{10}}}{0.4 \times 10^{3/2}} \ln\left(\frac{z}{10}\right)\right] \tag{2.56}$$

Furthermore, the fetch is assumed to be infinite and thus is not included in the spectrum. The integral of the Pierson-Moskowitz (P-M) spectrum is equal to the variance of the free-surface displacement η defined in Eq. (2.45), that is it holds

$$\int_0^\infty G_{PM}(\omega)d\omega = 2.74 \times 10^{-3}\frac{\bar{U}_{19.5}^4}{g^2} = \frac{H_{rms}^2}{8} = \eta_{rms}^2 \tag{2.57}$$

Consequently, the integral of the Bretschneider and Neumann spectrum, respectively, is eight times that of the Pierson-Moskowitz spectrum [McCormick 2009, p. 142]. The high-frequency part of the Pierson-Moskowitz and Bretschneider spectrum is modeled in agreement with Phillips's hypothesis [Phillips 1958] as ω^{-5} power law decay. He assumed that in a well-developed sea, there is an 'equilibrium range' of high frequencies in the spectrum in the form $S_F(\omega) \sim g^2\alpha_p\omega^{-5}$, determined by the physical parameters, namely the gravity acceleration, governing the formation of sharp crests in breaking waves. The Phillips parameter α_p is a constant, e.g. set to 0.0081 in the Pierson Moskowitz spectrum.
The three discussed spectra are eligible for the description of open-ocean wind-generated seas, that is, where the fetch is assumed to be infinite. However, in cases where the cite is located near the coast of a land mass, i.e. where the wave growth under steady wind conditions is limited by the distance from the shore, this assumption is not justified. To account for limited fetch, in [Hasselmann et al 1973] a modified P-M formula is suggested, which is based on 2500 measured spectra in the German Bight of the North Sea. The spectrum is known as JONSWAP spectrum as it was derived within the **J**oint **N**orth **S**ea **W**ave **P**roject and is given by the formula

$$\text{JONSWAP}: \; G(\omega) = \frac{\alpha g^2}{\omega^5}\exp\left(-\frac{5}{4}\frac{\omega_p^4}{\omega^4}\right)\gamma^{\exp\left(-\frac{(\omega-\omega_p)^2}{2\sigma^2\omega_p^2}\right)} \tag{2.58}$$

where α [-] denotes the energy scale parameter, which is a function of the dimensionless fetch $\tilde{F} = gF/\bar{U}_{10}^2$ [-] in wind direction and which is given by

$$\alpha = 0.07\tilde{F}^{-0.22}; \qquad 0.01 \le \tilde{F} \le 10^5 \tag{2.59}$$

γ [-] is the so-called peak enhancement factor which modifies the interval around the spectral peak leading to a much sharper peak than in the P-M spectrum. Otherwise, the shape of the

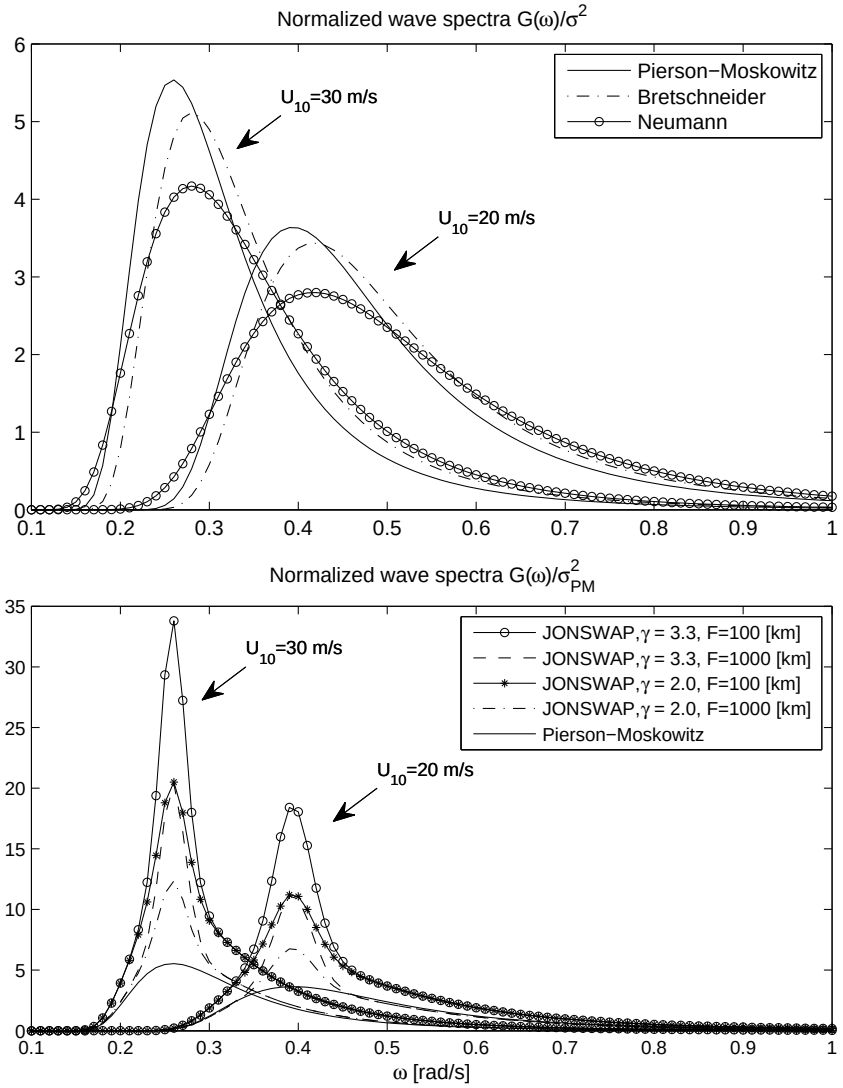

Figure 2.16: Top: Normalized wave spectra with respect to the area below the PSD function for the case of a mean wind velocity of $\bar{U}_{10} = 20, 30$ [m/s] at height $z = 10$ [m]; Bottom: Comparison of the P-M spectrum and the JONSWAP spectrum for different peak enhancement factors $\gamma = 2.0, 3.0$ [-] and for $\bar{U}_{10} = 20, 30$ [m/s]. The spectra are normalized with respect to the area below the P-M spectrum

JONSWAP and P-M spectrum is similar. It is defined by the ratio of the maximum value of the JONSWAP and the P-M spectrum, respectively, and calculated by

$$\gamma = \frac{G_{max}^{JONSWAP}(\omega)}{G_{max}^{PM}(\omega)} \tag{2.60}$$

The peak factor is typically of magnitude 1.5-6 and in the average of order 3.3. The peak shape parameter σ defines the left- and right-sided width of the spectral peak, respectively, and is given by

$$\sigma = \begin{cases} 0.07 & \omega \leq \omega_p \\ 0.09 & \omega > \omega_p \end{cases} \tag{2.61}$$

where ω_p denotes the modal frequency associated with the peak value of the spectrum, which, in contrast to the P-M spectrum, is an adjustable parameter.
The discussed wave spectra are depicted in Fig. (2.16) for different mean wind velocities measured at $z = 10$ [m] over ground. In the upper plot, the P-M, Bretschneider and Neumann spectrum are compared. It is evident that an increase of the mean wind speed leads to an increase of the peak values of the spectra and a shift to smaller frequencies, i.e. the wave height as well as the wave length increase. The spectra are normalized with respect to the area below the respective PSD functions. The mean wind velocities $\bar{U}_{7.5}$ [m/s] and $\bar{U}_{19.5}$ used in the formula of the Neumann and P-M spectrum, respectively, are calculated from Eq. (2.56). As the areas below the spectra proposed by Neumann and Bretschneider are both corresponding to the mean square value of the wave height H^2_{rms}, the significant wave height H_s needed in the equation of the Bretscheider spectrum is chosen in such a way, that the constraint $H^2_{rms} = H^2_{rms,N} = H^2_{rms,B}$ is satisfied. The lower plot of Fig. 2.16 compares the P-M spectrum with its modified version, the JONSWAP spectrum with peak enhancement factors $\gamma = 2.0, 3.3$ [-] and for a fetch of $F = 100, 1000$ [km]. Both spectra are normalized with respect to the area below the P-M spectrum. It is obvious that in the low frequency range and the high frequency range both spectra show a similar characteristic, but they differ significantly in the peak value. However, as expected the difference between the two spectra reduces with increasing fetch.

2.3.6 Wind-induced wave forces

Water waves which pass a circular cylinder of diameter D, cause wave-induced forces whose magnitude depends primarily on the scale of the diameter of the cylinder compared to the wave length and the wave heights, i.e. D/λ and H/D. Depending on these ratios, the forces can be split into three components, namely the viscous pressure force due to a combination of the boundary layer and the wake, the inertial force caused by the acceleration of the water, the structure, or both, and the diffraction force due to scattering, i.e. wave reflection and diffraction. Chakrabarti [Chakrabarti 2005, p. 164ff] summarized the dependency of the components on the length ratios graphically as shown in Fig. 2.17. The chart reveals that the ratio $\pi D/\lambda$ mainly determines if diffraction must be considered and thus is also called diffraction parameter. The second ratio defines the so-called Keulegan-Carpenter number $KC \approx \pi H/D$, valid in this form for deep water waves, and describes the effect of gravity and

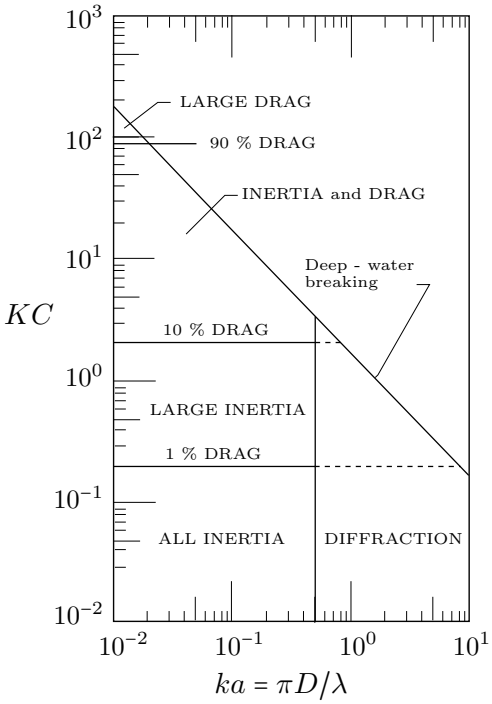

Figure 2.17: Graphical representation of the dominant wave force components (viscous pressure force, inertial force and diffraction force) depending on the diffraction parameter $\pi D/\lambda$ and the Keulegan-Carpenter number $KC \approx \pi H/D$ [McCormick 2009, p. 290]

drag. In the following the discussion will be restricted to structures whose dimensions are small compared to the wave length, i.e. $D/\lambda < 0.2$ [Li and Chen 2009, p. 66], and where the effect of diffraction can be neglected, i.e. $H/D > 2$ (or $KC > 6$).

Assuming non-braking waves, the resulting inertia and drag forces acting on the structure can be described by the so-called Morison equation. The inertia and the drag coefficients C_m [-] and C_d [-], respectively, are determined experimentally either in the laboratory or from field measurements [Chakrabarti 2005, p. 133]. For a vertical, infinitely stiff cylinder under the action of an ocean wave, the Morison equation is given by the following empirical formula

$$F(x,z;t) = \frac{1}{2}\rho_w C_d v(x,z;t)|v(x,z;t)| + \rho_w C_m \frac{\pi D^2}{4} a(x,z;t) \tag{2.62a}$$

where ρ_w is the density of the sea water [Li and Chen 2009] and where the summands

$$F_d(x,z;t) = \frac{1}{2}\rho_w C_d v(x,z;t)|v(x,z;t)| = K_d v(x,z;t)|v(x,z;t)| \tag{2.62b}$$

$$F_m(x,z;t) = \rho_w C_m \frac{\pi D^2}{4} a(x,z;t) = K_m a(x,z;t) \tag{2.62c}$$

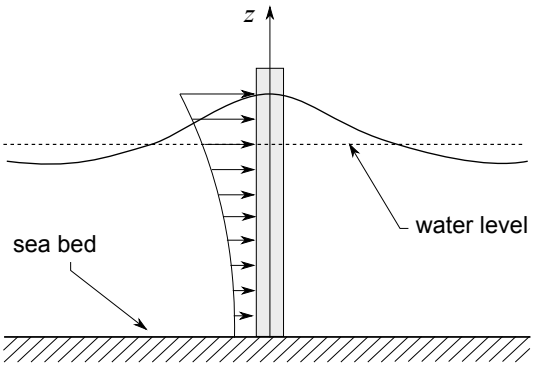

Figure 2.18: Distribution of the wave force [Li and Chen 2009, p. 67]

denote the horizontal drag and inertia forces $F_d(x,z;t)$, $F_m(x,z;t)$, respectively. The profile of the wave forces along the height of the piles is schematically depicted in Fig. 2.18. In general C_m ranges between $1.6 - 2.5$ and for a vertical cylinder $C_m = 2.0$ can be assumed. The drag coefficient C_d never falls below 0.6 and for a smooth cylinder $C_d = 1.0$ [Norton and Quarton 2003]. The functions $v(x,z;t)$, $a(x,z;t)$ describe the horizontal particle velocity and acceleration, respectively. While the former is in phase with the wave profile $\eta(x,t)$ given by Eq. (2.45), the horizontal acceleration is 90° out of phase. They are derived by linear wave theory, leading to

$$v(x,z;t) = H(\omega,z)\eta(x,t); \qquad a(x,z;t) = H(\omega,z)\dot{\eta}(x,t) \tag{2.63a}$$

where $H(\omega,z)$ is given by

$$H(\omega,z) = \begin{cases} \dfrac{\omega\cosh[k(z+h)]}{\sinh[kh]}; & \dfrac{h}{\lambda} \geq \dfrac{1}{2} \text{ (finite depth)} \\ \omega\exp(kz); & \dfrac{h}{\lambda} \leq \dfrac{1}{20} \text{ (deep water)} \end{cases} \tag{2.63b}$$

Due to the random nature of the wind waves, the surface displacement $\eta(x,t)$ can be regarded as random field. Assuming that the differences of the waves at different points along the x axis can be ignored, i.e. if the wave is assumed completely correlated along the x direction, then the random field $\eta(x,t)$ reduces to a random process $\eta(t)$. However, the physical relations given in Eq. (2.63) between the surface displacement $\eta(t)$ and the horizontal velocity and acceleration $v(z;t)$, $a(z;t)$ of the water particles in the wave process still hold.
The drag force in Eq. (2.62b) is a quadratic function of the wave velocity leading to a nonlinear relation between the surface evaluation and the wave-induced forces. Due to this nonlinearity, the exact calculation of the response statistics is difficult and thus, the quadratic factor $v(z;t)|v(z;t)|$ is replaced by a linear term $cv(z;t)$ where c is a constant and $v(z;t)$ a

zero mean Gaussian process with standard deviation σ_u. By employing the statistical least-square-error technique, the constant is derived by minimizing the expectation of the square error between the linear and quadratic functions, i.e. $E[(v(z;t)|v(z;t)| - cv(z;t))^2]$ leading to the value $c = \sqrt{8/\pi}\sigma_u$. Introducing the linearized drag force [Hu et al 1991]

$$F_d = \sqrt{\frac{8}{\pi}} K_d \sigma_u v(z;t) \tag{2.64}$$

into the Morison equation (2.62a) and taking into account the relations (2.63), yields the following simplified formula for the load process

$$F(z;t) = \sqrt{\frac{8}{\pi}} K_d \sigma_u H(\omega,z)\eta(t) + K_m H(\omega,z)\dot{\eta}(t) \tag{2.65a}$$

Assuming that the displacement and velocity $\eta(t)$, $\dot{\eta}(t)$ can be represented as stationary random processes whose PSD functions $G_\eta(\omega)$, $\dot{G}_\eta(\omega) = \omega^2 G_\eta(\omega)$ are known e.g. from measurements, then the PSD function of the load process can be easily calculated from Eq. (2.65a) leading to [Li and Chen 2009, p. 66-67]

$$G_F(z;\omega) = \left(\frac{8}{\pi} K_d^2 \sigma_u^2 + K_m^2 \omega^2\right) |H(\omega,z)|^2 G_\eta(\omega) \tag{2.65b}$$

Similar to the relation in Eq. (2.44) which relates the wind velocity spectrum to the spectrum of the wind force, this relation finally allows transferring the discussed wave spectra of the surface evaluation directly to the spectra characterizing the wave load process. Now, assuming that the load spectra is known from measurements or given by one of the modal spectra, the next step is the digital simulation of realizations of the random process with target PSD function, in order to include the load process as input in the response analysis or system identification. To this aim, in the next chapter different algorithms for the digital simulation of the target process are critically reviewed.

3 State-of-the-Art on Digital Simulation of Ambient Loads - Traditional Methods

The proposed identification algorithm is based on the concept, that the unmeasured load process is modeled as output of linear system driven by white noise which then can be added to the dynamic system of the structure. In order to apply the Kalman filter algorithm, the load model must be Gaussian and expressible in state space form. Furthermore, the digital simulation technique should be applicable to a wide range of processes, that is without restriction to the functional form of the PSD function. To this aim, in this chapter, different algorithms for the digital simulation of Gaussian random processes which are widely used in literature are reviewed as well as discusses with respect to these requirements. The different methods are classified in spectral representation approaches and digital filters schemes with band-limited white noise input as proposed in [Kareem 2008]. The first class is based on the superposition of sine and cosine functions with random phase either carried out in the time or in the frequency domain using fast Fourier transform (FFT) and are discussed in the following in section 3.1. In the second class described in section 3.2, the process is modeled as output of a linear system subjected to white noise represented either by convolution of the input process with the impulse response function or by integration of a differential equation driven by white noise. The former is based on the spectral factorization theorem and discussed in section 3.2.2 and the latter leads to parametric time series models such as autoregressive (AR), moving average (MA), and the combined ARMA models to simulate the time series of the random process (s. 3.2.1). Such time domain methods are of great importance e.g. in the response analysis and design of structural control.
In chapter 4 the concept of state space modeling is introduced and applied to the discussed parametric time series models (s. 4.2, 4.3) and the transfer function obtained by spectral factorization of the PSD function (s. 4.4). The state space form is needed in chapter 7 to include colored processes in the Kalman filter algorithm.

3.1 Wave superposition-based methods

The spectral representation methods, proposed in [Shinozuka and Jan 1972], belongs to the most popular methods for the digital simulation of random processes in the engineering community. It allows generating sample functions with target probabilistic characteristics of stationary/ non-stationary, homogeneous/non-homogeneous, one-dimensional/multi-dimensional, one-variate/multi- variate as well as Gaussian/non-Gaussian stochastic processes, fields or waves. Combined with the Monte Carlo Simulation algorithm, the method can be applied to a variety of engineering problems in stochastic mechanics such as nonlinear problems or problems related to the stochastic stability, parametric excitation, parameter and input uncertainties, risk assessment, etc.. Before the publication of the milestone paper [Shinozuka and Jan 1972] in the beginning of the seventies, most methods for the digital simulation of random processes were restricted to the univariate or unidimensional case. The first techniques which overcome this restriction were published by [Borgman 1969] and [Shinozuka 1971]. Borgman developed a method for the simulation of stationary, ergodic sea surface elevations by superposition of sine waves with weighted amplitude consistent with the energy in the target spectral density at that frequency. In [Shinozuka 1971] a similar method for the simulation of multivariate and multidimensional processes with given cross-power spectral density was developed. It is shown that the process can be generated as the sum of cosine functions with random frequency and random phase angle. The main drawback of the method is the time consuming generation of the random frequencies according to the cross power spectral density function which makes it cumbersome for the treatment of processes with high dimensionality. The representation proposed in [Shinozuka and Jan 1972] is a modification of the method which no longer requires the generation of random frequencies. It is based on the decomposition of the random process into a series of cosine functions with weighted amplitudes corresponding to the known PSD, evenly (possibly unevenly) spaced random frequencies and uniformly distributed random phase angles. If the PSD function is sampled with constant sample rate, then the resulting series representation can be calculated efficiently using the Fast Fourier transformation (FFT) as shown in [Yang 1972].

The univariate one-dimensional (1V-1D) zero-mean stationary stochastic process $\{F(t)\}$ with PSD $S_F(\omega)$ can be simulated by the following series [Shinozuka and Jan 1972; Schuëller 1997]

$$F(t) = \sqrt{2} \lim_{N\to\infty} \sum_{k=0}^{N-1} A_k \cos(\omega_k t + \phi_k) \tag{3.1}$$

where $k \in \mathbb{N}_0$, $\omega_k = k\Delta\omega$ and with $A_k = \sqrt{2S_F(\omega_n)\Delta\omega}$. The sampling rate $\Delta\omega = \omega_u/N$ is determined from the cut-off frequency ω_u beyond which the values of the PSD function are assumed to be zero. The random phase angles ϕ_k are independent and uniformly distributed over the interval $[0,2\pi]$. Hence, the process defined by Eq. (3.1) is the result of the superposition of many independent identical distributed (i.i.d.) random variables with finite variance. According to the central limit theorem the process is asymptotically Gaussian if $N \to \infty$. Furthermore, it must be noted, that the generated process is periodic with period $T_0 = 2\pi/\Delta\omega$. In order to assure ergodicity in the mean value and the autocorrelation function of each sample of the simulated process the constraint $A_0 = 0$ or $S_F(0) = 0$ must be satisfied and the length of the sample function is either equal to the period T_0 or tends to infinity [Schuëller 1997]. Otherwise, the mean value obtained by averaging of the generated signal over the simulation time is different from zero.

The efficiency of the simulation can be improved by rewriting Eq. (3.1) in polar coordinate form

$$F(t) = \sqrt{2\Delta\omega}Re\{X(t)\} \qquad \text{where} \qquad X(t) = \sum_{k=1}^{N}\left[\sqrt{2S_F(\omega_k)}e^{i\phi_k}\right]e^{i\omega_k t} \tag{3.2}$$

where $X(t)$ is the finite complex Fourier transform of $\sqrt{2S_F(\omega)}e^{i\phi}$. Applying the FFT leads to a significant saving in computer time [Yang 1972]. A review paper on the simulation of one-dimensional and uni-variate stationary stochastic processes is published by [Shinozuka and Deodatis 1991].

In order to describe the system's response of a structure excited by a stochastic field, e.g. by a wind field acting on a building, the variation of the dynamic load process in time as well as in spatial locations must be taken into account. Such a wind field can be represented by a discretized n-variate *one*-dimensional (nV-$1D$) stochastic vector process where the components of the n-dimensional zero-mean vector $\{\mathbf{F}(t)\} = [F_1(t), F_2(t), \ldots, F_n(t)]$ describe the along wind processes acting on n locations of the structure [Di Paola 1998][1]. In order to generate a realization of the process, the cross PSD (XPSD) matrix $S_F(\omega)$ (s. A.9a) is factored by applying the Cholesky decomposition leading to

$$\mathbf{S}_F(\omega) = \mathbf{H}(\omega)\mathbf{H}^*(\omega)^T \tag{3.3}$$

[1] In the annexe A.1.4.2 further detail on multivariate and multidimensional processes is given

where the asterisk indicates the complex conjugate and where $\mathbf{H}(\omega)$ is a lower triangular matrix of the form

$$\mathbf{H}(\omega) = \begin{bmatrix} H_{11}(\omega) & 0 & \dots & 0 \\ H_{21}(\omega) & H_{22}(\omega) & \dots & \dots \\ \dots & \dots & \dots & 0 \\ H_{n1}(\omega) & H_{n2}(\omega) & \dots & H_{nn}(\omega) \end{bmatrix} \tag{3.4}$$

Here it was assumed that the XPSD matrix is Hermitian and positive definite. For the general case of a non-negative definite XPSD matrix, see [Shinozuka and Jan 1972]. The diagonal elements $H_{jj}(\omega)$ are real and the off-diagonal terms $H_{jk}(\omega)$ are in general complex function of ω. They can be expressed in polar form as

$$H_{jk}(\omega) = |H_{jk}(\omega)|e^{i\theta_{jk}\omega} \qquad \text{where} \qquad \theta_{jk}(\omega) = \begin{cases} \tan^{-1}\left(\frac{ImH_{jk}(\omega)}{ReH_{jk}(\omega)}\right), & j \neq k \\ 0, & j = k \end{cases} \tag{3.5}$$

leading to the following series representation of the j-th component of the n-dimensional vector process $\{\mathbf{F}(t)\}$ given by

$$F_j(t) = 2 \lim_{N\to\infty} \sum_{m=1}^{n} \sum_{k=1}^{N} |H_{jm}(\omega_{mk})| \sqrt{\Delta\omega} \cos(\omega_{mk} - \theta_{mk}(\omega_{mk}) + \phi_{mk}) \tag{3.6}$$

where $\omega_{mk} = (k - (n-m)/n)\Delta\omega$ and the sampling rate is defined as before from the cut-off frequency $\Delta\omega = \omega_u/N$ of the PSD [Schuëller 1997]. In [Shinozuka 1974] the applicability of the FFT technique in the scope of the digital simulation of multidimensional processes is explained and illustrated in detail for the two dimensional case.

In [Yamazaki and Shinozuka 1988] an iterative procedure is developed which allows generating samples of non-Gaussian multidimensional homogeneous fields. The spectral representation method is used for the generation of Gaussian sample fields which are then transformed into non-Gaussian sample fields by applying an iterative mapping technique. The method is used for the simulation of a two-dimensional stochastic field with target power spectral density whose one-dimensional distribution function is described by a beta distribution. Recently, the technique is compared with a new spectral based method introduced by [Yura and Hanson 2011] which allows generating samples of a stochastic process with arbitrary given probability density function and specified power spectral density. The method relies on initially transforming a Gaussian white noise process into a corresponding Gaussian set of colored random numbers with the desired spectral distribution. In contrast to the previous method the desired probability distribution is obtained via an inverse transform which

is non-iterative which makes the method not as accurate but straightforward, efficient and computational fast.
Based on Priestley's evolutionary power-spectrum [Priestley 1965] a theory for non-stationary propagating seismic waves as well a technique for digitally generating samples of such waves is proposed in [Deodatis and Shinozuka 1989] which allows considering their stochastic characteristics in the time and space domain. The method is used for the digital generation of (non-dispersive) Rayleigh waves modeled as non-stationary stochastic waves with two-dimensional spatial non-homogeneity. The method is verified using acceleration data of the ground motion recorded during an earthquake in Lotung, Taiwan in 1981. Due to the lack of frequency-wave number analysis an artificial non-dispersional relationship between the wave numbers and the frequency was assumed. In [Deodatis et al 1990] this assumption was relaxed and a method for the digital simulation of seismic ground motion based on its frequency-wave number spectra is derived. Using an extension of the spectral representation method, the simulation is performed by superposing a number of plane waves, having amplitudes consistent with the frequency-wave number spectra which is derived analytically considering the seismic source as a point source located in an elastic half-space. The generation of non-stationary, multi-variate stochastic vector processes with evolutionary power spectral density are discussed in [Deodatis 1996a]: An iterative algorithm for the generation of seismic ground motion time histories at several locations on the ground surface is proposed using response spectra or evolutionary time-dependent cross-spectral density functions. The latter can be estimated by means of the short-time Fourier transform (STFT), the wavelet transform (WT) and the Hilbert-Huang transform (HHT) from measured response data as shown in [Liang et al 2007].
In case of non-stationary/non-homogeneous processes the conventional spectral representation method introduced by [Shinozuka and Jan 1972] does not generate ergodic sample functions. In [Deodatis 1996b] a modification of the method is presented which succeeds in generating ergodic sample functions of a stochastic vector process. After the first review paper on simulation of one-dimensional and uni-variate stationary stochastic process [Shinozuka and Deodatis 1991], a detailed review on simulation of multi-dimensional homogeneous stochastic fields using the spectral representation technique can be found in in [Shinozuka and Deodatis 1996].

From the literature review it can be summarized that the main limitations of the spectral representation method are: i) The stochastic process is modeled as (theoretical infinite) series of trigonometric functions; ii) Especially if processes with a large number of variates are considered, this leads to computational difficulties; iii) The use of the Fast Fourier transform improves the computational efficiency drastically, but not without the expense of increased

demand on computer storage [Kareem 2008]. Furthermore, the efficiency strongly depends on the frequency truncation and thus the algorithm is not suited for power-law spectra; These limitations are even more severe iv) if the simulation is to be performed over a long period of time, as the generation of the samples is, even in the one-dimensional univariate case, computational demanding [Samaras et al 1985]. Besides these difficulties, the crucial problem arises from the fact, that the obtained series representation of the process cannot be written in the required state space form in order to combine it with the later used system identification technique.
Besides, a similar problem occurs if the Karhunen-Loéve decomposition of the random process is used. This is based on linear superposition of deterministic functions where the combination factors are a set of uncorrelated random variables [Li and Chen 2009, p. 27 ff.]. Also in this approach the resulting equations cannot be written in state space form and hence the method is not appropriate.

3.2 Digital filter schemes

Digital filtering refers to methods which model the process as output of a linear system subjected to white noise represented either by integration of a differential equation driven by white noise or by convolution of the input process with the impulse response function. The former strategy leads to parametric time series models, discussed in the following and the latter is based on so-called shaping filters obtained by spectral factorization of the PSD function of the target process as shown in section 3.2.2.

3.2.1 Parametric time series-based methods

A different approach to the wave superposition method consists in using time series models whose parameters are tuned to match a target PSD function. This might be more efficent because digital filtering schemes, such as autoregressive (AR), moving average (MA) or their combination autoregressive moving averages (ARMA) generate the random process recursively on basis of previous samples. In contrast to FFT-based techniques, parametric models are characterized by the filter coefficient matrices and consequently, just a limited amount of information must be stored during the simulation. Hence, even long duration processes can be generated more efficiently from recursive relations. The main concerns in using these models regards firstly, the determination of the optimal parameters and secondly, the needed model order.

A weakly univariate stationary process $\{F_t\}$ with given AC function $R_F(\tau)$ is said to be an ARMA(p,q) series with autoregressive order $p \geq 0$ and moving-average order $q \geq 0$, if it is the solution of the following discrete difference equation[2]

$$F_k - a_1 F_{k-1} - \ldots - a_p F_{t-p} = W_k - b_1 W_{k-1} - \ldots - b_q W_{k-q} \tag{3.7}$$

where $\{W_t\}$ is a sample of a zero mean Gaussian white noise sequence with variance σ_W^2 (compare Eq. (2.11)). If $q = 0$ Eq. (3.7) reduces to an autoregressive series AR(p) of order p, while in case of $p = 0$, Eq. (3.7) is denoted as moving average series MA(q) of order q. MA models are widely used for the simulation of random processes characterized by an all-zero spectra, i.e. if the estimated PSD has no prominent peaks, in contrast to AR models which are more suitable for all-pole spectra, i.e. the PSD is characterized mainly by spectral peaks at distinct frequencies. Their combination, the ARMA model, yields a PSD with peaks and polynomial background [Spanos 1983; Broersen and De Waele 2003; Kantz and Schreiber 2008] which is suitable for a wide range of spectra with both poles and zeros. While the coefficients of the AR model can be derived by linear regression, the approximation of the process by the more general ARMA model leads to an highly non-linear minimization problem. Defining the autoregressive and moving-average polynomials $a(z)$ and $b(z)$, respectively by

$$a(z) = 1 - a_1 z - a_2 z^2 - \ldots - a_q z^q; \qquad b(z) = 1 - b_1 z - b_2 z^2 + \ldots - b_p z^p \tag{3.8}$$

where $z \in \mathbb{C}$, the ARMA model in Eq. (3.7) can be also written as

$$a(L) F_k = b(L) W_k \tag{3.9}$$

where L denotes the lag (or backward shift) operator with the property $L^k F_t = F_{t-k}$ for $k \in \mathbb{N}_0$. It can be shown that Eq. (3.9) defines a stationary process, if all roots of the characteristic equation $a(L) = 0$ lie outside the unit circle [Box et al 2008, p. 95], i.e. $|L| > 1$. To make this more clear, assume for instance the case of a first-order autoregressive model ($q = 1$, $p = 0$), i.e.

$$(1 - a_1 L) F_k = w_k \quad \text{or} \quad F_k = a_1 F_{k-1} + w_k \tag{3.10}$$

[2] It must be noted that in literature, e.g. [Box et al 2008], the ARMA series is sometimes defined using positive signs before the moving-average coefficients

it is easily verified[3] that the series increases exponentially after a short induction time, if a_1 lies outside the stationary range $|a_1| < 1$ [Box et al 2008, p. 95].
If the process is stationary and if the characteristic polynomial $b(L) = 0$ has additionally all its roots outside the unit circle, the process is said to be invertible [Box et al 2008, p. 79f.]. In this case, the stationary and finite ARMA(p,q) model can be transformed into an infinite MA(∞) series

$$F_k = c(L)W_k = \sum_{j=0}^{\infty} c_j W_{k-j} \tag{3.11}$$

where $c(L) = a^{-1}(L)b(L)$ and, if the process is invertible, into an infinite AR(∞) model

$$d(L)F_k = F_k - \sum_{j=1}^{\infty} d_j F_{k-j} = W_k \tag{3.12}$$

where $d(L) = b^{-1}(L)a(L)$. While stationarity implies that the weights c_j and d_j are absolutely summable, the invertibility of the ARMA process allows representing the ARMA process in terms of previous values of F_k and an innovation which is independent of the past. Thus, the invertibility is a necessary and sufficient condition for an ARMA series to be uniquely determinable (to a second order) from the knowledge of its autocovariance function [Holan et al 2010].

Though, while the coefficients of the AR model can be derived by linear regression, the approximation of the process by the more general ARMA model leads to a highly non-linear minimization problem[4]. In [Spanos and Mignolet 1986; Mignolet and Spanos 1987; Spanos and Mignolet 1987; Spanos and Zeldin 1996] the optimization problem is solved by two stage algorithms where first the process is approximated as high order AR series by autocorrelation matching and then in a second step a low order ARMA representation of the prior model is derived by matching of the output autocorrelations and input-output cross-correlations. The methods are verified by application to spectra encountered in earthquake engineering (Kanai-Tajimi spectrum), wind engineering (von Kármán velocity spectrum) and ocean engineering (Pierson-Moskowitz (P-M) spectrum). In case that the target spectrum exhibits zeros like the P-M spectrum or a slope discontinuity like the Davenport spectrum, the computation of reliable AR approximations need some further tuning of the ARMA model [Mignolet and Spanos 1991]. Zeros in the target spectrum leads indeed to high frequency fluctuation in the

[3] either by solving the characteristic equation, e.g. $(1 - a_1 L) = 0 \Rightarrow L = \frac{1}{a_1} \cap |L| > 1 \Rightarrow |a_1| < 1$ or by substitution of the equation recursively into itself, i.e. $F_k = \sum_{j=0}^{k} (a_1)^j W_{k-j} + (a_1)^{k+1} F_{k-j}$

[4] In annexe B.1.1 an iterative procedure is described exemplarily where first the AR coefficients are estimated by a least square algorithm and secondly, the MA coefficients are determined iteratively by solving a nonlinear system of equation.

corresponding AR spectrum whose amplitude decays slowly with increasing system order. The problem is discussed in detail in scope of the properties of the z-Transform in [Spanos and Mignolet 1986], where a Taylor series expansion of the P-M spectrum is proposed to reduce the effect of the zero in the spectrum. Instead of approximating the ARMA representation on basis of a high order AR model in [Spanos and Mignolet 1990] the problem is solved by a two stage approach, where the first step is to calculate a high order MA representation being more suited to model zeros is the spectrum. In [Mignolet and Spanos 1991] it is shown that the rate of convergence of this algorithm can be improved by adding a very small positive value to the target spectrum so that the zero, causing the numerical problems, is removed. Slope discontinuities in the spectrum also lead to a slow convergence of the AR model to the target process, in particular a kink at small frequency leads to a decrease of the convergence rate. A general shortcoming of ARMA-based algorithms is the fact, that they require a repetitive calculation of the AR and MA parameters in order to find the optimal order of these models. The model selection problem has been studied extensively and the proposed algorithms can be split into the information criterion based methods, such as the Akaike information criterion, the minimum describing length and the minimum eigenvalue criterion, and the linear algebraic methods which are based on determinant and rank testing algorithms [Sadabadi et al 2009]. A comparative study of several information criterion based methods is given in [Stoica and Selen 2004]. Though, at the best of the author's knowledge, there are not methods to a priori estimate the number of coefficients to be calculated for the AR and MA parts.

In [Di Paola and Zingales 2008] a time-continuous counterpart to the discrete-time AR models for the generation of stationary Gaussian processes was proposed. The method is applied for the simulation of random processes with Davenport and Kaimal velocity PSD. In contrast to the standard recursive ARMA representations which is based on difference equations, the continuous model allows the analysis using stochastic differential calculus which has been proved to be an efficient method for the evaluation of the statistics of linear and non-linear dynamical systems subjected to external and parametric white noises such as Poissonian and Lévy delta-correlated processes.

An important characteristic of ARMA-based models is that their AC function exhibits an exponential decay rate which will be shown in the following. To this aim assume a zero mean ARMA(p,q) process as defined by Eq. (3.7). Multiplying by F_{t-k} and taking the expectation yields a difference equation

$$\begin{aligned} R_F(k) = a_1 R_F(k-1) + a_2 R_F(k-2) + \ldots + a_p R_F(k-p) + \\ R_{FW}(k) - b_1 R_{FW}(k-1) - b_2 R_{FW}(k-2) - \ldots - b_q R_{FW}(k-q) \end{aligned} \tag{3.13}$$

in terms of the autocorrelation $R_F(k) = E[F_{t-k}F_t]$ and cross correlation function $R_{FW}(k) = E[F_{t-k}W_t]$, respectively. Using the infinite MA representation, it can be shown that the series $F_{t-k} = \sum_{n=0}^{\infty} c_n W_{t-k-n}$ only depends on the white noise sequence up to time $t-k$. Consequently, $R_{FW}(k) = 0$ for $k > 0$ and $R_{FW}(k) = c_{-k}\sigma_W^2$ for $k \leq 0$, yielding

$$\begin{aligned} R_F(k) = a_1 R_F(k-1) + a_2 R_F(k-2) + \ldots + a_p R_F(k-p) - \\ - \sigma_W^2 \left(b_k c_0 + b_{k+1} c_1 + \ldots + b_q c_{q-k}\right), \qquad k \leq q \end{aligned} \tag{3.14}$$

For $k > q$ Eq. (3.14) reduces to a pth order difference equations given by

$$R_F(k) = a_1 R_F(k-1) + a_2 R_F(k-2) + \ldots + a_p R_F(k-p), \qquad k > q \tag{3.15}$$

which can be written in compact form as

$$R_F(k) - \sum_{j=1}^{p} a_j R_F(k-j) = a(L) R_F(k) = 0, \qquad k > q \tag{3.16}$$

which is also known as modified Yule-Walker equations[5]. Solving Eq. (3.16) for the autocorrelation function $R_F(k)$ is very similar to solving homogeneous differential equations. Assuming that the characteristic polynomial $a(z)$ in Eq. (3.8) has distinct roots $\lambda_1, \lambda_2, \ldots, \lambda_p$, then the solutions to Eq. (3.14), can be expressed as linear combinations of geometric sequences, i.e. damped exponentials and sinusoidal, in the form [Rao 2008]

$$R_F(k) = \sum_{k=1}^{p} C_k \lambda_k^{-k} \tag{3.17}$$

where C_k are constants. Indeed, the autocorrelation function of stationary, causal ARMA models converges rapidly, i.e. exponentially, to zero as the lag approaches infinity, i.e. $k \to \infty$, and thus belong to the class of *short memory processes*. This leads to the following relation

$$|R_F(k)| \leq C\lambda^{-k} \qquad k = 1,2,\ldots \tag{3.18}$$

where $\lambda > 1$, $C < \infty$ are some constants. From Eq. (3.17) it follows, that the largest possible value of λ is defined by the magnitude of the largest root of $a(z)$ [Holan et al 2010], [Box et al 2008, p. 428f.].

In section 5.6 stationary processes with a more slowly decaying autocorrelation function are discussed, which are referred to as *long memory processes* (or long-correlated processes), and

[5] The name is motivated by the similarity to the Yule-Walker equations arising in the autoregressive modeling problem which have the form of Eq. (3.16) but with $k > 0$, i.e. for $q = 0$ [Kay 1993, p. 266ff.]

can be described by a modified form, the so-called fractionally integrated ARMA processes (ARFIMA) [Granger and Joyeux 1980] which can be interpreted as ARMA processes driven by fractionally integrated white noise [Box et al 2008, p. 428–436].
Besides, in the last decades many variants and extensions of ARMA models have been proposed to develop models with periodicities (e.g. SARMA, PARMA models), stochastic volatility (changing variances, e.g. ARCH, GARCH models) as well as multivariate series (VARMA, MGARCH models) and discrete counts (INARMA models). In [Holan et al 2010] a comparison of common variants of ARMA models as well as an extensive bibliography for further reading is provided.

3.2.2 Shaping filters

In the previous chapter it was shown that stochastic loads caused by wind turbulences and wind-waves of the fully developed sea can be modeled as stationary Gaussian processes and thus are characterized completely by the second order statistic. The next step, which will be discussed in the following, is the simulation of realizations of these processes with target PSD function, either known from measurements or using one of the discussed model spectra. A colored Gaussian noise process $\{F(t)\}$ with target PSD $S_F(\omega)$ can be represented as output of a linear differential equation, a so-called shaping filter, excited by a Gaussian white noise process $\{W(t)\}$. That is, the process can be expressed using a linear differential operator $\mathcal{L}(\cdot)$ in the form

$$\mathcal{L}(F(t)) = W(t) \tag{3.19}$$

where $\{W(t)\}$ denotes the standard Gaussian white noise process of intensity q_W as defined in (2.9). The corresponding input-output relation of a single-input-single-output (SISO) linear system can be characterized either in the frequency domain in terms of the transfer function $H(\omega)$

$$S_F(\omega) = |H(\omega)|^2 S_W(\omega) = \frac{q_W}{2\pi}|H(\omega)|^2 \tag{3.20a}$$

or in the time domain by the impulse response function $h(t)$ through the Duhamel integral

$$F(t) = \int_{-\infty}^{\infty} h(t-\tau)W(\tau)d\tau = \int_{-\infty}^{t} h(t-\tau)W(\tau)d\tau \tag{3.20b}$$

Here it is assumed that the process $\{F(t)\}$ is causal, that is $h(t) = 0$ for $t < 0$. Many methods exists to find $H(\omega)$ given the target PSD of $\{F(t)\}$, with the aim of simulating realizations

of the process $\{F(t)\}$. If the process is described by a rational PSD then determining a shaping filter is possible by the spectral factorization theorem as will be explained in the next section.

3.2.2.1 The spectral factorization theorem

The concept of the spectral factorization was proposed by Wiener in [Wiener 1949]. He showed, that a wide-sense stationary stochastic process with given PSD function, can be modeled as output of a time invariant system with white noise input, if the Paley-Wiener condition is met. The Paley-Wiener theorem says, that if the condition

$$\int_{-\infty}^{\infty} \frac{\ln \phi(\omega)}{1+\omega^2} d\omega < \infty \tag{3.21a}$$

is satisfied and if $\phi(\omega)$ is a real non-negative, quadratically integrable function, i.e.

$$\int_{-\infty}^{\infty} |\phi(\omega)|^2 d\omega < \infty, \tag{3.21b}$$

then there exists a factorization in the form

$$\phi(\omega) = g(\omega) g(-\omega) \tag{3.21c}$$

where $g(\omega)$ is the Fourier transform of a function $g(t)$ which vanishes for $t < 0$ and $g(-\omega) = g^*(\omega)$ is the conjugate complex. Hence, if the PSD of the process $S_F(\omega)$ satisfies the conditions Eq. (3.21a) and (3.21b) and the transfer function $g(\omega) = H(\omega)$ is obtained from Eq. (3.21c), the property $h(t) = 0$, for $t < 0$ guarantees the causality of the generated process. If discrete time processes are considered, then the fulfillment of the condition

$$\int_{-\pi}^{\pi} |\ln \phi(\omega)| d\omega < \infty \tag{3.21d}$$

is sufficient in order to allow the factorization [Åström 1970, p. 112f.]. However, if the target PSD of the process is of non-rational type, its factorization is difficult and a spectral factor can be only derived analytically in special cases. A survey of spectral factorization methods for both rational and non-rational PSD can be found in [Sayed and Kailath 2001].
In the following a process with rational PSD shall be considered. It can be expressed in the form

$$S_F(\omega) = \frac{a_0 + a_1\omega^2 + a_2\omega^4 + a_3\omega^6 + \dots}{b_0 + b_1\omega^2 + b_2\omega^4 + b_3\omega^6 + \dots} \tag{3.22a}$$

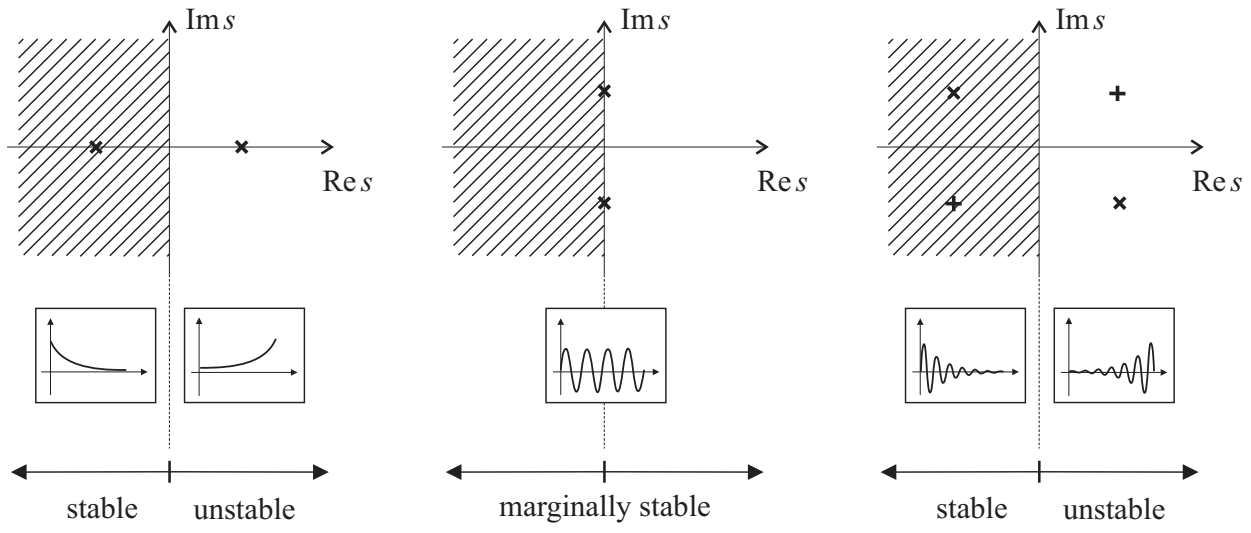

a) $d_j > 0$, *real* *b*) $d_j < 0$, *imaginary* *c*) $d_j = d_k^*$, *complex*

Figure 3.1: Roots and zeros of the PSD in the s plane

or alternatively in the Laplace domain

$$S_F(\omega) = \frac{a_0 - a_1 s^2 + a_2 s^4 - a_3 s^6 + \dots}{b_0 - b_1 s^2 + b_2 s^4 - b_3 s^6 + \dots} \tag{3.22b}$$

by replacing $\omega = is$, $\omega^2 = -s^2$, respectively. Since $S_F(\omega)$ is a even function and so is $S_F(s)$, there are no odd powers of ω, s, respectively. $S_F(s)$ can then always be factored in the form

$$S_F(s) = C \cdot \frac{(c_1 - s^2)(c_2 - s^2)\dots}{(d_1 - s^2)(d_2 - s^2)\dots} \tag{3.22c}$$

where C denotes a constant. As the parameters a_k, b_k are real-valued coefficients, the values c_k, d_j must be either real or appear in conjugate complex pairs. Consequently, the poles p_j of the polynomial will encounter one of the three cases

$$\begin{aligned} &d_j \in \mathbb{R},\ d_j > 0 && p_j = \pm\sqrt{d_j} = \pm a \\ &d_j \in \mathbb{R}\ d_j < 0 && p_j = \pm i\sqrt{d_j} = \pm i\omega_0 \\ &d_j = d_k^* \in \mathbb{C} && p_k = \pm(a + i\omega_0),\ p_j = p_k^* = \pm(a - i\omega_0) \end{aligned} \tag{3.23}$$

The zeros corresponding to the c_j in Eq. (3.22c) are treated analogously. As illustrated in Fig. 3.1 pure real or imaginary roots and poles appear as doubles and are symmetric about the imaginary and real axis, respectively (case a) and b)), while complex roots and poles occur in quadruplets and are symmetric about both the real and imaginary axes of the s plane

(case c)). The locations of the poles and zeros of the transfer function are directly related to the differential equation describing the process [Maybeck 1979, p. 186ff.]. In particular, the location of the poles in the s plane characterizes the components in the homogeneous part of the system response as depicted in Fig. 3.1: A negative real pole $p = -a$ in the left half plane corresponds to an exponentially decaying component, while a positive real pole $p = a$ leads to an unstable system with an unbounded exponential growth. An imaginary pure complex pole pair $p = \pm i\omega_0$ results in an oscillatory component with frequency ω_0 and constant amplitude; they are called marginally stable. Combining both characteristics, the complex conjugate pole pair $p = -a \pm i\omega$ in the left half plane leads to an exponentially decaying sinusoidal system response, while the pole pair $p = a \pm i\omega_0$ lying in the right half plane is unstable and corresponds to an exponentially increasing sinusoidal component.
In the next step, all stable factors corresponding to the zeros and poles lying in the left half of the s plane are collected in the factor $S_{F,L}(s)$ and, similarly, the unstable ones corresponding to the right half plane are gathered in the factor $S_{F,R}(s)$. The pairs of pure imaginary poles are distributed each arbitrarily between the both factors and the constant term is partitioned as $\sqrt{C}$. Finally this yields the sought factorization of the PSD

$$S_F(s) = S_{F,L}(s)S_{F,R}(s) = S_{F,L}(s)S_{F,L}(-s). \tag{3.24}$$

where the last equality results directly from the symmetry of the poles and zeros with respect to both coordinate axes as shown in Fig. 3.1. Using the relation in Eq. (3.20a) and $S_W(s) = q_W$, the shaping filter of the process can finally be derived by

$$H(s) = \frac{S_{F,L}(s)}{S_{W,L}(s)} = \sqrt{\frac{1}{q}}S_{F,L}(s) \tag{3.25}$$

The restriction that the poles belong to the left half of the s plane guarantees the stability of the process, i.e. the system response tends asymptotically against zero or a finite value as t increases. If the system has additionally more poles than finite zeros, then the system is said to be causal, that is the output just dependents on actual and previous inputs. If both, poles and zeros, are within the left half plane, the system is of minimum phase which guarantees that the system $H(s)$ as well as its inverse $1/H(s)$ are stable.
Finally, applying an inverse Laplace transform provides the impulse response function which convolved with the white noise input provides a sequence of the process using Eq. (3.20b). Alternatively, the transfer function can be represented in state space form as discussed in section 4.4.
It must be stressed that in the non-rational case or in the matrix case, the factorization of the PSD function in analytic form is in general not possible and difficulty arises from the fact

that the above factorization is non unique, unless it is assumed that the spectral factor is of minimum phase. In the scope of this work this is a severe limitation as from the comparison of the model spectra discussed in chapter 2, it is evident that their genetic form, resulting from theory, is non-rational. This was also observed in [Bagchi 2003] who studied the problem of modeling atmospheric turbulences in adaptive optics with von Kármán and Kolmogorov velocity spectrum, respectively. He proposed to first approximate the target PSD function in rational form by applying a Padé approximation [Padé 1892] before performing the spectral factorization. Though, similar to the discussed ARMA-based approaches, the model order of the optimal Padé approximate is not known beforehand, and different parameterizations must be tested to find the optimal order of the nominator/denominator polynomial. Furthermore, long memory processes which are characterized by a PSD function with power law decay cannot be represented by a rational transfer function. Indeed, the transfer function of ARMA processes, $H(\omega) = b(z)/a(z)$, is rational and it was proofed in Eq. (3.17), that this leads to an exponentially decaying AC function.

The next chapter introduces the concept of state space modeling later needed for the implementation of the Kalman filter algorithm and its modification for arbitrarily correlated loads. To this aim, equivalent state space formulations of the rational transfer function obtained by the discussed digital filter schemes, are derived.

4 State Space (Markovian) Modeling of Ambient Loads

Instead of using the explicit form of the ARMA model given in Eq. (3.7) or the convolution representation obtained by spectral factorization, a so-called state space or Markovian representation of the input-output relation is often more convenient as standard tools based on linear system theory for response analysis, optimization, and design of active control devices can be applied. Furthermore, the Kalman filter, discussed in chapter 6, which is widely used for state estimation and system identification in all engineering disciplines is based on state space modeling. In the following section the state space model is defined and its properties reviewed. Then, the relation between state space model and AR, MA (4.2), ARMA (4.3) and transfer function (4.4), respectively, is derived. Finally, the concept of state space augmentation is explained and illustrated by means of a short example. It will be later needed as reference solution for the verification of the proposed identification method.

4.1 Definition

A state space model for a (multivariate) process $\{\mathbf{X}_k\}$ is generated by two equations, the system and the observational equation. The latter describes the linear relation between the m-dimensional vector of observations $\mathbf{Z}_k$ at time $t = k\tau$ and the unobserved n-dimensional state vector $\mathbf{X}_k$

$$\mathbf{Z}_k = \mathbf{C}\mathbf{X}_k + \mathbf{V}_k \tag{4.1a}$$

where $\mathbf{C} \in \mathbb{R}^{m\times n}$ is a matrix of scalars and $\{\mathbf{V}_k\} \sim \mathrm{WN}(\mathbf{0}, \mathbf{Q}_k) \in \mathbb{R}^{m\times m}$ is an added m-dimensional Gaussian white noise vector process to consider random measurement errors e.g. due to sensor inaccuracy. The system equation

$$\mathbf{X}_{k+1} = \mathbf{A}_k\mathbf{X}_k + \mathbf{W}_k \tag{4.1b}$$

describes the temporal changes in the state of the linear dynamic system. The transfer matrix $\mathbf{A}_k \in \mathbb{R}^{n\times n}$ relates the state at the previous time step t to the state at time $t+1$. In case that the physical problem can be modeled as time-invariant process, the subscript k of system matrices can be dropped. The model uncertainties or disturbances are represented by the added m-dimensional Gaussian zero-mean white noise vector process $\{\mathbf{W}_t\} \sim \mathrm{WN}(\mathbf{0}, \mathbf{R}_t) \in \mathbb{R}^{n\times n}$. Furthermore, the noise processes $\{\mathbf{W}_k\}$ and $\{\mathbf{V}_k\}$ are assumed to be uncorrelated, i.e. $E[\mathbf{W}_s\mathbf{V}_k^T] = 0,\ \forall\ s,t$.
Eq. (4.1b), (4.4) can be rewritten in terms of previous states by substituting the equation recursively into itself, leading to

$$\begin{aligned}
\mathbf{X}_{k+1} &= \mathbf{A}_k\mathbf{X}_k + \mathbf{W}_k \\
\mathbf{X}_{k+1} &= \mathbf{A}_k(\mathbf{A}_{k-1}\mathbf{X}_{k-1} + \mathbf{W}_{k-1}) + \mathbf{W}_k \\
&\vdots \\
\mathbf{X}_{k+1} &= (\mathbf{A}_k\mathbf{A}_{k-1}\dots\mathbf{A}_1)\mathbf{X}_k + (\mathbf{A}_k\mathbf{A}_{k-1}\dots\mathbf{A}_2)\mathbf{W}_1 + \dots + \mathbf{A}_k\mathbf{W}_{k-1} + \mathbf{W}_k
\end{aligned}$$

which might be rewritten as

$$\mathbf{X}_{k+1} = f_{k+1}(\mathbf{X}_1, \mathbf{W}_1, \dots, \mathbf{W}_k) \tag{4.2a}$$

$$\mathbf{Z}_k = g_{k+1}(\mathbf{X}_1, \mathbf{W}_1, \dots, \mathbf{W}_k, \mathbf{V}_k) \tag{4.2b}$$

If the sequence $\mathbf{X}_1, \mathbf{W}_1, \dots, \mathbf{W}_k$ is independent, then the process is Markovian. This means that the probability distribution function given the sequence $\mathbf{X}_1, \mathbf{X}_2, \dots, \mathbf{X}_k$ is the same as the distribution of $\mathbf{X}_{k+1}$ given just the previous value $\mathbf{X}_k$. The simplicity of the state space representation is the result of the Markovian property, as it allows modeling the process as well as its observation in a recursive manner. For many physical systems a Markovian representation can be found by including sufficiently many past components in the specification of the state $\mathbf{X}_k$ [Brockwell and Davis 2002, p. 260f.] as will be shown in the following.
Furthermore, it must be noted, that state space representations are not unique, that is a certain set of state variables uniquely describes the system behavior, but there exists an infinite number of such sets. Some standard realizations are physical, standard controllable, standard observable, and canonical forms, where the first two are often used due to their simplicity: While the physical form is directly derived from the physical laws describing the relation between the state variables, the standard controllable realization is directly generated from the transfer function or the differential/difference equation of the process and will be used in the following. The canonical form leads to a decoupling of the modes of the dynamical system and thus simplifies both, system analysis and numerical solutions to the

state differential equation [Maybeck 1979, p. 27ff.].
The different state models are equivalent representations of the process and can be related through similarity transformations, i.e. the original n-dimensional state vector $\mathbf{X}_k$ is defined in terms of a new coordinate basis $\mathbf{X}_k^*$. The latter is obtained by multiplication of the original basis with an invertible matrix $\mathbf{S}_k$, i.e.

$$\mathbf{X}_k = \mathbf{S}_T \mathbf{X}_k^* \qquad \Leftrightarrow \qquad \mathbf{X}_k^* = \mathbf{S}_T^{-1} \mathbf{X}_k \tag{4.3a}$$

Substituting the first relation in Eq. (4.1a) yields

$$\mathbf{S}_T \mathbf{X}_{k+1}^* = \mathbf{A}_k \mathbf{S}_T \mathbf{X}_k^* + \mathbf{W}_k \tag{4.3b}$$

and pre-multiplying the result with $\mathbf{S}_T^{-1}$, leads to the equivalent representation

$$\begin{aligned} \mathbf{X}_{k+1}^* &= \mathbf{A}_k^* \mathbf{X}_k^* + \mathbf{B}^* \mathbf{W}_k \\ \mathbf{Z}_k^* &= \mathbf{H}_k^* \mathbf{X}_k^* + \mathbf{V}_k \end{aligned} \tag{4.3c}$$

where $\mathbf{A}_k^* = \mathbf{S}_T^{-1} \mathbf{A}_k \mathbf{S}_T$, $\mathbf{B}^* = \mathbf{S}_T^{-1}$ and $\mathbf{H}_k^* = \mathbf{H}_k \mathbf{S}_T$. Hence, the eigenvalues, determinant, trace, and characteristic polynomial remain unchanged under a similarity transformation. Consequently, such a transformation does not alter the dynamics of the system representation. A further discussion and examples of the different state space models can be found in [Maybeck 1979, p. 27ff.].

4.2 State space model of AR and MA series

In case of a causal univariate pth order AR(p) model,

$$a(L) F_k = w_k, \qquad F_k = a_1 F_{k-1} + a_2 F_{k-2} + \ldots a_p F_{k-p} + w_k \tag{4.4}$$

it is straight forward to formulate an equivalent state space representation. First note that the process at time $k+1$ can be expressed in the form

$$F_{k+1} = a_1 F_k + a_2 F_{k-1} + \ldots + F_{k-p+1} + w_{k+1} \tag{4.5}$$

Defining the state vector $\mathbf{X}_k$ which collects the p known components $F_k, F_{k-1}, \ldots, F_{k-p+1}$ of the right hand side of Eq. 4.5

$$\mathbf{X}_k = \begin{bmatrix} F_{k-p+1} \\ \vdots \\ F_{k-1} \\ F_k \end{bmatrix} \tag{4.6}$$

then the pth order difference equation in Eq. (4.5) reduces to a first order vector difference equation of form

$$\mathbf{X}_{k+1} = \begin{bmatrix} 0 & 1 & 0 & \ldots & 0 \\ 0 & 0 & 1 & \ldots & 0 \\ \vdots & \vdots & \vdots & \ddots & \vdots \\ 0 & 0 & 0 & \ldots & 1 \\ a_p & a_{p-1} & a_{p-2} & \ldots & a_1 \end{bmatrix} \mathbf{X}_k + \begin{bmatrix} 0 \\ 0 \\ \vdots \\ 0 \\ 1 \end{bmatrix} W_{k+1} \tag{4.7}$$

were the last row of the state vector $\mathbf{X}_k$ corresponds to the time series defined in Eq. (4.4) and the upper part of the coefficient matrix $\mathbf{A}_k$ updates the state vector $\mathbf{X}_k$ by dropping the latest value F_{k-p+1} and shifting the remaining entries $F_{k-p+2}, \ldots, F_{k-1}, F_k$ of the vector to the top row. While Eq. (4.7) corresponds to the system equation of the state space model defined in Eq. (4.1b), the observation equation provides the actual sample of the process by extracting F_k from the state vector $\mathbf{X}_k$ with the help of the observational equation

$$F_k = \begin{bmatrix} 0 & 0 & \ldots & 1 \end{bmatrix} \mathbf{X}_k \tag{4.8}$$

where the white noise disturbance is set $\mathbf{V}_k = 0$.
In case of a causal univariate qth order MA(q) model, given by

$$F_k = b(L) w_k, \qquad F_k = b_0 w_k + b_1 w_{k-1} + b_2 w_{k-2} + \ldots + b_q w_{k-q} \tag{4.9}$$

a similar approach can be used to express it in state space form. Defining the state vector $\mathbf{X}_k$ which collects the q past components of the white noise sequence $w_k, w_{k-1}, \ldots, w_{k-q}$, i.e.

$$\mathbf{X}_k = \begin{bmatrix} w_{k-q} \\ \vdots \\ w_{k-1} \\ w_k \end{bmatrix} \tag{4.10}$$

then the equivalent state space representation is given by the system equation

$$\mathbf{X}_{k+1} = \begin{bmatrix} 0 & 1 & 0 & \dots & 0 \\ 0 & 0 & 1 & \dots & 0 \\ \vdots & \vdots & \vdots & \ddots & \vdots \\ 0 & 0 & 0 & \dots & 1 \end{bmatrix} \mathbf{X}_k + \begin{bmatrix} 0 \\ \vdots \\ 0 \\ 1 \end{bmatrix} W_{k+1} \tag{4.11}$$

which updates the state vector $\mathbf{X}_k$ by dropping the latest value w_{k-q} and shifting the remaining entries $w_{k-q+1},\dots,w_{k-1},w_k$ of the vector to the top row, the observation equation provides the actual sample of the process F_k by weighting the state vector $\mathbf{X}_k$ by the moving average coefficients, i.e.

$$F_k = \begin{bmatrix} b_{k-q} & b_{k-q+1} & \dots & b_1 & b_0 \end{bmatrix} \mathbf{X}_k \tag{4.12}$$

where the white noise disturbance is set $\mathbf{V}_k = 0$.

4.3 State space model of an ARMA series

In case of the ARMA(p,q) model an equivalent state state representation of the difference equation

$$a(B)F_k = b(B)W_k, \qquad F_k = a_1F_{k-1} + a_2F_{k-2} + \dots + a_pF_{k-p} + b_0W_k - b_1W_{k-1} - \dots - b_qW_{k-q} \tag{4.13a}$$

can be formulated using the result from the previous section. Defining the AR(p) autoregressive process

$$a(B)U_k = W_k \tag{4.13b}$$

then the process can be simulated by the series

$$F_k = b(B)U_k \tag{4.13c}$$

as the following relation must hold

$$a(B)F_k = a(B)\cdot b(B)U_k = b(B)\cdot a(B)U_k = b(B)W_k \tag{4.13d}$$

Let $r = max(p,q+1)$, then the system equation of the ARMA(p,q) series follows directly from Eq. (4.13b) in connection with the result (4.7), yielding

$$\mathbf{X}_{k+1} = \begin{bmatrix} 0 & 1 & 0 & \dots & 0 \\ 0 & 0 & 1 & \dots & 0 \\ \vdots & \vdots & \vdots & \ddots & \vdots \\ 0 & 0 & 0 & \dots & 1 \\ a_r & a_{r-1} & a_{r-2} & \dots & a_1 \end{bmatrix} \mathbf{X}_k + \begin{bmatrix} 0 \\ 0 \\ \vdots \\ 0 \\ 1 \end{bmatrix} W_{k+1} \qquad \text{where} \qquad \mathbf{X}_k = \begin{bmatrix} U_{k-r+1} \\ U_{k-r+2} \\ \vdots \\ U_{k-1} \\ U_k \end{bmatrix} \tag{4.14}$$

where $a_j = 0$, if $j > p$. Te process generating observation equation is resulting from Eq. (4.13c) [Brockwell and Davis 2002, p. 268f.]

$$F_k = \begin{bmatrix} -b_{r-1} & -b_{r-2} & \dots & b_0 \end{bmatrix} \mathbf{X}_k. \tag{4.15}$$

where $b_0 = 1$ and $b_j = 0$, if $j > q$. The special form of the state space equations which were used here, is known as the controllable canonical form in control theory. Controllability means that all state variables in the model are affected by the input, i.e. it is possible to drive the dynamic system from any initial state to any other state in a finite interval of time by a control input [Maybeck 1979, p. 43].

4.4 Relation between state space model and transfer function

The following continuous linear state space model

$$\begin{aligned} \dot{\mathbf{X}}(t) &= \mathbf{A}_c\mathbf{X}(t) + \mathbf{G}_c W(t) \\ Z(t) &= \mathbf{C}_c\mathbf{X}(t) + D_c W(t) \end{aligned} \tag{4.16}$$

of a SISO system driven by a white noise process $\{W(t)\} \sim \text{WN}(0,Q_c)$ can be written in the Laplace domain as

$$\begin{aligned} s\mathbf{X}(s) - \mathbf{X}(0) &= \mathbf{A}_c\mathbf{X}(s) + \mathbf{G}_c W(s) \\ Z(s) &= \mathbf{C}_c\mathbf{X}(s) + D_c W(s) \end{aligned} \tag{4.17}$$

using the first time derivative property of the Laplace transform which states

$$\frac{\partial Y(t)}{\partial t} \quad \circ\!\!-\!\!\bullet \quad sY(s) - Y(0) \tag{4.18}$$

The coefficient matrices $\mathbf{A}_c \in \mathbb{R}^{n\times n}$, $\mathbf{G}_c \in \mathbb{R}^{n\times 1}$, $\mathbf{C}_c \in \mathbb{R}^{1\times n}$, $D_c \in \mathbb{R}$ are assumed to be time-invariant and the subscripts 'c' indicates that the evaluation of the model states is time-continuous. The output of the system $Z(t)$ is a realization of a Gaussian random process $\{F(t)\}$ characterized by its target PSD $S_F(\omega)$. Setting the initial conditions $\mathbf{X}(0) = \mathbf{0}$, where $\mathbf{X}(t) \in \mathbb{R}^m$, the transfer function of the input-output relation $Z(s) = H(s)W(s)$ is given by

$$H(s) = \mathbf{C}_c(\mathbf{I}s - \mathbf{A}_c)^{-1}\mathbf{G}_c + D_c \tag{4.19}$$

First the special case $D_c = 0$ is discussed: Using Cramer's rule the inverse $(\mathbf{I}s - \mathbf{A}_c)^{-1}$ can be express in the form [Dullerud and Paganini 2000, p. 90]

$$(\mathbf{I}s - \mathbf{A}_c)^{-1} = \frac{1}{\det(\mathbf{I}s - \mathbf{A}_c)}\operatorname{adj}(\mathbf{I}s - \mathbf{A}_c) \tag{4.20}$$

where $\operatorname{adj}(\cdot)$ denotes the classical adjoint of a matrix also referred to as adjugate matrix. The determinant of the matrix $(\mathbf{I}s - \mathbf{A}_c)$ is the characteristic polynomial of the transition matrix $\mathbf{A}_c$ and thus a polynomial of order n. The entries of the adjugate matrix are formed by taking the transpose of the cofactor matrix of $\mathbf{I}s - \mathbf{A}_c$ and hence leading to a matrix with polynomial entries of order less than n. Consequently, the term $\mathbf{C}_c(\mathbf{I}s - \mathbf{A}_c)^{-1}\mathbf{G}_c$ is a real, strictly proper function, i.e. the order of the denominator is higher than the one of the numerator. Thus, if $D_c = 0$, the transfer function defined in Eq. (4.19) can be expressed in the form [Dullerud and Paganini 2000, p. 90]

$$H_s(s) = \frac{c_{n-1}s^{n-1} + c_{n-2}s^{n-2} + \dots c_1 s + c_0}{s^n + a_{n-1}s^{n-1} + \dots a_1 s + a_0} \tag{4.21}$$

where the subscript s indicates the strictly proper case. In the more general case $D_c \neq 0$, the order of the numerator and denominator is equal, and thus the transfer function is said to be real and proper. Hence, the transfer function in Eq. (4.19) can be expressed as

$$H(s) = \frac{c_n s^n + c_{n-1}s^{n-1} + \dots c_1 s + c_0}{s^n + a_{n-1}s^{n-1} + \dots a_1 s + a_0} = H_s(s) + D_c \tag{4.22}$$

where $H_s(s)$ is strictly proper and D_c a real constant. Conversely, one can state, that if the transfer function obtained by spectral factorization in Eq. (3.25) is strictly proper and real rational, then there exists an equivalent state space realization of the process $(\mathbf{A}, \mathbf{B}, \mathbf{C}, D_c =$

0), e.g. using the controllable canonical form results in

$$\mathbf{A}_c = \begin{bmatrix} 0 & 1 & 0 & \dots & 0 \\ 0 & 0 & 1 & \dots & 0 \\ \vdots & \vdots & \ddots & \vdots & \vdots \\ 0 & 0 & 0 & \dots & 1 \\ -a_0 & -a_1 & -a_2 & \dots & -a_{n-1} \end{bmatrix}, \quad \mathbf{G}_c = \begin{bmatrix} 0 \\ 0 \\ \vdots \\ 0 \\ 1 \end{bmatrix}, \quad \mathbf{C}_c^T = \begin{bmatrix} c_0 \\ c_1 \\ \vdots \\ c_{n-2} \\ c_{n-1} \end{bmatrix}^T \tag{4.23}$$

Hence, the order of the state space model is directly linked to the number of poles in the transfer function. In case that the rational function is proper, the constant $D_c \neq 0$ must be derived from Eq. (4.22) [Dullerud and Paganini 2000, p. 92ff.] and included in the observation equation.

It must be stressed that the obtained state space representation is time-continuous. However, in many situations a discrete state space model is more appropriate in order to introduce sampled measurement data or control forces [Simon 2006, p. 107]. Thus, in the following the discretization of the obtained model is discussed.

The system model defined in Eq. (4.16) corresponds to a linear stochastic differential equation with constant coefficients in the form

$$\mathbf{dX}(t) = \mathbf{A}_c\mathbf{X}(t)dt + \mathbf{G}_c d\beta(t) \tag{4.24}$$

where $d\beta(t)$ is a sample of a Brownian motion process of diffusion $Q(t)$ for all $t = [0,T)$ whose derivative represents the Gaussian white noise as $d\beta(t) = W(t)dt$ (s. A.1.4.4). Its solution yields the process $\mathbf{X}(t)$ in a recursive form from the initial conditions $\mathbf{X}(0)$ at t_0

$$\mathbf{X}(t) = \mathbf{\Phi}(t,t_0)\mathbf{X}(0) + \int_{t_0}^{t} \mathbf{\Phi}(t,\tau)\mathbf{G}_c(\tau)d\beta(\tau) \tag{4.25a}$$

where $\mathbf{\Phi}(\cdot,\cdot) \in \mathbb{R}^{n\times n}$ is the state transition matrix satisfying the differential equation and initial condition [Maybeck 1979, p. 163ff.]

$$\frac{d}{dt}\mathbf{\Phi}(t,t_0) = \mathbf{A}_c\mathbf{\Phi}(t,t_0), \qquad \mathbf{\Phi}(t_0,t_0) = \mathbf{I} \tag{4.25b}$$

It must be noted that the integral in Eq. (4.25a) is a stochastic integral $I(t,\cdot)$. Since the integration is performed with respect to time and not with respect to the sample path of the Brownian motion, the integral can be considered as realization of a random variable defined in the mean square sense with zero mean and variance

$$E[I(t,\cdot)I(t,\cdot)] = \int_{t_0}^{t} \mathbf{\Phi}(t,\tau)\mathbf{G}_c(\tau)Q(\tau)\mathbf{G}_c^T(\tau)\mathbf{\Phi}^T(t,\tau)d\tau \tag{4.25c}$$

Hence the integral can be modeled as Gaussian white noise sequence with variance defined by Eq. (4.25c).
The state transition matrix is characterized by the following properties [Maybeck 1979, p. 40-42]:

1. $\mathbf{\Phi}(t,t_1)$ is uniquely defined for all t and t_1 in $[0,\infty)$.
2. For $t_1 < t_2 < t_3$ it holds $\mathbf{\Phi}(t_1,t_3) = \mathbf{\Phi}(t_1,t_2)\mathbf{\Phi}(t_2,t_3)$. This property is also called the 'semigroup' property, saying that the transition from $\mathbf{X}(t_1)$ to $\mathbf{X}(t_3)$ is the same as the transition from $\mathbf{X}(t_1)$ to $\mathbf{X}(t_2)$ followed by the transition $\mathbf{X}(t_2)$ to $\mathbf{X}(t_3)$
3. $\mathbf{\Phi}(t,t_0)$ is invertible, that is $\mathbf{\Phi}(t,t_1)\mathbf{\Phi}(t_1,t) = \mathbf{\Phi}(t,t) = \mathbf{I}$ so that $\mathbf{\Phi}(t,t_1)^{-1} = \mathbf{\Phi}(t_1,t)$.

In case of a time-invariant linear rational system, as considered here, the relation for the state transition matrix given in Eq. (4.25b) reduces to

$$\frac{d}{dt}\mathbf{\Phi}(t_s) = \mathbf{A}_c\mathbf{\Phi}(t_s), \qquad \mathbf{\Phi}(0) = \mathbf{I} \tag{4.26a}$$

which is depending on the time lag $t_s = t - t_0$ instead of the specific instances of time. Its solution is obtained either by using the matrix exponential function or alternatively by taking first the Laplace transform of Eq. (4.26) resulting in $\mathbf{\Phi}(s) = (Is - A_c)^{-1}$ for $t_0 = 0$ to which the inverse Laplace transformation is applied leading to [Kasdin 1995]

$$\mathbf{\Phi}(t - t_0) = \mathcal{L}^{-1}\left\{(Is - A_c)^{-1},t\right\} = e^{\mathbf{A}_c(t-t_0)} \tag{4.26b}$$

where $e^{\mathbf{A}_c(t-t_0)}$ is the matrix exponential function. The results (4.25c), (4.26b) are now used to obtain a simple, recursive formula for the generation of the process $\{\mathbf{X}(t)\}$ and thus the target process $\{Z(t)\}$ from the measurement equation. Solving the stochastic differential equation over a finite interval $t_s = t_{k+1} - t_k$ yields the sought discretized state space model of the process in the form

$$\mathbf{X}_{k+1} = \mathbf{A}_d\mathbf{X}_k + W_k \tag{4.26c}$$

$$Z_k = \mathbf{C}\mathbf{X}_k + DV_K \tag{4.26d}$$

where $\{V_k\}$ denotes the measurement noise sequence $\{V_k\} \sim \mathrm{WN}(0,Q_c/t_s)$ and where according to Eq. (4.26b) $\mathbf{A}_d = \mathbf{\Phi}(t_s) = e^{\mathbf{A}_c t_s}$. W_k is a zero mean white noise sequence with variance

$$Q_d = \int_0^{t_s} \mathbf{\Phi}(t_s)\mathbf{G}_c Q \mathbf{\Phi}^T(t_s)\mathbf{G}_c^T dt \tag{4.26e}$$

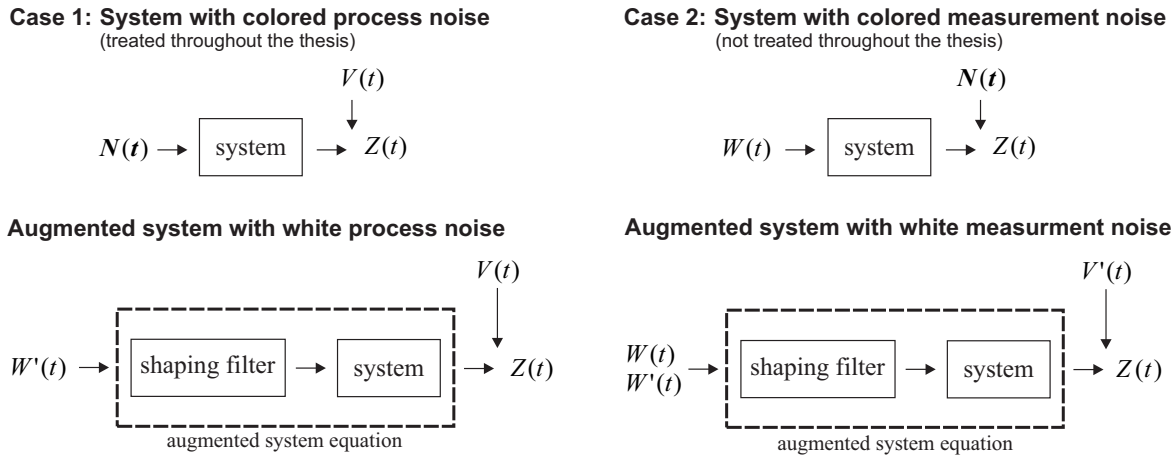

Figure 4.1: The linear system with colored input (left) and colored measurement noise $N(t)$ (right) is transformed into a linear system driven by white input $W(t)$,$W'(t)$ and measurement noise $V(t)$,$V'(t)$ by state space augmentation where the primes denote additional white processes

The integral equation for Q_d can be solved using an algorithm due to Van Loen [Kasdin 1995]. He showed that Q_d can be expressed by the matrix equation

$$Q_d = \mathbf{E}_{22}^T \mathbf{E}_{12} \tag{4.26f}$$

where the matrices $\mathbf{E}_{22}$, $\mathbf{E}_{12}$ are calculated from the matrix exponential

$$e^{\mathbf{F}t_s} \equiv \left[\begin{array}{c|c} \mathbf{E}_{11(n\times n)} & \mathbf{E}_{12(n\times n)} \\ \hline \mathbf{0}_{(n\times n)} & \mathbf{E}_{22(n\times n)} \end{array}\right] \quad \text{with} \quad \mathbf{F} = \begin{bmatrix} -\mathbf{A}_c & \mathbf{G}_c Q \mathbf{G}_c^T \\ \mathbf{0} & \mathbf{A}_c^T \end{bmatrix} \tag{4.26g}$$

4.5 State space augmentation

Up to now, it was assumed, that both process and measurement noise can be modeled as uncorrelated white noise sequences. However, in many cases the white noise assumptions is inadequate. In the following a method will be discussed which allows introducing colored process or measurement noise into the state space model defined in Eq. (4.1a-4.1b) in case the white noise assumption is inadequate and autocorrelations in the ambient loads or measurements must be considered. The method is based on the results obtained in the previous sections where it was shown that autocorrelated processes with known target PSD can be expressed as linear system driven by white noise either using ARMA-type models obtained by regression as discussed in section 3.2.1 or with the help of the spectral factorization theorem described in 3.2.2. In a procedure called state space augmentation, the colored process or measurement noise in the structural system is modeled indirectly in form of an added

linear system with white noise input leading to an overall system excited by white noise once again and to which standard tools based on linear system theory for response analysis, optimization, and design of active control devices can be applied [Chen and Kareem 2001]. The steps of the procedure are summarized in the following and illustrated in Fig. 4.1.
Starting point is a state space representation of the time-invariant linear system given by

$$\begin{aligned} \mathbf{X}_{k+1} &= \mathbf{A}\mathbf{X}_k + \mathbf{G}N_k \\ Z_k &= \mathbf{C}\mathbf{X}_k + V_k \end{aligned} \tag{4.27}$$

assuming for simplicity a SISO system where $\{V_k\} \sim \mathrm{WN}(0,R_d)$ and where $\{N_t\}$ is a second order stationary Gaussian noise sequence with known target PSD. Furthermore it is assumed that the processes $\{\mathbf{X}_t\}$, $\{V_t\}$ and $\{N_t\}$ are uncorrelated with each other. In the next step the colored process is represented in state space form e.g. resulting from the spectral factorization of the target PSD of the process

$$\begin{aligned} \mathbf{X}'_{k+1} &= \mathbf{A}'\mathbf{X}'_k + \mathbf{G}'W'_k \\ N_k &= \mathbf{C}'\mathbf{X}'_k + D'W'_k \end{aligned} \tag{4.28a}$$

where the primes denote additional variables and $\{W'_t\} \sim \mathrm{NW}(0,Q_d)$ the driving Gaussian white noise process with variance Q_d. Augmenting the state vector of the system $\mathbf{X}_k$ by the states of the noise process $\mathbf{X}'_k$ yields

$$\begin{aligned} \begin{bmatrix} \mathbf{X}_{k+1} \\ \mathbf{X}'_{k+1} \end{bmatrix} &= \begin{bmatrix} \mathbf{A} & \mathbf{G}\mathbf{C}' \\ \mathbf{0} & \mathbf{A}' \end{bmatrix} \begin{bmatrix} \mathbf{X}_k \\ \mathbf{X}'_k \end{bmatrix} + \begin{bmatrix} \mathbf{G}D' \\ \mathbf{G}' \end{bmatrix} W'_k \\ Z_k &= \begin{bmatrix} \mathbf{C} & \mathbf{0} \end{bmatrix} \begin{bmatrix} \mathbf{X}_k \\ \mathbf{X}'_k \end{bmatrix} + V_k \end{aligned} \tag{4.29a}$$

which can be written compactly in terms of the augmented state vector $\mathbf{X}_{a,k} = [\mathbf{X}_k, \mathbf{X}'_k]^T$

$$\begin{aligned} \mathbf{X}_{a,k+1} &= \mathbf{A}_a\mathbf{X}_{a,k} + \mathbf{G}_a W_k \\ Z_k &= \mathbf{C}_a\mathbf{X}_{a,k} + V_k \end{aligned} \tag{4.29b}$$

where the subscript a indicates the augmented matrices [Lewis et al 2008, p. 123-125]. Eq. (4.29b) is the sought result of an overall linear system driven by white noise which is the basis for many standard algorithms such as the Kalman filter widely used in active control, response analysis and prediction.
Similarly, the case of a system with white process noise $\{W_t\} \sim \mathrm{NW}(0,Q_d)$ and colored

measurement noise $\{N_t\}$ [Lewis et al 2008, p. 130-131]

$$\begin{aligned} \mathbf{X}_{k+1} &= \mathbf{A}\mathbf{X}_{k+1} + \mathbf{G}W_k \\ Z_k &= \mathbf{C}\mathbf{X}_k + N_k \end{aligned} \tag{4.30a}$$

can be rewritten in the form

$$\begin{aligned} \begin{bmatrix} \mathbf{X}_{k+1} \\ \mathbf{X}'_{k+1} \end{bmatrix} &= \begin{bmatrix} \mathbf{A} & \mathbf{0} \\ \mathbf{0} & \mathbf{A}' \end{bmatrix} \begin{bmatrix} \mathbf{X}_k \\ \mathbf{X}'_k \end{bmatrix} + \begin{bmatrix} \mathbf{G} & \mathbf{0} \\ \mathbf{0} & \mathbf{G}' \end{bmatrix} \begin{bmatrix} W_k \\ W'_k \end{bmatrix} \\ Z_k &= \begin{bmatrix} \mathbf{C} & \mathbf{C}' \end{bmatrix} \begin{bmatrix} \mathbf{X}_k \\ \mathbf{X}'_k \end{bmatrix} + DW'_k \end{aligned} \tag{4.30b}$$

by substitution of the colored process $\{N_t\}$ by its equivalent state space representation defined in Eq. (4.28a). Using the augmented state vector $\mathbf{X}_{a,k} = [\mathbf{X}_k, \mathbf{X}'_k]^T$ and system matrices, once again a linear system with white process and measurement noise is obtained

$$\begin{aligned} \mathbf{X}_{a,k+1} &= \mathbf{A}_a\mathbf{X}_{a,k} + \mathbf{G}_a\mathbf{W}_{a,k} \\ Z_k &= \mathbf{C}_a\mathbf{X}_{a,k} + V_k \end{aligned} \tag{4.30c}$$

Here, it must be noted, that for $D' \neq 0$, the white noise vector process $\mathbf{W}_k = [W_k, W'_k]^T$ and the white measurement noise $V_k = DW'_k$ are correlated with

$$E\left[W'_k \begin{bmatrix} W_k \\ W'_k \end{bmatrix}^T \right] = \begin{bmatrix} 0 & D'Q_d \end{bmatrix} \tag{4.31}$$

as they are both depending on the same sample of the white noise sequence $\{W'_t\} \sim \mathrm{WN}(0, Q_d)$. Hence, the noises are just uncorrelated in case $D' = 0$ which implies that if the state space model of the colored process is obtained by spectral factorization, that the underlying transfer function $H(s)$ is strictly proper as defined in Eq. (4.21). In case that an ARMA-based state space model defined in Eq. (4.14-4.15) is used, $D = 0$ in all cases.

4.5.1 Numerical example

In order to clarify the idea of the state space augmentation here a short example taken from [Lewis et al 2008] is discussed which is needed in section 7.1.3.1 as reference solution. In this example the (long period) longitudinal dynamics of an aircraft are approximated by the continuous state space model of a harmonic oscillator with natural eigenfrequency $\omega = \sqrt{k/m}$

and ratio of critically damping $D = c/(2m\omega)$ given by

$$\dot{\mathbf{x}}(t) = \begin{bmatrix} 0 & 1 \\ -\omega^2 & -2D\omega \end{bmatrix} \mathbf{x}(t) + \begin{bmatrix} 0 \\ 1/m \end{bmatrix} n(t) \tag{4.32}$$

where $\mathbf{x}(t) = [\phi(t), \dot{\phi}(t)]^T$ and $\phi(t)$ denotes the pitch angle, i.e. the angle between the longitudinal axis of the aircraft and the horizon. The colored process noise $n(t)$ represents wind gusts with exponential AC function $R(\tau) = \sigma^2 e^{-a|t|}$ and corresponding low-frequency spectrum

$$S_F(\omega) = \frac{a\sigma^2}{\pi(a^2 + \omega^2)} \tag{4.33a}$$

Performing the spectral factorization in the Laplace domain, yields (s. Eq. (3.24))

$$S_F(s) = S_{F,L}(s) S_{F_L}(-s) = \frac{\sqrt{2a}\sigma}{(s+a)} \cdot \frac{\sqrt{2a}\sigma}{(-s+a)} \tag{4.33b}$$

where $S_{F,L}(s)$, $S_{F,L}(-s)$ denote the stable/instable factor with negative/positive real valued pole $s = \mp a$ in the left/right half of the s-plane as illustrated in Fig. 3.1a. The shaping filter $H(s)$ of the colored noise $n(t)$ is then obtained from Eq. (4.16) in the form

$$H(s) = \frac{1}{a+s} \tag{4.33c}$$

where the white noise input is set to $S_W(s) = 2a\sigma_W^2$. Using the controllable canonical state space representation in Eq.(4.23), the obtained shaping filter $H(s)$ corresponds in the time domain to the first order Markov model

$$\dot{x}'(t) = -ax'(t) + w'(t); \qquad n(t) = x'(t) \tag{4.34}$$

which is excited by a Gaussian white noise $w'(t)$ with standard deviation $\sqrt{2a}\sigma_W$. It is used in order to augment the state space model in Eq. (4.32) leading to

$$\dot{\mathbf{x}}_a(t) = \begin{bmatrix} 0 & 1 & 0 \\ -\omega^2 & -2D\omega & 1/m \\ 0 & 0 & -a \end{bmatrix} \mathbf{x}_a(t) + \begin{bmatrix} 0 \\ 0 \\ 1 \end{bmatrix} w'(t) \tag{4.35}$$

where $\mathbf{x}_a(t) = [\phi(t), \dot{\phi}(t), x'(t)]^T$ denote the augmented state. After discretization of the augmented model, e.g. by Euler approximation or by using the matrix exponential function, a linear model excited by Gaussian white noise is obtained.

5 Fractional Representation of Stationary Gaussian Processes

From the literature review it can be summarized that at the state-of-the-art, the main limitations in the field of digital simulation of correlated Gaussian loads are: i) if the load is long-correlated[1], time series models require an infinite number of coefficients to properly simulate the inverse power-law decay; ii) the number of coefficients p and q of time series models, such as ARMA models, cannot be predicted a priori and, increasing them, requires the recalculation of the whole set of coefficients; iii) this limitation is more severe from the computational time point of view in multivariate and multidimensional cases; iv) efficient simulation methods, based on Karhunen-Loéve or wavelet methods, cannot be rewritten in state space form needed to combine them with the used identification algorithm; v) analytic approaches such as the spectral factorization method require a certain functional form of the PSD function, and thus are not applicable to arbitrarily correlated processes.
In [Cottone and Di Paola 2010c] a new method, called *fractional spectral moment (FSM) decomposition*, for the description of PSD and AC function is introduced. It was used in [Cottone et al 2010d] to derive a linear fractional differential equation, whose output is a stationary colored Gaussian process with target PSD. It will be shown, that this new digital filter allows solving the issues summarized above. It will be used in chapter 7 for the development of a new identification method by combining it with the widely used Kalman filter algorithm [Runtemund et al 2013].
The chapter starts with a brief overview of fractional calculus and its importance in engineering applications. In order to explain and clarify the idea of fractional calculus, the Grünwald-Letnikov form of fractional integral and derivative operators is derived which is commonly used for the discretization of such operators. Then the principles of the FSM decomposition proposed in [Cottone and Di Paola 2010c; Cottone et al 2010d] will be summarized and verified by three load processes which are of great relevance in wind and ocean engineering. Furthermore, the accuracy and efficiency of the method is discussed. The use of

[1] that is, the AC function of the process decays much slower than exponentially. See section 5.6 for further details about short and long memory processes.

an alternative discretization operator is proposed, which leads to a significant improvement of the accuracy and efficiency of the method. Finally, a modified form of the FSM decomposition is proposed and verified which makes the method applicable for the modeling of long memory processes with unbounded variance.

5.1 A short historical overview

The idea of generalizing G. W. Leibniz's notion of differentiation $d^n f(x)/dx^n$ to non-integer orders is as old as the differential calculus itself. Though, the problem was first addressed in 1695 by M. de L'Hopital who asked Leibniz about the possibility to extend his notation to fractals of order 1/2. Not knowing the answer, Leibniz responded prophetically "*This is an apparent paradox from which, one day, useful consequences will be drawn*" [Ross 1975, p. 1ff].
In the following 300 years many well known mathematicians among them N. H. Abel, M. Caputo, L. Euler, J. Fourier, A. K. Grünwald, J. Hadamard, G. H. Hardy, O. Heaviside, H. J. Holmgren, P. S. Laplace, G. W. Leibniz, A. V. Letnikov, J. Liouville, B. Riemann, M. Riesz, and H. Weyl, contributed to this field proposing varies definitions and notations of fractional integral operators, but which were in general valid just under certain assumptions [Sabatier et al 2007, p. 6-7]. Though, maybe due to the complexity of the theory, the fractional calculus remain almost unknown among engineers. A brief historical overview about the developments until the twenties century can be found e.g. in [Samko et al 1993, p.].
It was not before the last 30 years, that fractional calculus starts to attract interest in almost every field of science and engineering. Books such as the encyclopedia on fractional calculus by [Samko et al 1993] contribute decisively to this development by summarizing the classical and modern results of the theory in a unifying form as well providing a large number of historical and recent references of publications describing both, theory and applications in this field [Sabatier et al 2007].
Nowadays, in structural engineering, fractional order models are widely used for the description of mechanical material properties such as the frequency-dependence of damping properties in viscoelastic materials in the scope of response analysis [Di Paola et al 2012], seismic isolation [Koh and Kelly 1990; Makris and Constantinou 1991], control [Moreau et al 2002] and identification [Sivaprasad et al 2009], as well as strain-softening and time- dependent behavior of fracture of concrete [Barpi and Valente 2002] or long range dependencies such as relaxation and creeping of composite materials [Hedrih 2006].
In [Cottone and Di Paola 2010c] a new method, called *fractional spectral moment (FSM)*

decomposition, for the description of PSD and AC function is introduced which was used in [Cottone et al 2010d] to derive a linear fractional differential equation, whose output is a stationary colored Gaussian process with target PSD. These results will be used in chapter 7 for the development of a new identification method by rewriting the algorithm for the load generation in state space form and combining it with the widely used Kalman filter algorithm [Runtemund et al 2013].

5.2 Grünwald - Letnikov fractional integral

Various forms of fractional derivative and integral operators exists; here, the definition proposed by Grünwald and Letnikov is chosen for illustration purposes as it strongly resembles Leibniz's notation used in classical differential calculus.
Leibniz defined the first-order derivative of the function $f(x)$, by the finite backward difference [Podlubny 1999, p. 43]

$$f'(t) = \lim_{h\to 0} \frac{\Delta_h f(t)}{h} = \lim_{h\to 0} \frac{f(t) - f(t-h)}{h} \tag{5.1a}$$

For $h > 0$ the difference $\Delta_h f(t)$ is called left-sided (or backward) difference while for $h < 0$, it is denoted as right sided (or forward) difference [Kilbas et al 2006, p. 121ff]. Applying this definition twice, results in the second-order derivative

$$f''(t) = \lim_{h\to 0} \frac{\Delta_h^2 f(t)}{h^2} = \lim_{h\to 0} \frac{\Delta_h f(t) - \Delta_h f(t-h)}{h} = \lim_{h\to 0} \frac{f(t) - 2f(t-h) + f(t-2h)}{h^2} \tag{5.1b}$$

and by induction, the nth-order derivative can be expressed in the form

$$(D^n f)(t) = \lim_{h\to 0} \frac{\Delta_h^n f(t)}{h^n} = \lim_{h\to 0} \frac{(1-L)^n}{h^n} f(t); \tag{5.1c}$$

where L denotes the lag operator with the property $L^k f(t) = f(t-kh)$, $k > 0$ (compare section 3.2.1). Using the binomial expansion of the operator $(1-L)^n$

$$(1-L)^n = \sum_{k=0}^{n} \frac{\Gamma(k-n)}{\Gamma(k+1)\Gamma(-n)} L^k = \sum_{k=0}^{n} (-1)^k \binom{n}{k} L^k \qquad n \in \mathbb{N} \tag{5.1d}$$

Eq. (5.1c) can be rewritten in the form

$$(D^n f)(t) = \lim_{h\to 0} \sum_{k=0}^{n} (-1)^k \binom{n}{k} f(t-kh); \qquad n \in \mathbb{N} \tag{5.1e}$$

where the term in brackets denotes the binomial coefficient[2] and $\Gamma(\cdot)$ the Gamma function. The binomial expansion of $(1-L)^\gamma$ in Eq. (5.1d) can be easily extended for complex exponents $\gamma \in \mathbb{C}$, by changing the upper bound of the summation to infinity, leading to the right- and left-sided Grünwald-Letnikov fractional derivative operator of the continuous function $f(t)$, respectively, in the form [Kilbas et al 2006, p. 121ff]

$$(D_+^\gamma f)(t) = \lim_{h\to 0} \frac{\Delta_h^\gamma f(t)}{h^\gamma} = \lim_{h\to 0} \frac{1}{h^\gamma} \sum_{k=0}^{\infty} (-1)^k \binom{\gamma}{k} f(t-kh); \qquad \gamma \in \mathbb{C} \tag{5.2a}$$

$$(D_-^\gamma f)(t) = \lim_{h\to 0} \frac{\Delta_{-h}^\gamma f(t)}{h^\gamma} = \lim_{h\to 0} \frac{1}{h^\gamma} \sum_{k=0}^{\infty} (-1)^k \binom{\gamma}{k} f(t+kh); \qquad \gamma \in \mathbb{C} \tag{5.2b}$$

where $h > 0$. The corresponding right- and left-sided Grünwald-Letnikov (GL) fractional integral operator are obtained from Eqs. 5.2 by choosing $\gamma < 0$, that is, using the identities

$$(I_+^\gamma f)(t) = (D_+^{-\gamma} f)(t) \tag{5.3a}$$

$$(I_-^\gamma f)(t) = (D_-^{-\gamma} f)(t) \tag{5.3b}$$

It can be shown (see e.g. [Samko et al 1993, p. 387f]), that Eqs. (5.2) and (5.3) coincide as $h \to 0$ with the right- and left-sided Riemann Liouville fractional derivative and integral operators [Samko et al 1993, p. 34-35], respectively which are given by

$$(D_+^\gamma f)(t) = \frac{1}{\Gamma(1-\gamma)} \frac{d}{dt} \int_{-\infty}^{t} \frac{f(\tau)}{(t-\tau)^\gamma} d\tau; \qquad 0 < Re\gamma < 1 \tag{5.4a}$$

$$(D_-^\gamma f)(t) = -\frac{1}{\Gamma(1-\gamma)} \frac{d}{dt} \int_{t}^{\infty} \frac{f(\tau)}{(\tau-t)^\gamma} d\tau; \qquad 0 < Re\gamma < 1 \tag{5.4b}$$

and

$$(I_+^\gamma f)(t) = \frac{1}{\Gamma(\gamma)} \int_{-\infty}^{t} \frac{f(\tau)}{(t-\tau)^{1-\gamma}} d\tau \tag{5.4c}$$

$$(I_-^\gamma f)(t) = \frac{1}{\Gamma(\gamma)} \int_{t}^{\infty} \frac{f(\tau)}{(\tau-t)^{1-\gamma}} d\tau \tag{5.4d}$$

This result shows, that the GL fractional representation can be interpreted as fractional generalization of the ordinary discretization formulas for integer order derivative and integrals [Sousa 2012]. It will be needed in section 5.5 for the numerical calculation of fractionally integrated white noise. Some computational aspects of the GL series representation as well as its convergence and accuracy will be discussed in more detail in sections 5.5.1 and 5.5.3, respectively.

[2] $\binom{n}{k} = \frac{n!}{k!(n-k)!} = \frac{\Gamma(n+1)}{\Gamma(k+1)\Gamma(n-k+1)}$

5.3 Reconstruction of AC and PSD function by fractional spectral moment decomposition

In [Cottone and Di Paola 2010c] a new representation of the PSD and AC function in terms of so-called *fractional spectral moments* (FSMs) is introduced. The FSMs are a generalization of the classical integer order moments (2.8) proposed by Vanmarcke to the complex plane by choosing $\gamma \in \mathbb{C}$. In section 5.4 the concept is needed for the digital simulation of stationary Gaussian processes with given target PSD function and thus, the main steps are summarized in the following.

The FSMs are calculated from the one-sided PSD function $G_X(\omega)$ of the process $\{X(t)\}$ using

$$\Lambda_X(\gamma) = \int_{-\infty}^{\infty} |\omega|^{\gamma} S_X(\omega) \mathrm{d}\omega = \int_0^{\infty} \omega^{\gamma} G_X(\omega) \mathrm{d}\omega; \qquad \gamma \in \mathbb{C} \tag{5.5}$$

which coincide for $\gamma = 1,2,...$ with the classical spectral moments (SMs) $\lambda_X(\gamma)$ already define in 2.8. The FSMs are a function of the complex quantity γ and will be denoted as $\Lambda_X(\gamma)$ in the following. While the classical SMs cannot be used to reconstruct the PSD of the process, even if the complete set of SMs would be known, it was proofed in [Cottone and Di Paola 2010], that its fractional counterpart $\Lambda_X(\gamma)$ restores both, the PSD and its Fourier transform pair, the correlation function.

To this aim, the Riesz fractional integral of the AC function is introduced

$$\left(I^{\gamma} R_X\right)(\tau) = \frac{1}{2\nu(\gamma)} \int_{-\infty}^{\infty} \frac{R_X(t)}{|\tau - t|^{1-\gamma}} \mathrm{d}t; \qquad Re\gamma > 0, \gamma \neq 1,3,5,... \tag{5.6a}$$

where $\nu(\gamma) = \Gamma(\gamma)\cos(\gamma\pi/2)$. Using the relation between PSD and AC function defined in Eq. (2.7) and assuming that these functions are differentiable, it can be shown, that the inverse Fourier transform of the Riesz fractional integral operator in Eq. (5.6a) may be calculated by means of the property [Samko et al 1993, p. 137ff., 489ff.]

$$\mathcal{F}^{-1}\{\left(I^{\gamma} R\right)(\tau); \omega\} = |\omega|^{-\gamma} \mathcal{F}^{-1}\{R(\tau); \omega\} = |\omega|^{-\gamma} S_X(\omega) \tag{5.6b}$$

Finally, applying a Fourier transform to Eq. 5.6b, i.e.

$$\left(I^{\gamma} R_X\right)(\tau) = \int_{-\infty}^{\infty} |\omega|^{-\gamma} S_X(\omega) e^{i\omega\tau} \mathrm{d}\omega = \int_0^{\infty} |\omega|^{-\gamma} G_X(\omega) e^{i\omega\tau} \mathrm{d}\omega \tag{5.7}$$

which evaluated in $\tau = 0$, yields the meaningful result

$$\Lambda_X(-\gamma) = \left(I^{\gamma} R_X\right)(0) = \int_0^{\infty} \omega^{-\gamma} G_X(\omega) \mathrm{d}\omega; \qquad \gamma \in \mathbb{C},\ \ \gamma_0 < Re\gamma < \gamma_1 \tag{5.8}$$

which coincides with the fractional spectral moments, defined in Eq. (5.5). It must be stressed that $\gamma \in \mathbb{C}$ is chosen such, that the integral converges, that is, with the real part $\gamma_0 < Re\gamma < \gamma_1$. For symmetric functions, such as the autocorrelation function, the Riesz fractional integral in Eq. 5.10a can be simplified and rewritten in the form

$$\left(I^{\gamma} R\right)(0) = \frac{1}{\nu(\gamma)} \int_0^{\infty} t^{\gamma-1} R(t)\, dt = \frac{1}{\nu(\gamma)} \mathcal{M}\{R(t); \gamma\} \tag{5.9}$$

which can be directly interpreted as Mellin transform operator $\mathcal{M}$. Finally, applying an inverse Mellin transform[3] to Eq. (5.9) and substituting $\Lambda_X(-\gamma) = \left(I^{\gamma} R_X\right)(0)$, the sought representation of AC and corresponding PSD function (by means of Fourier transform) are obtained, yielding

$$R_X(t) = \frac{1}{2\pi i} \int_{\rho-i\infty}^{\rho+i\infty} \nu(\gamma) \Lambda_X(-\gamma) t^{-\gamma} \mathrm{d}\gamma \tag{5.10a}$$

$$S_X(\omega) = \frac{1}{4\pi i} \int_{\rho-i\infty}^{\rho+i\infty} \Lambda_X(-\gamma) \omega^{-\gamma} \mathrm{d}\gamma \tag{5.10b}$$

where $\nu(\gamma) = \Gamma(\gamma)\cos(\gamma\pi/2)$ and $\gamma_0 < \rho < \gamma_1$. It must be stressed, that both integrals are performed along the imaginary axis with fixed real part ρ which belongs to the fundamental strip of the Mellin transform. Similar to the characteristic function (CF) defined in Eq. (A.3) which can be reconstructed from the classical moments, i.e. the derivatives of the CF evaluated in zero, the AC and PSD functions $R_X(\tau)$ and $S_X(\omega)$ are obtained from the knowledge of the FSMs coinciding with Riesz factional integrals calculated in zero. Hence, Eqs. 5.10 can be interpreted as Taylor integral expansion and are therefore indicated as *generalized Taylor integral forms*. By discretization of the obtained integrals the resemblance to the Taylor series shall be emphasized. It requires a truncation of the integral along the imaginary axis with constant real part. Defining $\gamma_k = \rho + ik\Delta\eta$ the integral is calculated up to a certain value $\bar{\eta} = \mp m\Delta\eta$ by discretizing the interval into $2m+1$ small increments $\Delta\eta$. This leads to the following approximation

$$R(\tau) \approx \frac{\Delta\eta}{2\pi} \sum_{k=-m}^{m} \nu(\gamma_k) \Lambda_X(-\gamma_k) |t|^{-\gamma_k} \tag{5.11a}$$

[3] $f(t) = \mathcal{M}^{-1}\{f(\gamma); t\} = \frac{1}{2\pi i} \int_{\rho-i\infty}^{\rho+i\infty} \mathcal{M}\{f(t); \gamma\} t^{-\gamma} \mathrm{d}\gamma \quad$ where $\gamma = \rho + i\eta;\ \rho, \eta \in \mathbb{R}$

$$S(\omega) \approx \frac{\Delta\eta}{4\pi} \sum_{k=-m}^{m} \Lambda_X(-\gamma_k)|\omega|^{\gamma_k - 1} \tag{5.11b}$$

In annexe B.1.2.1 and B.1.2.3 the FSMs $\Lambda_X(\gamma)$ of the model wind velocity and wind wave PSD functions discussed in chapter 2 are summarized. It shall be highlighted that all of them could be calculated analytically by means of the computer algebra systems MATHEMATICA. In the derivation of the formulas it was considered, that the autocorrelation and consequently the PSD are symmetric and real functions. A more general extension to antisymmetric functions can be found in [Cottone et al 2010d]. It must be stressed, that this representation is valid for any Fourier pair, and was originally proposed for probability density and characteristic function in [Cottone and Di Paola 2010], and extended to multidimensional random variables [Cottone et al 2010b] and multivariate processes in [Cottone et al 2011; Cottone and Di Paola 2011].
In the following section the concept of the spectral moment decomposition is applied to the transfer function and used for the description of a stationary colored Gaussian process with target PSD function.

5.4 Reconstruction of impulse response and transfer function by H-FSM decomposition

As described in section 3.2.2, a colored Gaussian noise process $F(t)$ can be represented as output of a linear differential equation, excited by a Gaussian white noise process $\{W(t)\}$. Many methods exist to find the transfer function $H(\omega)$ characterizing the input-output relation in the frequency domain with the aim of simulating realizations of the process $\{F(t)\}$ with given target PSD. Though from the literature review in chapter 3 it can be concluded this is not a trivial task in general, especially if the PSD function is not rational and thus the factorization of the PSD function in general can not be formulated in analytic form. Moreover it was shown, that the discussed classical approaches are not eligible for the description of long memory processes.
The problem is solved on basis of the fractional spectral moment (FSM) decomposition described in section 5.3 which neither requires the factorization of the PSD nor any optimization procedure as shown in the following. The method proposed in [Cottone et al 2010d] is called *H-fractional spectral moments decomposition* as the coefficients for the noise simulation are calculated from the FSMs of the linear transfer function $H(\omega)$. In [Cottone et al 2011; Cottone and Di Paola 2011] it is applied for the simulation of univariate/multivariate

wind velocity fields, respectively.
In the following the main results of the method for the representation of colored Gaussian processes described in [Cottone et al 2010d] are summarized for clarity's sake.
Using this method the colored load process $\{F(t)\}$ with assigned PSD $S_F(\omega)$ is simulated as output of a linear system excited by Gaussian white noise. Due to the linearity of the underlying differential equation and the statistical independence of the Gaussian white noise process, the output remains a strict stationary Gaussian process. Following the steps derived in section 4.4 this can be expressed either using the linear differential operator $\mathcal{L}(\cdot)$ in the form $\mathcal{L}(F(t)) = W(t)$ or in the frequency domain by the corresponding input-output relation in terms of the transfer function in the form $S_F(\omega) = |H(\omega)|^2 S_W(\omega)$ where $\{W(t)\}$ denotes a zero mean white noise process with intensity q_W and PSD function $S_W(\omega) = q_W/2\pi$. Assuming

$$Im[H(\omega)] = 0 \tag{5.12}$$

the filter is defined from the target PSD function as

$$H(\omega) = |H(\omega)| = \sqrt{\frac{2\pi}{q_W} S_F(\omega)} \tag{5.13}$$

It must be noted that the assumption (5.12) leads to a non-causal system, i.e. $h(t) \neq 0$ for $t < 0$, hence, the generated time series of the process $\{F(t)\}$ is not just depending on the realizations $W(t_0), W(t_{-1}), W(t_{-2}), \ldots$ of the white noise process $\{W(t)\}$ for $t < 0$ but also on future values $W(t_1), W(t_2), \ldots$ for $t > 0$. In order to reconstruct the transfer function $H(\omega)$ and its Fourier transform one can follow the approach derived in the previous section for the AC function and PSD leading to the H-fractional spectral moments (H-FSM)

$$\Pi_H(\gamma) = \int_{-\infty}^{\infty} H(\omega)\,|\omega|^{\gamma}\,\mathrm{d}\omega \tag{5.14}$$

as shown in [Cottone and Di Paola 2010c]. Similar to Eqs. (5.10) the transfer function $h(t)$ and its Fourier transform $H(\omega)$ can be represented by

$$h(t) = \frac{1}{2\pi i} \int_{\rho - i\infty}^{\rho + i\infty} \nu(\gamma)\Pi_H(-\gamma)\,|t|^{-\gamma}\,\mathrm{d}\gamma \tag{5.15a}$$

$$H(\omega) = \frac{1}{4\pi i} \int_{\rho - i\infty}^{\rho + i\infty} \Pi_H(-\gamma)\,|\omega|^{\gamma - 1}\,\mathrm{d}\gamma \tag{5.15b}$$

with $\nu(\gamma) = \Gamma(\gamma)\cos(\gamma\pi/2)$. In some cases these contour integrals cannot be calculated in analytical form, but as the Gamma function $\Gamma(\gamma)$ decays exponentially fast in vertical strips,

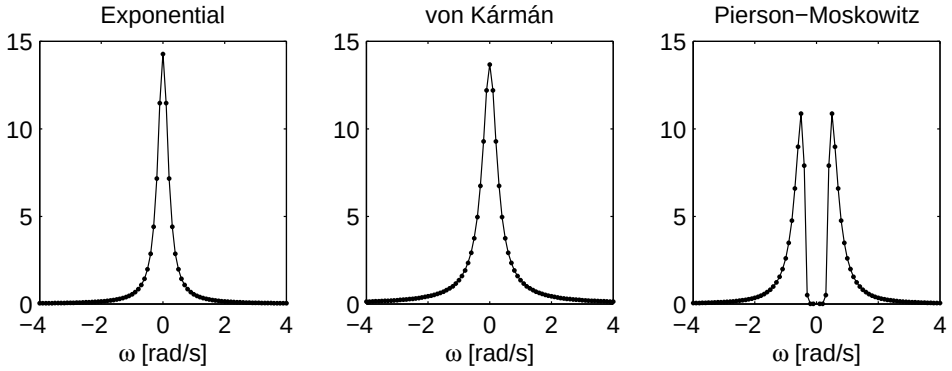

Figure 5.1: Exact (continuous) and approximated (dotted) power spectral densities for the three load cases: exponential AC, von Kármán and P-M PSD

i.e. for $Im\gamma \to \infty$, depending on the decay of $\Pi_H(\gamma)$, the integrals can be truncated along the imaginary axis with constant real part $Re\gamma = \rho$. Defining $\gamma_k = \rho + ik\Delta\eta$, the integral is calculated up to a certain value $\bar{\eta} = \mp m\Delta\eta$ by discretizing the interval into $2m + 1$ small increments $\Delta\eta$, yielding the approximation

$$h(t) \approx \frac{\Delta\eta}{2\pi} \sum_{k=-m}^{m} \nu(\gamma_k)\Pi_H(-\gamma_k)\,|t|^{-\gamma_k} \tag{5.16a}$$

$$H(\omega) \approx \frac{\Delta\eta}{4\pi} \sum_{k=-m}^{m} \Pi_H(-\gamma_k)\,|\omega|^{\gamma_k - 1} \tag{5.16b}$$

In the annexe B.1.2.1 and B.1.2.3 the H-FSMs $\Pi_H(\gamma)$ of the model wind velocity and wind wave PSD functions are summarized and in B.1.2.2 and B.1.2.4 the corresponding H-FSMs of the wind and wind-wave load spectra are given, respectively. Once again, in all cases the functions could be derived analytically by means of MATHEMATICA.

5.4.1 Numerical examples

Three load processes which are widely used in wind and ocean engineering are discussed, in particular wind turbulences characterized by an exponential AC function and von Kármán velocity PSD, respectively, and wind waves with Pierson Moskowitz PSD are examined for verification of the method.

5.4.1.1 Exponentially autocorrelated wind gusts

The most simplest model for the description of along wind turbulences is a process with exponential AC function $R(\tau) = \sigma^2 e^{-a|t|}$ and corresponding rational low-frequency power

spectrum $S_F(\omega)$ given by

$$S_{Exp}(\omega) = \frac{a\sigma^2}{\pi(a^2+\omega^2)} \tag{5.17a}$$

The H-FSMs of the transfer function $H(\omega)$ in Eq. (5.13) can be easily calculated by MATHEMATICA using Eq. (5.14) and are given by

$$\Pi_H(\gamma) = \left(\frac{1}{a^2}\right)^{-\gamma/2} \sqrt{\frac{2a\sigma^2}{q_W\pi}}\Gamma\left(-\frac{\gamma}{2}\right)\Gamma\left(\frac{1+\gamma}{2}\right); \qquad -1 < Re\gamma < 0 \tag{5.17b}$$

The PSD $S_F(\omega)$ of the process is reconstructed by the relation $S_F(\omega) = |H(\omega)|^2 q_W/(2\pi)$. The approximation of the transfer function $H(\omega)$ in Eq. (5.15b) is calculated choosing $a = 0.2$ [1/s], $\sigma = 3$ [N] and $\rho = 0.6$, $\Delta\eta = 0.2$ for the discretization of the integral involved taking into account $m = 20$ FSMs. From the results depicted in Fig. 5.1 it can be stressed that the proposed reconstruction leads to a good approximation of the analytic PSD function. Moreover, the quality of the approximation depends solely on the chosen discretization of the integral given in Eq. (5.15b).

5.4.1.2 Wind gusts with von Kármán velocity PSD

In general, if the PSD is rational it is not difficult to find a transfer function by spectral factorization [Maybeck 1979, p. 180–195] as shown in section 4.5.1 for the example of the exponentially correlated process. However, if the PSD of the process noise is given by a not rational function, there is no general method available for the analytically derivation of the transfer function $H(s)$ by spectral factorization and this is in fact a nontrivial task [Bagchi 2003]. This is the case for the widely used von Kármán spectrum of along-wind turbulences defined in Eq. (2.31) which is given here in the form

$$S_{u,Kar}(\omega) = \frac{\sigma^2 L}{\pi\bar{u}_z} \frac{1+\frac{8}{3}\left(1.339L\frac{\omega}{\bar{u}_z}\right)^2}{\left[1+\left(1.339L\frac{\omega}{\bar{u}_z}\right)^2\right]^{11/6}} \tag{5.18a}$$

where σ, L is the standard deviation of the fluctuating component of the wind speed at height z and the integral turbulence scale lengths, respectively, and $\bar{u}_z$ denotes the mean velocity with which the assumed frozen-turbulence field propagates in space (Taylor's frozen-in turbulence hypothesis [Holm 2005]). The PSD of the corresponding wind load is given by Eq. (2.44) using the aerodynamic admittance function $\chi_a(z,\omega)$ [Ruscheweyh 1982a,b]

discussed in section 2.2.3. Numerical values for the parameters for Germany can be taken e.g. from the national annexe of the "Eurocode 1: Actions on structures, Part 1-4: General actions/Wind actions" (DIN EN 1991-1-4:2010-12). In the example the parameters were chosen arbitrarily: $L = 10$ [m], $\sigma = 1$ [m/s], $z = 3$ [m], $\bar{u}_z = 18.25$ [m/s], $C_D = 1$ [-], $A = 0.1$ [m^2] and $\rho_a = 1.25$ [kg/m^3]. The associated H-FSMs follow from Eq. (5.14) using MATHEMATICA, yielding

$$\Pi_H(\gamma) = C(\gamma) + \sum_{k=0}^{2} \frac{D\Gamma[\frac{5+2c_k}{12}]\Gamma[\frac{-1}{6c_k}]{}_3F_2[1,\frac{2c_k+5}{24},\frac{2c_k+17}{24};\frac{c_k+6}{12},\frac{c_k+12}{12},\frac{-b^2L^4}{\bar{A}^2}]\bar{u}_z^{\frac{3}{2}+\gamma}}{(-1)^k b^{\frac{-1}{6c_k}} \bar{A}^{\frac{2(1+k)}{3}} L^{\frac{-c_k}{3}} \Gamma[\frac{5}{12}]} \tag{5.18b}$$

for $-1 < Re\gamma < 7/6$ with

$$C(\gamma) = -\frac{3i\pi D\bar{A}^{-\frac{1+\gamma}{2}} e^{\frac{3i\pi(1+\gamma)}{4}} (-ie^{\frac{3i\pi\gamma}{2}}(1-\frac{ibL^2}{\bar{A}})^{\frac{5}{12}} + (1+\frac{ibL^2}{\bar{A}})^{\frac{5}{12}})\bar{u}_z^{\frac{3}{2}+\gamma}}{(1+e^{3i\pi\gamma})(1+\frac{b^2L^4}{\bar{A}^2})^{\frac{5}{12}}}$$

where $c_k = 1 + 4k - 3\gamma$, $b = 70.8$, $\bar{A} = 4A$, $D = \sqrt{8\pi L(AC_d\sigma\rho_a)^2/q_W}$ and ${}_pF_q[a_1,...a_p;b_1,...b_q;z]$ is the generalized hypergeometric function. The analytical form of the H-FSMs leads, also in this case, to a very efficient application of the method. In Fig. 5.1 the results are illustrated, having chosen the following parameters: $\rho = 0.6$, $\Delta\eta = 0.15$, $m = 30$.

5.4.1.3 Wind waves with Pierson Moskowitz PSD

In this last example the process noise is generated from a wind wave PSD of fully developed sea introduced by Pierson and Moskowitz (P-M) given by (s. Eq. (2.50))

$$S_{PM}(\omega) = \frac{a}{|\omega|^5} e^{-\frac{b}{\omega^4}} \tag{5.19a}$$

where $a = 0.0081g^2$, $b = 0.74(g/\bar{u}_{19.5})^4$, g is the acceleration due to gravity and $\bar{u}_{19.5}$ denotes the mean velocity at height $z = 19.5$ [m] above the sea surface. Assuming a stationary process the wave force acting on a vertical pile with diameter D at height z follows from Eq. (2.65b). The H-FSMs are given, also in this case, in analytical form

$$\Pi_H(\gamma) = \frac{2^{c-2}}{b^{\frac{1}{8}}}\sqrt{\frac{a\cosh[k(h+z)]^2}{Aq_W\sinh[hk]^2}}\left(Ab^{\frac{\gamma}{4}}\sqrt{8\pi}\Gamma[c]{}_2F_2\left[-\frac{1}{4},\frac{1}{4};\frac{1}{2},1-c,-\frac{bB^2}{2A^2}\right]+\right.$$
$$\left.+\, b^{\frac{5}{8}-c}B\sqrt{\pi}\Gamma\left[c-\frac{1}{2}\right]{}_2F_2\left[\frac{1}{4},\frac{3}{4};\frac{3}{2},\frac{3}{2}-c;-\frac{bB^2}{2A^2}\right]+\right.$$

$$- 2^{\frac{3}{2}-c} b^{\frac{1}{8}} A^{1-2c} B^{2c} \Gamma\left[2c-\frac{1}{2}\right] \Gamma[-2c]_2F_2\left[c-\frac{1}{4},c+\frac{1}{4};c+\frac{1}{2},c+1;-\frac{bB^2}{2A^2}\right]\Bigg) \tag{5.19b}$$

for $Re\gamma < -1/2$ and $c = 1/8 - \gamma/4$, A=$8/\pi\sigma_u^2 K_d^2$ and $B = K_1^2$. In the example a pile with diameter $D = 0.1$ [m], drag coefficient $C_d = 0.6$ [-] and inertia coefficient $C_m = 2$ [-] which is excited by wind-induced ($\bar{u}_{19.5} = 20$ [m/s], $\sigma_u = 1$ [m/s]) ocean waves with wave length $\lambda = 20$ [m] and water depth $h = 15$ [m] is assumed. The corresponding PSD of the wave loads and the approximation using $m = 40$ FSMs and $\rho = 1.6$, $\Delta\eta = 0.3$ for the discretization of the integral involved is depicted in Fig. 5.1. Once again a good agreement between the approximated and the exact PSD is obtained.

5.5 Digital simulation of Gaussian random processes with target PSD function

The obtained fractional representation of the transfer function $H(\omega)$ given in Eq. (5.15a) can be now introduced in the input-output relation $F_k(\omega,T) = H(\omega)W_k(\omega,T)$

$$F_k(\omega,T) = \frac{1}{4\pi i}\int_{\rho-i\infty}^{\rho+i\infty} \Pi_H(-\gamma)\,|\omega|^{\gamma-1}\,W_k(\omega,T)d\gamma \tag{5.20}$$

where $0 < t < T$ and k denotes the index of the ensemble of the process $\{F(t)\}$, $\{W(t)\}$, respectively. The truncation of the time interval is needed as the stationary data theoretically persists forever and thus just the finite-range Fourier transforms exists [Bendat and Piersol 2010]. We introduce the definition of the Riesz fractional integral $(I^\gamma f)(t)$

$$(I^\gamma f)(t) = \frac{1}{2\nu(\gamma)}\int_{-\infty}^{\infty}\frac{f(\tau)}{|t-\tau|^{1-\gamma}}\mathrm{d}\tau; \qquad Re\gamma > 0, \gamma \neq 1,3,5,... \tag{5.21}$$

where $\nu(\gamma) = \Gamma(\gamma)\cos(\gamma\pi/2)$. For differentiable functions, it can be shown that the inverse Fourier transform of the Riesz fractional integral $(I^\gamma f)(t)$ from the time in the frequency domain is given by

$$\mathcal{F}^{-1}\{(I^\gamma f)(t);\omega\} = |\omega|^{-\gamma}\mathcal{F}^{-1}\{f(t);\omega\} = |\omega|^{-\gamma}F(\omega) \tag{5.22}$$

Rewriting Eq. (5.20) leads to

$$F_k(\omega,T) = \frac{1}{4\pi i}\int_{\rho-i\infty}^{\rho+i\infty} \Pi_H(-\gamma)\mathcal{F}^{-1}\{\left(I^{1-\gamma}W_k\right)(t,T)\,;\omega\}d\gamma \tag{5.23}$$

Applying a finite Fourier transform finally leads to a reconstruction of the correlated noise process $\{F(t)\}$ in terms of the H-FSMs given by

$$F(t) = \lim_{T\to\infty} E\left[F_k(t,T)\right] = \frac{1}{4\pi i}\int_{\rho-i\infty}^{\rho+i\infty} \Pi_H(-\gamma)(I^{1-\gamma}W)(t)\mathrm{d}\gamma \tag{5.24}$$

where $E\left[F_k(t,T)\right]$ is the ensemble average over the ensemble index k. In [Cottone and Di Paola 2011] a computational efficient algorithm for the digital simulation of wind loads based on Eq. (5.24) is introduced.
Using the approximation of the transfer function $H(\omega)$ given in Eq. (5.15b), the integral representation of the colored load process defined in Eq. (5.24) can be approximated by the truncated sum

$$F(t) \approx \frac{\Delta\eta}{4\pi}\sum_{k=-m}^{m} \Pi_H(-\gamma_k)(I^{1-\gamma_k}W)(t) \tag{5.25}$$

Hence, the main difficulty in the simulation of the process lies in the efficient calculation of the Riesz fractional integral $(I^{1-\gamma_k}W)(t)$ of the Gaussian white noise process $\{W(t)\}$. It can be shown that the Riesz integral form can be expressed in terms of Riemann-Liouville (RL) fractional integrals [Samko et al 1993, p. 214]

$$(I^{\gamma}W)(t) = \frac{1}{2\nu(\gamma)}\left[\int_{-\infty}^{t}\frac{W(\tau)}{|t-\tau|^{1-\gamma}}d\tau + \int_{t}^{\infty}\frac{W(\tau)}{|\tau-t|^{1-\gamma}}d\tau\right] = \frac{(I_{+}^{\gamma}W)(t)+(I_{-}^{\gamma}W)(t)}{2\cos(\gamma\pi/2)} \tag{5.26}$$

with $-\infty < t < \infty$ and $\nu(\gamma) = \Gamma(\gamma)\cos(\gamma\pi/2)$ and where $(I_{+}^{\gamma}W)(t)$, $(I_{-}^{\gamma}W)(t)$ denote the left-, right-handed RL fractional integral, respectively. Assuming that the process $\{W(t)\}$ is discretized on a finite interval $[0,n\tau]$, where $n \in \mathbb{N}$, $\tau > 0$, and zero elsewhere, the RL integrals can be calculated numerically using fractional order differences [Samko et al 1993, p. 385–388] as illustrated in section 5.2. This leads to the Grünwald - Letnikov form of the Riesz fractional integral given by:

$$(I^{\gamma}W)(j\tau) \approx \lim_{\tau\to+0}\sum_{k=0}^{j}\alpha_k(\gamma)W(j\tau-k\tau) + \lim_{\tau\to+0}\sum_{k=0}^{n-j}\alpha_k(\gamma)W(j\tau+k\tau) \tag{5.27}$$

where

$$\alpha_k(\gamma) = \frac{(-1)^k\tau^{\gamma-1}}{2\cos(\gamma\pi/2)}\binom{-\gamma}{k} \tag{5.28}$$

The latter can be calculated either by fast Fourier transform (see e.g. [Podlubny 1999, p. 208]) or using the recursion

$$\alpha_0(\gamma) = \frac{\tau^{\gamma-1}}{2\cos(\pi\gamma/2)} \qquad \text{and} \qquad \alpha_k(\gamma) = \frac{k+\gamma-1}{k}\alpha_{k-1}; \qquad k = 1, 2, \ldots \tag{5.29}$$

The first sum in Eq. (5.27) includes the weighted sequence of past white noises $W_0, W_1, \ldots, W_j$ up to the actual time $j\tau$, while the second sum represents the weighted sequence of future white noises $W_j, W_{j+1}, \ldots, W_n$. As mentioned in section 5.4, the dependence on the future, that is the non-causality of the generated process, is caused by disregarding the imaginary part of the transfer function in Eq. 5.12.
Eq. (5.27) can be efficiently calculated in matrix form by $\mathbf{Z}(\gamma) = \mathbf{A}(\gamma)\mathbf{W}$

$$\mathbf{Z}(\gamma) = \begin{bmatrix} (I^\gamma W)(0) \\ (I^\gamma W)(\tau) \\ \ldots \\ (I^\gamma W)(n\tau) \end{bmatrix}; \quad \mathbf{A}(\gamma) = \begin{bmatrix} 2\alpha_0 & \alpha_1 & \ldots & \alpha_n \\ \alpha_1 & 2\alpha_0 & \ldots & \ldots \\ \ldots & \ldots & \ldots & \alpha_1 \\ \alpha_n & \ldots & \alpha_1 & 2\alpha_0 \end{bmatrix}; \quad \mathbf{W} = \begin{bmatrix} W(0) \\ W(\tau) \\ \ldots \\ W(n\tau) \end{bmatrix} = \begin{bmatrix} G_0 \\ G_1 \\ \ldots \\ G_n \end{bmatrix} \tag{5.30}$$

where the discretized white noise process $\mathbf{W}$ in the interval $[0,n\tau]$ is described by the realizations of a zero-mean Gaussian random process $G_0, G_1, \ldots, G_n$ with standard deviation $\sqrt{q_W \tau}$. Finally, the vector of the colored load process $\mathbf{F} = [F(0), F(\tau), \ldots, F(n\tau)]^T$ is obtained by

$$\mathbf{F} = \frac{\Delta\eta}{4\pi} \sum_{k=-m}^{m} \Pi_H(-\gamma_k)\mathbf{Z}(1-\gamma_k) = \sum_{k=-m}^{m} \mathbf{H}(\gamma_k)\mathbf{W} \tag{5.31}$$

by means of the matrix transfer function $\mathbf{H}(\gamma_k) = \Delta\eta(4\pi)^{-1}\Pi_H(-\gamma_k)\mathbf{A}(1-\gamma_k)$.
In the following section, the short memory principle will be introduced, which is needed for the efficient generation of a long time series. Furthermore, it will be shown, that the coefficient matrix $\mathbf{A}(\gamma)$ defined in Eq. (5.30) must be truncated in order to obtain a stationary sequence.

5.5.1 Short memory principle

It must be noted that the evaluation of the fractional integral approximation (5.27) requires at each iteration the re-calculation and summation of every previous time point and thus becomes increasingly cumbersome for large times $0 << n\tau$ where a significant numbers of computations and memory storage is needed. However, [Podlubny 1999, p. 203f] observed, that the Grünwald Letnikov coefficients $\alpha_k(\gamma)$ defined in Eq. (5.28) decay with increasing

value k and can be set to zero for $k > p$. For illustration purposes, Fig. 5.2 depicts exemplarily the absolute values of the coefficients $\alpha_k(\gamma)$ for a sampling interval of $\tau = 0.05$ [s] in dependence of the chosen order of integration $\gamma = \rho + 1i$ where the real part is varied in the range $\rho = 0...0.9$. Instead of taking into account the complete history of the process $\{W(t)\}$ starting from $t = 0$, [Podlubny 1999, p. 203f] proposed to truncate the infinite sum after a finite number of values. This leads to the so-called *short memory principle*, based on which the fractional integral is calculated from the recent past of the function defined by the time interval $[t-M,t]$, where M denotes the considered process's memory. Defining $p = M/\tau$, the series representation in Eq. (5.27) can be truncated, yielding

$$(I^{\gamma}W)(j\tau) \approx \lim_{\tau\to+0} \sum_{k=0}^{\min(j,p)} \alpha_k(\gamma) W(j\tau - k\tau) + \lim_{\tau\to+0} \sum_{k=0}^{\min(p,n-j)} \alpha_k(\gamma) W(j\tau + k\tau) \tag{5.32}$$

Consequently, the coefficient matrix $\mathbf{A}(\gamma)$ needed for the generation of the process discretized in the time interval $[0,n\tau]$ shows the following band structure

$$\mathbf{A}(\gamma) = \begin{pmatrix}
2\alpha_0 & \alpha_1 & \dots & \alpha_p & 0 & \dots & 0 & 0 & \dots & 0 & 0 \\
\alpha_1 & 2\alpha_0 & \alpha_1 & \dots & \alpha_p & 0 & & & & & 0 \\
\vdots & \ddots & \ddots & \ddots & \dots & \ddots & \ddots & & & & \vdots \\
\alpha_p & \dots & \alpha_1 & 2\alpha_0 & \alpha_1 & \dots & \alpha_p & 0 & & & 0 \\
0 & \alpha_p & \dots & \alpha_1 & 2\alpha_0 & \alpha_1 & \dots & \alpha_p & 0 & & 0 \\
\vdots & \ddots & \ddots & \dots & \ddots & \ddots & \ddots & \dots & \ddots & \ddots & \vdots \\
0 & & 0 & \alpha_p & \dots & \alpha_1 & 2\alpha_0 & \alpha_1 & \dots & \alpha_p & 0 \\
0 & & & 0 & \alpha_p & \dots & \alpha_1 & 2\alpha_0 & \alpha_1 & \dots & \alpha_p \\
\vdots & & & & \ddots & \ddots & \dots & \ddots & \ddots & \ddots & \vdots \\
0 & & & & & 0 & \alpha_p & \dots & \alpha_1 & 2\alpha_0 & \alpha_1 \\
0 & 0 & \dots & 0 & 0 & \dots & 0 & \alpha_p & \dots & \alpha_1 & 2\alpha_0
\end{pmatrix} \tag{5.33}$$

where the lower and upper triangular part of the $n \times n$-matrix includes the weights of the past and future realizations of the Gaussian white noise process, respectively. It must be noted, that for an input vector $\mathbf{W}$ of length n, the first and last p samples of the output sequence $\mathbf{F}$ can be regarded as transition states whereas the remaining $n - 2p$ samples, are the steady states needed for the simulation of a stationary time series. The transition states are caused by the fact, that the process is discretized on a finite time interval, i.e. due to the

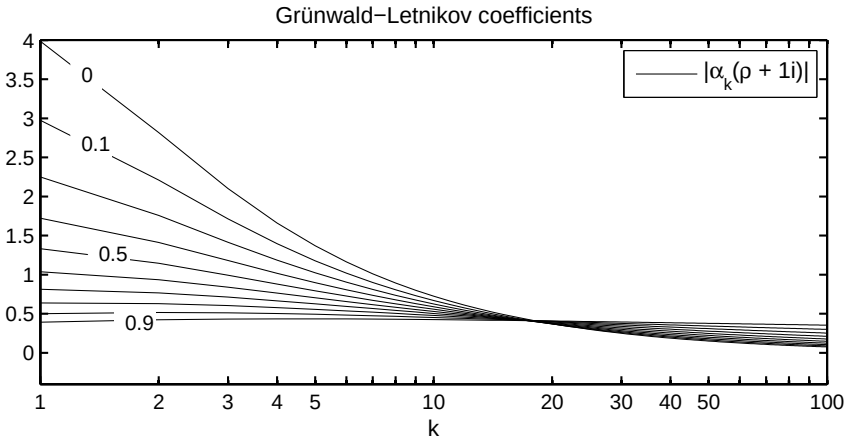

Figure 5.2: Evaluation of the coefficients of the Grünwald-Letnikov approximation choosing the order of integration equals $\gamma = \rho + 1i$, where ρ takes values between 0.1 and 0.9

assumption that the process vanish for $n\tau < t < 0$. Consequently, the first and last p rows of the coefficient matrix, contain an incomplete number of coefficients. The box indicates the part of the coefficient matrix which is characterized by a complete set of p past and future weights, and which, if multiplied with a white noise sequence, leads to a stationary process.

5.5.2 Numerical examples

The result in Eq. (5.31) is once again verified by means of the three load cases. In order to obtain a stationary time series, the truncated coefficient matrix defined in Eq. (5.33) is used for the simulation. In Fig. 5.3 (Bottom) the three generated time series and the corresponding AC functions (Top) are depicted. It can be stressed that there is a good agreement between the normalized analytic AC function and the one obtained from the generated time series. For the latter a sampling interval of $\tau = 0.05$ [s] and the following parameters are used:

i) Exponentially correlated wind gusts: $p = 300$, $m = 30$, $\rho = 0.6$, $\Delta\eta = 0.2$

ii) Wind gusts with von Kármán velocity PSD: $p = 250$, $m = 50$, $\rho = 0.6$, $\Delta\eta = 0.15$

iii) Wind waves with P-M PSD: $p = 500$, $m = 100$, $\rho = 1.6$, $\Delta\eta = 0.3$

where p denotes the number of considered α coefficients.
Though, comparing the standard deviation of the sampled AC functions $\hat{\sigma}_{Exp}$, $\hat{\sigma}_{Kar}$, $\hat{\sigma}_{PM}$ with the corresponding target values, it must be mentioned that the these values slightly deviate from the expected ones by about 5 [%]. It can be shown, that this error decreases with decreasing sampling interval τ. In the following the dependence of the accuracy on the

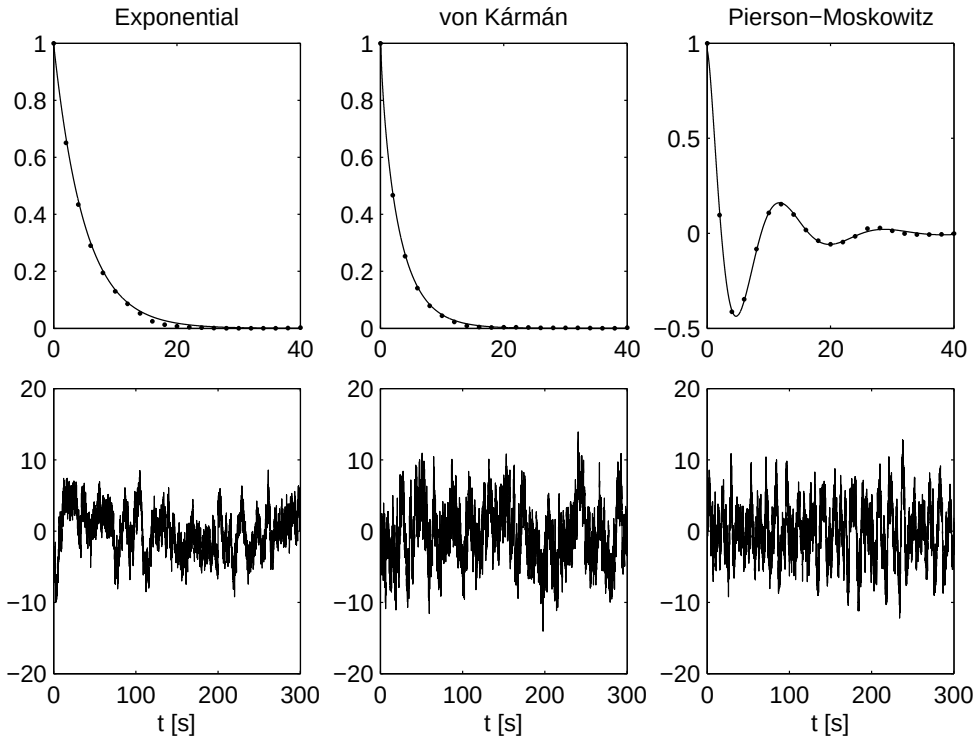

Figure 5.3: Top: Exact (continuous) and approximated (dotted) normalized AC functions, Bottom: Generated time series for the three load cases: exponential AC, von Kármán and P-M PSD

chosen sampling interval and the numbers of coefficients will be discussed in more detail. Furthermore, the use of an alternative Grünwald Letnikov (GL) operator, denoted as centered GL form, is proposed, which allow increasing both, the accuracy as well as the efficiency of the algorithm.

5.5.3 Investigation of the simulation accuracy: discretization and truncation errors

In the previous section the number of coefficients $p = M/\tau$ needed for the generation of the random process was chosen in such a way, that its AC function agrees accurately with the target function. Inaccuracies are caused by the approximation of the fractional integral: The Grünwald Letnikov form of the integral leads to two types of errors, a discretization error depending on the size of the chosen sampling interval τ and an error caused by truncating the infinite sum in Eq. 5.27 after a finite number of values, that is, by considering just the recent past of the process, defined by the time interval $[t - M,t]$ instead of taking into account the complete process's history. The effect of the chosen sampling interval τ and the considered memory M on the simulation result is now investigated on the example of the exponentially

correlated random process with AC function $R(t) = \sigma^2 e^{-a|t|}$.
As a measure of accuracy, the mean square error (MSE) between the approximated AC function $\hat{R}(t)$ of the generated time series and the analytic function is calculated, using

$$MSE = \frac{1}{L}\sum_{0}^{N}\left(\hat{R}(j\tau) - R(j\tau)\right)^2; \qquad N = L/\tau \tag{5.34}$$

where L denotes the length of the process beyond which the AC function is negligible, and, choosing $a = 0.2$, $\sigma = 10$ [N], is set to $L = 50$ [s]. For $t > L$, the AC function drops below a value of $R(50) = 0.0045$ and thus can be considered to be zero.
In the first test, 5000 samples of fixed length $T = 200$ [s] each are generated as weighted sum of p past and future Gaussian white noises by means of Eq. (5.31) setting $\alpha_k = 0$ for $k > p$. In order to investigate the effect of the discretization error, five parameterizations are tested: Keeping the considered memory of the process M constant by setting $M = 25$ [s], the sampling interval τ is varied between 0.025 and 0.5 [s] and the number of coefficients results from $p = M/\tau$. Fig. 5.4a shows the calculated AC functions and the corresponding MSEs: It is evident, that with increasing sampling interval τ, the variance of the process is over-estimated (Top), while the tail of the AC function is approximated in all cases with comparable accuracy up to a lag of 24 [s] (Bottom). Instead of choosing a smaller sampling interval in order to ensure a good fit of the peak value, of course, the variance problem can be solved, by scaling the simulated sequence by the target variance after its generation. However, if the algorithm for the load generation is combined with other methods, for instance with a system identification algorithm, as in the following, a subsequent correction is not possible.
The truncation error, that is the effect of the choice of the considered memory M on the accuracy of the simulation, is investigated by varying the considered memory between 2.5 and 25 [s], while the sampling interval is kept constant and the number of coefficients are set $p = M/\tau$. In order to keep the discretization error small, the process is discretized choosing a small sampling interval, setting $\tau = 0.025$ [s]. The result is depicted in Fig. 5.4b. From the upper plot it is evident that a too short length M mainly causes the AC function to decrease much faster then the target function and leads to small errors in the peak value. The bottom plot shows the result in a semi-logarithmic scale. It can be concluded that the sampling interval mainly influences the scaling, that is the variance of the process, while the choice of the considered memory M effects the range, in which the AC function is approximated well. There exists different strategies for the reduction of the discretization and the truncation error. The simplest approach is a refinement of the discretization grid and an increase of the considered memory, respectively. It allows making these errors arbitrary small, but not

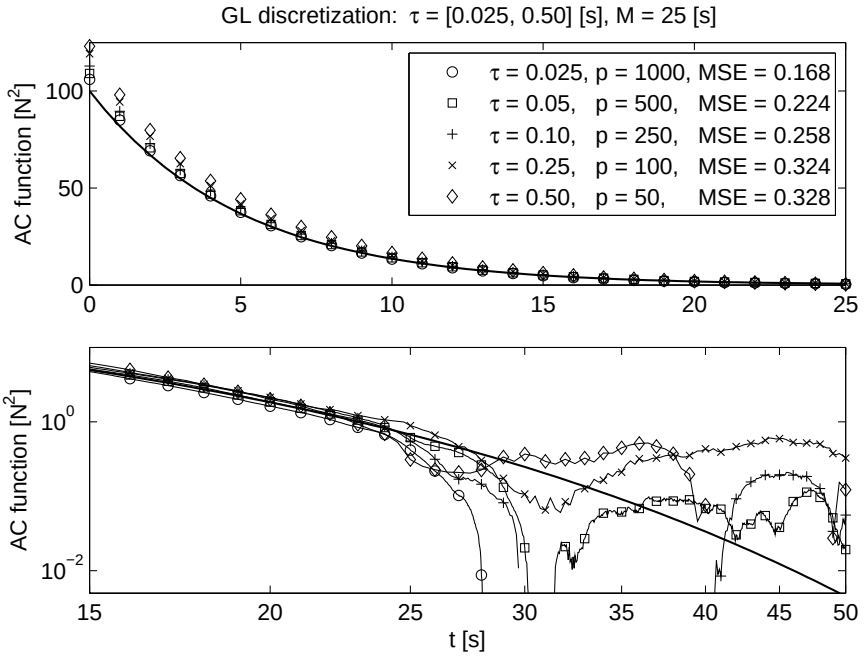

(a) Keeping the considered process memory constant $M = 25$ [s], the number of coefficients $p = M/\tau$ and varying the sampling interval τ between 0.025 and 0.5 [s].

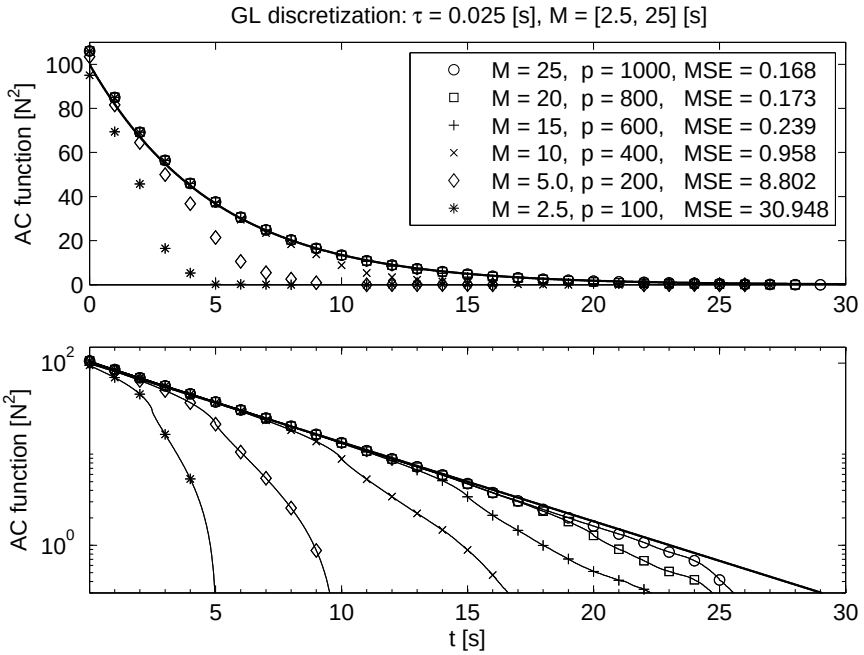

(b) Keeping the sampling interval constant $\tau = 0.025$ [s], the number of coefficients $p = M/\tau$ and varying the considered process memory M between 2.5 and 25 [s].

Figure 5.4: Exact (continuous) and approximated (dotted) normalized and corresponding semi-logarithmic plot of the tail of the AC functions of the exponentially correlated process for different parameterizations generated using the Grünwald-Letnikov approximation

without a fast increase of the computational demand and memory storage. More efficient strategies are the adaptive memory principle [Sprouse et al 2010], higher order approximations for fractional operators [Lubich 1986; Lin and Liu 2007] and a modified Grünwald Letnikov approach using centered differences [Ortigueira 2006, 2008]: In contrast to the used short memory principle, the adaptive sampling method does not truncate the convolution operator, but uses a non-equidistant sampling of the process's history. By including progressively fewer samples along the process's past, a temporally weighted history is computed including contributions from the whole past of the process, and thus leading to an increased accuracy and, at the same time, resulting in a higher computational efficiency. However, the non-equidistant sampling interval does not allow expressing the process in state space form which is later needed to combine it with the Kalman filter algorithm.

While the standard GL approximation is based on a first order Taylor series expansion, the method proposed by Lubich makes use of higher order approximations and thus is applicable with higher accuracy for larger time steps. Though, the coefficients of the Taylor series expansion are not readily defined in analytic form but must be calculated numerical and, in addition, starting weights must be determined by solving a linear set of equations. Thus, in contrast to the first order approximation, the implementation is not straight forward, especially, if the fractional integral must be evaluated for different fractional orders, as it is needed here.

In contrast to the GL approximation of the fractional integral given in (5.28) which result from the fractional generalization of the forward and backward difference operator, respectively, as shown in section 5.2, in [Ortigueira 2006] a modified GL form based on a generalization of centered differences $\Delta_c = f(t+\tau/2) - f(t-\tau/2)$ to fractional orders, is proposed, yielding

$$(D_c^\gamma f)(t) = \lim_{\tau\to 0} \frac{\Delta_c^\gamma f(t)}{\tau^\gamma} = \lim_{\tau\to 0} \frac{\Gamma(\gamma+1)}{\tau^\gamma} \sum_{k=-\infty}^{\infty} \frac{(-1)^k}{\Gamma(\frac{\gamma}{2}-k+1)\Gamma(\frac{\gamma}{2}+k+1)} f(t-k\tau) \tag{5.35a}$$

where $\gamma \in \mathbb{C}$. It is shown in [Ortigueira 2006], that for $\gamma < 0$, Eq. 5.35a coincides with the Riesz fractional integral operator defined in Eq. (5.21). Assuming that the function $f(t)$ is discretized on a finite interval $[0, n\tau]$, where $j, n \in \mathbb{N}$, $\tau > 0$ and zero elsewhere, then the sum in Eq. (5.35a) can be truncated and used to express the Riesz fractional integral operator $(I^\gamma W)(t)$ of the white noise process needed in 5.24 evaluated at $t = j\tau$ in the form

$$(I_c^\gamma W)(j\tau) = \lim_{\tau\to 0} \sum_{k=0}^{n-j} \alpha_{c,k}(\gamma)\, W(j\tau + k\tau) + \lim_{\tau\to 0} \sum_{k=0}^{j} \alpha_{c,k}(\gamma)\, W(j\tau - k\tau) \tag{5.35b}$$

using $(I_c^{\gamma} W)(t) = (D_c^{-\gamma} W)(t)$. The coefficients are defined as

$$\alpha_{c,k}(\gamma) = \frac{\tau^{\gamma-1}(-1)^k \Gamma(1-\gamma)}{\Gamma(1-\frac{\gamma}{2}-k)\Gamma(1-\frac{\gamma}{2}+k)} \tag{5.35c}$$

and can be calculated recursively, by means of

$$\alpha_{c,0}(\gamma) = \frac{\tau^{\gamma-1}\Gamma(1-\gamma)}{\Gamma^2(1-\gamma/2)} \qquad \text{and} \qquad \alpha_{c,k}(\gamma) = \frac{2(k-2)+b}{2(k-1)-b}\,\alpha_{c,k-1}; \tag{5.35d}$$

where $k \in \mathbb{N}$. Thus, due to the similarity to Eq. (5.27) this discretization method, denoted in the following as centered GL approximation, can be easily combined with the proposed algorithm by introducing the modified coefficients where needed.

In order to compare the centered GL representation with the classical one, again the errors introduced by discretization and truncation of the integral are investigated. To this aim, the two examples are re-run for the new representation using the same white noise sequence as input data.

Fig. 5.5a (Top) shows the calculated AC functions setting the considered process memory $M = 25$ [s], the number of coefficients $p = M/\tau$ and varying the sampling interval τ between 0.025 and 0.5 [s]. By visual inspection of the plot it is evident, that the process is generated in all cases with high accuracy. Though, in contrast to the standard GL approximation, the variance of the generated time series agrees well with the target value independently from the chosen sampling interval. The higher accuracy is reflected by an enormous reduction of the MSEs by about about 55 [%] for small sampling intervals and about 80 [%] for long sampling intervals of $\tau \geq 0.1$. The log-log-plot in Fig. 5.5a (Bottom) reveals that again a good agreement between the results is obtained for times $t \leq 22$ and that the small discretization errors are caused by the approximation of the tail of the AC function. It can be concluded that a change in the sampling interval has an inverse proportional effect on the required number of coefficients, i.e. if the sampling interval is halved, twice as much coefficients are needed in order to simulate the process with comparable accuracy.

The effect of the truncation of the fractional integral is again investigated by setting the number of coefficients $p = M/\tau$ and varying the considered process memory M between 2.5 and 25 [s]. For a better comparison with the results of the classical GL approximation, again a small sampling interval of $\tau = 0.025$ [s] is used. The result is depicted in Fig. 5.5b. The upper plot illustrates that a short memory M leads to errors in the peak value and causes the AC function to decrease much faster then the target function. The bottom plot shows the result in a semi-logarithmic scale. Similar to the results of the GL approximation, it is evident that the choice of the length M influences the range, in which the AC function is approximated well. Comparing the MSEs of the two approaches, it must be stressed, that

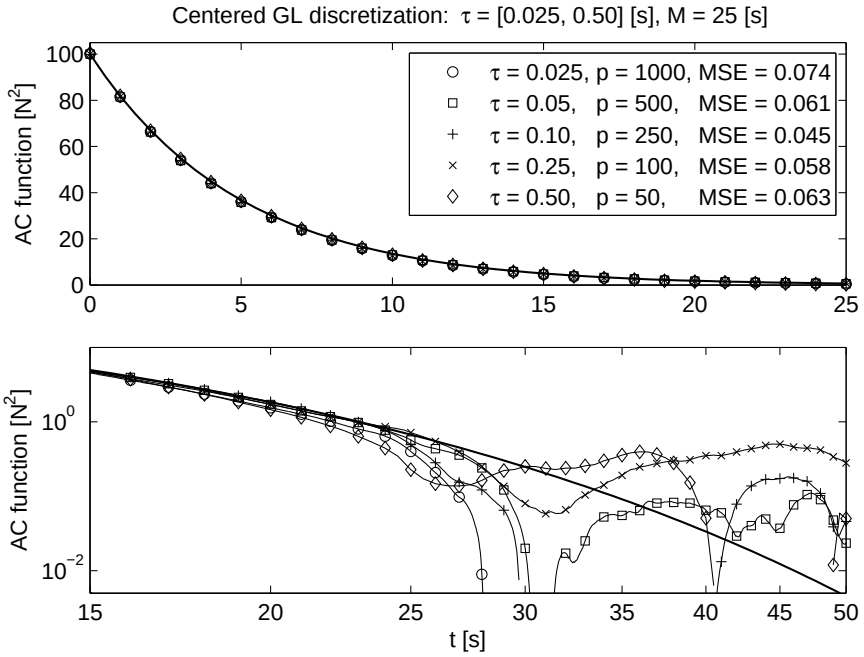

(a) Keeping the considered process memory constant $M = 25$ [s], the number of coefficients $p = M/\tau$ and varying the sampling interval τ between 0.025 and 0.5 [s].

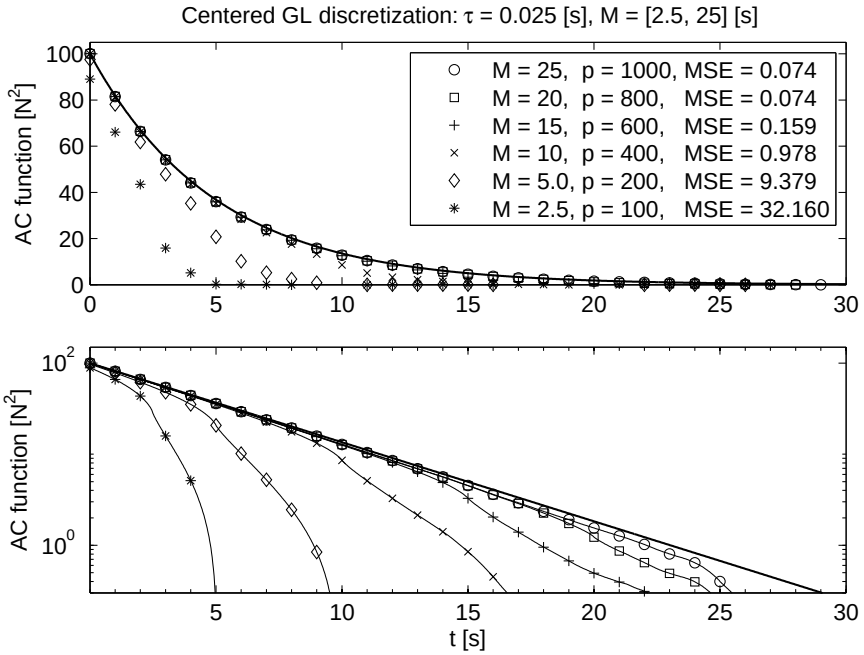

(b) Keeping the sampling interval constant $\tau = 0.025$ [s], the number of coefficients $p = M/\tau$ and varying the considered process memory M between 2.5 and 25 [s].

Figure 5.5: Exact (continuous) and approximated (dotted) normalized and corresponding semi-logarithmic plot of the tail of AC functions of the exponentially correlated process for different parameterizations generated using the centered Grünwald-Letnikov approximation

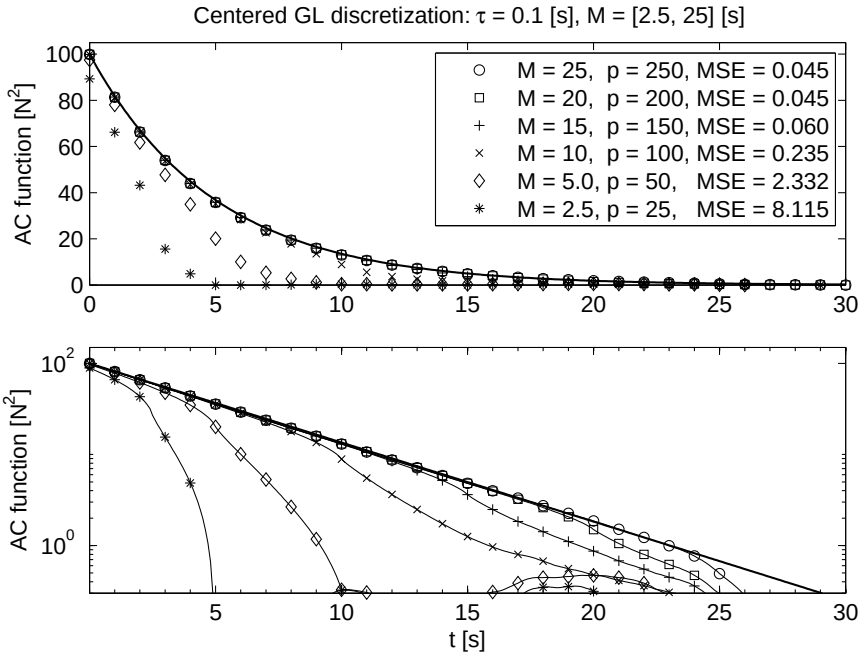

Figure 5.6: Top: Exact (continuous) and approximated (dotted) normalized AC functions of the exponentially correlated process setting the sampling interval $\tau = 0.1$ [s], the number of coefficients $p = M/\tau$ and varying the considered process memory M between 2.5 and 25 [s]. Bottom: Corresponding semilogarithmic plot of the AC function

while the centered GL leads to better results for $M \geq 15$ reducing the error by about 35 - 55 [%], for $M \leq 10$, the results of the classical approach are slightly better.

The strength of the centered GL approximation is evidently the fact, that it is applicable with high accuracy for larger sampling intervals as illustrated by Fig. 5.6. Once again, the considered memory is varied between 2.5 and 25 [s], but in this example, the sampling interval is increased from $\tau = 0.025$ [s] by a factor of four, setting $\tau = 0.1$ [s]. It shall be highlighted, that the larger sampling interval increases the accuracy, and at the same time, reduces the required number of coefficients to a forth.

From these results the following procedure for the use of the centered Grünwald-Letnikov approximation is proposed: (i) As prior guess, set the considered memory M according to the time range in which the AC function shall be approximated with high accuracy; (ii) choose a large sampling interval τ and set the numbers of coefficients $p = M/\tau$ [4]; (iii) increase/reduce the length M until the required accuracy of the simulation is obtained; (iv) after finding the optimal length M, the process can be generated, choosing the required sampling interval and determine the number of coefficients by $p = M/\tau$. In the following, all examples are based

[4] As shown above, an increase of the sampling interval reduces the required number of coefficients and thus makes the computation more efficient. Though, in order to avoid aliasing, the sampling rate $1/\tau$ should meet the Nyquist–Shannon sampling theorem, i.e. it must exceed $1/\tau > 2f_c$, where f_c denotes the cut-off frequency of the spectrum [Brigham 1988, p. 79ff.]

on the centered GL approximation combining the Eqs. (5.31), (5.33) and (5.35).

5.6 Long-memory processes

So far, the H-FSM decomposition was applied successfully for the generation of Gaussian random processes with short memory, that is, where the AC function decays with exponential rate as mentioned previously. However, it shall be highlighted that in contrast to the classical digital simulation methods discussed in chapter 3, the introduced fractional representation of the process, allows the generation of processes with much slower decaying AC function. To this aim, in the following section, the most important properties of long-memory processes are summarized and in section 5.6.2, a modification of the H-FSM decomposition is proposed which allows modeling long memory processes with infinite variance.

5.6.1 Properties

The phenomenon of long memory had been observed in fields such as hydrology and climatology long before suitable stochastic models for their description were available. In general, long memory in time or space, refers to empirically observed autocorrelations which exhibits a much slower decay to zero than can be explained by classical ARMA-type models. As shown previously, the AC function $R(k)$ of such models decays exponentially to zero as the lag approaches infinity, i.e. $k \to \infty$, leading to the relation

$$|R(k)| \leq C\lambda^{-k} \qquad k = 1,2,\ldots \tag{5.36a}$$

where $\lambda > 1$, $C > 0$ are some constants (compare Eqs. (3.17-3.18)). Due to that rapid decay, such processes are denoted as *short memory processes*. In contrast, *long memory processes* are characterized by a much slower decaying AC function of form

$$R(k) \sim Ck^{-\alpha}, \qquad \text{as } k \to \infty \tag{5.36b}$$

where the constants $0 < \alpha < 1$ and $C > 0$. It can be shown that the function decays to zero hyperbolically and thus the autocorrelations are not absolute summable, i.e. $\sum_{k=-\infty}^{\infty} |R(k)| \to \infty$. Another characteristic property is the decay of the variance of the sample mean $\bar{X} = 1/n \sum_{k=1}^{n} X_k$ of the sequence $X_1, X_2, \ldots, X_n$ with increasing sample size n. In general for independent and identically distributed random variables the variance decreases inverse

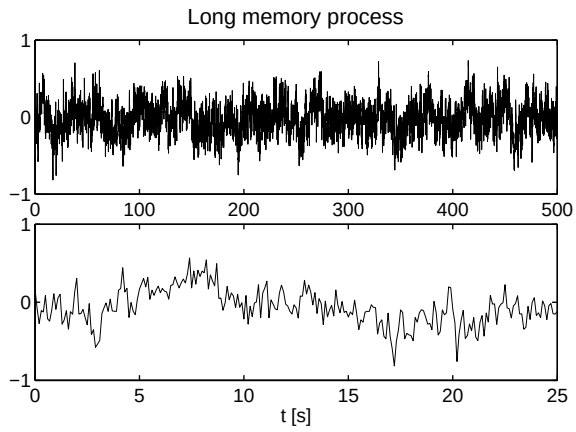

(a) Typical time series of a long memory process (Top) and a close up view (Bottom)

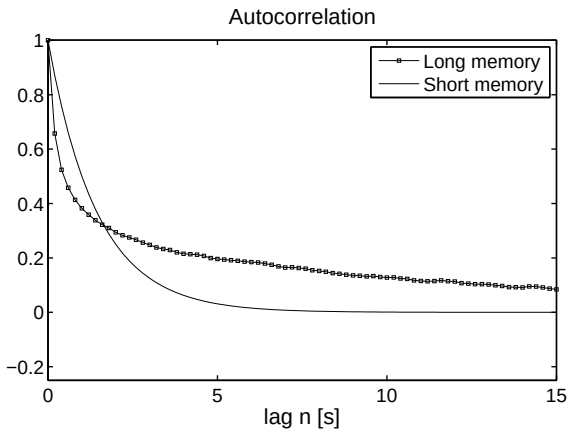

(b) Corresponding AC function of the long memory process compared with a AC function of exponential form $R(t) = 0.5^t$

Figure 5.7: Long memory process

proportionally to the sample size, i.e. $var(\bar{X}) = \sigma^2 n^{-1}$ where σ^2 denotes the variance of the signal. In contrast, if the autocorrelations are neither zero nor significantly small to be negligible, the error of the sample mean decays much slower to zero and the process is said to be of long memory, if

$$var(\bar{X}) \sim Cn^{-\alpha}, \qquad \text{as } n \to \infty \tag{5.36c}$$

where $0 < \alpha < 1$. Alternatively, in the frequency domain, the long term dependence of the process is characterized by the behavior of the PSD function at low frequencies, which approaches

$$S(\omega) \sim C\omega^{-\beta}, \qquad \text{as } \omega \to 0 \tag{5.36d}$$

where $0 < \beta < 1$. That is the PSD function is unbounded at zero frequency, which, of course, is the consequence of the divergence of the sum of autocorrelations.
In Fig. 5.7a a realization of a long memory process of $T = 500$ [s] and a close up of $T = 50$ [s] is depicted. Fig. 5.7b compares the corresponding AC function of the process with a typically exponentially decaying function of a short memory process. The process exhibits two typical features of long range dependency: Looking at the whole series, it seems that relatively long periods where the data tends to stay at a high level are followed by long periods with low levels. However, these cycles are irregular with random period and without persistent upwards or downwards trend. In contrast, if a shorter period of the time series is examined, then the signal shows a random nature with superposed cyclic trend [Beran 1994, p. 41]. Such

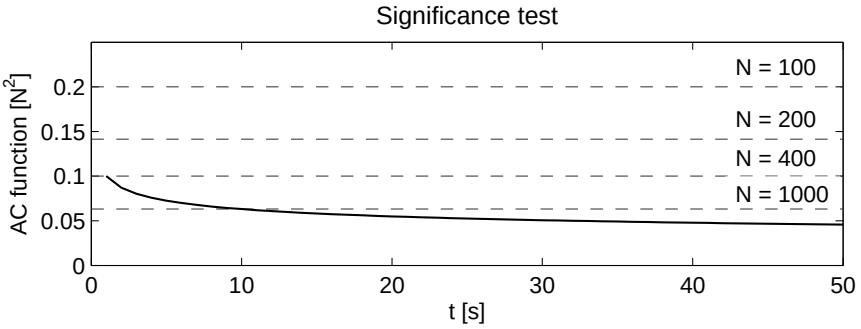

Figure 5.8: AC function $\hat{R}(k) = 0.1|k|^{2d-2}$, where $d = 0.9$ (line) and 5 % confidence bands $\pm 2N^{-1/2}$ for sample sizes $N = 100, 200, 400, 1000$ (dashed)

behavior has been noted in different data sets of yearly minimal water levels of the Nile River by [Hurst 1950], who observed the tendency of wet years to cluster into wet periods, or of dry years to cluster into drought periods. Motivated by Hurst's findings, it was [Mandelbrot and Van Ness 1968] and coworkers who introduced the concept of fractional calculus for the description of long range dependencies and proposed the concept of fractionally integrated Gaussian noise as a statistical model with long memory. Later, [Granger and Joyeux 1980] and [Hosking 1981] introduced the fractionally integrated ARMA (ARFIMA) models which nowadays, belongs to the most widely used class of long memory processes.

It shall be stressed that the properties 5.36 just give information about the asymptotic characteristics of the long memory process and thus describe solely the limiting behavior of the correlations and spectrum as the lag tends to infinity or the frequency approaches zero. E.g. the rate of convergence of the AC function does not provide any information about the absolute size of the values for any particular lag. Indeed, they can be arbitrarily small making the detection of slowly decaying correlations just by visual inspection of the data difficult. This is illustrated by means of the following example [Beran 1994, p. 43f]: Consider a time series of length N whose estimated AC function has the form $\hat{R}(t) = 0.1|k|^{-0.2}$. Consequently, due to the slow decay it might be difficult to detect non-zero but very small correlations by looking at the classical $\pm 2/\sqrt{N}$-confidence band[1]. To this aim, in Fig. 5.8 the AC function as well as the confidence bands for $N = 100, 200, 500, 1000$ are depicted. The autocorrelations are said to deviate significantly from zero if they fall outside the confidence band. Though, in this example, this is just the case for sample sizes evidently greater than $N = 400$ and consequently, if a too small data set is used, the test leads to the spurious assumptions that the autocorrelations are insignificant, even if the estimated sample AC function coincides with the true function. Though, the effect on statistical inference is by far not negligible

[1] In the limiting case of a Gaussian white noise process, the deviation of the sample mean $\bar{X}$ from the true value μ is normally distributed with $N(0,\sigma^2/N)$ where N is the sample size. That is with 95 % confidence the true value lies in the band $\pm 1.96/\sqrt{N}$. Thus, the ACs are said to deviate significantly from zero, if they exceed the confidence interval $\pm 2/\sqrt{N}$ [Priestley 1981, p. 340]

even for small sample sizes [Beran 1994, p. 43f].
The example shows, that without an investigation of the asymptotic properties of the process, long-range dependencies are not necessarily evident and might be missed if not explicitly investigated. Indeed, classical tests such as the $\sqrt{\sigma^2/n}$-significant method might confirm the spurious assumption of short term dependence, especially if a too short time series is used. Furthermore, the digital simulation of such processes is computational demanding, since the AC function decays slowly, and thus, the estimation of the model parameters e.g. by applying the maximum likelihood procedure, requires the consideration of all autocorrelations including those with large time lags. Moreover, the introduced standard methods such as ARMA-type approaches or the spectral factorization methods, are not adequate for modeling long range dependencies due to their exponential decay rate.
This leads to the development of fractional calculus based method such as the ARFIMA models or fractional integrated Gaussian noise models. Further literature on common signal modeling techniques for the generation of time series with power law decay such as fractional Brownian motion method, Fourier transform based-methods and wavelet-based methods is given in [Ferdi et al 2008].
So far the H-FSM decomposition was applied for the simulation of short-memory processes. Though, by means of the following example, it will be shown, that the method is also eligible for the modeling of long range dependencies. It must be stressed, that the applicability of the method to both short and long memory processes makes the method unique among the classical simulation approaches.

5.6.2 Proposed modification of the H-FSM decomposition for the representation of Gaussian processes with power-law decay

In the following, processes with AC and PSD function of form

$$R(\tau) = C_1 |\tau|^{-a} \tag{5.37a}$$

$$S(\omega) = \frac{C_1 \Gamma(1-a) \sin(\frac{a\pi}{2})}{\pi} |\omega|^{a-1} = C_2(a) |\omega|^{a-1} \tag{5.37b}$$

will be discussed, which, pursuant to the properties 5.36, show long-term behavior, if the constant a is chosen from the interval $0 < a < 1$. Though, due to the characteristic pole of the PSD function at $\omega = 0$, the FSMs of the transfer function $H(\omega) = \sqrt{2\pi S(\omega)/q}$

$$\Pi(\gamma) = \sqrt{\frac{2\pi C(a)}{q}} \int_{-\infty}^{\infty} |\omega|^{\gamma + \frac{1}{2}(a-1)} d\omega \tag{5.38a}$$

diverge. To overcome this problem, a modified fractional integral defined as

$$\tilde{\Pi}(\gamma) = \int_{-\infty}^{\infty} H(\omega) \frac{|\omega|^{\gamma}}{1+|\omega|} d\omega \tag{5.38b}$$

is proposed, which results in

$$\tilde{\Pi}(\gamma) = \sqrt{\frac{(2\pi)^3 C_2(a)}{q \cos^2(\frac{a\pi}{2} + \pi\gamma)}}; \qquad -\frac{(1+a)}{2} < Re\gamma < \frac{(1-a)}{2} \tag{5.38c}$$

Introducing the modified H-FSMs in 5.15b provides a reconstruction formula of the expression $H(\omega)/(1+|\omega|)$, which multiplied by $(1+|\omega|)$ finally yields the sought relation for the representation of the transfer function and corresponding unit response function in the form

$$H(\omega) = \frac{1}{4\pi i} \int_{\rho-i\infty}^{\rho+\infty} \tilde{\Pi}(-\gamma) \left\{ |\omega|^{\gamma-1} + |\omega|^{\gamma} \right\} d\gamma \tag{5.39a}$$

$$h(t) = \frac{1}{2\pi i} \int_{\rho-i\infty}^{\rho+\infty} \tilde{\Pi}_H(-\gamma) \left\{ \nu(\gamma)|t|^{-\gamma} - \Gamma(1+\gamma) \sin(\frac{\pi\gamma}{2}) |t|^{-1-\gamma} \right\} d\gamma \tag{5.39b}$$

where $\nu(\gamma) = \Gamma(\gamma)\cos(\pi\gamma/2)$. Comparing the result with the relations in Eq. (5.15) shows, that the modification leads to an additional term in the brackets, but the functional form of the reconstruction is still the same.

5.6.2.1 Numerical example

The result will be now verified on the example of the process characterized by an AC function with power law decay of order $a = 1/2$ choosing $C_1 = 10$. To this aim the corresponding PSD function is reconstructed by means of Eq. (5.39a) using the relation $S(\omega) = |H(\omega)|^2 q/(2\pi)$. The integral (5.39a) along the imaginary axis is truncated and discretized on the interval $[-m\Delta\eta, m\Delta\eta]$ as shown in 5.16, setting $\rho = 0.2$, $m = 50$ and $\Delta\eta = 0.05$. In Fig. 5.9 the analytic PSD function and the approximated one are compared. Especially, the log-log plot illustrates the high accuracy of the approximation in a wide frequency band.

5.6.3 Digital simulation of a Gaussian random process with power-law decay by H-FSM decomposition

The concept of the H-FSM decomposition for the digital simulation of a Gaussian random processes introduced in section 5.5 can be easily extended for the modified expression of the

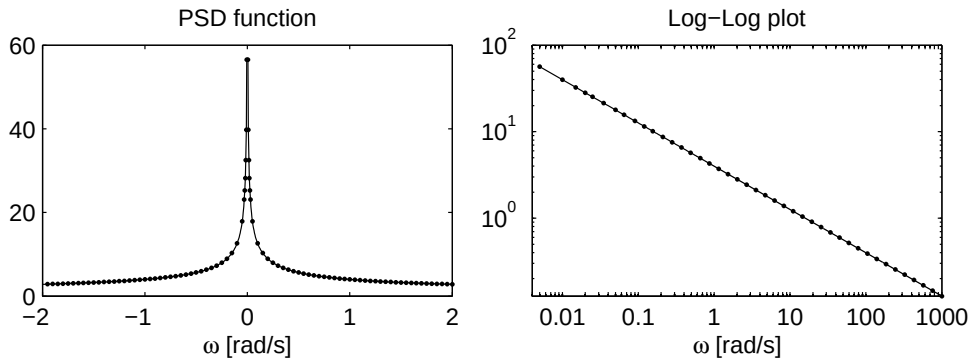

Figure 5.9: Exact (continuous) and approximated (dotted) power spectral densities of a process with power-law decay of order $a = 1/2$

transfer function (5.39a): Introducing the latter in the input-output relation (5.20)

$$F_k(\omega,T) = \frac{1}{4\pi i}\int_{\rho-i\infty}^{\rho+\infty} \tilde{\Pi}_H(-\gamma)\left\{|\omega|^{\gamma-1}+|\omega|^{\gamma}\right\} W_k(\omega,T)d\gamma \tag{5.40a}$$

and following the steps 5.21-5.24 leads to a quite similar integral representation of the Gaussian process and its series approximation in the form

$$F(t) = \frac{1}{4\pi i}\int_{\rho-i\infty}^{\rho+i\infty} \tilde{\Pi}_H(-\gamma)\left\{(I^{1-\gamma}W)(t)+(I^{-\gamma}W)(t)\right\} d\gamma \tag{5.40b}$$

$$F(t) \approx \frac{\Delta\eta}{2\pi}\sum_{k=-m}^{k=+m} \tilde{\Pi}_H(-\gamma_k)\left\{(I^{1-\gamma_k}W)(t)+(I^{-\gamma_k}W)(t)\right\}; \qquad \gamma_k = \rho + ik\Delta\eta \tag{5.40c}$$

where $(I^{1-\gamma}W)(t)$ and $(I^{-\gamma}W)(t)$ denote the Riesz fractional integrals of the Gaussian white input process $\{W(t)\}$. Finally, discretizing the fractional integrals on a finite interval $[0,n\tau]$ by means of the centered Grünwald-Letnikov representation 5.35, provides a realization of the colored load process $\mathbf{F} = [F(0),F(\tau),\ldots,F(n\tau)]^T$ in the form

$$\mathbf{F} = \frac{\Delta\eta}{4\pi}\sum_{k=-m}^{m} \tilde{\Pi}_H(-\gamma_k)\left\{\mathbf{A}(1-\gamma)+\mathbf{A}(-\gamma)\right\}\mathbf{W} \tag{5.41}$$

where the elements of the noise vector $\mathbf{W} \in \mathbb{R}^{n\times 1}$ are samples of a zero-mean Gaussian random process with standard deviation $\sigma = \sqrt{\tau q}$ and the coefficient matrices $\mathbf{A}(\gamma)$, $\mathbf{A}(-\gamma)$ are constructed based on the short memory principle using the definitions (5.35) and (5.33).

5.6.3.1 Numerical example

The algorithm is again verified on the example of a Gaussian random process with AC function of power law type defined in Eq. (5.37), choosing $a = 1/2$ and $C_1 = 10$. The process

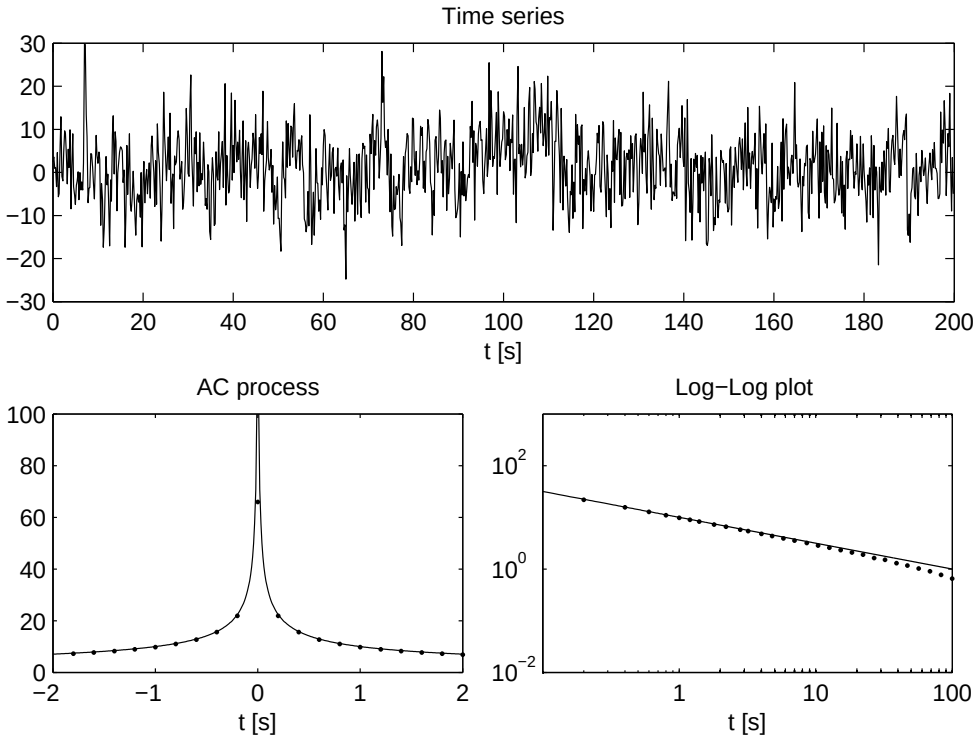

Figure 5.10: Top: Generated time series of a process with power law decay of order $a = 1/2$ by means of the H-FSM decomposition. Bottom: Exact (continuous) and sample AC function (dotted) of the generated time series

is generated choosing a sampling interval of $\tau = 0.25$ [s] and setting $p = 1000$, $\rho = 0.2$, $m = 50$, $\Delta\eta = 0.05$. Fig. (5.10) depicts the generated time series (Top) and compares the analytic and calculated sample AC function of the process (Bottom). Again a very good agreement between the exact and approximated function is observed in a wide range. It must be stressed, that the sample variance of the generated time series is not unbounded This is of course due to the fact that it is calculated from a finite time series. Though, for lags of order of the chosen sampling interval (that is for $t \geq \tau$), the AC function is approximated accurately, and thus the error in the peak value can be made arbitrarily small choosing a smaller sampling interval.

5.7 Summary of the main findings

It was shown that the H-FSM decomposition is an efficient method for the simulation of stationary Gaussian random processes with target PSD function. Due to its analytic form, its implementation is straight forward as illustrated by Fig. 5.11. It is applicable to arbitrarily correlated processes, without restriction to the functional form of the PSD function. Indeed,

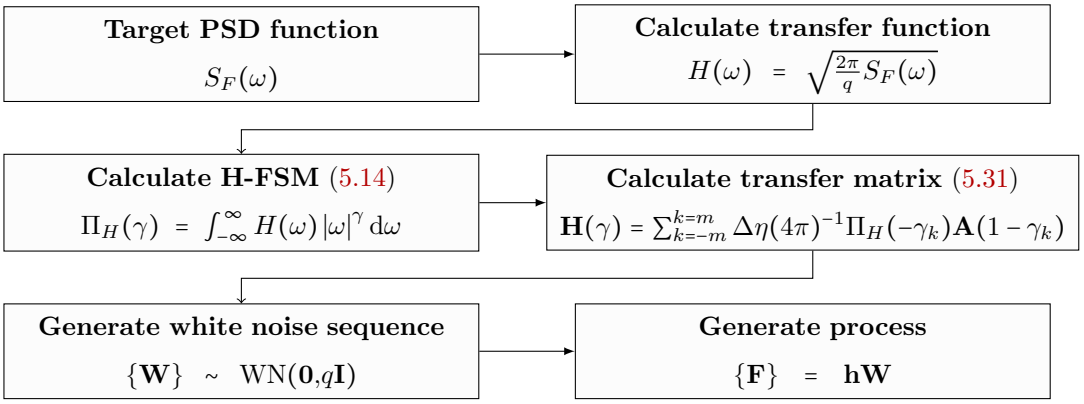

Figure 5.11: Workflow of the H-FSM decomposition used for digital simulation of Gaussian random processes. the coefficient matrix $A(\gamma)$ is calculated based on the short memory principle (5.31) and the centered GL discretization scheme (5.35)

the H-FSMs $\Pi_H(\gamma)$ of the wind velocity and wind wave model spectra discussed in chapter 2 could be derived analytically and are summarized in annexe B.1.2.

Due to the genetic form of the algorithm, in chapter 7 a general state space representation is derived, which can be given directly, once the H-FSMs are calculated, and be combined with the Kalman filter algorithm.

The accuracy of the simulation is directly related to the accuracy of the numerical evaluation of the fractional integral operator involved. [Cottone et al 2010d] proposed the use of the Grünwald-Letnikov (GL) series representation leading to a discretization error depending on the chosen sampling interval and a truncation error caused by the choice of the process's memory. A sensitivity analysis revealed, that i) the accuracy of the GL discretization strongly depends on the chosen sampling interval; ii) a too large sampling interval ($\tau \geq 0.025$) leads to an erroneous variance of the generated time series; iii) the sample AC function of the generated time series decays to fast if a too short memory is chosen; iv) the required number of coefficients and thus, the efficiency of the algorithm, increases inverse proportionally to the sampling interval and proportionally to the memory; i.e. it holds $p = M/\tau$.

It was shown that the discretization error can be significantly decreased by the use of the centered GL discretization. The sensitivity analysis revealed that the accuracy of the approximation is almost independent from the chosen sampling interval leading to a significant reduction of the discretization error, to be precise by about about 55 [%] for small sampling intervals and about 80 [%] for long sampling intervals of $\tau \geq 0.1$. Furthermore, due to the inverse proportional dependence of the number of coefficients on the sampling interval, a significant improvement of the efficiency is archived. Based on these properties, an efficient procedure for selecting the optimal number of model coefficients is developed.

Finally, a modified form of the H-FSM decomposition is proposed which makes the method

applicable for the modeling of long memory processes with unbounded variance. The modification is needed as the PSD function of long memory processes exhibits a characteristic pole at zero frequency and thus causes the classical H-FSM to diverge. It must be stressed, that the applicability to both, short and long memory processes, makes the method unique among the classical digital filter schemes.

6 Structural Parameter Identification by Kalman Filter Approaches

Many experimental modal identification methods for output-only measurements are available if the load process can be modeled as a stochastic white noise process: i) The peak picking method [Bendat and Piersol 1993, p. 196-203] in which the eigenfrequencies of the system are determined from the resonant peaks of the averaged normalized power spectral densities (ANPSDs) of the system response, is widely used in civil engineering due to its simplicity and computational efficiency. In case of a broad-band excitation, well separated modes and low damping, the method provides reliable estimates of the eigenfrequencies [Gentile and Saisi 2007]. ii) The stochastic subspace identification method [Peeters et al 1995; De Roeck et al 2000] belongs to the most advanced time-domain methods which identifies the system matrices of a stochastic state space model from which the modal parameters can be extracted using numerical techniques such as singular value decomposition (SVD) or QR factorization. The unknown input is introduced as zero-mean white process noise in the system equation. Hence, if the input contains some dominant frequencies, they cannot be distinguished from the eigenvalues of the system matrices used for the parameter identification [Ren and Zong 2004]. iii) The natural excitation technique (NExT) is based on the fact that the theoretical cross-correlation function between two response output channels from an ambient excited structure has the same analytical form as the free vibration response of the structure [James et al 1993]. For completeness' sake, in the annexe D.1 a conceptional description and discussion of the above mentioned time-domain identification methods is given.

In the present work the focus lies on the parameter identification of structures subjected to correlated loads with known PSD functions, that is where the white noise assumption is no longer appropriate and thus the above cited time-domain methods are not applicable. In chapter 7 a new output-only identification algorithm is proposed which is capable to estimate simultaneously the systems parameters and the unmeasured system's excitation. This method can be understood as a modification of the classical white noise Kalman filter for arbitrarily correlated loads. Thus, this chapter reviews the classical Kalman filter theory as well as its extension to parameter identification problems.

This chapter starts with a conceptual description of the Kalman filter in order to clarify the filter problem. After summarizing the model assumption and defining the state space representation of the physical model, the filter equations are derived based on a probabilistic approach also known as Bayesian modeling. Then the nonlinear filter problem of adaptive parameter identification is discussed leading to the extended Kalman filter (EKF), which is one of the most widely used nonlinear estimation techniques. Finally, a weighted global iteration scheme is introduced into the EKF algorithm which allows evaluating the filter convergence by means of an objective function. The method, denoted as weighted EKF (W-EKF) is applied for the identification of the stiffness and damping parameters of a three story shear building excited by a white noise process including a sensitivity analysis of the filter performance on the chosen initialization.

6.1 Kalman filter

Filtering usually refers to amplifying signals in a specified frequency range and suppressing those frequency components outside that range of interest. In the early 1940s Norbert Wiener and Andrei N. Kolmogorov investigated a different filter problem, namely the separation of the noise from the signal if their spectra are significantly overlapping and thus a separation of signal and noise is difficult. They solved the problem independently from each other leading to the Wiener filter [Wiener 1949] (originally published in 1942 as a classified document) formulated in the frequency domain and its time-domain counterpart proposed by Kolmogorov in [Kolmogorov 1941]. They belong to the class of linear-minimum-mean-square error (MMSE) filters providing a best separation of signal and noise in the minimum mean-square error sense. The Wiener filter is based on the assumption that both, signal and noise, are random processes of infinite length with known spectral characteristics. In order to ensure the existence of the needed auto- and cross-correlation functions, the method is applicable under the constraints of linearity, time-invariance and stationarity of the signals, which is of course a significant restriction [Brown and Hwang 1997, p. 159-160].
In 1960, Rudolf Emil Kálmán [Kálmán 1960] provided an alternative approach to the same problem using state-space formulations which allow to loosen some of the restrictions of the Wiener filter. Indeed, it can be shown, that the Kalman filter applied to a stationary process arising from a linear time-invariant system over an infinite time horizon approaches the causal Wiener filter. However, its implementation in the time-domain allows considering time-variant linear systems, non-stationary noises as well as a finite observation record length [Maybeck 1979, p. 273]. By removing the requirement of stationarity of the Wiener

filter, the Kalman's sequential solution to the time-varying linear filtering problem made a significant contribution to the field of linear filtering. A historical retrospect of the early events that resulted in the discovery of the Kalman filter, its role in the Apollo mission and the events in the following years and its extension for nonlinear estimation problems can be found in [McGee and Schmidt 1985].

The Kalman filter can be regarded as an *optimal recursive data processing tool* which provides a best estimate of the states of a physical, dynamic model which is indirectly observed through noisy measurements. The states of the system is a set of dynamic variables such as position, velocities, accelerations orientation, etc. describing the physical states of the system. The dynamic system is often assumed to be affected by so-called process noise which, in general, does not imply that the system has a stochastic nature, but the stochasticity is only used for representing uncertainties in the model or inputs. Similarly, the noise in the measurement can be understood as measurement inaccuracies. The word *optimal* implies that the Kalman filter provides an estimate of the desired variables in such a manner that the error is minimized statistically by combining i) prior knowledge about the system and measuring device dynamics, ii) statistical information about both, the measurement errors and the process noise and iii) any available information about initial values of the variables of interest. Another important feature of the Kalman filter is that it works *recursively*, which allows a simple implementation of the algorithm but, above all, avoids the storage and reprocessing of all previous data once a new measurement have been taken.

Figure 6.1 illustrates a typical situation where the Kalman filter can be applied advantageously: A dynamic system is driven by some known inputs (controls), and its outputs are measured. However, the states of the system cannot be observed directly and thus a tool is needed which allows inferring these states of interest from the available information of its inputs and outputs. This is not a trivial task and difficulties arise from the fact that the actual inputs as well as the relationship between the measured quantities and the various state variables of the system are just known with some degree of uncertainty. Consequently, in general, the modeled physical system and controls differ from the actual system and its inputs. Additionally to these system errors, measurement errors due to the corruption of the measurement data by noise, bias and/or device inaccuracies must be considered in order to extract the required information from the noisy data.

In a probabilistic approach (see 6.1.2) the uncertain parameters of the system and the measurements are modeled as random variables characterized by their probability density function (PDF). Starting from a prior density function including all available information about the parameters, the density function of the variables of interest is estimated at each time step conditional on the actual data coming form the measurement device. The uncertainty in the estimate is directly related to the width of the conditional PDF, that is, if the uncer-

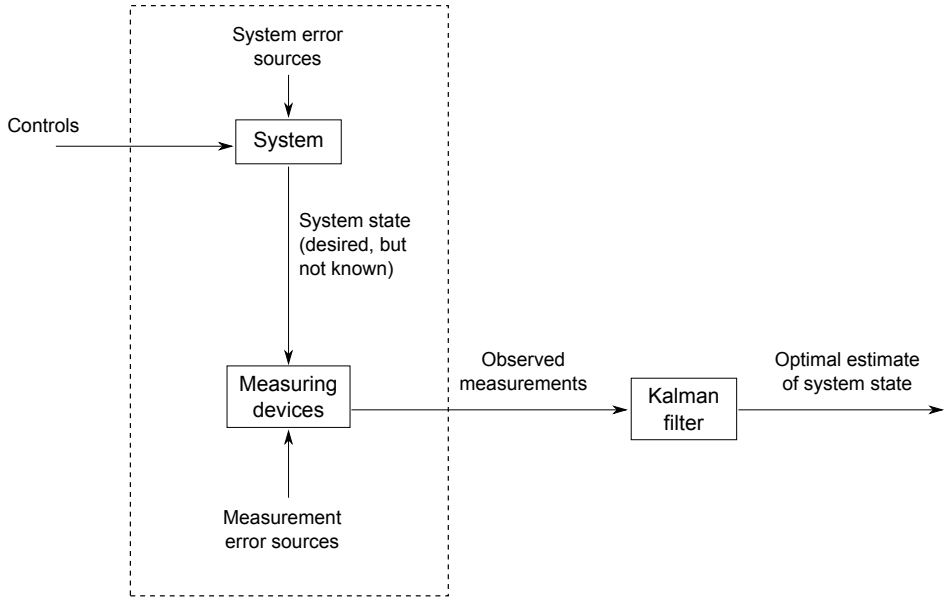

Figure 6.1: Application of the Kalman filter [Maybeck 1979, p. 5]

tainties are low, the probability weight is concentrated in a narrow range of values leading to a peaked PDF while in the converse case the probability weight is spread over a wider range of values. The choice of the optimal value is depending on the functional form of the PDF, where appropriate and widely used measures are for instance the mean value, the mode corresponding to the maximum of the PDF, or the median of the PDF describing the value with 50 % exceeding probability.

The Kalman filter algorithm is based on the assumptions that the physical system is linear and that the system and measurement noises can be modeled as uncorrelated Gaussian white noise processes. Under these constraints, it can be shown that the conditional PDF characterizing the state estimate follows a normal distribution. This is an important result because mean, mode, median or any other reasonable choice of the optimal estimate coincide in the Gaussian case and thus the optimization problem has an unique solution. Indeed, if the condition of linearity, Gaussianity and whiteness are met, among all linear filters, the Kalman filter provides the best possible state estimate [Maybeck 1979, p. 3-7].

6.1.1 Model assumptions

The following derivations are based on the information taken from [Brown and Hwang 1997, Ch. 5.5], [Simon 2006, Ch. 5.0-5.1] and [Reid 2003, Part 2]. A detailed discussion of linear stochastic system models driven by white Gaussian noises and the application of Kalman filter to such models can be found in [Maybeck 1979]. For further reading about compensation

of linear model inadequacies, adaptive estimation based upon linear models with uncertain parameters, nonlinear stochastic system models and estimation algorithms, the second volume [Maybeck 1982] is recommended. [Lewis et al 2008] gives an introduction to stochastic control theory including a extensive discussion of the discrete and continuous Kalman filter and reflects recent developments in estimation theory and design techniques as well as the problem of filter robustness.
The Kalman filter is based on a linear state space model consisting of two equations, that is the system equation

$$\mathbf{x}_{k+1} = \mathbf{A}_k\mathbf{x}_k + \mathbf{B}_k\mathbf{u}_k + \mathbf{G}_k\mathbf{w}_k \tag{6.1a}$$

representing the nth order dynamics of the physical model and the observation or measurement equation

$$\mathbf{z}_k = \mathbf{C}_k\mathbf{x}_k + \mathbf{v}_k \tag{6.1b}$$

where $\mathbf{A}_k \in \mathbb{R}^{n\times n}$, $\mathbf{B}_k \in \mathbb{R}^{n\times u}$, $\mathbf{G}_k \in \mathbb{R}^{n\times l}$ and $\mathbf{C}_k \in \mathbb{R}^{m\times n}$ are the transfer matrices, $\mathbf{u}_k$ is a deterministic control and $\mathbf{w}_k \in \mathbb{R}^u$ and $\mathbf{v}_k \in \mathbb{R}^m$ are samples of uncorrelated stationary zero-mean white noise processes. The transfer matrix $\mathbf{A}_k$ relates the actual state $\mathbf{x}_k$ to the state at the next time step $k+1$. The vector of controls $\mathbf{u}_k$ collects the known inputs and is related to the state by the transfer matrix $\mathbf{B}_k$. The matrix $\mathbf{C}_k$ describes the linear relation between the m-dimensional vector of observations $\mathbf{z}_k$ and the unobserved state vector $\mathbf{x}_k$. Similarly, the process noise $\mathbf{w}_k \in \mathbb{R}^l$ is related to the state by the matrix $\mathbf{G}_k$.
The KF is based on a Gaussian noise model, i.e. the random measurement errors $\mathbf{v}_k \in \mathbb{R}^m$, e.g. due to sensor inaccuracy, as well as the process noise $\mathbf{w}_k$, resulting from model uncertainties or unmeasured disturbances, are modeled as independent, zero mean Gaussian white noises, characterized by the covariance matrices

$$E[\mathbf{w}_k\mathbf{w}_i^T] = \begin{cases} \mathbf{Q}_k, & i = k \\ \mathbf{0}, & i \neq k \end{cases} \tag{6.2a}$$

$$E[\mathbf{v}_k\mathbf{v}_i^T] = \begin{cases} \mathbf{R}_k, & i = k \\ \mathbf{0}, & i \neq k \end{cases} \tag{6.2b}$$

$$E[\mathbf{w}_k\mathbf{v}_i^T] = \mathbf{0}, \qquad \text{for all } k \text{ and } i \tag{6.2c}$$

The aim of the KF is to estimate the state vector $\mathbf{x}_k$ based on the knowledge of the system dynamics and the available noisy measurement data $\mathbf{z}_k$. The algorithm is characterized by an iterative prediction-correction structure as shown in Fig. 6.2.

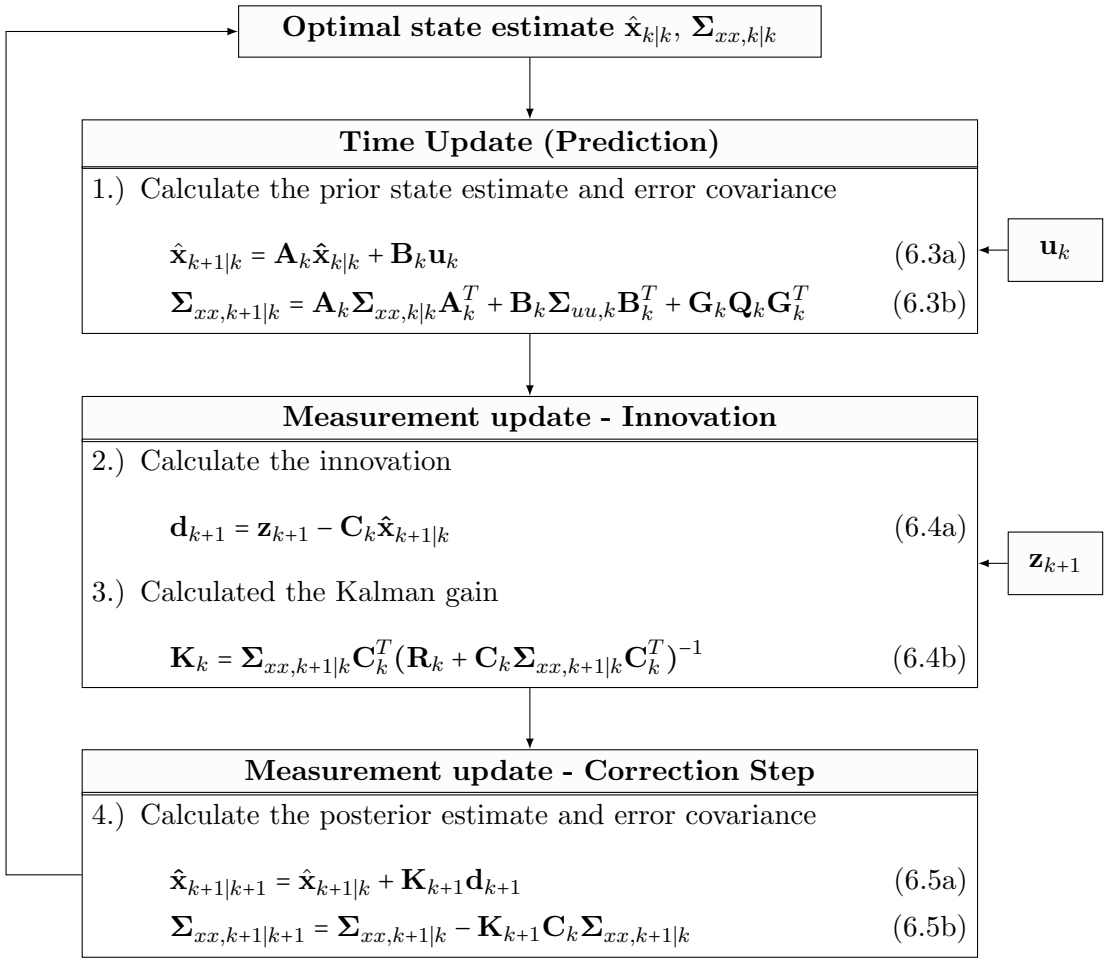

Figure 6.2: Kalman filter algorithm

In the following the Kalman filter equations are derived in a probabilistic framework, also known as Bayesian analysis, instead of the commonly used least square approach which is summarized for completeness' sake in the annexe C.1.1. The Bayesian approach can be sought of being the most general estimation methods which includes e.g. maximum likelihood, weighted least square, least square and also the Kalman filter as special cases [Isermann 1988a, p. 19]. Due to its generalized form it gives a better understanding of both, the assumptions made in the derivation of the Kalman filter as well as its restrictions.

6.1.2 Bayesian approach to the Kalman filter

Bayesian filtering is a probabilistic approach of the filter problem where the states of the physical model and the measured outcomes are treated as random variables. The assigned probability distribution functions quantify both, the model uncertainties as well as the physical randomness. That is, the probabilistic modeling does not necessarily imply that the

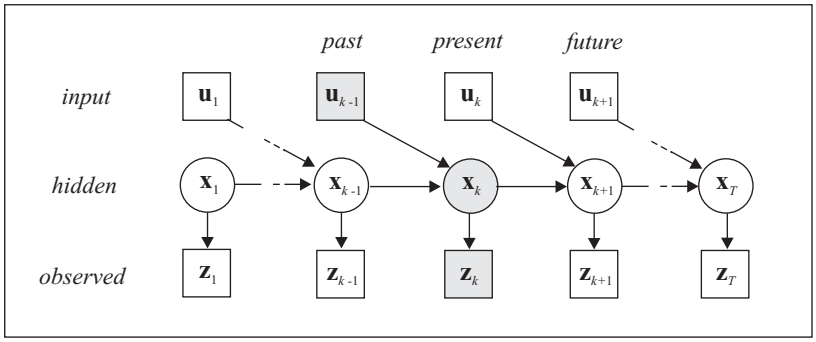

Figure 6.3: Bayesian dynamic network: Each slice characterizes the state of the system at a certain time step; nodes represent random variables, lack of links represent conditional independencies

physical model or parameters are truly random, but rather randomness is a mathematical tool for modeling the uncertainty in a dynamic phenomenon [Särkkä 2012].
The Bayesian model consists out of a probabilistic prior model $p(\boldsymbol{\phi})$ which represents all information on the parameter vector $\boldsymbol{\phi}$ characterizing the system and the measurement model $p(\mathbf{z}|\boldsymbol{\phi})$, also known as likelihood function, determining the stochastic mapping from the parameter to the measurements. The Bayesian inference provides then the probability distribution of the parameters, conditional on the observed measurements applying the so-called Bayesian rule given by

$$\overbrace{p(\boldsymbol{\phi}|\mathbf{z})}^{posterior} = \underbrace{\frac{\overbrace{p(\mathbf{z}|\boldsymbol{\phi})}^{likelihood}\overbrace{p(\boldsymbol{\phi})}^{prior}}{\int_{-\infty}^{\infty} p(\mathbf{z}|\boldsymbol{\phi})p(\boldsymbol{\phi})d\boldsymbol{\phi}}}_{normalization} = \frac{p(\mathbf{z}|\boldsymbol{\phi})p(\boldsymbol{\phi})}{p(\mathbf{z})} \tag{6.6}$$

where the conditional posterior distribution $p(\boldsymbol{\phi}|\mathbf{z})$ represents the state of knowledge about the parameters to be estimated when all available information from the measurements and the model are combined.
Ho and Lee [Ho and Kálmán 1966] were among the first authors who discussed iterative Bayesian filtering and discovered that the Kalman filter can be easily derived in a Bayesian framework. In a Bayesian approach, the Kalman filter can be interpreted as recursive Bayesian estimator of the conditional PDF of the actual system state $\mathbf{x}_k$ given the measurement data $\mathbf{Z}_k = \mathbf{z}_1, \mathbf{z}_2, \ldots, \mathbf{z}_k$ and the inputs $\mathbf{U}_k = \mathbf{u}_1, \mathbf{u}_2, \ldots, \mathbf{u}_k$, denoted as $p(\mathbf{x}_k, |\mathbf{Z}_k, \mathbf{U}_k)$. Using the incoming measurements and the observation model describing the physical relationship between the states to be estimated and the measurements, the recursive Bayesian estimator determines the unknown PDF recursively in time while the standard Kalman filter calculates recursively the true values of observations. In both cases the underlying dynamic system model can be described by a dynamic Bayesian network as shown in Fig. 6.3 which

represents graphically the dependency structure between variables of a multivariate probability distribution. Each slice characterizes the state of the system at a certain time step where the node corresponds to a random variables and the absence of a link between two variables indicates their conditional independence [Roweis and Ghahramani 1999]. The network shown in Fig. 6.3 is homogeneous, i.e. the slices are all identical, and Markovian, that is there are just links from one slice to the next one. A Markovian model is characterized by the following two properties [Särkkä 2012, p. 32]:

a) **Markov property of states:** The states form a Markov chain, that is the state $\mathbf{x}_{k+1}$ (and actually the whole future $\mathbf{x}_{k+2}$, $\mathbf{x}_{k+3}$, ...) is independent of everything that happened in the past given the present state $\mathbf{x}_k$ and the input $\mathbf{u}_k$, i.e.

$$p(\mathbf{x}_{k+1}|\mathbf{X}_k,\mathbf{Z}_k,\mathbf{U}_k) = p(\mathbf{x}_{k+1}|\mathbf{x}_k,\mathbf{u}_k) \tag{6.7a}$$

where $\mathbf{X}_{k-1} = \mathbf{x}_1,\mathbf{x}_2,\ldots,\mathbf{x}_{k-1}$, $\mathbf{U}_{k-1} = \mathbf{u}_1,\mathbf{u}_2,\ldots,\mathbf{u}_{k-1}$ and $\mathbf{Z}_{k-1} = \mathbf{z}_1,\mathbf{z}_2,\ldots,\mathbf{z}_{k-1}$. Conversely, also the past is independent of the future given the present

$$p(\mathbf{x}_{k-1},\mathbf{u}_{k-1}|\mathbf{X}_{k:T},\mathbf{Z}_{k:T},\mathbf{U}_{k:T-1}) = p(\mathbf{x}_{k-1},\mathbf{u}_{k-1}|\mathbf{x}_k) \tag{6.7b}$$

where $\mathbf{X}_{k:T} = \mathbf{x}_k,\mathbf{x}_{k+1},\ldots,\mathbf{x}_T$, $\mathbf{U}_{k:T-1} = \mathbf{u}_k,\mathbf{u}_{k+1},\ldots,\mathbf{u}_{T-1}$ and $\mathbf{Z}_{k:T} = \mathbf{z}_k,\mathbf{z}_{k+1},\ldots,\mathbf{z}_T$.

b) **Conditional independence of measurements:** The current measurement $\mathbf{z}_k$ is conditionally independent of the measurement and state history given the actual state $\mathbf{x}_k$, i.e.

$$p(\mathbf{z}_k|\mathbf{X}_k,\mathbf{Z}_{k-1},\mathbf{U}_{k-1}) = p(\mathbf{z}_k|\mathbf{x}_k) \tag{6.8}$$

These properties lead to a significant simplification of the dependency structure and are the core elements for the derivation of a recursive Bayesian filter as will be shown in the following.

6.1.2.1 Recursive Bayesian filtering

The Bayesian estimator calculates the PDF of the posterior state at time k from the PDF of the prior estimate and the likelihood applying the Bayes' rule [Du Plessis 1997]

$$p(\mathbf{x}_{k+1}|\mathbf{Z}_{k+1},\mathbf{U}_k) = \frac{p(\mathbf{z}_{k+1}|\mathbf{x}_{k+1})p(\mathbf{x}_{k+1}|\mathbf{Z}_k,\mathbf{U}_k)}{p(\mathbf{z}_{k+1}|\mathbf{Z}_k,\mathbf{U}_k)} \tag{6.9}$$

Similar to the Kalman filter the recursive Bayesian estimation is based on a *prediction step* prior to the observation and a *correction step* after obtaining the measurement data using the measurement likelihood. The underlying probabilistic state space model

$$p(\mathbf{x}_{k+1}|\mathbf{x}_k,\mathbf{u}_k) \sim N(\mathbf{A}_k\mathbf{x}_k + \mathbf{B}_k\mathbf{u}_k,\ \mathbf{G}_k\mathbf{Q}_k\mathbf{G}_k^T) \tag{6.10a}$$

$$p(\mathbf{z}_k|\mathbf{x}_k) \sim N(\mathbf{C}_k\mathbf{x}_k,\ \mathbf{R}_k) \tag{6.10b}$$

can be derived from the assumed mathematical description of the model (6.1) assuming Gaussian noise statistics (6.2) and applying standard rules of linear transformation of random variables.

Starting at time k the PDF of the state $\mathbf{x}_k$ is given by the posterior conditional distribution known from the previous time step

$$p(\mathbf{x}_k|\mathbf{Z}_k,\mathbf{U}_k) \sim N(\hat{\mathbf{x}}_{k|k},\ \mathbf{\Sigma}_{xx,k|k}) \tag{6.11}$$

which is assumed to be Gaussian with conditional expectation $\hat{x}_{k|k}$ and error covariance matrix $\mathbf{\Sigma}_{xx,k|k}$.

In the *prediction step* first the joint density of $\mathbf{x}_{k+1},\mathbf{x}_k$ conditional on the input and the observation up to time k is calculated using the PDF of the prediction $p(\mathbf{x}_{k+1}|\mathbf{x}_k,\mathbf{u}_k)$ resulting from the probabilistic system model (6.1a) and the posterior distribution $p(\mathbf{x}_k|\mathbf{Z}_k,\mathbf{U}_k)$ known from the previous time step

$$p(\mathbf{x}_{k+1},\mathbf{x}_k|\mathbf{Z}_k,\mathbf{U}_k) = p(\mathbf{x}_{k+1}|\mathbf{x}_k,\mathbf{u}_k)p(\mathbf{x}_k|\mathbf{Z}_k,\mathbf{U}_{k-1}) \tag{6.12a}$$

The prior distribution is obtained by marginalization, i.e. integration over $\mathbf{x}_k$

$$p(\mathbf{x}_{k+1}|\mathbf{Z}_k,\mathbf{U}_k) = \int_{-\infty}^{\infty} p(\mathbf{x}_{k+1},\mathbf{x}_k|\mathbf{Z}_k,\mathbf{U}_k)d\mathbf{x}_k$$

$$p(\mathbf{x}_{k+1}|\mathbf{Z}_k,\mathbf{U}_k) \sim N(\hat{\mathbf{x}}_{k+1|k},\ \mathbf{\Sigma}_{xx,k+1|k}) \tag{6.12b}$$

where $\hat{x}_{k+1|k}$, $\mathbf{\Sigma}_{xx,k+1|k}$ denote the expectation and the covariance of the prior state estimate given in Eq. (6.3).

In the *correction step* the likelihood $p(\mathbf{z}_{k+1}|\mathbf{x}_{k+1})$ incorporates the new measurement into the prior PDF of the state estimate. It can be interpreted as the likeliest observation $\mathbf{z}_{k+1}$ for the given prior state estimate $\hat{\mathbf{x}}_{k+1|k}$. Once the new measurement $\mathbf{z}_{k+1}$ have been obtained, the residual $\mathbf{d}_{k+1}$

$$\mathbf{d}_{k+1|k} = \mathbf{z}_{k+1} - \hat{\mathbf{z}}_{k+1} = \mathbf{z}_{k+1} - \mathbf{C}_k\hat{\mathbf{x}}_{k+1|k} \tag{6.13a}$$

between the actual measurement $\mathbf{z}_{k+1}$ and the predicted measurement $\mathbf{C}_k\hat{\mathbf{x}}_{k+1|k}$ is calculated. As the prior estimate is known form the previous time step, observing the error $\mathbf{d}_{k+1|k}$ and observing $\mathbf{z}_{k+1}$ are equally likely [Meinhold and Singpurwalla 1983]. Thus, using the observational equation (6.1b) the likelihood is given by

$$p(\mathbf{z}_{k+1}|\mathbf{x}_{k+1}) \sim N(\mathbf{C}_k\hat{\mathbf{x}}_{k+1|k}, \mathbf{R}_k) \tag{6.13b}$$

In order to obtain the posterior distribution the normalization factor $p(\mathbf{z}_{k+1}|\mathbf{Z}_k, \mathbf{U}_k)$ is computed using the prior PDF of the state estimate (6.12b) and the likelihood (6.13b) by marginalization of

$$p(\mathbf{z}_{k+1},\mathbf{x}_{k+1}|\mathbf{Z}_k,\mathbf{U}_k) = p(\mathbf{z}_{k+1}|\mathbf{x}_{k+1})p(\mathbf{x}_{k+1}|\mathbf{Z}_k,\mathbf{U}_k) \tag{6.14a}$$

with respect to $\mathbf{x}_{k+1}$, yielding

$$\begin{aligned} p(\mathbf{z}_{k+1}|\mathbf{Z}_k,\mathbf{U}_k) &= \int_{-\infty}^{\infty} p(\mathbf{z}_{k+1},\mathbf{x}_{k+1}|\mathbf{Z}_k,\mathbf{U}_k)d\mathbf{x}_{k+1} \\ p(\mathbf{z}_{k+1}|\mathbf{Z}_k,\mathbf{U}_k) &\sim N(\mathbf{A}_k\hat{\mathbf{x}}_{k+1|k}, \mathbf{A}_k\boldsymbol{\Sigma}_{xx,k+1|k}\mathbf{A}_k^T + \mathbf{Q}_{k+1}) \end{aligned} \tag{6.14b}$$

Finally, the posterior density is computed by introducing the obtained PDFs (6.12b), (6.13b), (6.14b) into (6.9) and applying the Bayes' rule, leading to

$$p(\mathbf{x}_{k+1}|\mathbf{Z}_{k+1},\mathbf{U}_k) \sim N(\hat{\mathbf{x}}_{k+1|k+1}, \boldsymbol{\Sigma}_{xx,k+1|k+1}) \tag{6.15a}$$

In the general case, the most probable estimate would be the mode of the posterior distribution, the so-called maximum a-posteriori estimate (MAP), which is defined by the condition [Chen 2003]

$$\left.\frac{\partial p(\mathbf{x}_{k+1}|\mathbf{Z}_{k+1},\mathbf{U}_k)}{\partial \mathbf{x}_{k+1}}\right|_{\mathbf{x}_{k+1}=\hat{\mathbf{x}}_{k+1}^{MAP}} = \mathbf{0}$$

and the associated error covariance follows from

$$\boldsymbol{\Sigma}_{k+1}^{MAP} = E\left[(\tilde{\mathbf{x}}_{k+1} - \hat{\mathbf{x}}_{k+1}^{MAP})(\tilde{\mathbf{x}}_{k+1} - \hat{\mathbf{x}}_{k+1}^{MAP})^T\right] \tag{6.15b}$$

In the Gaussian case, the mode of the posterior distribution and error covariance $\hat{\mathbf{x}}_{k+1}^{MAP}$, $\boldsymbol{\Sigma}_{k+1}^{MAP}$ are readily defined by the mean value and covariance $\hat{\mathbf{x}}_{k+1|k+1}$, $\boldsymbol{\Sigma}_{xx,k+1|k+1}$ of the posterior distribution $p(\mathbf{x}_{k+1}|\mathbf{Z}_{k+1},\mathbf{U}_k)$, i.e.

$$\hat{\mathbf{x}}_{k+1}^{MAP} = \hat{\mathbf{x}}_{k+1|k+1}$$

$$\begin{aligned}\hat{\mathbf{x}}_{k+1}^{MAP} &= \hat{\mathbf{x}}_{k+1|k} + \mathbf{K}_{k+1}\left(\mathbf{z}_{k+1} - \mathbf{C}_k\hat{\mathbf{x}}_{k+1|k}\right) = \hat{\mathbf{x}}_{k+1|k} + \mathbf{K}_{k+1}\mathbf{d}_{k+1|k} \\ \boldsymbol{\Sigma}_{k+1}^{MAP} &= \boldsymbol{\Sigma}_{xx,k+1|k+1} \\ &= \boldsymbol{\Sigma}_{xx,k+1|k} - \mathbf{K}_{k+1}\mathbf{C}_k\boldsymbol{\Sigma}_{xx,k+1|k} \end{aligned} \tag{6.15c}$$

where

$$\mathbf{K}_{k+1} = \boldsymbol{\Sigma}_{xx,k+1|k}\mathbf{C}_k^T(\mathbf{R}_k + \mathbf{C}_k\boldsymbol{\Sigma}_{xx,k+1|k}\mathbf{C}_k^T)^{-1} \tag{6.15d}$$

denotes the Kalman gain matrix. That is, in the correction step, the residual $\mathbf{d}_{k+1|k}$ is weighted by the Kalman gain matrix and used to correct the prior state estimate $\hat{\mathbf{x}}_{k+1|k}$. Thus, the residual is often denoted as innovation, as the difference can be interpreted as the part of the measurement, which contains new information about the state. It can be shown that under optimal conditions, the innovation is a zero mean Gaussian process with covariance matrix $\boldsymbol{\Sigma}_{dd} = \mathbf{C}_k\boldsymbol{\Sigma}_{xx,k+1|k}\mathbf{C}_k + \mathbf{R}_k^T$ and thus provides an important measure of the filter performance which can be used to check the consistency of the filter. E.g. if the innovation is colored, of nonzero-mean, or if the covariance deviates from its nominal value, it may indicate mis-modeling of the dynamic and/or measurement model, failure of sensors, and outliers in the data [Simon 2006, p. 298ff]. A review on different monitoring schemes and statistical tests of the innovation sequence as well as the relevant literature can be found in [Salzmann 1988, Ch. 5]. In section 6.1.3.3, an objective function which is based on the posterior residual $\mathbf{d}_{k+1|k+1}$ between the obtained posterior estimate and the measurement is introduced in order to detect the divergence of the filter.

A comparison with the result obtained by the classical Kalman filter given in Eq. (6.5) shows, that the estimate of the recursive Bayesian filter and the Kalman filter coincide. However, it must be highlighted that in the Bayesian approach it was neither demanded that the estimator is unbiased, i.e. $E\left[\hat{\mathbf{x}}_k|\mathbf{Z}_k\right] = \tilde{\mathbf{x}}_k$, as in Eq. (C.5b) of the classical derivation, nor assumed that there is a linear relation between the estimate and the measurements in the form Eq. (C.4). Instead, this came out naturally as a consequence of the Gaussian assumption and the choice of the conditional mean as optimal estimate. Consequently, one can conclude, that in the Gaussian case, the Kalman filter is not just the best among all available linear filters, but, in fact, it is the best within the class of all filters, linear or nonlinear [Brown and Hwang 1997, p. 231].

If the Gaussian assumption of the process and measurement noise is violated and thus the assumed linear form of the optimal estimator in Eq. (C.4) is no longer justified, the estimated mean value and error covariance $\hat{\mathbf{x}}_{k+1|k+1}$, $\boldsymbol{\Sigma}_{xx,k+1|k+1}$ provided by the Kalman filter, do not coincide with the conditional mean value and error covariance $\hat{\mathbf{x}}_{k+1}^{MAP}$, $\boldsymbol{\Sigma}_{k+1}^{MAP}$ of the posterior PDF. As a result, the Kalman estimate is biased and does not provide a minimum variance

estimate and thus, there might be nonlinear filters which perform better. However, among the linear filters it is still the best linear minimum variance estimator.

6.1.3 Nonlinear state estimation

So far, it was assumed that the system dynamics and measurement relations are adequately described by a linear model in order to develop optimal estimators. However, in reality, linear systems either are approximations of the nonlinear system's behavior and thus just valid over a certain range and under predefined conditions, or they result from the lack of knowledge about the system being modeled. In order to solve the nonlinear filter problem, various nonlinear estimation techniques were developed during the last decades which include particle filters, sigma-point filters, sequential Monte Carlo methods and unscented transform methods [Grewal and Andrews 2008] as well as nonlinear extensions of the classical Kalman filter, e.g. the ensemble Kalman filter, the unscented Kalman filter or the extended Kalman filter (EKF). Among them, the EKF is certainly the most widely used nonlinear state estimation technique [Simon 2006, p. 396].
The nonlinear estimation problem which will be discussed in the following, results from incomplete knowledge about the system model, that is model parameters such as elements of the state or force transition matrices such as stiffness or damping coefficient, the inputs, or the covariances of the noise processes are not completely known [Grewal and Andrews 2008, p. 333]. Typically, prior information about these parameters are available, but the variability of the material properties or simplifications in the material and/or structural modeling lead to uncertainties, so that just a range of physically admissible values can be given. In civil engineering typical examples for such uncertainties are related to the scattering of the Young's modulus within the structure, changes due to temperature or damage, the improper modeling of the composite material properties as the bond between steel and concrete or result from the unknown stiffness of the beam-column connections and disregarded friction effects, respectively.
The simultaneous estimation of the system's states and a number of uncertain parameters in the dynamics or measurement model is often termed combined state estimation and system identification or also known as *adaptive estimation*. If the set of unknown parameters is constant or slowly time-varying, this can be achieved by state space augmentation, that is by treating the unknown parameters as additional state variables. It leads to a nonlinear estimation problem as both, the states as well as the system matrices depend on the parameters to be estimated. This may have first been suggested by [Kopp and Orford 1963] who applied the newly developed Kalman filter to solve the adaptive control problem [Simon

2006, p. 450], that is the problem of controlling a process (here it was a aerospace vehicle) where imperfect or limited information about the system's parameters are available or are changing in time.
In the following the nonlinear estimation problem will be solved using the extended Kalman filter which is certainly the most widely used nonlinear state estimation technique that has been applied in the past decades.

6.1.3.1 Derivation of the extended Kalman filter for adaptive estimation

Starting point is again a linear state space model as defined in Eq. (6.1), but with the difference that the system matrices $\mathbf{A}_k, \mathbf{B}_k$ and $\mathbf{G}_k$ and measurement matrix $\mathbf{C}_k$ depend in a nonlinear way on an unknown parameter vector $\mathbf{p}_k \in \mathbb{R}^p$, i.e.

$$\mathbf{x}_{k+1} = \mathbf{A}_k(\mathbf{p}_k)\mathbf{x}_k + \mathbf{B}_k(\mathbf{p}_k)\mathbf{u}_k + \mathbf{G}_k(\mathbf{p}_k)\mathbf{w}_k \tag{6.16a}$$

$$\mathbf{z}_k = \mathbf{C}_k(\mathbf{p}_k)\mathbf{x}_k + \mathbf{v}_k \tag{6.16b}$$

If the set of unknown parameters is constant or slowly time-varying, then its evolution can be model by a random walk process, i.e.

$$\mathbf{p}_{k+1} = \mathbf{p}_k + \mathbf{w}_{p,k} \tag{6.16c}$$

where $\mathbf{w}_{p,k} \in \mathbf{R}^p$ is a small artificial additive Gaussian white noise term with zero mean and covariance matrix $\mathbf{Q}_{p,k}$. In order to estimate the parameters and the states of the dynamic system simultaneously, the unknown parameters are included in the state vector

$$\mathbf{x}'_k = \begin{bmatrix} \mathbf{x}_k \\ \mathbf{p}_k \end{bmatrix} \tag{6.17a}$$

and then the system equation is augmented by the parameter update equation (6.16c), yielding

$$\begin{bmatrix} \mathbf{x}_{k+1} \\ \mathbf{p}_{k+1} \end{bmatrix} = \underbrace{\begin{bmatrix} \mathbf{A}_k(\mathbf{p}_k) & \mathbf{0}_{n\times p} \\ \mathbf{0}_{p\times n} & \mathbf{I}_{p\times p} \end{bmatrix}}_{\mathbf{A}'_k(\mathbf{p}_k)} \begin{bmatrix} \mathbf{x}_k \\ \mathbf{p}_k \end{bmatrix} + \underbrace{\begin{bmatrix} \mathbf{B}_k(\mathbf{p}_k) \\ \mathbf{0}_{p\times u} \end{bmatrix}}_{\mathbf{B}'_k(\mathbf{p}_k)} \mathbf{u}_k + \underbrace{\begin{bmatrix} \mathbf{G}_k(\mathbf{p}_k) & \mathbf{0}_{n\times p} \\ \mathbf{0}_{p\times u} & \mathbf{I}_{p\times p} \end{bmatrix}}_{\mathbf{G}'_k(\mathbf{p}_k)} \begin{bmatrix} \mathbf{w}_k \\ \mathbf{w}_{p,k} \end{bmatrix} \tag{6.17b}$$

where $\mathbf{I}_{p\times p}$ denotes the $p\times p$ identity matrix, $\mathbf{0}_{a\times b}$ an $a\times b$ matrix of zeros and $\mathbf{A}'_k(\mathbf{p}_k)$, $\mathbf{B}'_k(\mathbf{p}_k)$, $\mathbf{G}'_k(\mathbf{p}_k)$ the extended state transition matrices.

Assuming that the unknown parameters are not directly observable, the measurement equation can be written as

$$\mathbf{z}_k = \begin{bmatrix} \mathbf{C}_k(\mathbf{p}_k) & \mathbf{0}_{m\times p} \end{bmatrix} \begin{bmatrix} \mathbf{x}_k \\ \mathbf{p}_k \end{bmatrix} + \mathbf{v}_k \tag{6.17c}$$

Eq. (6.17) can be rewritten in compact form as

$$\mathbf{x}'_{k+1} = f(\mathbf{x}'_k, \mathbf{u}_k, \mathbf{w}'_k) \tag{6.18a}$$

$$\mathbf{z}_k = h(\mathbf{x}'_k) + \mathbf{v}_k \tag{6.18b}$$

where $\mathbf{w}'_k = [\mathbf{w}_k, \mathbf{w}_{p,k}]^T$ is the augmented noise vector and where $f(\cdot)$ and $h(\cdot)$ denote the vectorial nonlinear system and measurement functions, respectively, depending on the extended state vector $\mathbf{x}'_k$ to be identified. Thus, the identification problem can now be solved by any nonlinear filter which is run on the extended model in order to obtain an estimate of the augmented state vector, i.e. of the system's states as well as of the unknown parameters [Simon 2006, p. 422-423].

In case of weak nonlinearities the identification problem is solved using the EKF which linearizes about the current mean and covariance by applying a first order Taylor expansion of the Eqs. (6.18) near the current state $\mathbf{x}'_k = \hat{\mathbf{x}}'_k$ estimate and $\mathbf{w}'_k = \hat{\mathbf{w}}'_k$. Assuming a zero-mean process noise and thus $\hat{\mathbf{w}}'_k = \mathbf{0}$, the linearized system equation is given by

$$\mathbf{x}'_{k+1} \approx f(\hat{\mathbf{x}}'_k, \hat{\mathbf{u}}_k, \mathbf{0}) + \mathbf{A}'_{k,L}(\mathbf{x}'_k - \hat{\mathbf{x}}'_k) + \mathbf{B}'_{k,L}(\mathbf{u}_k - \hat{\mathbf{u}}_k) + \mathbf{G}'_{k,L}\mathbf{w}'_k \tag{6.19a}$$

where the extended and linearized matrices $\mathbf{A}'_{k,L}$, $\mathbf{B}'_{k,L}$, $\mathbf{G}'_{k,L}$ are given by the partial derivative matrices

$$\begin{aligned} \mathbf{A}'_{k,L} &= \left.\frac{\partial f}{\partial \mathbf{x}'_k}\right|_{\mathbf{x}'_k=\hat{\mathbf{x}}'_k} = \begin{bmatrix} \mathbf{A}_k(\mathbf{p}_k) & \left.\frac{\partial \mathbf{x}_k}{\partial \mathbf{p}_k}\right|_{\mathbf{p}_k=\hat{\mathbf{p}}_k} \\ \mathbf{0}_{p\times n} & \mathbf{I}_{p\times p} \end{bmatrix}; \qquad \mathbf{B}'_{k,L} = \left.\frac{\partial f}{\partial \mathbf{u}_k}\right|_{\mathbf{u}_k=\hat{\mathbf{u}}_k} = \begin{bmatrix} \mathbf{B}_k(\mathbf{p}_k) \\ \mathbf{0}_{p\times u} \end{bmatrix} \\ \mathbf{G}'_{k,L} &= \left.\frac{\partial f}{\partial \mathbf{w}'_k}\right|_{\mathbf{w}'_k=\mathbf{0}} = \begin{bmatrix} \mathbf{G}_k(\mathbf{p}_k) & \left.\frac{\partial \mathbf{x}_k}{\partial \mathbf{w}_{p,k}}\right|_{\mathbf{w}_{p,k}=\mathbf{0}} \\ \mathbf{0}_{p\times n} & \mathbf{I}_{p\times p} \end{bmatrix} \end{aligned} \tag{6.19b}$$

It must be noted that the non-diagonal elements of the system matrices $\mathbf{A}'_{k,L}$, $\mathbf{B}'_{k,L}$, $\mathbf{G}'_{k,L}$ relate the parameters $\mathbf{p}_k$ to the system states and thus describe how a change in the parameters effects the dynamics of the system. Consequently, an update of the Kalman state estimates leads to a simultaneous correction of the parameter estimates.

Taking the expectation of Eq. (6.19a) conditional on the measurements up to time k, yields

the approximated prior state estimate in the form

$$\begin{aligned} E[\mathbf{x}'_{k+1}|\mathbf{Z}_k] &\approx f(\hat{\mathbf{x}}'_k, \hat{\mathbf{u}}_k, \mathbf{0}) + \mathbf{A}'_{k,L} E[\mathbf{e}_{x,k}|\mathbf{Z}_k] + \mathbf{B}'_{k,L} E[\mathbf{e}_{u,k}|\mathbf{Z}_k] \\ \hat{\mathbf{x}}'_{k+1|k} &\approx f(\hat{\mathbf{x}}'_k, \hat{\mathbf{u}}_k, \mathbf{0}) \end{aligned} \tag{6.20a}$$

where $\mathbf{e}_{x,k} = \mathbf{x}'_k - \hat{\mathbf{x}}'_{k|k}$ and $\mathbf{e}_{u,k} = \mathbf{u}'_k - \hat{\mathbf{u}}_k$ denote the discrepancies between the true and estimated values. The last equality is based on the assumption that the Kalman estimate of the previous time step is unbiased so that the conditional expectation of the estimation errors vanish. Using Eq. (6.19), the prior prediction error and resulting prior error covariance matrix can be written as

$$\mathbf{e}_{x,k+1|k} = \mathbf{x}'_{k+1} - \hat{\mathbf{x}}'_{k+1|k} \approx \mathbf{A}'_{k,L}(\mathbf{x}'_k - \hat{\mathbf{x}}'_k) + \mathbf{B}'_{k,L}(\mathbf{u}_k - \hat{\mathbf{u}}_k) + \mathbf{G}'_{k,L}\mathbf{w}'_k \tag{6.20b}$$

$$\boldsymbol{\Sigma}'_{xx,k+1|k} = \mathbf{A}'_{k,L}\boldsymbol{\Sigma}'_{xx,k|k}\mathbf{A}'^{T}_{k,L} + \mathbf{B}'_{k,L}\boldsymbol{\Sigma}_{uu,k}\mathbf{B}'^{T}_{k,L} + \mathbf{G}'_{k,L}\mathbf{Q}'_k\mathbf{G}'^{T}_{k,L} \tag{6.20c}$$

The prediction is then used to linearize the measurement equation with respect to $\mathbf{x}_{k+1} = \hat{\mathbf{x}}_{k+1|k}$ and $\mathbf{v}_{k+1} = \mathbf{0}$ in order to keep the zero-mean of the measurement noise. The linearized measurement equation can then be written as

$$\mathbf{z}_{k+1} \approx h(\hat{\mathbf{x}}'_{k+1|k}) + \mathbf{C}'_{k,L}(\mathbf{x}'_{k+1} - \hat{\mathbf{x}}'_{k+1|k}) + \mathbf{v}_k \tag{6.21a}$$

where the extended measurement matrix is given by the partial derivative matrix

$$\mathbf{C}'_{k,L} = \left.\frac{\partial h}{\partial \mathbf{x}'_{k+1}}\right|_{\mathbf{x}'_{k+1}=\hat{\mathbf{x}}'_{k+1|k}} = \begin{bmatrix} \mathbf{C}_k & \left.\frac{\partial h}{\partial \mathbf{p}_{k+1}}\right|_{\mathbf{p}_{k+1}=\hat{\mathbf{p}}_{k+1|k}} \end{bmatrix} \tag{6.21b}$$

For the correction step, the innovation $\mathbf{d}_{k+1|k} = \mathbf{z}_{k+1} - h(\hat{\mathbf{x}}'_{k+1|k})$ between the actual measurement and the predicted measurement must be calculated. Based on the measurement model, the likeliest measurement results from the conditional expectation and is of form

$$\begin{aligned} E[\mathbf{z}_{k+1}|\mathbf{Z}_{k+1|k}] &\approx h(\hat{\mathbf{x}}'_{k+1|k}) + \mathbf{C}'_{k,L} E[\mathbf{e}_{x,k}|\mathbf{Z}_{k+1}] \\ \hat{\mathbf{z}}_{k+1} &\approx h(\hat{\mathbf{x}}'_{k+1|k}) \end{aligned} \tag{6.22}$$

As in the linear case, the optimal estimate results from a linear combination of the prior estimate and the measured response, and is given by

$$\hat{\mathbf{x}}'_{k+1|k+1} = \hat{\mathbf{x}}'_{k+1|k} + \mathbf{K}_{k+1}\left(\mathbf{z}_{k+1} - h(\hat{\mathbf{x}}'_{k+1|k})\right) \tag{6.26a}$$

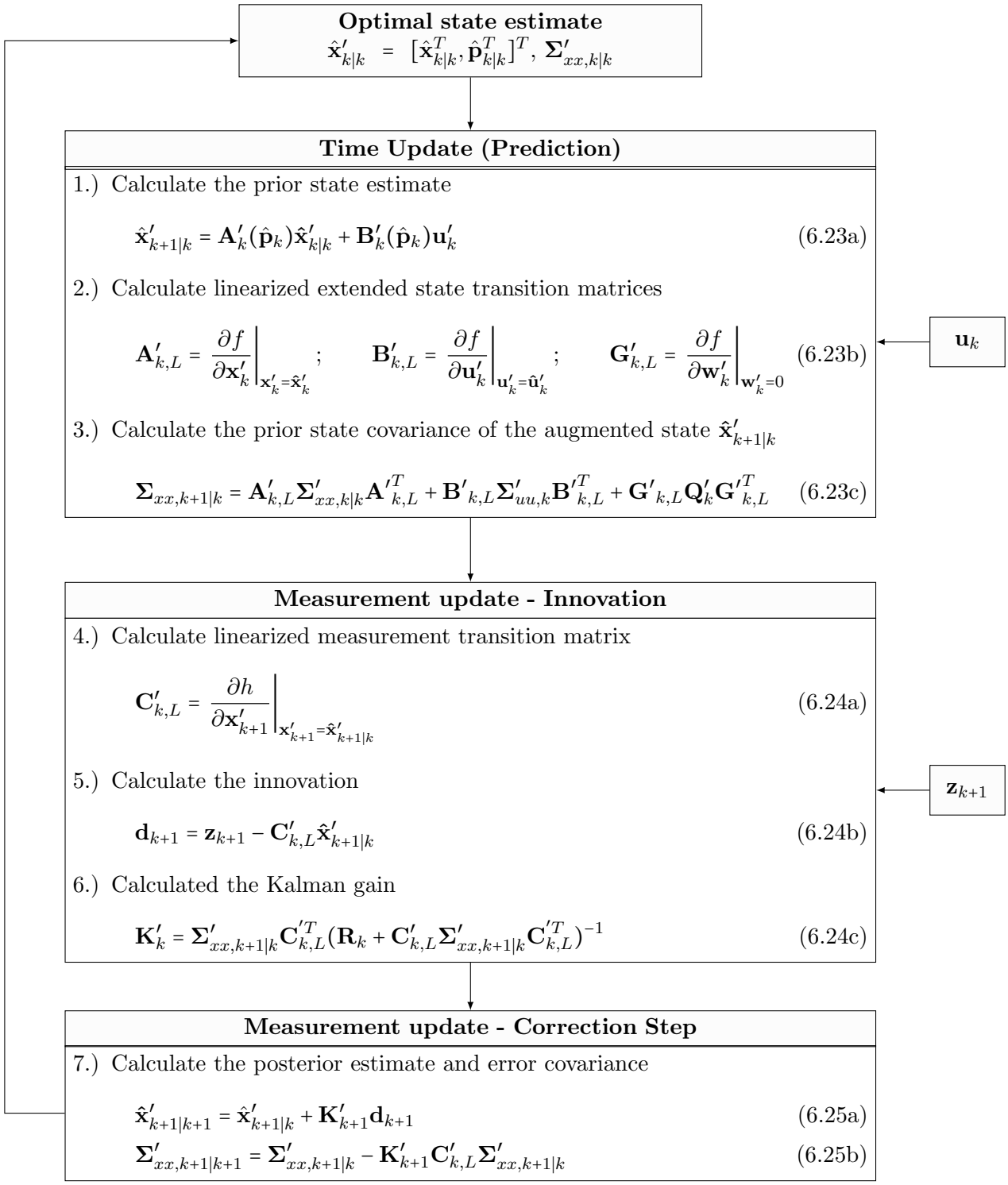

Figure 6.4: Extended Kalman filter algorithm

The corresponding posterior error covariance

$$\mathbf{\Sigma}_{xx,k+1|k+1} = \mathbf{\Sigma}'_{xx,k+1|k} - \mathbf{K}_{k+1}\mathbf{C}'_{k,L}\mathbf{\Sigma}'_{xx,k+1|k} \tag{6.26b}$$

and the Kalman gain matrix

$$\mathbf{K}_{k+1} = \mathbf{\Sigma}'_{xx,k+1|k}\mathbf{C}'^{T}_{k,L}(\mathbf{R}_k + \mathbf{C}'_{k,L}\mathbf{\Sigma}'_{xx,k+1|k}\mathbf{C}'^{T}_{k,L})^{-1} \tag{6.26c}$$

are calculated based on the linearized model following the steps summarized in Fig. 6.4.

Comparing the procedure with the linear KF algorithm depicted in Fig. 6.2, it is evident that the general structure is kept, but that the linearizion with respect to the actual state estimate requires the recalculation of the transition matrices at each iteration step. Furthermore, it must be stressed, that in contrast to the linear problem the estimate given by the extended Kalman filter is biased as in the nonlinear case the assumption

$$E[f(\hat{\mathbf{x}}_{k|k})] = f\left(E[\hat{\mathbf{x}}_{k|k}]\right) \tag{6.27}$$

is violated and thus the obtained estimate does not coincide with the mean value of the posterior distribution. That is in the presence of nonlinearities, the approximates of posterior distribution as Gaussian is not always justified and leads to poor results if the true posterior distribution is for instance heavily tailed or multi-modal [Chen 2003].
Having derived the linearized model, the next step is the initialization of the filter equation which will be discussed in the next section.

6.1.3.2 Initialization of the Kalman filter algorithm

Before the Kalman filter can be run on the linearized model, the prior error covariance $\mathbf{\Sigma}_{xx,0}$ for $k = 0$ as well as the process and measurement noise covariances $\mathbf{Q}_k$ and $\mathbf{R}_k$, respectively, for $k \geq 0$ must be chosen. Rewriting Eq. (6.5) of the optimal state estimate for a single-input-single-output system, i.e.

$$\begin{aligned}\hat{x}_{k+1|k+1} &= \hat{x}_{k+1|k} + K_{k+1}(z_{k+1} - \hat{x}_{k+1|k}) \\ \sigma^2_{xx,k+1|k+1} &= \sigma^2_{xx,k+1|k} - K_{k+1}\sigma^2_{xx,k+1|k}\end{aligned} \tag{6.28}$$

where

$$K_{k+1} = \frac{\sigma^2_{xx,k+1|k}}{R_k + \sigma^2_{xx,k+1|k}} \qquad \text{with} \qquad \sigma^2_{xx,k+1|k} = A_k^2\sigma^2_{xx,k+1|k} + G_k^2 Q_k$$

it becomes obvious that the update of the posterior state estimate $\hat{x}_{k+1|k+1}$ and associated error covariance $\sigma^2_{xx,k+1|k+1}$ strongly depends on the choice of these parameters. This depen-

dency shall be investigated further by considering two limiting cases: First, assume that the measurement noise R_k approaches zero. Pursuant to Eq. (6.28) the Kalman gain weights the residual more heavily and in the limit, i.e. $K_{k+1} \to 1$, the optimal state estimate is given by

$$\lim_{R_k \to 0} \hat{x}_{k+1|k+1} = z_{k+1} \tag{6.29a}$$

That is, the prior estimate $\hat{x}_{k+1|k}$ derived from the system model is completely ignored and the new measurement denotes the optimal estimate. Secondly, assume that the measurement noise $R_k \to \infty$ or equivalently, the prior error covariance and the process noise vanish, i.e. $\sigma^2_{xx,k+1|k}$, $Q_k \to 0$, then in the limit, the Kalman gain approaches zero and Eq. (6.28) yields

$$\lim_{\sigma^2_{xx,k+1|k} \to 0} \hat{x}_{k+1|k+1} = \lim_{R_k \to \infty} \hat{x}_{k+1|k+1} = \hat{x}_{k+1|k} \tag{6.29b}$$

This implies that little confidence is put in a very noisy measurement and in the limit would be completely ignored [Maybeck 1979, p. 14-15].
Assume now the case, that the measurement noise covariance is time-invariant, i.e. $R_k = R$, the process noise $Q_k = 0$ and the initial error covariance $\sigma^2_{xx,0} > 0$. Then at each time step the posterior error covariance $\sigma^2_{xx,k+1|k+1}$ in Eq. (6.28) decreases by $K_{k+1}\sigma^2_{xx,k+1|k+1}$. If $\sigma^2_{xx,k+1|k+1} \to 0$, the filter will reach a steady solution where, pursuant to Eq. (6.29b), any new measurement will be ignored. Similarly, in case that the process noise is time-invariant, i.e. $Q_k = Q$ and $Q > 0$, the error covariance and thus the Kalman gain will decrease at each time step until it converges to a constant value.
Throughout the thesis, the process noise models the unmeasured load process and thus its variance is related to the intensity of the excitation. The measurement accuracy is in general dependent on the measurement range of the used sensor. Thus, in the numerical examples discussed in the following, the statistics of the measurement noise are assumed to be known and time-invariant. From the above discussion it can be concluded, that a larger prior error covariance makes the filter more sensitive to the incoming measurement and thus is favorable in order to accelerate the filter convergence. This was also observed by [Hoshiya and Saito 1984] who proposed a weighted iterated extended Kalman filter, denoted as W-EKF, which will be discussed in the following section.

6.1.3.3 The weighted extended Kalman filter algorithm (W-EKF)

[Hoshiya and Saito 1984] investigated the stability and convergence of the EKF with respect to the initial conditions and introduced a weighted global iteration procedure into the Kalman

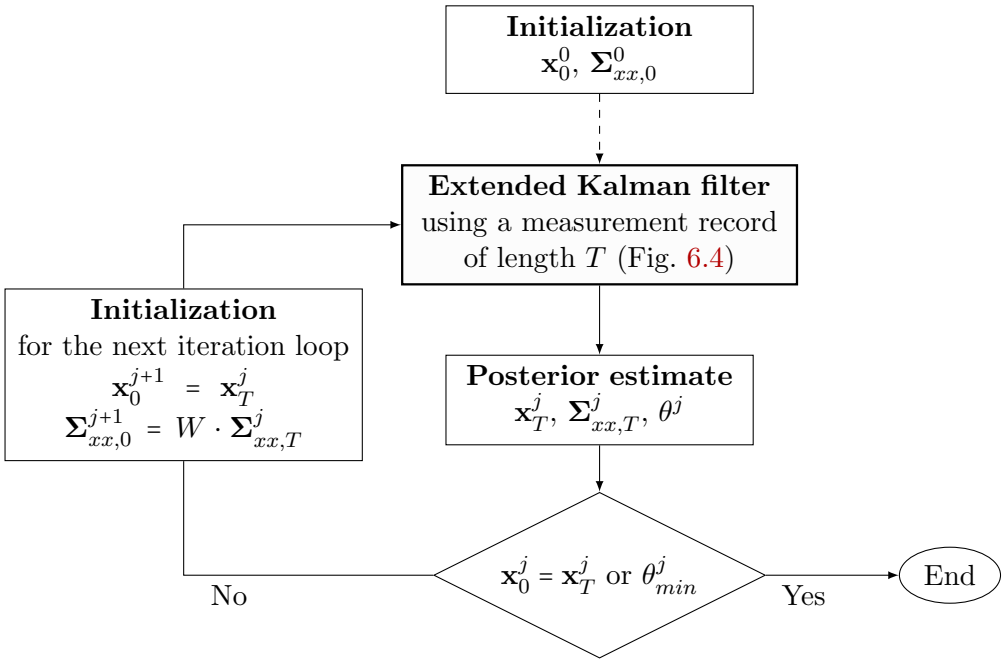

Figure 6.5: W-EKF algorithm: In each iteration j, the EKF is run using a measurement record of length T. The obtained state estimates $\mathbf{x}_T^j$ are used for the initialization of the next iteration loop. The iteration is aborted either if the cost function θ^j is minimized or the estimates converge.

filter algorithm containing an objective function to estimate the stability. That is, while, the iterative scheme improves the accuracy of the approach, especially if the first guess of the parameters to be identified is poor, the calculation of the objective function allows assessing the accuracy of the filter and avoids the divergence to erroneous identification results [Kijewski and Kareem 2000]. In [Hoshiya and Saito 1984] the method is applied successfully for the parameter identification of a linear multiple degree of freedom system and a bilinear hysteretic system. In [Hoshiya and Maruyama 1987] the problem of a beam excited by a moving load is discussed and the method is used for the identification of both, the weight and velocity of the excitation as well as the parameters of the beam. In [Hoshiya and Sutoh 1993] the method is coupled with the Finite Element Method and applied for the parameter estimation of a non-homogeneous stochastic plane strain field.

The algorithm is illustrated in Fig. 6.5 and can be summarized as follows: First, the Kalman filter is initialized choosing the initial state estimate and associated covariance matrix $\mathbf{x}_0^1$, $\mathbf{\Sigma}_{xx,0}^1$ as well as defining the process noise covariance matrix $\mathbf{Q}_0$. The statistics of the measurement noise $\mathbf{R}_0$ are assumed to be time-invariant and known. Then the EKF is run using a finite measurement record of length T [s] until the estimated parameters converge. They are used for the initialization of the next iteration loop, that is, setting $\mathbf{x}_0^2 = \mathbf{x}_T^1$, $\mathbf{\Sigma}_{xx,0}^2 = W \cdot \mathbf{\Sigma}_{xx,T}^1$ where W denotes a weighting factor. As shown by Eq. (6.29b), the Kalman filter will reach a steady solution after a certain time as the belief in the model

increases with decreasing error covariance. The weighting prevents the filter from ignoring new measurement data and thus accelerates the convergence of the filter. [Hoshiya and Saito 1984] observed that a large initial covariance is favorable in order to accelerate the extended Kalman filter's convergence, but it also might affect the stability of the filter. Thus, an objective function θ^j is suggested which is calculated at the end of each iteration loop j along with the state estimate and error covariance. The iteration is repeated until the prior estimate become essentially constant, that is $\mathbf{x}_0^{j+1} \approx \mathbf{x}_T^j$ or until the objective function θ^j is minimized. The latter is given by

$$\theta^j = \frac{1}{m} \sum_{i=1}^{m} \sum_{k=0}^{N-1} \left(d_{k+1|k+1}^j \right)^2 \tag{6.30a}$$

where $N = T/t_s$ denotes the number of sampling points of the measurement record, m is the dimension of the measurement vector and $d_{i,k+1|k+1}^j$ describes the ith component of the posterior residual

$$\mathbf{d}_{k+1|k+1}^j = \mathbf{z}_{k+1} - \mathbf{C}\hat{\mathbf{x}}_{k+1|k+1}^j \tag{6.30b}$$

Here, it must be noted that, in contrast to the previous defined innovation process (compare Eq. (6.13a)), the posterior estimate $\hat{\mathbf{x}}_{k+1|k+1}$ is used for the calculation of the residual in order to obtain an estimate of the filter accuracy. The objective function gives the average of all prediction square errors and thus θ_{min}^j indicates that the global error between each observation and corresponding estimate becomes totally minimum [Hoshiya and Saito 1984]. [Hoshiya and Saito 1984] show that the choice of W influences mainly the rate of convergence as well as the identification result. The optimal value is found by comparing the minimum global values θ_{min}^j and the number of needed iterations for different choices of W.

6.1.4 Application to a three story shear building

In order to verify the method, the W-EKF algorithm is now used for the identification of the stiffness and damping parameters characterizing the dynamic behavior of a three story shear building excited at the top floor by a white noise process. Assuming that i) the total mass of the structure is concentrated at the floor levels, ii) the columns are axially rigid and the floor beams are infinitely rigid as compared to the columns, iii) the interstory stiffness is distributed constantly over the stories, iv) the deflection of the structure is independent of the axial forces in the columns and v) the structure can be modeled as lumped three degrees of freedom (DOF) system, corresponding to the horizontal displacements at the floor levels

as depicted in Fig. 6.6.
The system's dynamics of the three story building subjected to a white noise excitation are given by the second order stochastic differential equation

$$\mathbf{M}\ddot{\mathbf{y}}(t) + \mathbf{C}\dot{\mathbf{y}}(t) + \mathbf{K}\mathbf{y}(t) = \mathbf{G}w(t) \tag{6.31a}$$

where $\mathbf{M}$, $\mathbf{K}$ and $\mathbf{C}$ are the time-invariant mass, stiffness and damping matrices, respectively, given by

$$\mathbf{M} = \begin{bmatrix} m_1 & 0 & 0 \\ 0 & m_2 & 0 \\ 0 & 0 & m_3 \end{bmatrix}; \quad \mathbf{K} = \begin{bmatrix} k_1 + k_2 & -k_2 & 0 \\ -k_2 & k_2 + k_3 & -k_3 \\ 0 & -k_3 & k_3 \end{bmatrix}; \quad \mathbf{C} = \begin{bmatrix} c_1 + c_2 & -c_2 & 0 \\ -c_2 & c_2 + c_3 & -c_3 \\ 0 & -c_3 & c_3 \end{bmatrix} \tag{6.31b}$$

and where $\mathbf{y}(t)$, $\dot{\mathbf{y}}(t)$ and $\ddot{\mathbf{y}}(t)$ denote the vectors of the horizontal displacements, velocities and accelerations of the floor levels and $w(t)$ is the zero mean Gaussian white noise process describing the unmeasured load at the top level of the system. The state vectors and the load transition matrix $\mathbf{G}$ are given by

$$\mathbf{y}(t) = \begin{bmatrix} y_1(t) \\ y_2(t) \\ y_3(t) \end{bmatrix}; \quad \dot{\mathbf{y}}(t) = \begin{bmatrix} \dot{y}_1(t) \\ \dot{y}_2(t) \\ \dot{y}_3(t) \end{bmatrix}; \quad \ddot{\mathbf{y}}(t) = \begin{bmatrix} \ddot{y}_1(t) \\ \ddot{y}_2(t) \\ \ddot{y}_3(t) \end{bmatrix}; \quad \mathbf{G} = \begin{bmatrix} 1 \\ 0 \\ 0 \end{bmatrix} \tag{6.31c}$$

Furthermore, the structural damping is assumed to be of Rayleigh type, a form of viscous damping, which allows expressing the damping matrix as linear combination of the mass and/or stiffness coefficients, i.e. it holds

$$\mathbf{C} = a\mathbf{M} + b\mathbf{K} \tag{6.32a}$$

The coefficients are real valued and determined by choosing the modal damping ratios D_j, D_k (where $D_j = c_j/(2m_j\omega_j) = c_j/c_{crit}$) for two modes and solving the relation

$$a = \frac{\omega_j\omega_k(\omega_j D_k - \omega_k D_j)}{\omega_j^2 - \omega_k^2}; \qquad b = \frac{\omega_j D_j - \omega_k D_k}{\omega_j^2 - \omega_k^2} \tag{6.32b}$$

The damping in the remaining modes follows then immediately from Eq. (6.32a). Due to the mass and stiffness proportionality, the Rayleigh model ensures that the eigenvalues of the damped system remain real and allows the decoupling of the system equation by the modeshapes of the undamped system.

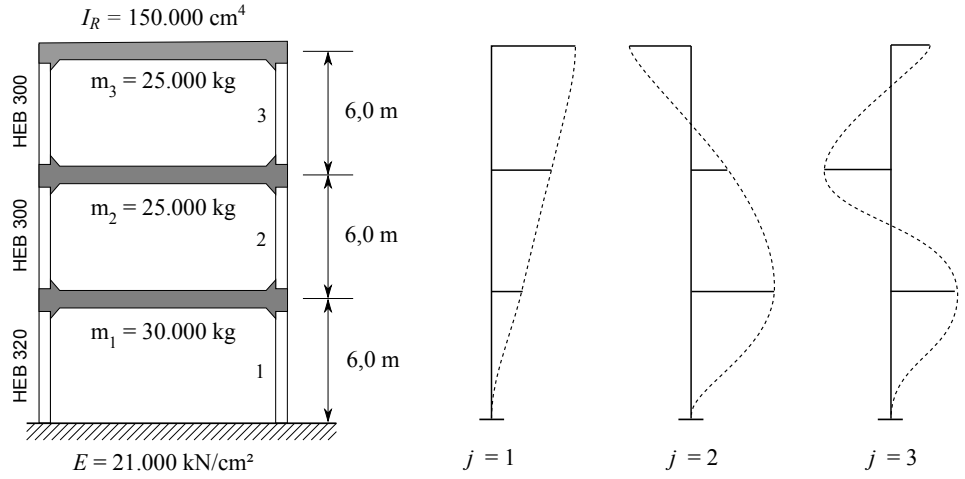

(a) Idealized model **(b)** Eigenmodes

Figure 6.6: Three-story shear building [Petersen 2000, p. 676]

Thus, the classical modal analysis procedure can be used to analyze damped systems in a similar manner. By pre- and postmultiplying the damping matrix by the jth modeshape, and using the relation $D_j = c_j/(2m_j\omega_j)$, the corresponding damping ratio satisfies

$$D_j = \frac{1}{2\omega_j}a + \frac{\omega_j}{2}b \tag{6.32c}$$

Assuming a uniform column whose ends are fixed against rotation, the theoretical stiffness constant is given by

$$k = 2 \cdot \frac{12EI}{h^3} \tag{6.33}$$

where E, I, h denote the Young's Modulus, the second moment of area and and length of the column and where the factor two considers the fact, that there are two columns per story. For the columns of the first story a HEB 320 profile and for the upper to levels a HEB 300 profile are chosen. This leads to the following model parameters

$$\begin{aligned}
&E = 21.000\ [\mathrm{kN/cm^2}] \\
&I_1 = 30820\ [\mathrm{cm^4}]\ (\text{HEB 320});\ I_2 = I_3 = 25170\ [\mathrm{cm^4}]\ (\text{HEB 300}) \\
&h_1 = h_2 = h_3 = 6\ [\mathrm{m}] \\
&m_1 = 30000\ [\mathrm{kg}];\ m_2 = m_3 = 25000\ [\mathrm{kg}]
\end{aligned} \tag{6.34a}$$

damping estimates			stiffness estimates		
$\lvert\hat{c}_{i,0} - c_i\rvert/c_i$			$\lvert\hat{k}_{i,0} - k_i\rvert/k_i$		
$\hat{c}_{1,0}$	$\hat{c}_{2,0}$	$\hat{c}_{3,0}$	$\hat{k}_{1,0}$	$\hat{k}_{2,0}$	$\hat{k}_{3,0}$
37%	30%	37%	30%	20%	30%

Table 6.1: Prior relative estimation error used for the initialization of the Extended Kalman filter at $k = 0$

Using Eq. (6.32a) and Eq. (6.33) the stiffness and damping parameters of the ideal model are given by

$$\begin{aligned}
&\hat{k}_1 = 7.191.333 \text{ [N/m]}; \; \hat{k}_2 = \hat{k}_3 = 5.873.000 \text{ [N/m]} \\
&\hat{D}_1 = 0.03; \; \hat{D}_3 = 0.07 \text{ (i.e. } \hat{a} = 0.1775, \; \hat{b} = 0.0049) \\
&\hat{c}_1 = 40.736 \text{ [Ns/m]} \\
&\hat{c}_2 = 28.919 \text{ [Ns/m]} \\
&\hat{c}_3 = 33.357 \text{ [Ns/m]}
\end{aligned} \tag{6.34b}$$

They are used as prior estimates needed for the initialization of the EKF. The system's parameters of the structure differ from the assumed model parameters. They are set to

$$\begin{aligned}
&k_1 = 0.7 \, \hat{k}_1 = 5.033.933 \text{ [N/m]} \\
&k_2 = 0.8 \, \hat{k}_2 = 4.698.400 \text{ [N/m]} \\
&k_3 = 0.7 \, \hat{k}_3 = 4.111.100 \text{ [N/m]} \\
&D_1 = 0.03; \; D_3 = 0.06 \text{ (i.e. } a = 0.1886, \; b = 0.0047) \\
&c_1 = 29.656 \text{ [Ns/m]} \\
&c_2 = 22.397 \text{ [Ns/m]} \\
&c_3 = 24.313 \text{ [Ns/m]}
\end{aligned} \tag{6.34c}$$

leading to a prior relative estimation error of 20 %-30 % in case of the stiffness estimates and of about 30 %-40 % in case of the damping estimates as summarized in Tab. 6.1. The system is assumed to be excited at the top story level by a zero mean Gaussian white noise process with standard deviation

$$\sigma_w = 2000 \text{ [N]} \tag{6.34d}$$

Defining the state vector as $\mathbf{x}(t) = [\mathbf{y}^T(t), \dot{\mathbf{y}}^T(t)]^T$, the second order differential equation

(6.31) can be easily written in state space form as

$$\dot{\mathbf{x}}(t) = \mathbf{A}_c\mathbf{x}(t) + \mathbf{G}_c w(t) \tag{6.35a}$$

where the system matrices are given by

$$\mathbf{A}_c = \begin{bmatrix} \mathbf{0}_{3\times3} & \mathbf{I}_{3\times3} \\ -\mathbf{M}^{-1}\mathbf{K} & -\mathbf{M}^{-1}\mathbf{C} \end{bmatrix}; \qquad \mathbf{G}_c = \begin{bmatrix} \mathbf{0}_{3\times3} \\ \mathbf{M}^{-1}\mathbf{G} \end{bmatrix} \tag{6.35b}$$

In order to apply the Kalman filter to the identification problem, the unknown parameters $\mathbf{p}(t) = [k_1, k_2, k_3, c_1, c_2, c_3]$ are included in the state vector. If the parameters are time-invariant, then they can be modeled as random walk process, which is expressed in the continuous case as random bias plus noise [Maybeck 1982, p. 51]

$$\dot{\mathbf{p}}(t) = \mathbf{w}_p(t) \tag{6.36a}$$

$\mathbf{w}_p(t) \sim N(\mathbf{0},\mathbf{Q}_{p,c})$ is a small artificial Gaussian white noise term that allows the Kalman filter changing its estimate of $\mathbf{p}(t)$. Using the augmented state vector $\mathbf{x}'(t) = [\mathbf{x}^T(t),\mathbf{p}^T(t)]^T$, the resulting state space model is defined as

$$\dot{\mathbf{x}}'(t) = \mathbf{A}'_c(\mathbf{p})\mathbf{x}'(t) + \mathbf{G}'_c\mathbf{w}'(t) = f\left(\mathbf{x}'(t),\mathbf{w}'(t)\right) \tag{6.36b}$$

where $\mathbf{w}'(t) = [\mathbf{w}^T(t),\mathbf{w}_p^T(t)]^T$ denote the augmented noise vector and where the extended system matrices are given by

$$\mathbf{A}'_c(\mathbf{p}) = \begin{bmatrix} \mathbf{0}_{6\times6} & \mathbf{I}_{6\times6} & \mathbf{0}_{6\times6} \\ -\mathbf{M}^{-1}\mathbf{K} & -\mathbf{M}^{-1}\mathbf{C} & \mathbf{0}_{6\times6} \\ \mathbf{0}_{6\times6} & \mathbf{0}_{6\times6} & \mathbf{0}_{6\times6} \end{bmatrix}; \qquad \mathbf{G}'_c = \begin{bmatrix} \mathbf{0}_{3\times1} & \mathbf{0}_{3\times6} \\ \mathbf{M}^{-1}\mathbf{G} & \mathbf{0}_{3\times6} \\ \mathbf{0}_{3\times1} & \mathbf{I}_{6\times6} \end{bmatrix} \tag{6.36c}$$

The state transition matrix $\mathbf{A}_c(\mathbf{p}_k)$ in the system equation depends nonlinearly on the unknown parameters in the state vector. In order to apply the discrete Kalman filter the system needs to be linearized as well as discretized. There are two alternative orders in performing these operations, that is either to first linearize the model with respect to the previously state estimate and then to discretize the resulting linear model, or, conversely, to first discretize the model and then to linearize the discrete model around the previous estimated state. The former procedure is denoted *discretized linearization* while the other is also known as *linearized discretization* [Gustafsson and Isaksson 1996].
Here the former approach will be used as the discrete state transition matrix calculated by the matrix exponential function $\mathbf{A}_d = e^{\mathbf{A}_c t_s}$ (compare Eqs. (4.26)), in general, cannot be de-

rived in closed form. In contrast the linearization of the time continuous model in Eq. (6.36b) can be derived analytically in many cases and thus the discretization can then be calculated numerically when the filter is implemented (here MATLAB is used). That is, the discretized linearization requires the following steps: i) Calculate analytically the linearized transition matrices $\mathbf{A}'_{c,L}(\mathbf{p})$, $\mathbf{G}'_{c,L}(\mathbf{p})$ of the continuous state space model by the partial matrix differentials given in the annexe (C.13-C.14) and implement the obtained functions in MATLAB; ii) At each time step, update these matrices by the new parameter estimates $\mathbf{p}_k$; iii) The discretized and linearized transition and covariance matrix $\mathbf{A}'_{d,L}(\mathbf{p}_k)$, $\mathbf{Q}'_d(\mathbf{p}_k)$ is calculated numerically at each time step by means of the matrix exponential operator following the steps summarized in (4.26).

It is assumed that the displacements as well the velocities of all three story levels are measured. Thus, the observation transition matrix which relates the states to the measurements consists of zeros and ones in order to collect the measured states from the state vector, i.e. it is independent of the parameters to be estimated. The resulting augmented observation model is given by

$$\mathbf{z}_{k+1} = \mathbf{C}'_d\mathbf{x}'_k + \mathbf{v}_k; \qquad \text{where} \quad \mathbf{C}'_d = \begin{bmatrix}\mathbf{I}_{6\times6} & \mathbf{0}_{6\times6}\end{bmatrix}, \quad \mathbf{v}_k \sim \mathrm{WN}(\mathbf{0},\mathbf{R_d}) \tag{6.37}$$

Initialization of the W-EKF

In the following it is assumed that the statistics of the load process are known and the process noise level corresponding to the variance of the load process is set to $\sigma_w = 2000$ [N] as defined in (6.34d). Besides, the filter is initialized using the following parameterizations:

$$\begin{aligned}
\hat{\mathbf{y}}_0 &= [-0.02, 0.03, 0.01]^T \text{ [m]}, \ \sigma_{y,0} = 1 \text{ [m]}, \\
\hat{\dot{\mathbf{y}}}_0 &= [-0.1, 0.5, 0.2]^T \text{ [m/s]}, \ \sigma_{\dot{y},0} = \sqrt{5} \text{ [m/s]} \\
\hat{\mathbf{p}}_0 &= [7.19\times10^6,\ 5.87\times10^6,\ 5.87\times10^6,\ 0.03,\ 0.07] \text{ see 6.34b} \\
\sigma_{k,0} &= \sqrt{10^6}\ldots\sqrt{10^{11}} \text{ [N/m]} \ ; \sigma_{c,0} = \sqrt{10^6}\ldots\sqrt{10^{11}} \text{ [Ns/m]} \ ; \\
\mathbf{R}\delta_{ij} &= 1,\ 10 \text{ and } 100 \text{ [\%] of MS}_i \text{ see Eq. (6.40a)}
\end{aligned} \tag{6.38}$$

The prior estimates of the displacement and velocity vector $\hat{\mathbf{y}}_0$, $\hat{\dot{\mathbf{y}}}_0$ are chosen in agreement with the measurement data $\mathbf{z}_0$. The prior error covariance matrix has diagonal form, and is

given by

$$\boldsymbol{\Sigma}_{xx,0} = \begin{bmatrix} \boldsymbol{\Sigma}_{yy,0} & & \mathbf{0} \\ & \boldsymbol{\Sigma}_{\dot{y}\dot{y},0} & \\ \mathbf{0} & & \boldsymbol{\Sigma}_{pp,0} \end{bmatrix}$$

where

$$\boldsymbol{\Sigma}_{yy,0} = \sigma_{y,0}^2 \mathbf{I}_{3\times3}; \quad \boldsymbol{\Sigma}_{\dot{y}\dot{y},0} = \sigma_{\dot{y},0}^2 \mathbf{I}_{3\times3}; \quad \text{and} \quad \boldsymbol{\Sigma}_{pp,0} = \begin{bmatrix} \sigma_{k,0}^2 \mathbf{I}_{3\times3} & 0 \\ 0 & \sigma_{c,0}^2 \mathbf{I}_{3\times3} \end{bmatrix} \tag{6.39}$$

The chosen variances $\sigma_{y,0}^2$, $\sigma_{\dot{y},0}^2$, $\sigma_{k,0}^2$, $\sigma_{c,0}^2$ are given in Eq. (6.38). Furthermore, the measurement error covariance matrix is assumed to be time-invariant, i.e. $\mathbf{R}_k = \mathbf{R}$. In order to investigate the influence of the choice of the initial error covariance and measurement noise matrix $\boldsymbol{\Sigma}_{xx,0}$, $\mathbf{R}$ on the parameter identification result, different initializations are tested. To be precise, the prior standard deviation of the parameter estimates $\sigma_{k,0}^2$ [(N/m)], $\sigma_{c,0}^2$ [N/s] is varied between $\sqrt{1\times10^6} \ldots \sqrt{1\times10^{11}}$ while the measurement noise covariance matrix is kept constant.

In order to investigate the sensitivity of accuracy of the parameter identification on the measurement noise intensity, three cases corresponding to 1, 10, and 100 [%] of the mean-square of the undisturbed system response (i.e. $\mathbf{R} = \mathbf{0}$) are considered. It is defined as

$$MS_i = \frac{1}{N} \sum_{k=0}^{N-1} \tilde{z}_{i,k}^2 \tag{6.40a}$$

where $\tilde{z}_{i,k}$ denotes the ith component of the undisturbed measurement vector $\tilde{\mathbf{z}}_k = \mathbf{C}\tilde{\mathbf{x}}_k$ of the true states $\tilde{\mathbf{x}}_k$. In all cases, the W-EKF is run iteratively using a measurement record of $T = 500$ [s] length of the story velocities and displacements until the filter converges. As described in section 6.1.3.3 At the begin of jth iteration, the W-EKF is initialized by the previous state estimate and error covariance matrix $\mathbf{x}_{500}^{j-1}$ and $\boldsymbol{\Sigma}_{xx,500}^{j-1}$ multiplied by a weight, W, here set to 1000. In the following section the results of the sensitivity analysis will be discussed.

Results of the sensitivity analysis

In Fig. 6.7, a sequence of the used noisy measurement data, the true, i.e. undisturbed displacement y_3 (Top) and velocity $\dot{y}_3$ (Bottom) as well as the estimation results are depicted exemplarily for the top floor of the three story shear building taking into account a mea-

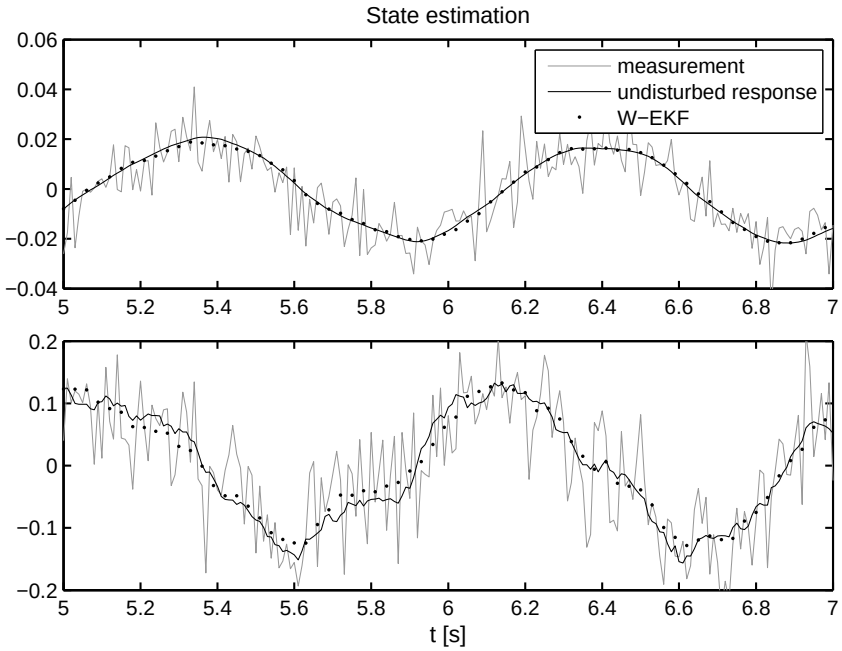

Figure 6.7: Noisy measurement (grey), undisturbed (solid) and estimated displacement (dotted) y_3 [m] (Top) and velocity $\dot{y}_3$ in [m/s] (Bottom) of the top floor of the three story shear building using the W-EKF for 100 % measurement noise and $\sigma_{k,0}$ [N/m], $\sigma_{c,0}$ [Ns/m] of order $\sqrt{10^8}$

surement noise level of 100 % of the mean-square of the undisturbed system response and an initial error covariance $\sigma_{k,0}$ [N/m] and $\sigma_{c,0}$ [Ns/m] of order $\sqrt{1 \times 10^8}$. The quality of the estimation of the observable states can be used as visual indicator of the accuracy of the parameter estimation. E.g. here, the states are estimated with high accuracy, however a close look reveals that the quality of the estimation of the level displacements seems to be slightly more accurate than the estimation of the velocities. Hence, assuming viscous damping, the latter might be an indicator for errors in the damping estimation.

In all cases the W-EKF was iterated 6 times, however, convergence was already obtained after 2-3 iterations as depicted in Figs. 6.8a, 6.9a, 6.10a, setting the measurement noise $\mathbf{R}\delta_{ij} = 1, 10, 100$ [%], respectively. The figures show the identification result of the parameters at the end of each cycle in dependence on the chosen initial error standard deviations $\sigma_{k,0}$ [N/m] and $\sigma_{c,0}$ [Ns/m]. As expected, with increasing covariance, a faster convergence is observed. In order to obtain the optimal estimate, the algorithm is aborted either if the objective function θ^j is minimized and/or if the filter converges. The given identification errors are calculated as relative deviation from the true values, e.g. the relative identification error of the stiffness estimate $\hat{k}_1$ is given by $error = (\hat{k}_1 - k_1)/k_1$ and summarized in Figs. 6.8b, 6.9b and 6.10b. Two errors are compared: the error after convergence corresponds to the estimation error where the filter reaches its steady solution. The second error corresponds to the estimate where the global error θ_{min} in the state estimation is minimized. As highlighted

in bold, the minimum value is obtained after about 2-3 iterations. It must be noted that cases where the objective function reaches its minimum value before the filter converges, could be an indicator for the divergence of the filter. However, it is encouraging to note that in all cases both criteria leads almost to identical estimation results. One can observe, that the objective function θ_{min} tends to greater values with increasing measurement noise leading to the question, which magnitude is reasonable. Rewriting the posterior error in the form

$$\mathbf{d}_{k|k} = \mathbf{z}_k - \mathbf{C}\hat{\mathbf{x}}_{k|k} = \mathbf{C}(\tilde{\mathbf{x}}_k - \hat{\mathbf{x}}_{k|k}) + \mathbf{v}_k \tag{6.41}$$

it is obvious, that in the optimal case, i.e. where the posterior estimate $\hat{\mathbf{x}}_{k|k}$ and the true state $\tilde{\mathbf{x}}_k$ are equal, the posterior error $\mathbf{d}_{k|k}$ corresponds to the measurement noise, i.e. $\mathbf{d}_{k|k} = \mathbf{v}_k$. Thus, in this case, the mean square of the ith element of the posterior error $d_{i,k|k}$, that is

$$\gamma_i = \frac{1}{N}\sum_{k=0}^{N-1} d_{i,k|k}^2 \tag{6.42a}$$

should tend to corresponding element of the measurement error covariance $\mathbf{R}_{ii}$. Taking into account that the measurement error is given with respect to the mean square value of the undisturbed system response given in Eq. (6.40a), here the normalized square errors

$$\gamma_i^N = \frac{\sum_{k=0}^{N-1} d_{i,k|k}^2}{\sum_{k=0}^{N-1} \tilde{z}_{i,k}^2} \tag{6.42b}$$

should agree with the measurement noise intensities of 1, 10 and 100 [%], respectively. Thus, the same must be true for the normalized objective function

$$\theta_{min}^N = \frac{1}{m}\sum_{i=1}^{m} \gamma_i^N \tag{6.42c}$$

which gives the mean square value of the trace of the measurement noise. Of course, in reality the undisturbed system response $\tilde{\mathbf{z}}_k = \mathbf{C}\tilde{\mathbf{x}}_k$ is unknown as just the noisy data $\mathbf{z}_k = \mathbf{C}\tilde{\mathbf{x}}_k + \mathbf{v}_k$ is available. However, in the optimal case, i.e. if $\hat{\mathbf{x}}_{k|k} \approx \tilde{\mathbf{x}}_{k|k}$ and thus $\mathbf{d}_{k|k} \approx \mathbf{v}_k$, then the relations (6.42b) and (6.42c) can be expressed in terms of the noisy measurement data, yielding

$$\hat{\gamma}_i^N = \frac{\sum_{k=0}^{N-1} d_{i,k|k}^2}{\sum_{k=0}^{N-1} (\tilde{z}_{i,k} + v_{i,k})^2} = \frac{\sum_{k=0}^{N-1} d_{i,k}^2}{\sum_{k=0}^{N-1} \tilde{z}_{i,k}^2 + \sum_{k=0}^{N-1} v_{i,k}^2 + \underbrace{\sum_{k=0}^{N-1} \tilde{z}_{i,k} v_{i,k}}_{\approx 0}} \approx \frac{1}{(\gamma_i^N)^{-1} + 1} \tag{6.43a}$$

$$\hat{\theta}_{min}^N = \frac{1}{m}\sum_{i=1}^{m} \hat{\gamma}_i^N \tag{6.43b}$$

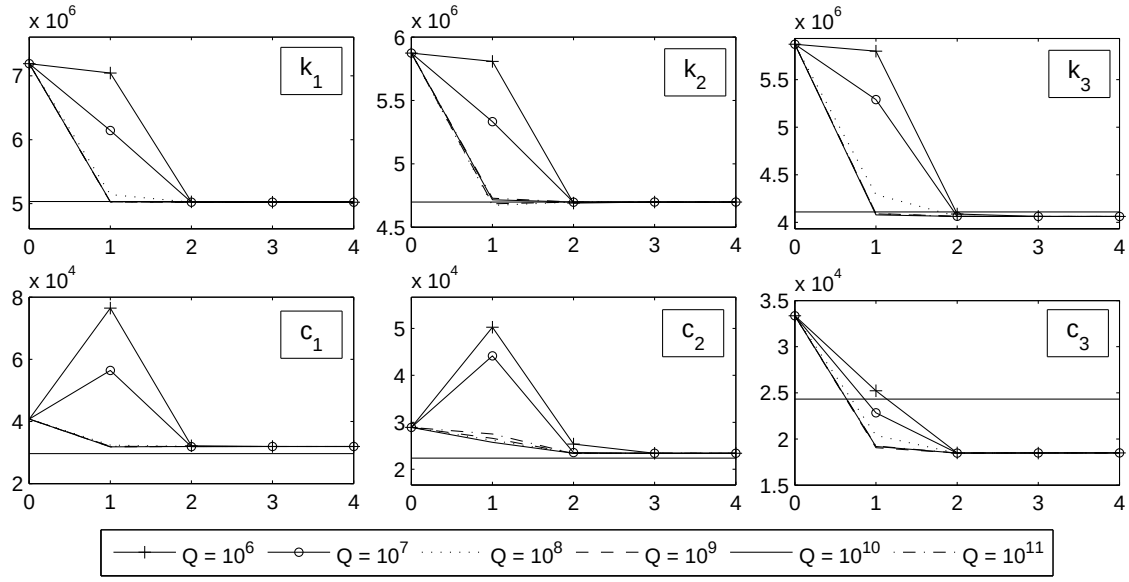

(a) Identification results (where $Q = \sigma^2_{k,0}, \sigma^2_{c,0}$)

$\mathbf{R}\delta_{ik} = 0.01\mathrm{MS}_i$ and $\sigma^2_{k,0}, \sigma^2_{c,0} = 1\times10^6 \ldots 1\times10^{11}$							
$\hat{\mathbf{p}}_{500}$	error in [%]	1×10^6	1×10^7	1×10^8	1×10^9	1×10^{10}	1×10^{11}
$\hat{k}_1$	after convergence	-0.226	-0.226	-0.226	-0.226	-0.226	-0.226
	for θ_{min}	-0.225	-0.226	-0.225	-0.224	-0.224	-0.226
$\hat{k}_2$	after convergence	-0.014	-0.014	-0.014	-0.014	-0.014	-0.014
	for θ_{min}	-0.009	-0.014	-0.014	-0.006	-0.007	-0.014
$\hat{k}_3$	after convergence	-1.173	-1.173	-1.173	-1.173	-1.173	-1.173
	for θ_{min}	-1.172	-1.173	-1.172	-1.171	-1.171	-1.173
$\hat{c}_1$	after convergence	7.592	7.592	7.592	7.592	7.592	7.592
	for θ_{min}	7.607	7.593	7.631	7.619	7.608	7.592
$\hat{c}_2$	after convergence	4.528	4.528	4.528	4.528	4.528	4.528
	for θ_{min}	4.506	4.526	4.430	4.497	4.496	4.527
$\hat{c}_3$	after convergence	-23.960	-23.960	-23.960	-23.960	-23.960	-23.960
	for θ_{min}	-23.996	-23.963	-24.077	-24.019	-24.001	-23.959
θ^j	1	1.590721	1.222611	0.476710	0.308953	0.285114	0.289822
	2	**0.296054**	**0.276986**	**0.276282**	**0.276286**	**0.276287**	0.276288
	3	0.276286	0.276287	0.276287	0.276287	0.276287	**0.276287**
	4	0.276287	0.276287	0.276287	0.276287	0.276287	0.276287
θ^N_{min}	in [%]	0.856	0.856	0.856	0.856	0.856	0.856

(b) Estimation error

Figure 6.8: Identification results (a) and errors (b) of the stiffness and damping coefficients $\hat{k}_1$-$\hat{k}_3$ and $\hat{c}_1$-$\hat{c}_3$, respectively, using the W-EKF in dependence on the chosen initial error covariance σ^2_p and 1 % measurement noise. Two errors are compared: The error corresponding to the steady solution of the filter and the one associated with the estimate where the global error θ^N_{min} in the state estimation is minimized.

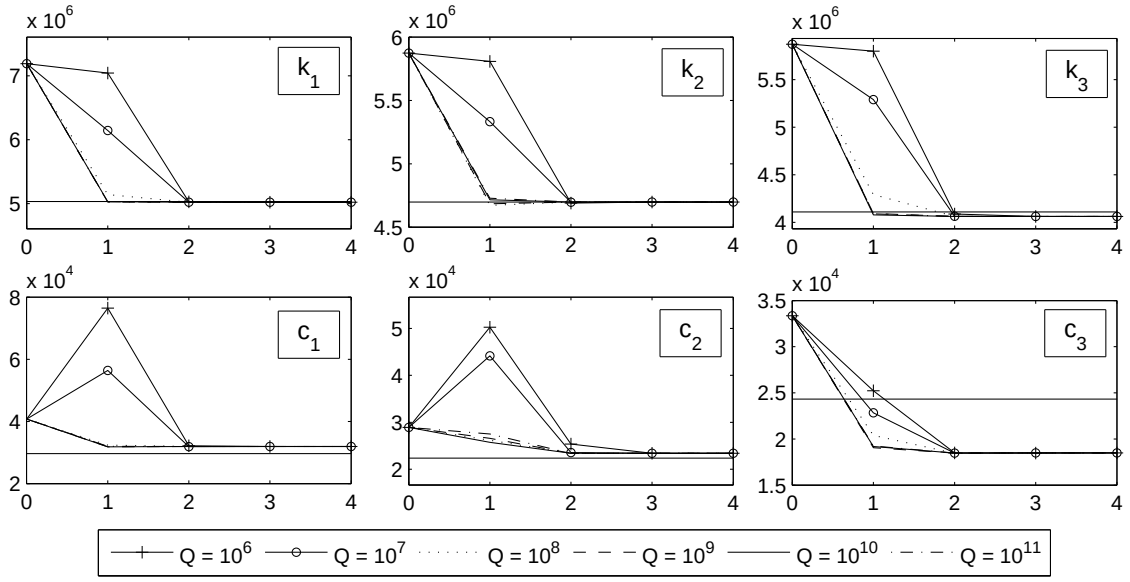

(a) Identification results (where $Q = \sigma^2_{k,0}, \sigma^2_{c,0}$)

$\mathbf{R}\delta_{ik} = 0.1\mathrm{MS}_i$ and $\sigma^2_{k,0}, \sigma^2_{c,0} = 1\times10^6 \ldots 1\times10^{11}$							
$\hat{\mathbf{p}}_{500}$	error in [%]	1×10^6	1×10^7	1×10^8	1×10^9	1×10^{10}	1×10^{11}
$\hat{k}_1$	after convergence	-0.411	-0.411	-0.411	-0.411	-0.411	-0.411
	for θ_{min}	-0.410	-0.410	-0.411	-0.410	-0.410	-0.411
$\hat{k}_2$	after convergence	0.038	0.038	0.038	0.038	0.038	0.038
	for θ_{min}	0.039	0.041	0.039	0.038	0.041	0.037
$\hat{k}_3$	after convergence	-1.301	-1.301	-1.301	-1.301	-1.301	-1.301
	for θ_{min}	-1.300	-1.301	-1.301	-1.300	-1.301	-1.302
$\hat{c}_1$	after convergence	8.393	8.393	8.393	8.393	8.393	8.393
	for θ_{min}	8.412	8.405	8.395	8.412	8.404	8.390
$\hat{c}_2$	after convergence	6.453	6.453	6.453	6.453	6.453	6.453
	for θ_{min}	6.376	6.436	6.452	6.377	6.434	6.439
$\hat{c}_3$	after convergence	-24.103	-24.103	-24.103	-24.103	-24.103	-24.103
	for θ_{min}	-24.200	-24.131	-24.107	-24.199	-24.130	-24.101
θ^j	1	5.377263	5.328509	4.797749	3.826868	3.651922	3.635838
	2	3.824161	3.650661	3.632934	3.632081	**3.632142**	**3.632156**
	3	**3.632081**	**3.632143**	**3.632158**	**3.632160**	3.632160	3.632160
	4	3.632160	3.632160	3.632160	3.632160	3.632160	3.632160
θ^N_{min}	in [%]	9.158	9.158	9.158	9.158	9.158	9.158

(b) Estimation error

Figure 6.9: Identification results (a) and errors (b) of the stiffness and damping coefficients $\hat{k}_1$-$\hat{k}_3$ and $\hat{c}_1$-$\hat{c}_3$, respectively, using the W-EKF in dependence on the chosen initial error covariance σ^2_p and 10 % measurement noise. Two errors are compared: The error corresponding to the steady solution of the filter and the one associated with the estimate where the global error θ^N_{min} in the state estimation is minimized.

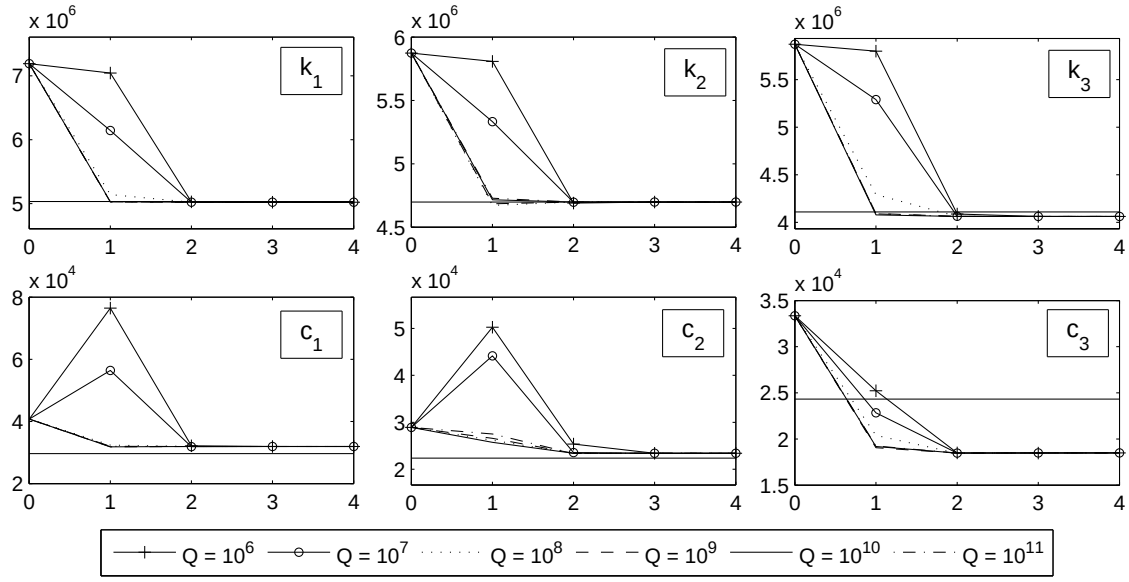

(a) Identification results (where $Q = \sigma^2_{k,0}, \sigma^2_{c,0}$)

$\mathbf{R}\delta_{ik} = 1\mathrm{MS}_i$ and $\sigma^2_{k,0}, \sigma^2_{c,0} = 1\times10^6 \ldots 1\times10^{11}$							
$\hat{\mathbf{p}}_{500}$	error in [%]	1×10^6	1×10^7	1×10^8	1×10^9	1×10^{10}	1×10^{11}
$\hat{k}_1$	after convergence	-0.898	-0.898	-0.898	-0.898	-0.898	-0.898
	for θ_{min}	-0.898	-0.903	-0.898	-0.898	-0.903	-0.898
$\hat{k}_2$	after convergence	0.042	0.042	0.042	0.042	0.042	0.042
	for θ_{min}	0.042	0.021	0.042	0.042	0.021	0.042
$\hat{k}_3$	after convergence	-0.782	-0.782	-0.782	-0.782	-0.782	-0.782
	for θ_{min}	-0.782	-0.783	-0.782	-0.782	-0.783	-0.782
$\hat{c}_1$	after convergence	11.653	11.653	11.653	11.653	11.653	11.653
	for θ_{min}	11.653	11.684	11.653	11.653	11.687	11.653
$\hat{c}_2$	after convergence	15.611	15.611	15.611	15.611	15.611	15.611
	for θ_{min}	15.611	15.969	15.611	15.611	15.988	15.611
$\hat{c}_3$	after convergence	-23.838	-23.838	-23.838	-23.838	-23.838	-23.838
	for θ_{min}	-23.838	-23.892	-23.838	-23.838	-23.893	-23.838
θ^j	1	45.82925	46.11427	46.15507	44.73402	42.37916	42.09499
	2	44.74202	42.38037	42.09646	42.07152	42.07010	42.07034
	3	42.07144	42.07008	42.07029	42.07016	42.07012	42.07012
	4	42.07016	42.07012	42.07012	**42.07011**	**42.07011**	**42.07011**
	5	**42.07011**	**42.07011**	**42.07011**	42.07011	42.07011	42.07011
θ^N_{min}	in [%]	96.273	96.273	96.273	96.273	96.273	96.273

(b) Estimation error

Figure 6.10: Identification results (a) and errors (b) of the stiffness and damping coefficients $\hat{k}_1$-$\hat{k}_3$ and $\hat{c}_1$-$\hat{c}_3$, respectively, using the W-EKF in dependence on the chosen initial error covariance σ^2_p and 100 % measurement noise. Two errors are compared: The error corresponding to the steady solution of the filter and the one associated with the estimate where the global error θ^N_{min} in the state estimation is minimized.

$\gamma_{y_1}^N$	$\gamma_{y_2}^N$	$\gamma_{y_3}^N$	$\gamma_{\dot{y}_1}^N$	$\gamma_{\dot{y}_2}^N$	$\gamma_{\dot{y}_3}^N$	θ_{min}^N
0.981	0.988	0.967	0.952	0.963	0.286	0.856

Table 6.2: Normalized square error in [%] of the posterior state estimate for 1 [%] measurement noise and $\sigma_p = \sqrt{1 \times 10^8}$ [N]

where the independence of the measurement noise $v_{i,k}$ and the undisturbed observation $\tilde{z}_{i,k}$ was used.

For the three cases of measurement noise with intensity of 1, 10 and 100 [%] of the mean-square of the undisturbed system response, the target values of γ_i^N and $\hat{\gamma}_i^N$ in [%] should approach in the optimal case

$$\begin{aligned}
&\mathbf{R}\delta_{ik} = 0.01\mathrm{MS}_i: && \gamma_i^N = 1\ [\%]; && \hat{\gamma}_i^N = 100/101\ [\%] \\
&\mathbf{R}\delta_{ik} = 0.1\mathrm{MS}_i: && \gamma_i^N = 10\ [\%]; && \hat{\gamma}_i^N = 100/11\ [\%] \\
&\mathbf{R}\delta_{ik} = 1\mathrm{MS}_i: && \gamma_i^N = 100\ [\%]; && \hat{\gamma}_i^N = 50\ [\%]
\end{aligned} \tag{6.44a}$$

and thus are related by

$$\begin{aligned}
&\mathbf{R}\delta_{ik} = 0.01\mathrm{MS}_i: && \gamma_i^N = 1.01\hat{\gamma}_i^N \\
&\mathbf{R}\delta_{ik} = 0.1\mathrm{MS}_i: && \gamma_i^N = 1.1\hat{\gamma}_i^N \\
&\mathbf{R}\delta_{ik} = 1\mathrm{MS}_i: && \gamma_i^N = 2\hat{\gamma}_i^N
\end{aligned} \tag{6.44b}$$

As the values γ_i^N, ϕ_{min}^N are directly related to the intensity of the measurement noise, they are used in the following for the evaluation of the filter performance. They are calculated based on the noisy measurement using Eq. (6.43) and the relations (6.44b).

The value θ_{min} tends in the three cases to about 0.86, 9.1 and 96.0 [%] and thus the expected values of 1, 10 and 100 [%] are slightly underestimated. In order to explore the reason for the underestimation, exemplarily, in Tab. 6.2 the values γ_1^N-γ_3^N and γ_4^N-γ_6^N in [%], corresponding to the mean square error of the estimated displacements and velocities, respectively, for the case of 1 [%] measurement noise and an initial error standard deviations $\sigma_{k,0}$ [N/m], $\sigma_{c,0}$ [Ns/m] of order $\sqrt{1 \times 10^8}$ are given. It is encouraging to observe that the values γ_1^N-γ_5^N agree well with the rate of noise contained in the observation. However, the quantity γ_6^N corresponding to the velocity of the third floor underestimate the strength of the measurement noise strongly and thus leads to the conclusion, that the accuracy in the damping estimate $\hat{c}_3$ is much lower. Comparing the results summarized in Tab. 6.8b confirms this assumption and shows that the estimation error decreases, if γ_j^N approaches the target value of 1 [%]. All in all, it can be concluded that the magnitude of the objective function should agree with

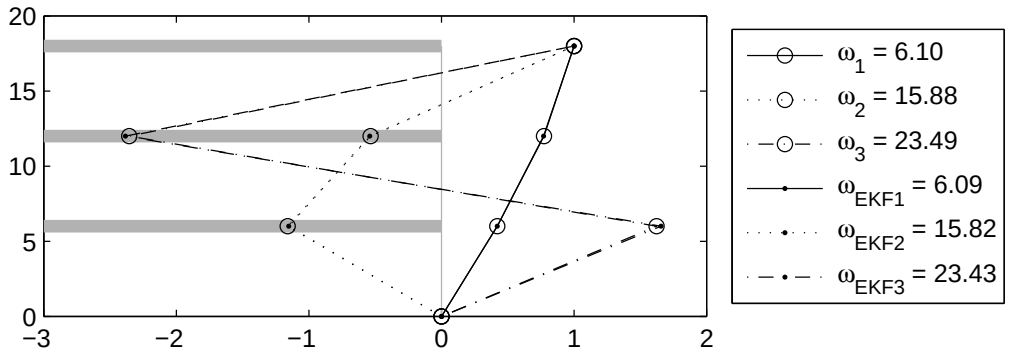

Figure 6.11: Comparison of the exact and estimated eigenfrequencies and modeshapes for the case $\sigma_p^2 = 1 \times 10^6$ and a measurement noise of 10 [%]

the global level of measurement noise.

Independent from the chosen measurement noise level and initial error covariance, the stiffness parameters $\hat{k}_1$, $\hat{k}_2$ and $\hat{k}_3$ are estimated with high accuracy leading to an estimation error of less than 1 [%]. The estimation errors of the damping parameters $\hat{c}_1$, $\hat{c}_2$ are much higher, varying between 4-8 [%] for the coefficients $\hat{c}_1$, $\hat{c}_2$ and of about 24 [%] for $\hat{c}_3$. Fig. 6.11 and 6.7 illustrate, that the damping parameters of the here considered weakly damped system have no significant effect on the modal frequencies and the observed system response. In [Ceravolo 2004] it is observed that in case of naturally excited systems, commonly[1], the accuracy of the damping estimation is not very high and even in numerical simulations errors of about 20 % are not unusual. Thus the obtained results can be considered to be of satisfying accuracy. Furthermore, it must be emphasized that the identification results are almost identical independent from the choice of prior error covariance confirming the high stability of the algorithm.

Up to now it was assumed that the system's excitation can be modeled as white noise process. However, if this assumption is violated, the EKF filter will lead to poor estimation results. In order to apply the filter to a wider class of processes, in the following chapter, a new output-only identification algorithm is proposed, which allows introducing arbitrarily correlated Gaussian processes into the (weighted) EKF algorithm.

[1] assuming a broad-banded excitation without dominant frequency components close to the system's eigenfrequencies

7 A New Parameter Identification Method of Structures Excited by Random Loads

In this chapter a new extended Kalman filter-based algorithm for the parameter identification of structures excited by correlated random loads is proposed. Focus lies on the stochastic excitation by wind turbulences and wind waves. In contrast to classical ambient vibration identification techniques, which model the unmeasured load process as white noise and thus are not applicable in case of non-white excitations, the proposed method takes into account additional information about the second-order statistics of the load process, e.g. obtained from measurements in the vicinity of the structure, and thus allows estimating both, the unknown system parameters as well as the unmeasured load process.
The new filter is called *H-fractional extended Kalman filter* as it combines the classical extended Kalman filter algorithm with the H-fractional spectral moment decomposition needed for introducing the unmeasured load process into the filter equations. After deriving the latter, the method is applied to estimate the stiffness and damping parameters of single- and multi-degree of freedom systems as well as the unmeasured load process exciting the structure. Finally, a sensitivity analysis is undertaken, in order to investigate the dependence of the accuracy of the load and parameter identification on the chosen parameterization of the load process.

7.1 Proposed modification of the EKF algorithm

The new method is based on a concept found in [Lewis et al 2008, p. 123-125] where it is shown that colored process noise and measurement noise with rational PSD function, respectively can be introduced into the Kalman filter algorithm by state space augmentation: That is, the colored noise is modeled indirectly as output of a linear state space model driven by

white noise obtained by means of the spectral factorization method (s. 4.4) and then, this linear system is added to the structural state space model resulting in an overall system, driven by white noise to which the Kalman filter can be applied in order to estimate the states of interest. For further details, see section 4.5, where the concept is applied for the modeling of a single degree of freedom system subjected to exponentially correlated wind gusts.

The restriction of the applicability of the concept to processes with rational PSD function results directly from the limitations of the spectral factorization method discussed in section 4.4 where it is shown that, the spectral factorization problem can be solved analytically, in general, just in the rational case.

In order to apply the concept to a wider class of processes, in the following, the method is combine with the H-fractional spectral moment decomposition discussed in section 5.4. Based on these results a state space representation of general form is proposed which allows modeling arbitrarily correlated processes in a uniform manner. Then, following the concept described above, the obtained state space model is augmented to the state space representation of the structural model leading to a linear system with white noise input to which the (weighted) extended Kalman filter can be applied in order to solve the parameter identification problem.

7.1.1 Generalized state space representation of colored random processes

Based on Eq. (5.30) given in section 5.5, in the following, a general state space representation for colored load processes is developed, which is valid for arbitrary correlated Gaussian processes and can be given directly once the H-FSMs in Eq. (5.14) are calculated.

Due to the Toeplitz form of the coefficient matrix $\mathbf{A}(\gamma)$ (5.30), the matrix transfer function $\mathbf{h}(\gamma_k)$ in Eq. (5.31) can be calculated easily. As discussed in section 5.5.1, if $Re\gamma > -1$ is chosen, then the coefficients $\alpha_k(\gamma)$ decrease with inverse power law behavior as k increases and can be neglected after a finite number of terms p (also known as *short memory principle*). Furthermore, it was shown, that for an input vector $\mathbf{W}$ of length n, the first and last p samples of the output $\mathbf{F}$ can be regarded as the *transition states* whereas the remaining $n-2p$ samples are the *steady states* which are needed in the following for the formulation of a recursive state space form. Using the truncated coefficient matrix $\mathbf{A}(\gamma)$ defined in Eq. (5.33), the calculation of one steady state realization $F_j = F(j\tau)$ of the discrete load process $\mathbf{F}$, with $j = 0,1,\ldots,n$ is given by

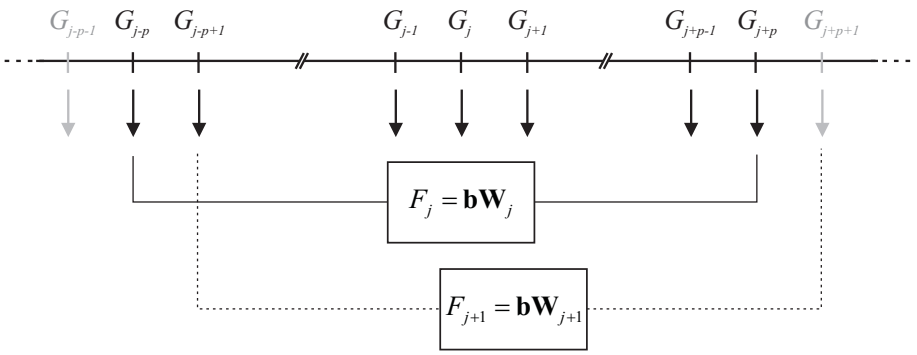

Figure 7.1: Steady state realization of the load process: the load F_{j+1} of the next time step is generated by shifting the p-dimensional vector $\mathbf{W}_j$ of increments of white noise

$$F_j = \frac{\Delta\eta}{4\pi}\sum_{k=-m}^{m}\Pi(-\gamma_k)\begin{bmatrix}\alpha_{c,p}(1-\gamma_k)\\ \alpha_{c,p-1}(1-\gamma_k)\\ \cdots\\ 2\alpha_{c,0}(1-\gamma_k)\\ \cdots\\ \alpha_{c,p-1}(1-\gamma_k)\\ \alpha_{c,p}(1-\gamma_k)\end{bmatrix}^T\begin{bmatrix}G_{j-p}\\ G_{j-p+1}\\ \cdots\\ G_j\\ \cdots\\ G_{j+p-1}\\ G_{j+p}\end{bmatrix} = \begin{bmatrix}\beta_p\\ \beta_{p-1}\\ \cdots\\ 2\beta_0\\ \cdots\\ \beta_{p-1}\\ \beta_p\end{bmatrix}^T\begin{bmatrix}G_{j-p}\\ G_{j-p+1}\\ \cdots\\ G_j\\ \cdots\\ G_{j+p-1}\\ G_{j+p}\end{bmatrix} = \mathbf{bW}_j \quad (7.1)$$

where

$$\beta_p = \frac{\Delta\eta}{4\pi}\sum_{k=-m}^{m}\Pi_H(-\gamma_k)\alpha_{c,p}(1-\gamma_k) \quad (7.2)$$

and where $\Pi_H(-\gamma_k)$ are the fractional spectral moments of the transfer function defined by Eq. 5.14 and $\alpha_{c,p}(\gamma_k)$ are the coefficients given by Eq. (5.35d). As one can see from Eq. (7.1) the actual sample $F_j = \mathbf{bW}_j$ of the load process is calculated by a time-variant white noise sequence $\mathbf{W}_j = [G_{j-p}, ..., G_j, ..., G_{j+p}]$ of p previous and past samples of the zero-mean Gaussian white noise process with standard deviation $\sqrt{q\tau}$ which are weighted by a time-invariant coefficient vector $\mathbf{b} = [\beta_p, \beta_{p-1}, ..., 2\beta_0, ..., \beta_{p-1}, \beta_p]$. The order p of the model is related to the process memory $M = p\tau$, where τ is the sampling interval as shown in section 5.5.3. As rule of thumb, the choice of the process order p defines the time interval M in which the AC function of the process is approximated accurately.

As illustrated in Fig. 7.1 the load process is generated by shifting the Gaussian white noise sequence $\mathbf{W}_j$ at each time step one position further in time and weighting it by the coefficient vector $\mathbf{b}$. It must be stressed that the result in Eq. (7.1) coincides with a (non-causal[1])

[1]The non-causality of the process, that is the dependency on future realizations $G_{j+1}, G_{j+2}, ..., G_{j+p}$ of the Gaussian white noise process is caused by the assumption that the imaginary part of the transfer function vanishes (s. Eq. (5.12))

MA representation of the process. Though, in contrast to classical approaches where the coefficients of the MA models are calculated by solving a non-linear optimization problem, it shall be highlighted that here the coefficients are given analytically.
Noting that a MA representation is obtained, it is now straight forward to define a state space representation of Eq. (7.1) using the result in section 4.2, yielding

$$\begin{aligned} \mathbf{x}'_{k+1} &= \mathbf{A}'_d \mathbf{x}'_k + \mathbf{B}'_d w'_k \\ F_k &= \mathbf{C}'_d \mathbf{x}'_k \end{aligned} \tag{7.3a}$$

where $\mathbf{x}'_k = [G_{k-p}, G_{k-p+1}, ..., G_k, ..., G_{k+p-1}, G_{k+p}]^T$ and with time-invariant transfer matrices $\mathbf{A}'_d$, $\mathbf{B}'_d$ and $\mathbf{C}'_d$

$$\mathbf{A}'_d = \begin{bmatrix} 0 & 1 & 0 & \dots & \dots & 0 & 0 \\ \dots & 0 & 1 & 0 & \dots & \dots & 0 \\ \dots & \dots & 0 & 1 & 0 & \dots & \dots \\ \dots & \dots & \dots & 0 & \cdots & \dots & \dots \\ \dots & \dots & \dots & \dots & \dots & \dots & \dots \\ 0 & \dots & \dots & \dots & \dots & 0 & 1 \\ 0 & 0 & \dots & \dots & \dots & 0 & 0 \end{bmatrix}; \quad \mathbf{B}'_d = \begin{bmatrix} 0 \\ 0 \\ \dots \\ \dots \\ \dots \\ 0 \\ 1 \end{bmatrix}; \quad \mathbf{C}'_d = \begin{bmatrix} \beta_p \\ \beta_{p-1} \\ \cdots \\ 2\beta_0 \\ \cdots \\ \beta_{p-1} \\ \beta_p \end{bmatrix}^T \tag{7.3b}$$

In the following the subindex d for discrete-time will be omitted for simplicity of notation. Comparing Eq. (7.3) with the state space representation (4.28a) obtained by spectral factorization, the strong resemblance of these two representations is obvious.
Though, it shall be highlighted that Eq. (7.3) is a general state space representation of stationary arbitrarily colored load processes without any restriction to the functional form of the PSD function. That is, once, the H-FSM of the PSD are determined using Eq. (5.14) the corresponding state space form is readily defined by Eq. (7.3).

7.1.2 Generalized state space model of structures subjected to random loads

The result can now be used to introduce the unmeasured system's excitation with given target PSD function into the Kalman filter algorithm by state space augmentation. Starting point is the structural state space model, given by the system equation

$$\mathbf{x}_{k+1} = \mathbf{A}_k \mathbf{x}_k + \mathbf{G}_k N_k \tag{7.4a}$$

and measurement equation

$$\mathbf{z}_k = \mathbf{C}_k \mathbf{x}_k + \mathbf{v}_k \tag{7.4b}$$

where $\mathbf{A}_k \in \mathbb{R}^{n\times n}$, $\mathbf{G}_k \in \mathbb{R}^{n\times 1}$ and $\mathbf{C}_k \in \mathbb{R}^{m\times n}$ are the transfer matrices, $\mathbf{x}_k \in \mathbb{R}^n$ and $\mathbf{z}_k \in \mathbb{R}^m$ are state and measurement vector, respectively. While the measurement noise is modeled as white noise process, i.e. $\mathbf{v}_k \in \mathbb{R}^m \sim \mathrm{WN}(\mathbf{0},\mathbf{R})$, the process noise $N_k \in \mathbb{R}$, representing the unmeasured load process F_k exciting the structure, is described as stationary colored Gaussian process with given target PSD function, e.g. known from measurements in the vicinity of the structure. Introducing the augmented state vector $\mathbf{x}_{a,k} = \left[\mathbf{x}_k, \mathbf{x}'_k\right]^T$ and using the result (7.3), the state space model with colored process noise (5.12) can be rewritten in the form

$$\begin{aligned} \begin{bmatrix} \mathbf{x}_{k+1} \\ \mathbf{x}'_{k+1} \end{bmatrix} &= \begin{bmatrix} \mathbf{A}_k & \mathbf{G}_k\mathbf{C}' \\ \mathbf{0} & \mathbf{A}' \end{bmatrix} \begin{bmatrix} \mathbf{x}_k \\ \mathbf{x}'_k \end{bmatrix} + \begin{bmatrix} \mathbf{0} \\ \mathbf{B}' \end{bmatrix} w'_k \\ \mathbf{z}_{a,k} &= \begin{bmatrix} \mathbf{C}_k & \mathbf{0} \end{bmatrix} \begin{bmatrix} \mathbf{x}_k \\ \mathbf{x}'_k \end{bmatrix} + \mathbf{v}_k \end{aligned} \tag{7.5}$$

which is once again a linear system excited by white noise. Hence, after rewriting Eq. (7.5)

$$\mathbf{x}_{a,k+1} = \mathbf{A}_a \mathbf{x}_{a,k} + \mathbf{G}_a \mathbf{w}_k \qquad \mathbf{z}_{a,k} = \mathbf{C}_a \mathbf{x}_{a,k} + \mathbf{v}_k \tag{7.6}$$

the KF algorithm summarized in Fig. 6.2 and its nonlinear extension, the EKF or weighted EKF, given in 6.4 and 6.5 can be run on the augmented state space model (7.5) using the modified transfer matrices $\mathbf{A}_a$, $\mathbf{G}_a$ and $\mathbf{C}_a$, respectively.
It must be stressed that the derived augmented state space model has a genetic form whose derivation neither required the factorization of the PSD nor any optimization procedure, but which can be given immediately, once the H-fractional spectral moments of the transfer function have been calculated. Furthermore, it's valid for arbitrarily correlated Gaussian processes with long as well as short memory (s. chapter 5).

7.1.3 Parameter identification of a SDOF dynamical structure

7.1.3.1 Case study 1: Exponentially correlated wind gusts

The proposed method is now applied to a single degree of freedom (SDOF) system excited by wind gusts w_c with exponential AC function $R(\tau) = \sigma^2 e^{-a|t|}$ in order to estimate the

stiffness and damping parameters, respectively. In this example the (long period) longitudinal dynamics of an aircraft are approximated by the continuous state space model of a harmonic oscillator with natural eigenfrequency $\omega = \sqrt{k/m}$ and ratio of critically damping $D = c/(2m\omega)$. The system's state $\mathbf{x}(t) = [\phi(t), \dot{\phi}(t)]^T$ is characterized by the pitch angle and velocity $\phi(t)$, $\dot{\phi}(t)$ describing the evaluation of angle between the longitudinal axis of the aircraft and the horizon. Due to the rational form of the PSD function of the process noise $w_c(t)$, a state space model of the colored process can be derived analytically by applying the spectral factorization theorem as shown in section 4.5.1 leading to the first order Markov model

$$\dot{x}'(t) = -ax'(t) + w'(t) \qquad F(t) = x'(t) \tag{7.7}$$

which is excited by a Gaussian white noise $w'(t)$ with standard deviation σ (compare section 4.5.1). By state space augmentation the following state space model is obtained

$$\dot{\mathbf{x}}_a(t) = \begin{bmatrix} 0 & 1 & 0 \\ -\omega^2 & -2D\omega & 1/m \\ 0 & 0 & -a \end{bmatrix} \mathbf{x}_a(t) + \begin{bmatrix} 0 \\ 0 \\ 1 \end{bmatrix} w(t) \tag{7.8}$$

where $\mathbf{x}_a(t) = [\phi(t), \dot{\phi}(t), x'(t)]^T$ denote the augmented state. The discretized model can be obtained by applying an explicit Euler approximation, that is by expressing the time derivative of the state vector $\dot{\mathbf{x}}_a(t)$ in Eq. (7.8) as forward difference

$$\frac{d\mathbf{x}_a(t)}{dt} \approx \frac{\mathbf{x}_a(t+\tau) - \mathbf{x}_a(t)}{\tau} = \frac{\mathbf{x}_{a,k+1} - \mathbf{x}_{a,k}}{\tau} \tag{7.9a}$$

and solving the resulting equation for the future state $\mathbf{x}_{a,k+1}$, yielding

$$\mathbf{x}_{a,k+1} = (\mathbf{A}_{a,c}\tau + \mathbf{I}_{3\times 3})\mathbf{x}_{a,k} + \mathbf{G}_{a,c}d\beta \tag{7.9b}$$

where τ is the sample interval and $d\beta(t) = \tau w(t)$ denotes the increment of a Brownian motion process. As shown in the annexe A.1.4.4, the latter can be simulated as Gaussian white noise process with variance $\sqrt{\tau}\sigma$. Thus, the discretization of Eq. (7.8) yields the following linear model

$$\mathbf{x}_{a,k+1} = \begin{bmatrix} 1 & \tau & 0 \\ -\omega^2\tau & 1 - 2D\omega\tau & \tau/m \\ 0 & 0 & 1 - a\tau \end{bmatrix} \mathbf{x}_{a,k} + \begin{bmatrix} 0 \\ 0 \\ 1 \end{bmatrix} w_k \tag{7.10}$$

$$\mathbf{z}_{a,k} = \begin{bmatrix} 1 & 0 & 0 \\ 0 & 1 & 0 \end{bmatrix} \mathbf{x}_{a,k} + \mathbf{v}_k \tag{7.11}$$

excited by the Gaussian white noises $w_k \sim (0,\sigma^2\tau)$ and $\mathbf{v}_k \sim (\mathbf{0},\mathbf{R}_c/\tau)$. Here, it must be mentioned, that the Euler discretization is used for illustrative purposes, in the numerical calculations the discretization is obtain by means of the matrix exponential function (s. section 4.4). This model will be used in this example for the generation of the 'true' measurement of the pitch angle $\phi(t)$ used in the KF algorithm.

By means of the approach using fractional calculus the augmented state space model is obtained by the following procedure: (i) the system's state space representation is formulated, (ii) the H-FSMs are calculated from the target PSD and the weights β_k of the Gaussian white noise are determined using Eq. (7.2), (iii) the initial vector $\mathbf{x}'_0$ of increments of Gaussian white noise and the system matrices of the generalized state space model in Eq. (7.3) are stored and introduced in Eq. (7.5) to obtain the augmented state space model. Again using the Euler discretization this model has the following form

$$\mathbf{x}_{a,k+1} = \begin{bmatrix} 1 & \tau & 0 & 0 & \dots & 0 & \dots & 0 & 0 \\ -\omega^2\tau & 1-2D\omega\tau & \frac{\tau\beta_p}{m} & \frac{\tau\beta_{p-1}}{m} & \dots & \frac{2\tau\beta_0}{m} & \dots & \frac{\tau\beta_{p-1}}{m} & \frac{\tau\beta_p}{m} \\ 0 & 0 & 0 & 1 & 0 & \dots & \dots & 0 & 0 \\ \dots & \dots & \dots & 0 & 1 & 0 & \dots & \dots & 0 \\ \dots & \dots & \dots & \dots & 0 & 1 & 0 & \dots & \dots \\ \dots & \dots & \dots & \dots & \dots & 0 & \cdots & \dots & \dots \\ \dots & \dots & \dots & \dots & \dots & \dots & \dots & \dots & \dots \\ 0 & \dots & \dots & \dots & \dots & \dots & \dots & 0 & 1 \\ 0 & 0 & 0 & 0 & \dots & \dots & \dots & 0 & 0 \end{bmatrix} \mathbf{x}_{a,k} + \begin{bmatrix} 0 \\ \dots \\ \dots \\ \dots \\ \dots \\ \dots \\ \dots \\ 0 \\ 1 \end{bmatrix} w_k \tag{7.12}$$

$$\mathbf{z}_k = \begin{bmatrix} 1 & 0 & 0 & \dots & \dots & \dots & \dots & \dots & 0 \\ 0 & 1 & 0 & \dots & \dots & \dots & \dots & \dots & 0 \end{bmatrix} \mathbf{x}_{a,k} + \mathbf{v}_k \tag{7.13}$$

with the augmented state $\mathbf{x}_{a,k} = [\phi_k, \dot{\phi}_k, G_{k-p}, \dots, G_k, \dots, G_{k+p}]$ and the white noises $w_k \sim (0,\tau)$, $\mathbf{v}_k \sim (\mathbf{0},\mathbf{R}_d)$. It must be noted that this state space model is valid for arbitrarily correlated Gaussian process noises with known PSD function. Only varying parameter is the number of coefficients p needed to approximate the correlation structure of the process with sufficient accuracy. In the following, the KF algorithm based on this approach will be indicated as *H-fractional KF* (H-KF) and the corresponding process noise is denoted as *H-fractional noise*, respectively.

In the first example, the system's parameters are assumed to be known and the evaluation

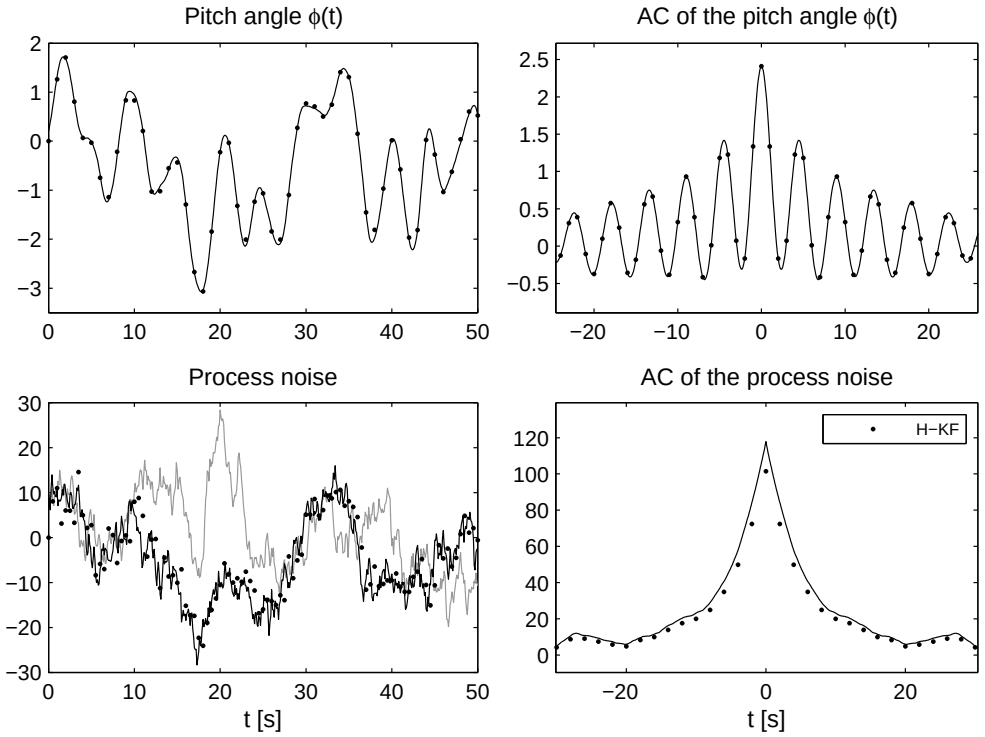

Figure 7.2: Top: Evaluation of the pitch angle $\phi(t)$ [rad] and AC function $R_\phi(t)$ [rad] for $\omega = \sqrt{2}$ [rad/s], $D = 0.05$ [-] of the system excited by exponentially correlated wind gusts, Bottom: Colored process noise generated by spectral factorization (line), by H-FSMs (gray) and estimated by the fractional KF (points) and corresponding AC function $R_F(t)$ [N] in [N^2]

of the pitch angle and the input force is estimated from output-only measurements applying the H-fractional KF using the following parameters: $a = 0.2$, $\sigma = 10$ [N], $k = 10$ [N/m], $c = 0.707$ [Ns/m] ($D = 0.05$), $m = 5$ [kg] and a sampling interval of $\tau = 0.1$ [s]. The fractional noise is parametrized choosing $p = 150$, $m = 30$, $\rho = 0.5$, $\Delta\eta = 0.2$. Fig. 7.2 depicts the evaluation and AC of the pitch angle $\phi(t)$ (Top) and the corresponding process noise exciting the system (Bottom). In order to illustrate that the KF algorithm not just updates the pitch angle $\phi(t)$ but also the H-fractional noise, the load process is depicted in gray for the case without consideration of the measurement date and in black-dotted after applying the KF algorithm. It can be stressed that both, the unmeasured load as well as the pitch angle, are estimated with high accuracy. The estimated correlation function of the load process is identical in the form, the estimated maximum value $\hat{R}(0) \approx 96$ [N^2] is just slightly lower than the target value of $\sigma^2 = 100$ [N^2].

In order to estimate the system's stiffness $k = 10$ [N/m] and damping constant $c = 0.707$ [Ns/m] ($D = 0.05$) now the so-called *H-fractional EKF* (H-EKF) as well as the so-called *spectral-EKF* (S-EKF) based on the Markov noise model (7.7) obtained by spectral factorization is applied. It is assumed that noisy measurement date of the pitch angle $\phi(t)$ and the veloc-

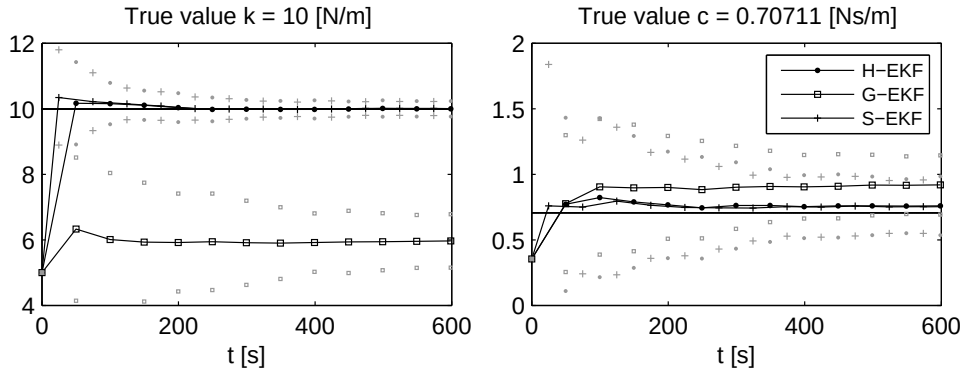

(a) Estimation of the stiffness k [N/m] and damping constant c [Ns/m] by means of H-fractional EKF (points), the spectral EKF (plus sign) and the Gaussian EKF (squares). The upper and lower bounds represent the corresponding 90 % confidence intervals.

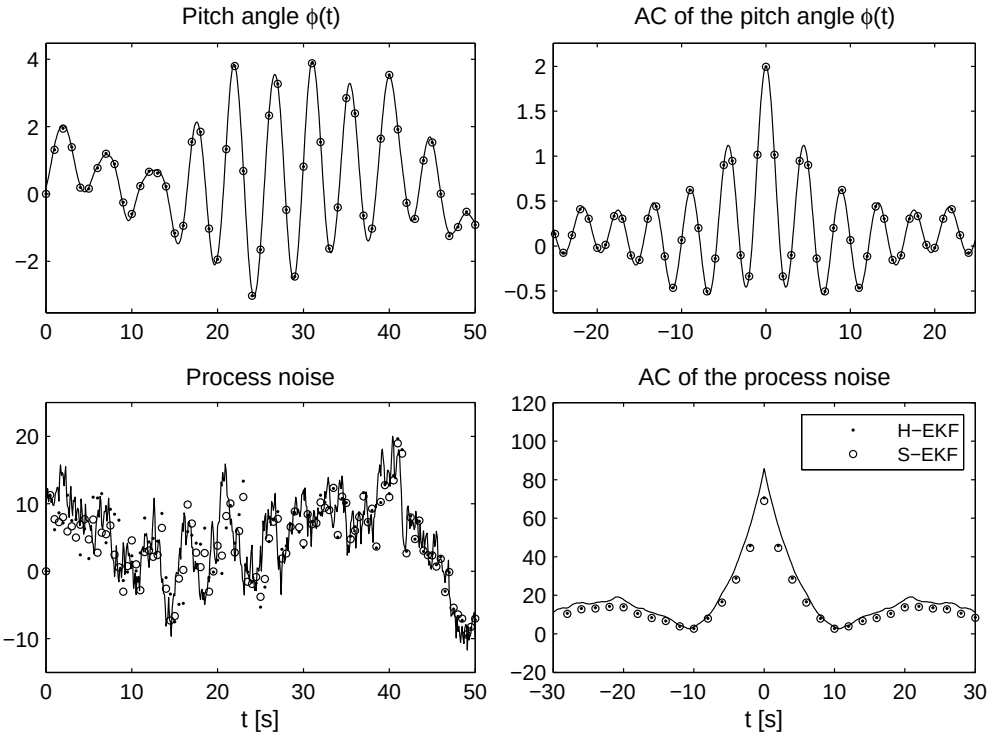

(b) Top: Evaluation of the pitch angle $\phi(t)$ [rad] and AC function $R_\phi(t)$ [rad^2] for $\omega = \sqrt{2}$ [rad/s], $D = 0.05$ [-], Bottom: Actual process noise generated by spectral factorization (line) and estimated input by the H-fractional EKF (points) and the spectral EKF (circles) and corresponding AC functions $R_F(t)$ [N^2]

Figure 7.3: SDOF system excited by exponentially correlated load process

ity $\dot{\phi}(t)$ is available taking into account a measurement error corresponding to 10 % of the mean-square of the undisturbed system response (compare Eq. (6.40a)). It is assumed that a set of 20 measurements of a duration of 10 [min.] each are available. The H-EKF and spectral-EKF as well as the standard Kalman filter is run on the samples. In the latter case

Case	initial estimate		identified parameters		standard deviation		identification error	
	$\hat{k}_0$ [N/m]	$\hat{c}_0$ [Ns/m]	$\hat{k}$ [N/m]	$\hat{c}$ [Ns/m]	$\sigma_{\hat{k}}$ [N/m]	$\sigma_{\hat{c}}$ [Ns/m]	e_k [%]	e_c [%]
Exponential	5.00	0.35	10.00	0.76	0.24	0.22	0.00	7.19
von Kármán	5.00	0.35	10.02	0.75	0.22	0.14	0.24	5.70
Pierson Moskowitz	5.00	0.35	10.02	0.73	0.20	0.18	0.20	2.92
true values	$k = 10$ [N/m], $c = 0.707$ [Ns/m]							

Table 7.1: Identification results for the different load cases

the correlation of the load process is neglected and modeled as Gaussian white noise with equivalent standard deviation of $\sigma = 10$ [N] and thus denoted as *Gaussian-EKF* (G-EKF). The G-EKF is used in order to show the error introduced into the parameter identification by the erroneous white noise assumption.

The initial values of the stiffness and damping parameter $\hat{k}_0$, $\hat{c}_0$ are selected considering an estimation error $e_{k_0} = |\hat{k}_0 - k|/k$, $e_{c_0} = |\hat{c}_0 - c|/c$ of 50 % and the associated initial error covariance is set to $\sigma_k = 10$ [N/m] and $\sigma_c = 2$ [Ns/m]. The mean value as well as the corresponding 90 % confidence intervals of the identified model parameters are depicted in Fig. (7.3a).

It is encouraging to note, that the H-EKF and the spectral-EKF provide almost identical identification results which confirms the consistency of the proposed method. In both cases, the stiffness parameter is estimated with high accuracy while the identification of the damping parameter leads to an error of 7.2 %. The higher error is caused by the fact, that in the example considered here, the damping parameter has no significant effect on the modal frequencies and the observed system response. As the update of the parameters is based on the minimization of the error between the obtained measurement and the predicted system's response, it is in general difficult to identify parameters whose estimation has almost no impact on the prediction error.

Neglecting the correlation of the load process leads to poor identification results as shown by means of the G-EKF which fails to identify both the stiffness and damping parameter. The results of the parameter identification of the H-fractional EKF are summarized in Tab. 7.1. Fig. 7.3b depicts the estimated evaluation of the pitch angle and the input force as well as the corresponding AC functions applying the H-EKF (black dotted) and the spectral-EKF (black circles). It can be stressed that the H-EKF and the S-EKF succeeded in estimating simultaneously the system state as well as the input process with high accuracy. In the latter case it takes about 30 [s] until the estimated process noise closely approaches the actual input process. It must be stressed, that in case where the loading is characterized by a ratio-

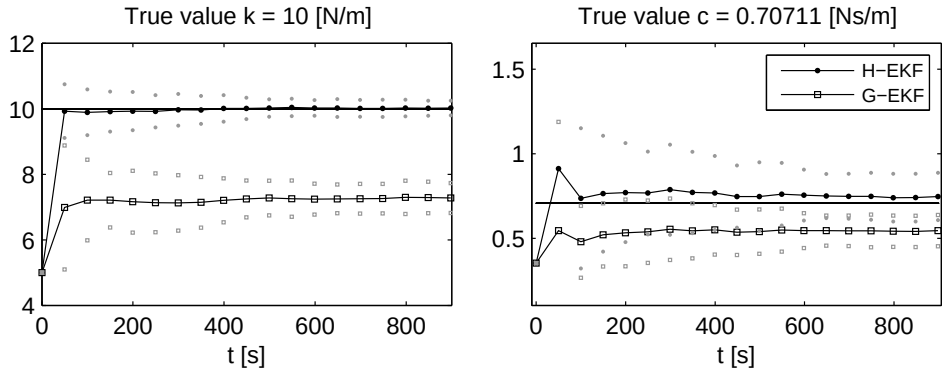

(a) Estimation of the stiffness k [N/m] and damping constant c [Ns/m] of the by means of H-fractional EKF (points) and the Gaussian EKF (squares). The dotted lines represent the corresponding 90 % confidence intervals.

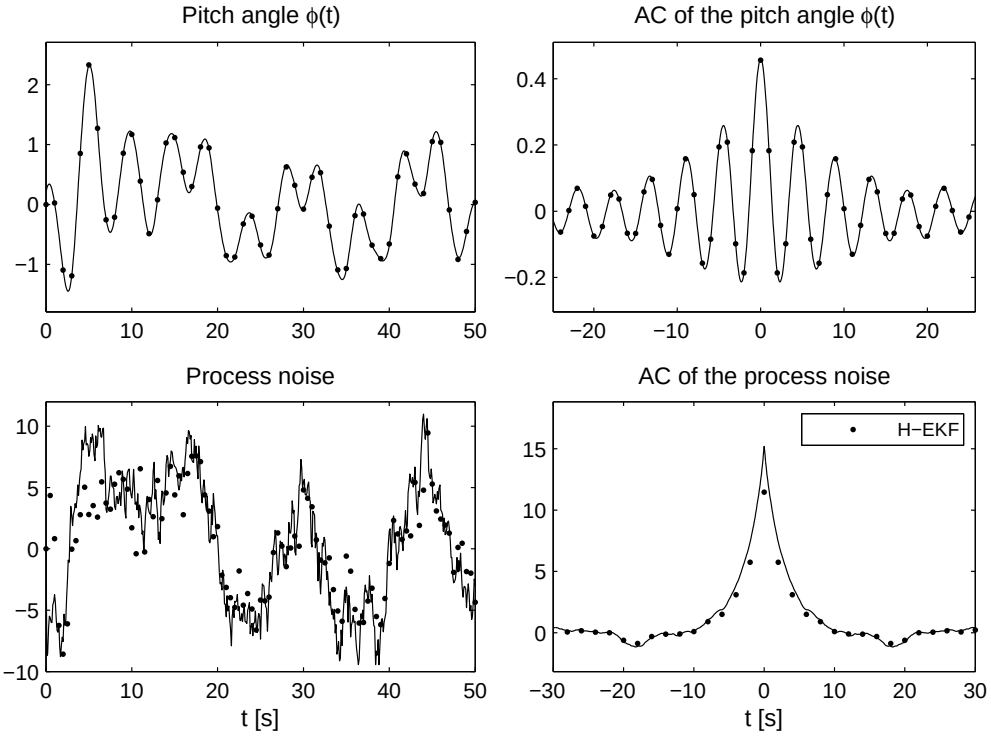

(b) Top: Evaluation of the pitch angle $\phi(t)$ [rad] and AC function $R_\phi(t)$ [rad^2] for $\omega = \sqrt{2}$ [rad/s], $D = 0.05$ [-], Bottom: Actual process noise (line) and estimated input by the H-fractional EKF (points) and corresponding AC function R_F [N^2]

Figure 7.4: SDOF system excited by wind loads with von Kármán velocity PSD

nal PSD function, the standard spectral factorization method outperforms the H-fractional Kalman filter from a computational point of view as it leads to a state space representation of lower order. However, the strength of the proposed method is its general applicability to arbitrary spectra and its straight forward implementation as shown in the following by means of wind turbulences with von Kármán velocity function and wind waves with Pierson

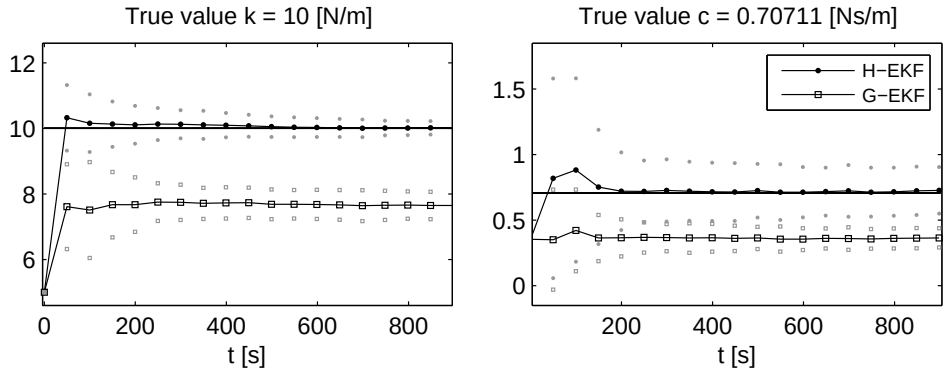

(a) Estimation of the stiffness k [N/m] and damping constant c [Ns/m] by means of H-fractional EKF (points) and the Gaussian EKF (squares). The dotted lines represent the corresponding 90 % confidence intervals.

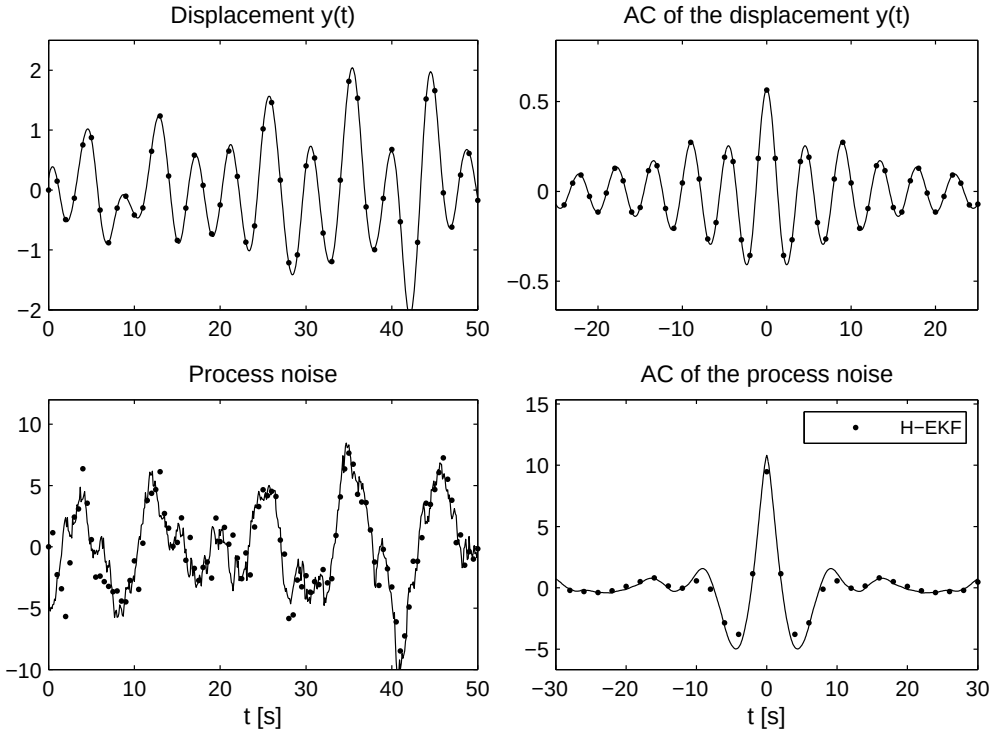

(b) Top: Evaluation of the displacement $y(t)$ [m] and AC function $R_y(t)$ [m^2] for $\omega = \sqrt{2}$ [rad/s], $D = 0.05$ [-], Bottom: Actual process noise generated by spectral factorization (black) and estimated input by the H-fractional EKF (black dotted) and the spectral EKF (black circles) and corresponding AC functions $R_F(t)$ [N^2.]

Figure 7.5: SDOF system excited by wind waves with P-M PSD

Moskowitz PSD function.

7.1.3.2 Case Study 2: Wind gusts with von Kármán velocity PSD

The von Kármán wind velocity spectrum is widely used in wind engineering applications as discussed in section 2.2.2.3. The spectrum is of non-rational form and thus there is no analytic method available to simulate the random process directly from the knowledge of the PSD function. As shown in section 5.5 the corresponding H-FSMs are different, but the implementation of the filter is the same as in the previous example. Choosing again a sampling interval of $\tau = 0.1$ [s], the fractional noise is parameterized setting: $p = 150$, $m = 50$, $\rho = 0.6$, $\Delta\eta = 0.15$. The results of the parameter identification for the H-Fractional KF and the standard EKF are illustrated in Fig. 7.4a. The mean values and corresponding 90 % confidence interval are calculate based on 20 measurements each of 15 [min.] length. Once again the standard EKF leads to poor identification results while the introduced method allows estimating the stiffness and damping parameter with high accuracy. Furthermore, Fig. 7.4b illustrations that also in this case the system state as well the unmeasured process noise is estimated accurately.

7.1.3.3 Case Study 3: Wind waves with Pierson-Moskowitz PSD

The results of the parameter identification are shown in Fig. 7.5a. The estimated stiffness and damping parameter corresponds to the generalized quantities of the first eigenmode of a clamped vertical pile which is excited by wind-induced ocean waves. Both parameter are again estimated accurately by means of the H-Fractional EKF. As in the previous example 20 measurements of 15 [min.] length with a sampling interval of $\tau = 0.1$ [s] were used. The fractional noise is parameterized choosing: $p = 200$, $m = 50$, $\rho = 1.6$, $\Delta\eta = 0.2$. Similarly, the estimated evaluation and AC function of the deflections and the process noise agree well with the measurement and actual loading of the system as illustrated in Fig. 7.5b.

7.1.4 Enhancing the method's efficiency by the weighted H-fractional extended Kalman filter

In the previous example the parameter estimates are calculated by averaging the identification results based on 20 samples of measurement data, choosing the same initializations for each run. However, in cases where just a small number of measurements is available, the weighted iterated EKF algorithm is more appropriate as it solves the parameter identification problem iteratively using only one measurement sample as input and re-initializing

the filter in the next iteration loop by the obtained estimates. Moreover, the computational efficiency of the H-fractional EKF mainly depends on the dimension of the state vector and thus on the number of coefficients needed to generate the fractional noise. As discussed in section 5.5.3, the order of the state space model of the noise process is dependent on the needed sampling interval, the memory of the process and the needed accuracy. Assuming a high order state space model, it is not efficient to re-run the H-EKF on many measurement samples and to calculate the parameters by averaging. As shown in the numerical example of the three story shear building, in contrast the W-EKF is applicable even if just one measurement record is available and converges already after a small number of iterations. The accuracy of the W-EKF is evaluated based on the global error θ^j pursuant to Eq. (6.30a) between the state estimate and the corresponding measurement to be calculated at each iteration j. The optimal state estimate is obtained either when the global error is minimized or if the filter converges. At the end of each iteration the error covariance matrix is increased by a factor $W = 100$ in order to prevent the filter from ignoring the incoming measurement data in the next iteration. The identification results for the stiffness and damping estimate for the three load cases by means of the weighted H-fractional EKF algorithm (H-WEKF) is summarized in Tab. 7.2. For the parametrization of the fractional noises the same values as in the previous section were chosen. The filter was run based on one measurement record of $T = 25$ [min.] length, taking into account a measurement noise of 10 [%] of the mean-square of the undisturbed system response (compare Eq. (6.40a)).
It is encouraging to note that in all cases, two iterations are sufficient to identify the parameters with an accuracy which is comparable to the results obtained by means of the H-fractional EKF algorithm. The accuracy of the estimation result is checked by the normalized minimum global square error θ^N_{min} between the state estimates and the measurements defined in Eq. (6.42c) which should approach, in the optimal case, the measurement noise level of 10 [%]. In addition, the normalized errors γ^N_ϕ, $\gamma^N_{\dot\phi}$ are given separately for the error of the displacement and velocity measurement and thus are related to the accuracy of the stiffness and damping estimations. The values confirm that the parameter estimation errors decrease if these errors approaches the target value of 10 [%].

7.1.5 Parameter identification of a three story shear building

In the following section the weighted H-fractional EKF algorithm is applied to the three story shear building discussed in section 6.1.4 subjected to wind gusts with exponentially AC and Kármán velocity PSD function, respectively. In section 7.1.5.1.1 and 7.1.5.1.2 the

		Exponential		von Kármán		Pierson Moskowitz	
iterations		$\hat{k}$	$\hat{c}$	$\hat{k}$	$\hat{c}$	$\hat{k}$	$\hat{c}$
j	0	5.000	0.354	5.000	0.354	5.000	0.354
	1	10.032	0.665	9.921	0.652	9.973	0.674
	2	10.034	0.665	9.922	0.652	9.974	0.674
	3	10.034	0.665	9.922	0.652	9.974	0.674
true value		10.000	0.707	10.000	0.707	10.000	0.707
error in [%]		0.339	5.977	0.778	7.775	0.264	4.734
θ^j	1	3815.69		1165.84		1397.77	
	2	3815.49		1165.87		1397.74	
	3	3815.49		1165.87		1397.74	
θ^N_{min} in [%]		11.38		11.45		10.93	
γ^N_ϕ in [%]		13.25		13.68		12.58	
$\gamma^N_{\dot{\phi}}$ in [%]		12.31		12.57		11.75	

Table 7.2: Identification results for the H-fractional W-EKF for the three load cases taking into account 10 [%] measurement noise. θ_j: global square error for the jth iteration between posterior state estimate and measurement pursuant to Eq. (6.30a); γ_i^N: normalized minimal square error in [%] calculated separately for the displacement and velocity estimate pursuant to Eq. (6.42b); θ^N_{min} normalized minimal global error in [%] of the state estimation pursuant to Eq. (6.42c).

dependence of the filter convergence and identification accuracy on the chosen sampling interval and the number of coefficients used for the load approximation, respectively.

7.1.5.1 Case Study 1: Exponentially correlated wind gusts

In the numerical example discussed in section 6.1.4, the stiffness and damping parameters k_1 - k_3 and c_1 - c_3, respectively, of the idealized lumped model of a three story shear building excited by an uncorrelated white load process at the top level of intensity σ_w = 2000 [N] are identified by means of the weighted EKF algorithm. Now, an exponentially autocorrelated load process of same intensity (a = 0.2, σ = 2000 [N]) is applied at the top floor. The load process used for the simulation of the displacement and velocity measurements at the floor levels is generated by the first order Markov model derived in Eq. (7.7). A measurement error of 10 [%] of the undisturbed system response is assumed, setting $\mathbf{R}\delta_{ik}$ = 0.1MS$_i$ pursuant to Eq. (6.40a). As in the example 6.1.4, the model is initialized introducing an estimation error of 30 [%] for the stiffness parameters $\hat{k}_1$, $\hat{k}_3$ and 20 [%] for the parameter $\hat{k}_2$, 37 [%] for the damping parameters $\hat{c}_1$, $\hat{c}_3$ and an error of 30 [%] in case of $\hat{c}_2$. In the example 6.1.4 it was shown that the number of iterations decreases with increasing initial error covariances $\sigma^2_{k,0}$ [(N/m)^2] and $\sigma_{c,0}$ [(Ns/m)^2], and hence, they are set equal 1×10^{11}. In order to accelerate the convergence of the filter, the error covariance $\mathbf{\Sigma}_{pp}$ is weighted by the factor W = 1000.

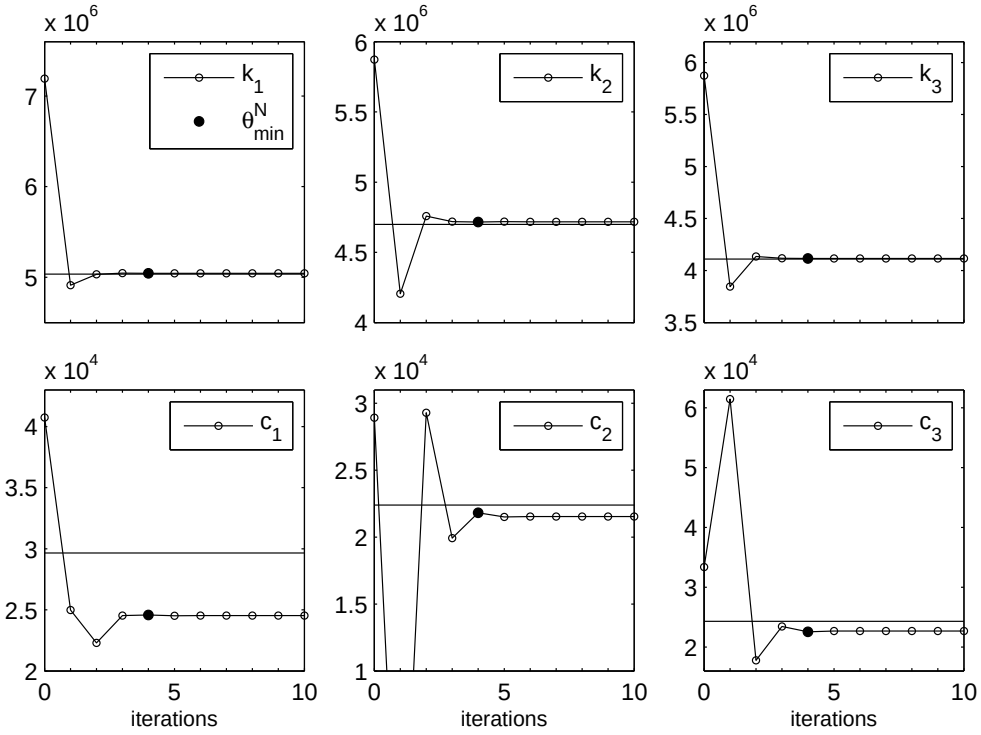

Figure 7.6: Identification results of the stiffness and damping coefficients $\hat{k}_1$ - $\hat{k}_3$ and $\hat{c}_1$ - $\hat{c}_3$ of the three story building subjected to exponentially autocorrelated wind gust using the H-fractional W-EKF choosing a measurement noise of variance $\mathbf{R}\delta_{ik} = 0.1\text{MS}_i$ and a sampling interval of $\tau = 0.1$ [s]. The optimal value where the global error θ^N_{min} between the measurement and the predicted state estimates is minimized, is indicated as black dot.

The H-fractional W-EKF is run $N = 10$ times and the results obtained at the end of each iteration is depicted in Fig. 7.6 and summarized in Tab. 7.3. The minimal global error $\theta_{min} = 8.15$ [%] is reached after 4 iterations and lower than the target value of 10 [%]. The normalized errors γ^N_i between the displacement and velocity estimates and the measurements used for the calculation of the global error indicate, that the estimation error mainly results from the inaccuracies of the velocity estimation at the first and third floor and thus higher identification errors of the damping estimates can be expected. To be precise, the stiffness parameters $\hat{k}_1$ - $\hat{k}_3$ are estimated with high accuracy leading to an identification error of less than 1 [%] and the damping coefficients $\hat{c}_1$ - $\hat{c}_3$ are identified with satisfying accuracy with relative errors of about 17, 3 and 7 [%], respectively. Again choosing a sampling interval of $\tau = 0.1$ [s], the fractional noise was parameterized, setting $p = 150$, $m = 30$, $\rho = 0.5$, $\Delta\eta = 0.2$. In Fig. 7.7 the estimated and actual load process exciting the structure are compared. It is encouraging to note, that the proposed filter succeed in estimating the evaluation of the process accurately from output only measurements.

	iterations	$\hat{k}_1$	$\hat{k}_2$	$\hat{k}_3$	$\hat{c}_1$	$\hat{c}_2$	$\hat{c}_3$
θ_{min}	0	7191333	5873000	5873000	40736	28919	33357
	1	4911314	4204710	3845910	24988	-10083	61451
	2	5031342	4758707	4134715	22293	29290	17781
	3	5045749	4719323	4117561	24526	19917	23424
	4	**5042847**	**4715290**	**4115281**	**24578**	**21812**	**22545**
	5	5043517	4718198	4116343	24509	21511	22680
	6	5043382	4717395	4116060	24530	21536	22661
	7	5043404	4717545	4116122	24526	21541	22663
	8	5043402	4717529	4116111	24526	21538	22663
true value		5033933	4698400	4111100	29656	22397	24313
error in [%]	for $N = 8$	0.188	0.407	0.122	-17.296	-3.833	-6.789
	for θ_{min}	0.177	0.359	0.102	-17.121	-2.614	-7.273
θ^j	1	0.05530					
	2	0.05340					
	3	0.05340					
	4	**0.05337**					
	5	0.05338					

in [%]	θ^N_{min}	$\gamma^N_{y_1}$	$\gamma^N_{y_2}$	$\gamma^N_{y_3}$	$\gamma^N_{\dot{y}_1}$	$\gamma^N_{\dot{y}_2}$	$\gamma^N_{\dot{y}_3}$
	8.15	8.65	8.80	8.66	7.24	8.04	7.53

Table 7.3: Estimation result of the stiffness and damping coefficients $\hat{k}_1$-$\hat{k}_3$ and $\hat{c}_1$-$\hat{c}_3$, respectively, for the three story building subjected to exponentially autocorrelated wind gust taking into account 10 [%] measurement noise and a sampling interval of $\tau = 0.1$ [s]. θ_j: global square error for the jth iteration between posterior state estimate and measurement pursuant to Eq. (6.30a); γ_i^N: normalized minimal square error in [%] calculated separately for the displacement and velocity estimate pursuant to Eq. (6.42b); θ^N_{min} normalized minimal global error in [%] of the state estimation pursuant to Eq. (6.42c).

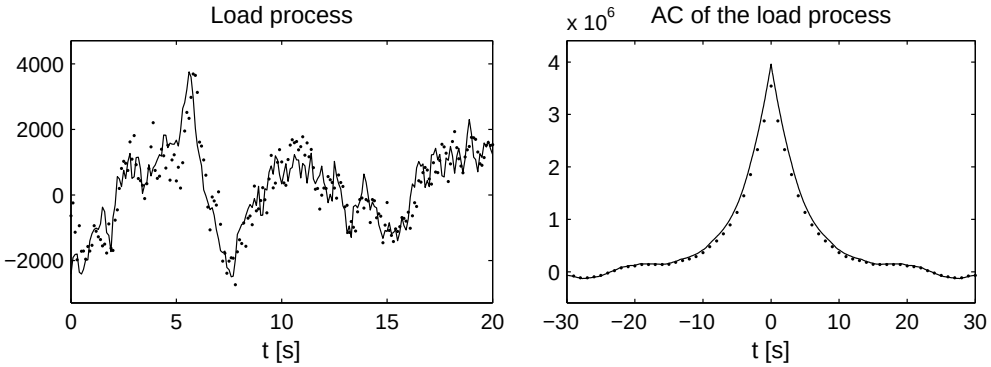

Figure 7.7: Estimated (dotted) and true (line) evaluation of the load process $\{F(t)\}$ [N] and AC function $R_F(t)$ [N^2] of the exponentially correlated load process exciting the structure at the top floor using a sampling interval of $\tau = 0.1$ [s].

7.1.5.1.1 Influence of the sampling interval on the filter convergence

To keep the order of the state space model of the fractional noise small, again a sampling in-

	iterations	$\hat{k}_1$	$\hat{k}_2$	$\hat{k}_3$	$\hat{c}_1$	$\hat{c}_2$	$\hat{c}_3$
true value		5033933	4698400	4111100	29656	22397	24313
error in [%]	for $N = 6$	-0.648	3.002	0.105	-0.082	8.461	-4.703
	for $\theta_{min}^{j=4}$	-0.648	3.002	0.105	-0.086	8.454	-4.701
in [%]	θ_{min}^{N}	$\gamma_{y_1}^{N}$	$\gamma_{y_2}^{N}$	$\gamma_{y_3}^{N}$	$\gamma_{\dot{y}_1}^{N}$	$\gamma_{\dot{y}_2}^{N}$	$\gamma_{\dot{y}_3}^{N}$
	8.89	9.06	9.52	9.52	8.49	8.66	8.09

Table 7.4: Estimation result of the stiffness and damping coefficients $\hat{k}_1$-$\hat{k}_3$ and $\hat{c}_1$-$\hat{c}_3$, respectively, for the three story building subjected to exponentially autocorrelated wind gust taking into account 10 [%] measurement noise and a sampling interval of $\tau = 0.05$ [s]. γ_i^N: normalized minimal square error pursuant to Eq. (6.42b); normalized minimal global error pursuant to Eq. (6.42c)

terval of $\tau = 0.1$ [s] was used. Though, the large sampling interval causes the filter to converge slowly, as the prediction error increases with increasing time step width and thus the updated parameters vary strongly in the first filter steps. Consequently, it takes more updates until the filter reaches its steady solution. While in the example 7.1.4 of the SDOF system subjected to exponentially correlated load convergence is obtained after about $T = 25$ [min.], in the example of the three story building discussed here, a measurement duration of about 65 [min.] is required, where the stationarity of the load process becomes questionable.
With the aim to accelerate the convergence, the filter is re-run using a measurement record with a smaller sampling interval of $\tau = 0.05$ [s]. As discussed in section 5.5.3, if the sampling interval is halved, twice as much coefficients ($p = 300$) are needed for the generation of the load process with comparable accuracy. The increases of computational demand of the Kalman filter at each time update, is compensated by the drastic reduction of the computation time by a factor of 10 due to the fast convergence after $T = 6.5$ [min.]. The identification results are depicted in Fig. 7.8 and summarized in Tab. (7.4). Again the parameters are identified with a high accuracy which is comparable to the previous result. Also in this case, the filter succeeded in estimating the evaluation and AC function of the force from output-only measurements as illustrated by Fig. (7.9)

7.1.5.1.2 Influence of the accuracy of the load modeling on the filter performance

Up to know, the state space representation of the load process has been modeled with high accuracy by choosing the number of coefficients in such a way, that a good agreement with the target AC function is obtained. In the previous example of the exponentially correlated process, this let to $p = 300$ coefficients at a sampling interval of $\tau = 0.05$ [s]. It was shown that in this case, the system's parameters and the time series of the unmeasured load process are estimated accurately. Of course, the question arises, if a model reduction of the load process is possible, and consequently, how the resulting decrease of the considered number

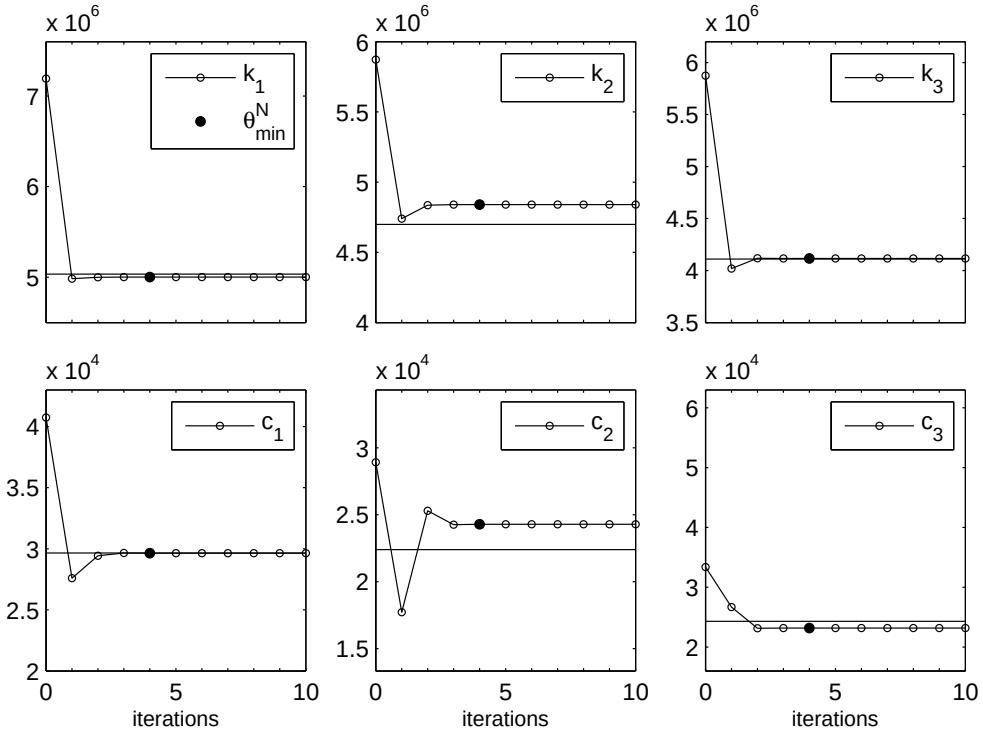

Figure 7.8: Identification results of the stiffness and damping coefficients $\hat{k}_1$ - $\hat{k}_3$ and $\hat{c}_1$ - $\hat{c}_3$ of the three story building subjected to exponentially autocorrelated wind gust using the H-fractional W-EKF choosing a measurement noise of variance $\mathbf{R}\delta_{ik} = 0.1\text{MS}_i$ and a sampling interval of $\tau = 0.05$ [s]. The optimal value where the global error θ^N_{min} between the measurement and the predicted state estimates is minimized, is indicated as black dot.

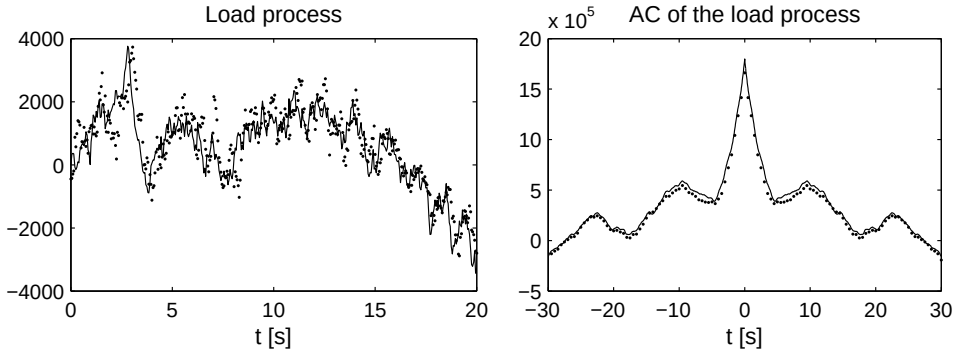

Figure 7.9: Estimated (dotted) and true (line) evaluation of the load process $\{F(t)\}$ [N] and AC function [N^2] of the exponentially correlated load process exciting the structure at the top floor using a sampling interval of $\tau = 0.05$ [s].

of coefficients, influences these identification results.

To this aim, the sampling interval is again set to $\tau = 0.05$ [s] and the number of coefficients is successively reduced, setting $p = [\,300, 250, 200, 150, 100, 50, 25]$. In order to illustrate the effect of such a reduction, in Fig. 7.10a the target AC function and the sample AC functions corresponding to the generated time series using the H-FSM decomposition are depicted in

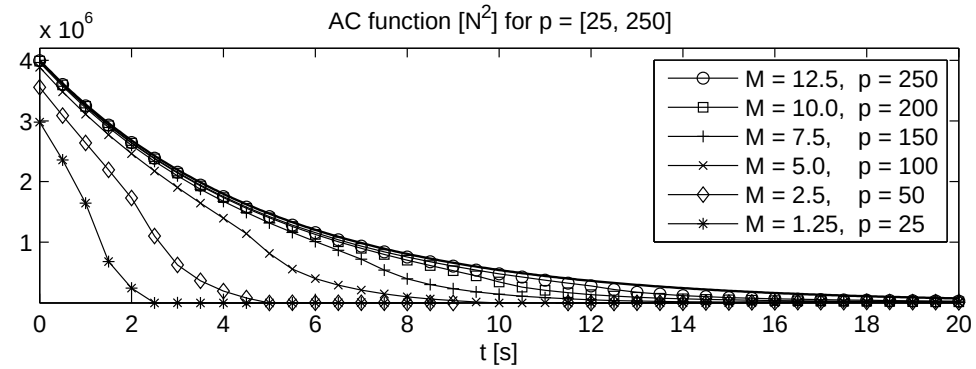

(a) Comparison of the target AC function of the exponentially correlated process with standard deviation $\sigma = 2000$ [N] (line) and the approximated function calculated from the generated times series choosing a sampling interval of $\tau = 0.05$ and varying the number of load coefficients in the interval $p = [25, 250]$.

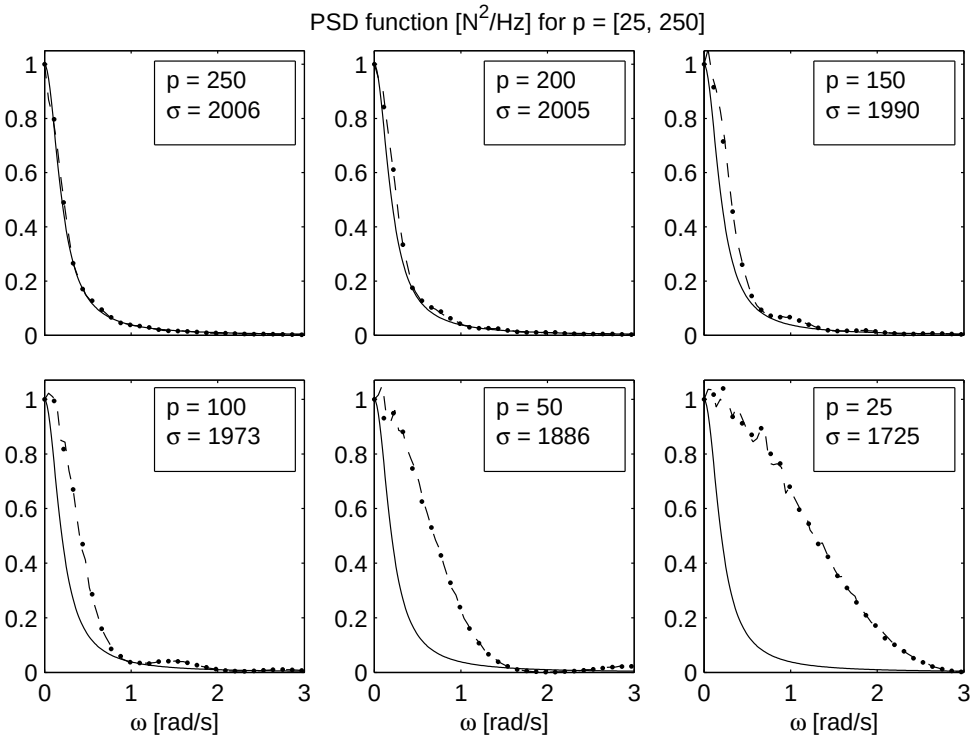

(b) Comparison of the analytic PSD function of the exponentially correlated process with standard deviation $\sigma = 2000$ [N]) (line) and the approximated function calculated from the generated time series setting the sampling interval $\tau = 0.05$ [s] and varying the number of load coefficients in the interval $p = [25, 250]$. The spectrum is normalized with respect to $S_F(\omega = 0)$ and the standard deviation σ of the generated time series is given for comparison.

Figure 7.10: Case study 1: Exponentially autocorrelated wind gusts

dependence on the chosen number of load coefficients, i.e. the considered memory of the process $M = p\tau$. It is evident, that for $p < 150$, the variance of the target process $\sigma = 2000$ is underestimated and that the approximated AC function decays much too fast.

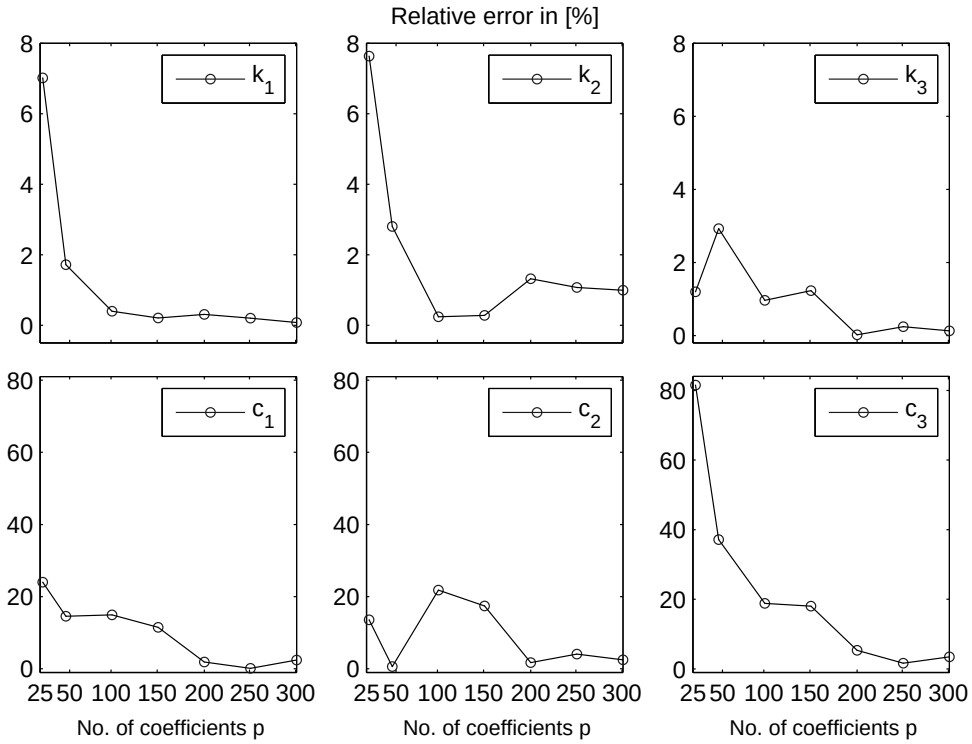

(a) Relative estimation error for the stiffness (Top) and damping estimates (Bottom) in dependence on the number of load coefficients.

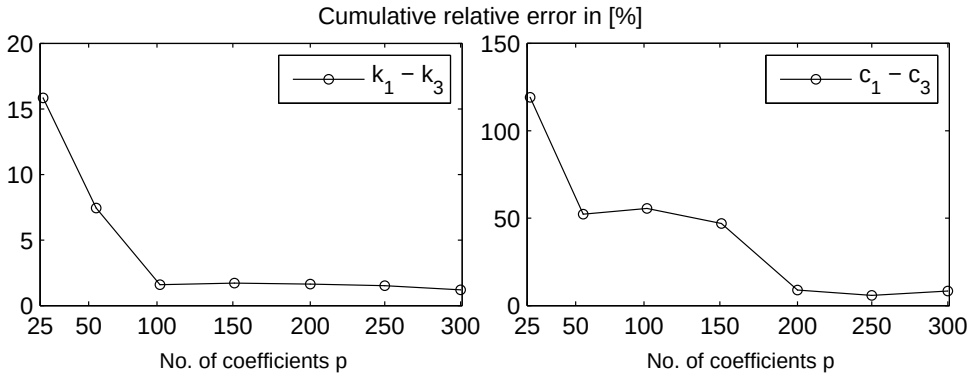

(b) Cumulative relative estimation errors including both, stiffness and damping estimates (Left), the error including the stiffness estimates (Center) and the error including the damping estimates (Right), respectively, in dependence on the number of load coefficients.

Figure 7.11: Case study 1: Exponentially autocorrelated wind gusts

A frequency analysis of the load process confirms these results: For this purpose in Fig. 7.10b the analytic PSD function of the exponentially correlated process is compared with the densities calculated from the generated time series for the different parameterizations. As expected, the reduction of the number of parameters leads to a too broad PSD function. Though, in order to approximate the target spectrum with satisfying accuracy, just about $p = 150 - 200$ coefficients must be taken into account.

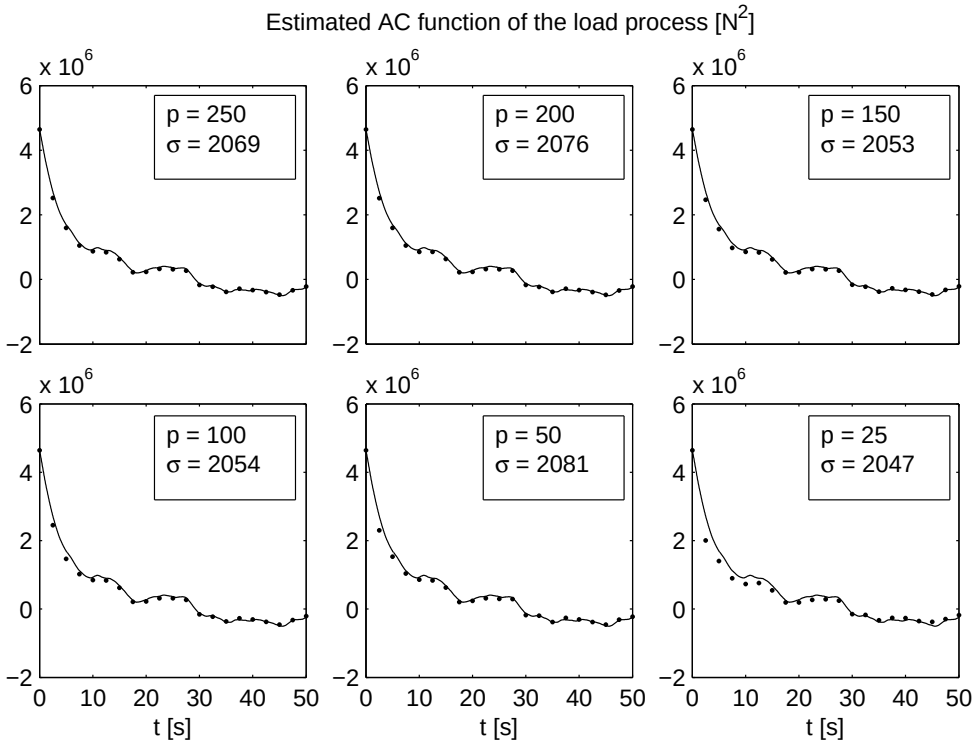

Figure 7.12: Case study 1: Comparison of the actual load process with exponential AC ($\sigma = 2154$ [N]) exciting the structure at the top floor and the estimated AC functions by means of the H-WEKF in dependence on the considered number of load coefficients p. For the calculation a time series of 5 [min.] length (6000 samples) is taking into account.

Using the same initialization as in the previous example, the H-WEKF is now run for the different load models. In all cases, about $j = 2 - 4$ iterations are needed, until the objective function θ^j reaches its minimum. The identification results (especially the damping estimates) converge slower with decreasing model accuracy, and thus, for the different cases, a measurement record of length $T = [5, 10, 10, 15, 25, > 50, > 50]$ [min.] is required. In the case $p \leq 50$, the filter diverges, so here, the given estimates correspond to the result obtained after $T = 50$ [min.]. Fig. 7.11a depicts the relative identification error in [%] in dependence on the chosen number of coefficients. In order to evaluate the global performance of the filter for the different parameterizations, in Fig. 7.11b the corresponding cumulative errors, obtained by summing up the relative errors of the stiffness (Left) and damping estimates (Right), are given. It can be stressed that the overall errors in the stiffness estimation vary for $p \geq 100$ in a narrow band of about 1 - 2 [%] while the errors in the damping estimation show a stronger dependence on the number of parameters and reach a constant error level for $p \geq 200$.
The results of the load identification are illustrated in Fig. 7.12 where the AC function of the actual load process, exciting the structure at the top floor, and the one calculated from the estimated time series by means of the H-WEKF are compared. For comparison sake,

the sample AC functions are calculated in all cases taking into account the first 5 [min.] of the generated time series. It is encouraging to note, that even in the case $p \leq 50$, where the results of the parameter identification diverge, a good estimation is obtained. Comparing the estimation of the peak value, in all cases a slight underestimation of the target standard deviation is observed.
From these results the following conclusions can be drawn:

(i) The filter converge slower, with decreasing number of load coefficients and diverges, if a too small number of parameters is chosen (here if $p \leq 50$) .

(ii) The quality of the load identification is almost independent from the number of coefficients.

(iii) The damping estimation results depend stronger on the number of coefficient and the divergence of the filter is more prominent.

(iv) It is interesting to note, that the range $p \geq 200$ where the total error is minimized, coincides with the number of coefficients, required for a good approximation of both, the variance of the process as well as the analytic PSD function. Below that value, the variance of the process starts deviate from the target value, the AC function decreases much quicker and the PSD function is evidently broader, respectively, than the analytic functions.

That is, as a rule of thumb, the load process must be parameterized in such a way, that the PSD function of the load process is approximated well. With the aim to confirm these results, in the following example, the three story shear building subjected to wind gusts with Kaŕmán velocity PSD is discussed.

7.1.5.2 Case Study 2: Wind gusts with von Kármán velocity PSD

First, the actual load, exciting the structure at the top floor, is generated as in the previous example, choosing a sampling interval of $\tau = 0.05$ [s] leading to $p = 240$ coefficients to obtain a high accuracy. However, for this sampling interval, the damping estimates converge slowly, leading to a long iteration time of more than $T > 25$ [min]. Thus, using the result obtained in section 7.1.5.1.1, the sample interval is increased in order to accelerate the convergence of the filter, setting $\tau = 0.025$ [s]. As shown in section 5.5.3, this leads to about $p = 500$ load coefficients, in order to generate the process with comparable accuracy. The remaining parameters are set as before, choosing $m = 50$, $\rho = 0.6$, $\Delta\eta = 0.15$.
In order to verify the results of the previous example, again different parameterization for

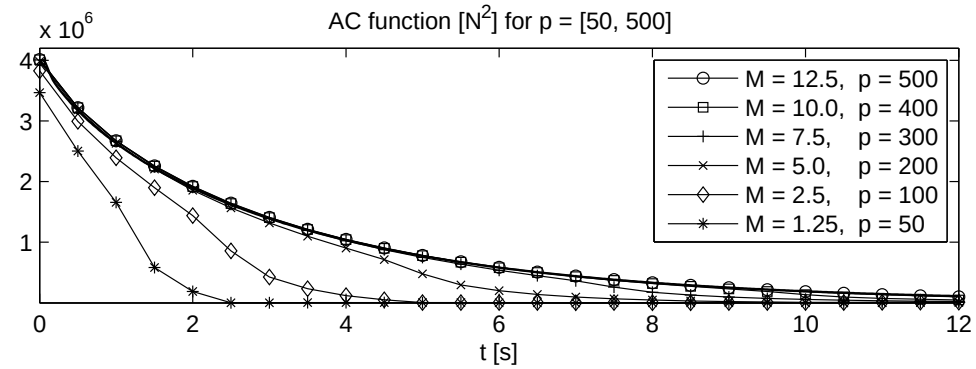

(a) Comparison of the target AC function of the process with Kármán velocity PSD with standard deviation $\sigma = 2000$ [N] (line) and the approximated function calculated from the generated times series choosing a sampling interval of $\tau = 0.025$ and varying the number of load coefficients in the interval $p = [50, 500]$.

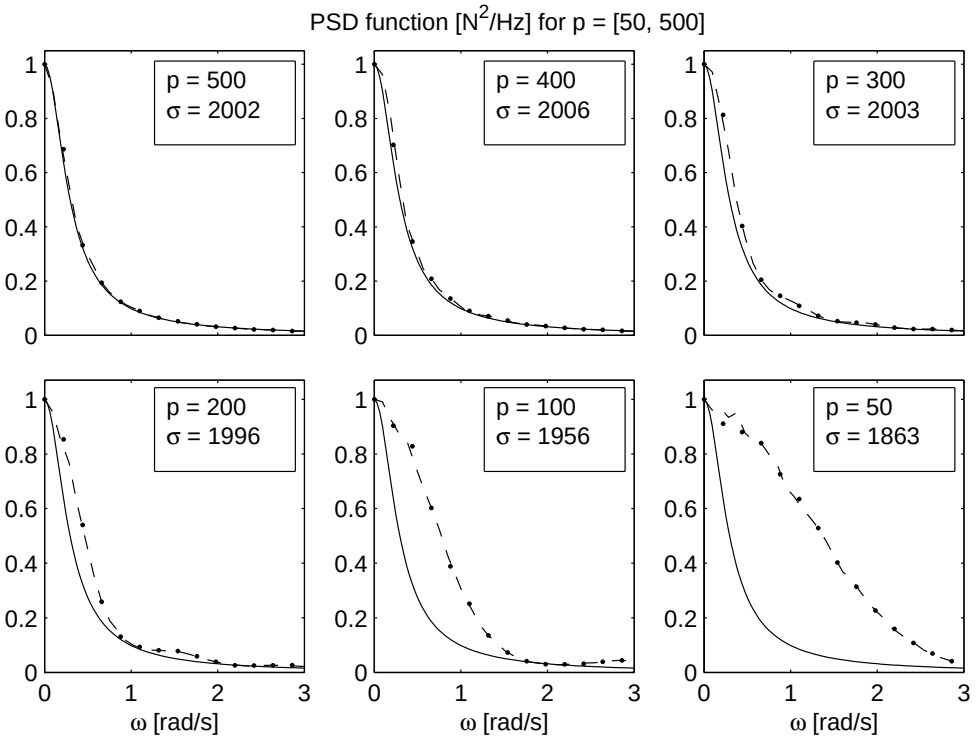

(b) Comparison of the analytic PSD function of the with Kármán velocity PSD (line) and the approximated function calculated from the generated time series setting the sampling interval $\tau = 0.025$ [s] and varying the number of load coefficients in the interval $p = [50, 500]$. The spectrum is normalized with respect to $S_F(\omega = 0)$ and and the standard deviation σ of the generated time series is given for comparison.

Figure 7.13: Case study 2: Wind gusts with von Kármán velocity PSD function

the estimation of the process are used, reducing the number of coefficients successively, choosing $p = [500, 400, 300, 200, 100, 50]$. In order to illustrate the modeling accuracy for these parameterizations, the resulting sample AC and PSD functions are depicted in Fig. 7.13a and

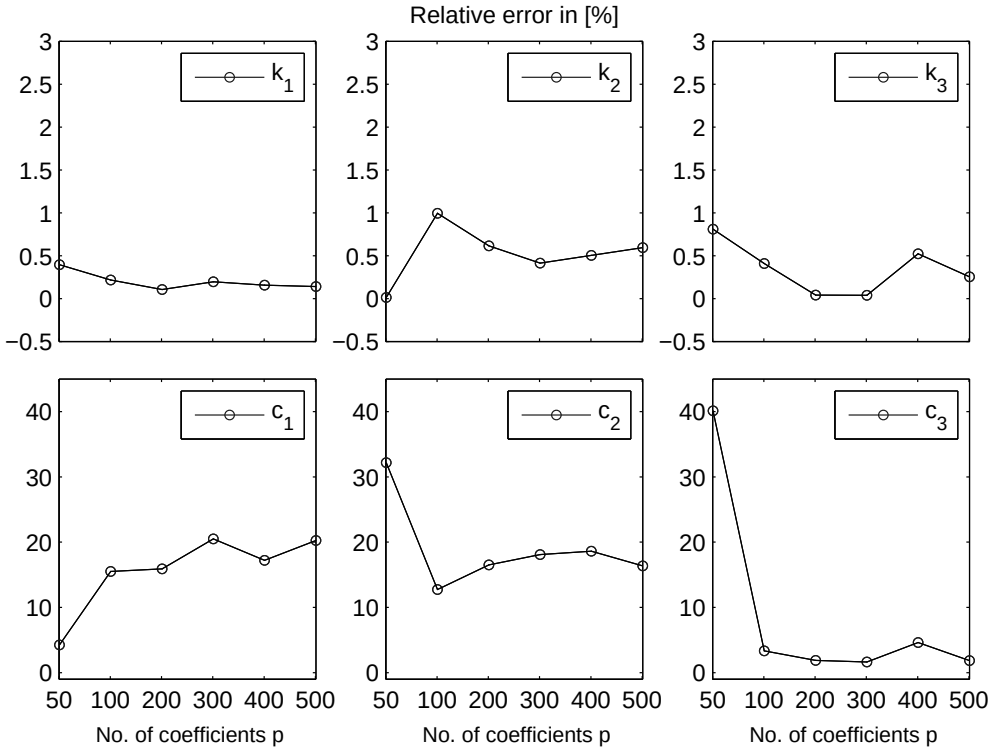

(a) Relative estimation error for the stiffness (Top) and damping estimates (Bottom) in dependence on the number of load coefficients.

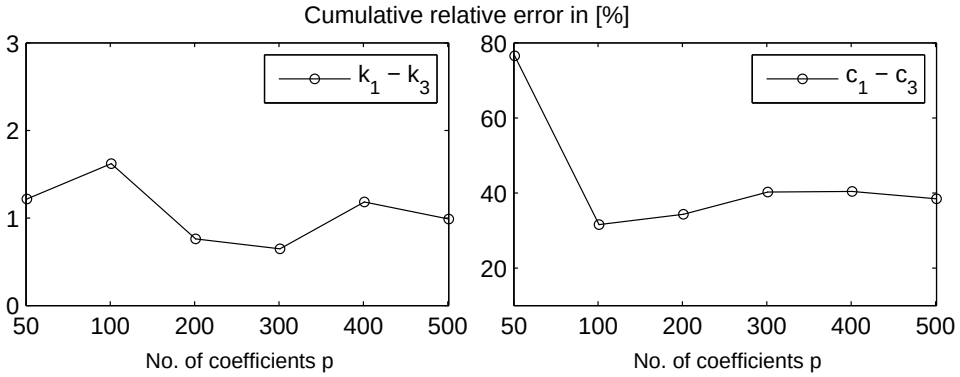

(b) Cumulative relative estimation errors including both, stiffness and damping estimates (Left), the error including the stiffness estimates (Center) and the error including the damping estimates (Right), respectively, in dependence on the number of load coefficients.

Figure 7.14: Case study 2: Wind gusts with von Kármán velocity PSD function

Fig. 7.13b, respectively, in dependence on the chosen number of coefficients. It is evident, that for $p \geq 300$, the PSD function is approximated well and the variance of the series starts to deviate from the target value (σ = 2000 [N]) for $p < 200$. Thus, using the results from the previous example, the H-WEKF should provide a good identification result, if the load process is approximated using about $p = 200 - 300$ coefficients.

This assumption is now verified by applying the H-WEKF for the different parameterizations

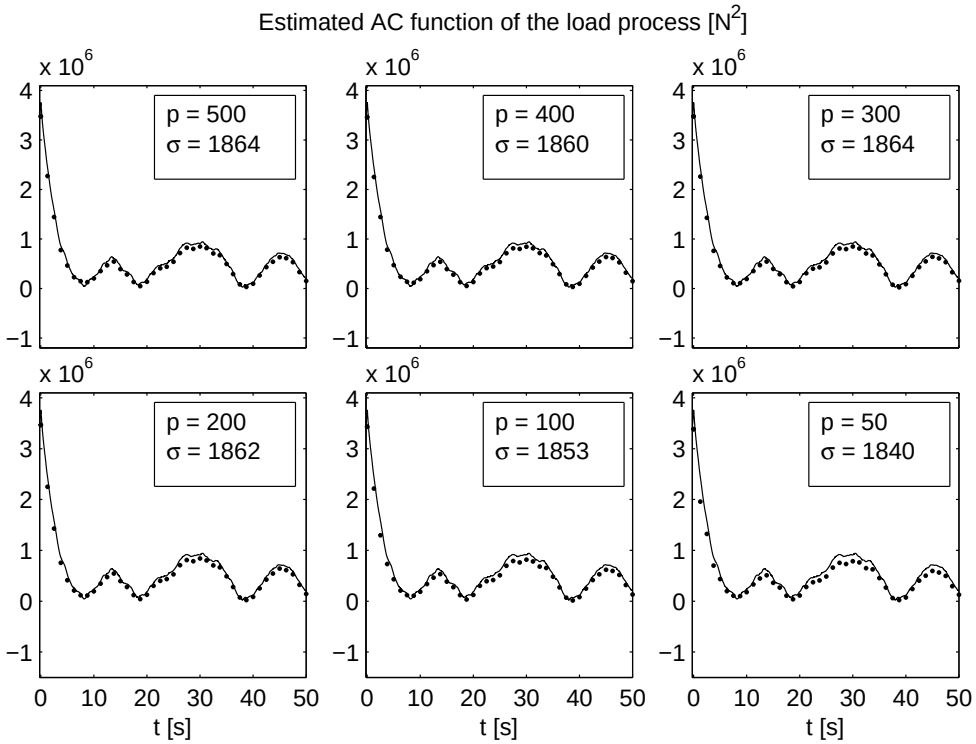

Figure 7.15: Case study 2: Comparison of the actual load process with Kármán velocity PSD (σ = 1938 [N]) exciting the structure at the top floor and the estimated AC functions by means of the H-WEKF in dependence on the considered number of load coefficients p. In all cases, a time series of 5 [min.] length (12000 samples) is taking into account for the calculation.

which initialized as before taking into account a measurement noise of 10 [%]. Again, with decreasing model accuracy the convergence of the filter (here, especially of the damping identification) is slower, and thus, successively, a longer measurement record of length $T = [5, 5, 5, 7.5, 7.5, > 25]$ [min.] is needed. Once again, a too small number of coefficients, here if $p \leq 50$, the damping estimates diverge. In all cases, the objective function θ^j is minimized after just one iterations. The identification results are again compared in terms of the relative estimation errors plotted in Fig. 7.14a and the resulting cumulative relative errors depicted in Fig. 7.14b with respect to the chosen number of coefficients.

Both, the stiffness and damping identification results reach an almost constant error level for $p \geq 50$ and $p \geq 100$, respectively, i.e. the mentioned divergence of the filter for $p = 50$ is just evident in the damping estimation. It is interesting to note, that a higher number of coefficients, does not lead to an improvement of the identification results. This behavior might be caused by an over-parameterization of the load process, that is by specifying $2p + 1$ state variables in order to estimate the unmeasured load process. Consequently, with increasing model order, a larger number of states must be estimated a priori in order to initialize the model. Of course, the initialization of the load process can be done in a

straight forward manner, as it just requires the generation of a set of Gaussian random numbers, but nevertheless, the introduced initial error as well as the number of states which must be updated at each time step, increases with increasing model order. Moreover, a comparison of the AC functions of the estimated load process and the one of the actual process exciting the structure shows, that the accuracy of the load identification is, as in the previous example, again almost independent from the number of coefficients as illustrated by Fig. 7.15. Even, the variances of the estimated time series are for the cases $p \leq 200$ nearly identical. This confirms, that due to the information gained from the measurement of the system response, the load can be modeled using a much smaller number of coefficients.
All in all, it is encouraging to note, that indeed, the best result is obtained, for $p = 200 - 300$ confirming the assumptions, that the required number of coefficients coincides with the number needed for an adequate approximation of the PSD function and the process's variance. This result is important also from a computational point of view, as, the resulting number is in general evidently smaller than the one needed in order to approximate the AC function with comparable accuracy.

8 Conclusions and Outlook

In the present thesis a new extended Kalman filter-based algorithm for the parameter identification of structures excited by correlated random loads is proposed. Focus lies on the stochastic excitation by wind turbulences and wind waves. In contrast to classical ambient vibration identification techniques, which model the unmeasured load process as white noise and thus are not applicable in case of non-white excitations, the proposed method takes into account additional information about the second-order statistics of the load process, e.g. obtained from measurements in the vicinity of the structure, and thus allows estimating both, the unknown system parameters as well as the unmeasured load process.
The work was divided into two subparts, namely the characterization and modeling of such loads and the identification of the modal parameters using output-only measurements of the system response.

Part 1: Modeling of Stochastic Excitations

It is shown that wind turbulences and wind waves of the fully developed sea can be modeled as stationary Gaussian random processes from the knowledge of the second order statistics. A detailed comparison of the most important model spectra is given and their applicability for wind and ocean engineering problems is discussed.
Then the-state-of-the-art on classical algorithms for the digital simulation of Gaussian random processes is reviewed, among them the spectral representation method and digital filter schemes either obtained from the spectral factorization of the PSD function or by means of time series modeling using ARMA-based approaches. From the literature review it can be summarized that at the state-of-the-art, the main limitations in the field of digital simulation of correlated Gaussian loads are: i) the methods are not applicable to long memory processes with power law decay; indeed, ii) if the load is long-correlated, time series models require an infinite number of coefficients to properly simulate the inverse power-law decay; iii) the number of coefficients p and q of time series models, such as ARMA models, cannot be predicted a priori and, increasing them, requires the recalculation of the whole set of coefficients;

iv) this limitation is more severe from the computational time point of view in multivariate and multidimensional cases; vi) efficient simulation methods, based on Karhunen-Loève or Wavelet methods, cannot be rewritten in state space form needed to combine them with the used identification algorithm; vii) analytic approaches such as the spectral factorization method require that the PSD function is of rational form, which is not the case for the discussed wind and wind wave model spectra.

It is shown that these short comings can be overcome, by the use of a recently introduced method, called H-fractional spectral moment (H-FSM) decomposition. Due to its analytic form, its implementation is straight forward and it is applicable to arbitrarily correlated processes, without restriction to the functional form of the PSD function. This is illustrated by applying the method to three processes of engineering interest, namely a process with (i) exponential autocorrelation function and (ii) von Kármán power spectral density, which are extensively used in wind engineering in order to model along wind turbulences, and (iii) with Pierson Moskowitz power spectral density which is widely used in coastal engineering applications for the description of wind induced waves. Furthermore, a list of the FSMs of the discussed wind velocity and wind wave model spectra as well as the corresponding wind load and wind wave load model spectra is provided.

It is shown that the accuracy of the simulation is directly related to the accuracy of the numerical evaluation of the fractional integral operator involved. In [Cottone et al 2010d] the use of the Grünwald-Letnikov (GL) series representation is proposed. It was shown that this approximation leads to a discretization error depending on the chosen sampling interval and a truncation error caused by the truncation of the infinite series after a finite number of values, that is, by considering just the recent past of the process, instead of taking into account the complete process's memory. A sensitivity analysis revealed, that i) the accuracy of the GL discretization strongly depends on the chosen sampling interval; ii) a too large sampling interval ($\tau \geq 0.025$) leads to an erroneous variance of the generated time series; iii) the sample AC function of the generated time series decays to fast if a too short memory is chosen; iv) the required number of coefficients and thus, the efficiency of the algorithm, increases inverse proportionally to the sampling interval and proportionally to the memory. It is shown that the discretization error can be significantly decreased by the use of an alternative sampling scheme, the so-called centered GL discretization. The sensitivity analysis revealed that the accuracy of the approximation is almost independent from the chosen sampling interval and leads to a significant reduction of the discretization error, to be precise by about about 55 [%] for short sampling intervals and about 80 [%] for large sampling intervals of $\tau \geq 0.1$. Furthermore, due to the inverse proportional dependence of the number of coefficients on the sampling interval, a significant improvement of the efficiency is archived by the use of the proposed algorithm. Based on these properties, an efficient procedure for

selecting the optimal number of model coefficients is developed.
Finally, a modified form of the H-FSM decomposition is proposed which makes the method applicable for the modeling of long memory processes with unbounded variance. The modification is needed as the PSD function of long memory processes exhibits a characteristic pole at zero frequency and thus causes the classical H-FSM to diverge. It must be stressed, that the applicability to both, short and long memory processes, makes the method unique among the classical digital filter schemes.

PART 2: Parameter Identification under Correlated Random Loads

The proposed identification algorithm is based on a modification of the classical extended Kalman filter to arbitrarily correlated load processes. Thus, first the main characteristics of the Kalman filter and its non-linear extension, the extended Kalman filter (EKF), needed to solve the identification problem, are reviewed. In case of a stochastic excitation, it is a common approach to run the EKF on a set of measurements and to represent the identification results by the sample mean and the corresponding sample deviation indicating the estimation uncertainties. As this strategy is not appropriate if just a small number of measurements is available, the use of the so-called weighted extended Kalman filter (W-EKF) algorithm is proposed. It is based on a weighted global iteration procedure which i) improves the accuracy of the identification, especially if the first guess of the unknown parameters is poor; ii) is applicable even if just one measurement record is available; iii) allows assessing the filter accuracy as well as indicates the divergence to erroneous identification results by means of an objective function; and, as the filter convergences in general after a small number of iterations, iv) is more efficient.
In order to verify the implementation and stability of the method, it is applied to a three story shear building excited at the top floor by a white noise process in order to estimate the stiffness and damping parameters of the structure. A sensitivity analysis is undertaken in order to investigate the dependence of the accuracy of the parameter identification on the chosen initialization of the filter and the intensity of the measurement noise. It is observed, that i) the filter provides stable estimates also in the presence of strong measurement noise after just 2 - 5 iterations; whereat ii) the identification results converge faster with decreasing measurement noise intensity and with increasing error covariance of the prior parameter estimates; iii) in all cases, the stiffness parameters of the lumped model are estimated with high accuracy while the damping parameters are estimated with satisfying accuracy. The lower accuracy can be explained by the fact, that in the example considered here, the damping parameters have no significant effect on the modal frequencies and the observed system

response. As the update of the parameters is based on the minimization of the error between the obtained measurement and the predicted system's response, it is in general difficult to identify parameters whose estimation has almost no impact on the prediction error.
In case of non-white excitations such as wind turbulences or wind waves, the EKF filter as well as the classical ambient vibrations identification techniques lead to poor estimation results as the white noise assumption is no longer justified. In order to solve the identification problem under correlated loads a new extended Kalman filter-based algorithm is proposed which allows the simultaneous estimation of the unknown structural parameters and the unmeasured load process by taking into account additional information about the second-order statistics of the process, e.g. obtained by wind measurements in the vicinity of the structure. The new filter is called *H-fractional (weighted) extended Kalman filter* as it combines the (weighted) extended Kalman filter algorithm with the H-fractional spectral moment decomposition needed for the modeling of the load process. Based on the latter a state space representation of arbitrarily correlated load processes is derived in analytic form which neither requires the factorization of the PSD function nor any optimization procedure, but which can be given immediately, once the H-fractional spectral moments of the transfer function have been calculated. Augmenting the state space model of the dynamical system by the obtained linear model of the load process, results in an overall linear system driven by white noise once again to which standard tools as the Kalman filter based on linear system theory for response analysis, optimization, and design of active control devices can be applied.
In order to verify the method, it is applied to a SDOF system to estimate the stiffness and damping parameter using noisy measurement data of the system response. Three load cases are discussed, namely wind turbulences with (i) exponential autocorrelation function and (ii) von Kármán velocity power spectral density, respectively, as well as wind waves with (iii) Pierson Moskowitz power spectral density function. First, the H-fractional EKF (H-EKF) algorithm and the H-fractional W-EKF (H-WEKF) is run on the augmented state space model. While in the former case a set of 20 measurements is used for the calculation of the sample mean and covariance of the parameter estimates, the latter is run iteratively using just a single sample of the system response until the objective function is minimized. The identification results are compared with those obtained by the classical EKF where the unmeasured load process is introduced as Gaussian white noise with equivalent standard deviation. The following conclusions can be drawn: i) Both, the H-EKF and the H-WEKF succeed in estimating the stiffness and damping parameter as well as the system's excitation with comparable high accuracy; ii) the H-WEKF requires just about three iterations until the filter converges and thus is much more efficient than the H-EKF; iii) The classical EKF leads in all three load cases to poor estimation results confirming the need of a more advanced identification algorithm in case of non-white excitations.

It must be stressed, that in case where the loading is characterized by a rational PSD function, the standard spectral factorization method outperforms the H-WEKF from a computational point of view as it leads to a state space representation of lower order. However, the strength of the proposed method is its general applicability to arbitrary spectra and its straight forward implementation.

In order to investigate the H-WEKF with respect to accuracy and efficiency in more detail, the filter is applied for the identification of the stiffness and damping parameters of the previously discussed three story shear building subjected at the top floor to exponentially correlated wind gusts as well as wind turbulences with von Kármán velocity PSD function. As the efficiency of the method strongly depends on the dimension of the state space model describing the load process, two model reduction strategies are investigated: The first is the reduction of the sampling interval using the fact, that the number of required load coefficients p depends inverse proportionally on the sampling interval. As the state space model is of order $2p+1$, halving the sampling interval, increases the model order by a forth. The second strategy is the less accurate modeling of the process. To this aim, a sensitivity analysis is undertaken where the number of coefficients is first chosen in such a way that the second order statistics are modeled with high accuracy and then the number is reduced successively until the filter diverges. The obtained results can be summarized as follows: i) A larger sampling interval leads to a slower convergence of the parameter identification which might be problematic, if the required length of the measurement record exceeds a duration where the stationarity of the signal becomes questionable; thus this strategy is not recommended; ii) The parameter identification, especially the damping estimation converges slower with decreasing model order and diverges if a too small number of coefficients is used; iii) The best estimates are obtained in case that the number of coefficients was chosen such, that the frequency content, i.e. the PSD function is modeled accurately. The latter is achieved using just half as much coefficients needed for the modeling of the AC function with comparable accuracy[1]; iv) A very high number of coefficients does not necessarily lead to better identification results. This might be caused by an over-parameterization of the load process, that is by specifying $2p+1$ variables in order to estimate the unmeasured load process; thus with increasing model order, a larger number of states must be updated based on the information obtained from the system response; v) A comparison of the sample AC functions of the estimated load process and the one of the actual process exciting the structure reveals, that the accuracy of the load identification is almost independent from the chosen number of coefficients supporting the assumption above.

[1]Though, in order to avoid aliasing, the chosen sampling rate $1/\tau$ should exceed the Nyquist–Shannon criterion, i.e. $1/\tau > 2f_c$, where f_c is the cut-off frequency of the spectrum

Summing up, the relevant properties of the proposed identification method are: i) it is applicable for arbitrarily correlated loads, i.e. without any restriction to the functional form of the PSD function; ii) it is efficient also in case of long-memory processes; iii) the coefficients of the model for the process are known in analytical form and their number can be arbitrarily increased to achieve higher accuracy without recalculation; iv) it can be efficiently combined with the centered Grünwald-Letnikov discretization scheme leading to a significant increase of the accuracy and efficiency of the method v) due to its analytic form, a general state space representation can be derived, once the H-fractional spectral moments are calculated which neither requires the spectral factorization of the PSD function nor any optimization scheme; and thus vi) it can be efficiently combined with the (weighted) extended Kalman filter or any other state-space model-based identification algorithm; vii) it allows estimating both, the system parameters and the unmeasured system excitation.

Outlook

The present work focused on the dynamic excitation of structure by (i) stationary, (ii) univariate, (iii) Gaussian random loads in the scope of parameter identification. While the Gaussianity of the input process is a constraint resulting from the model assumptions of the Kalman filter algorithm used for the parameter identification, the remaining assumptions are simplification made in the modeling process. Using the results presented in [Cottone et al 2011; Cottone and Di Paola 2011], where the H-fractional spectral moment decomposition is applied for the digital simulation of multivariate wind velocity fields, it is believed that the proposed method is easily extensible to the identification problem of structures subjected to multivariate loads.

Of course, the high dimensionality of the state space representation of the load process might lead to computational difficulties in the multivariate case. The problem is linked to the non-causality[2] of the generated time series, which was caused by the neglect of the imaginary part of the transfer function in order to simplify the spectral factorization of the PSD function (s. Eq. (5.12)). The problem of finding the causal transfer function remains to be solved in further research. As the latter allows halving the number of load coefficients the solution would lead to a significant reduction of the computational costs. Furthermore, in earthquake engineering, the generation of causal time series is of great importance for the modeling of the seismic ground motion as well as the description of the transition states of the structural response. The problem might be solved by an approach found in [Dietrich and Newsam 1997; Chan 1999], initially proposed for the digital simulation of stationary

[2] i.e. the dependence of the actual sample on both, past and future values of the weighted white noise process

Gaussian processes. In order to factor the covariance matrix, its Toeplitz form is used to embed it in a circulant matrix. It is shown, that the latter has some particular features[3], allowing a fast and efficient factorization of the covariance matrix by means of FFT. Noting that the matrix transfer function $\mathbf{H}(\gamma)$ (5.31) is of Toeplitz form, the concept might be used for its factorization $\mathbf{H}(\gamma) = \mathbf{h}(\gamma)\mathbf{h}^*(\gamma)^T$ where $\mathbf{h}(\gamma)$ is the causal transfer matrix. Similar to the non-casual transfer function $\mathbf{H}(\omega)$ whose elements are linked to the FSMs of the process, it is believed that the coefficients of the causal function $\mathbf{h}(\gamma)$ corresponds to an alternative fractional integral operator leading to a modified set of FSMs.

Due to the time-domain formulation of the Kalman filter algorithm, non-stationary excitations can be introduced by means of a time-variant state space model of the load process. Using the concept of evolutionary spectra, the non-stationary load process $\{X(t)\}$ is obtained by multiplying a stationary process $\{X_s(t)\}$ with given PSD function, by a deterministic modulation function $f(t)$. That is, in order to introduce the non-stationary process in the proposed method, first a state space representation of the stationary process $\{X_s(t)\}$ is derived, whose output is then multiplied by the modulation function. In future works, the identification of the modulation function by means of the proposed method might be of interest in the scope of load identification.

In the discussed examples, the error in the damping estimation was significantly higher than in the stiffness estimation. It was argued that higher errors are caused by the small impact of the damping on the structural response and thus, little information about the damping can be extracted from the measurements. Of course, if the system is excited close to the eigenfrequency, then the damping has a significant influence on the system's response. Thus in future works a sensitivity analysis needs to be undertaken, in order to investigate the influence of the frequency content of the systems excitation on the accuracy of the parameter estimation.

[3] e.g. the eigenvalues of the circulant matrix $\mathbf{C}$ is the FFT of any row from $\mathbf{C}$, the eigenvectors of $\mathbf{C}$ are independent from $\mathbf{C}$ and the modal matrix is an unitary matrix [Chan 1999]

Annexe

A.1 Definitions

A.1.1 Characteristic function

The characteristic function (CF) provides an alternative form for giving a complete description of a probability distribution. It is defined as the Fourier transform of the probability density function and is obtained from Eq. (2.3b), setting $g(X) = e^{i\omega X}$, i.e.

$$\phi(\omega) = E\left[e^{i\omega X}\right] = \int_{-\infty}^{\infty} e^{i\omega x} p(x) dx \tag{A.1}$$

where $x \in \mathbb{R}$, $i = \sqrt{-1}$. An important feature of the CF is its moment-generation property, which leads to the relation

$$\left.\frac{\partial \phi^j(\omega)}{\partial \omega^j}\right|_{\omega=0} = i^j E\left[X^j\right] \tag{A.2}$$

That is, instead of calculating the moments of the random variable by evaluating the integral (2.3b), they can be obtained directly from the CF by differentiating of the characteristic function and evaluating the derivative at $\omega = 0$ using the relation A.2. Finally, using the Taylor series expansion of the CF, the following relation can be used for the reconstruction of the CF from the knowledge of the integer moments (provided that they exists):

$$\phi(\omega) = \sum_{j=0}^{\infty} E\left[(iX)^j\right] \frac{x^j}{j!} \tag{A.3}$$

It must be stressed that the integer moments might diverge, e.g. if the probability density function is heavily tailed as it is the cases for the α-stable distribution. Thus the relation (A.3) is not applicable to all types of density functions.

A.1.2 Stationarity

Stationary processes are a special class of time series, which are based on the assumption that the stochastic process $\{X(t)\}$ is in a particular state of statistical equilibrium. In section 2.1.1 the stationarity of the second order statistics, denoted as wide sense stationarity, was introduced. Clearly, the concept of second order stationarity can be extended to higher-order moments, i.e. the process $\{X(t)\}$ is said to be stationary up to order m if for any finite collection of times $t_1 < t_2 ... < t_n$ the joint moments up to order m exists and are invariant under time shift τ, i.e. for all positive integers m_1,m_2,..,m_n where $m_1 + m_2 + ... + m_n \leq m$, it holds [Priestley 1981, ch. 3]

$$E\left[X(t_1)^{m_1}X(t_2)^{m_2}...X(t_n)^{m_n}\right] = E\left[X(t_1+\tau)^{m_1}X(t_2+\tau)^{m_2}...X(t_n+\tau)^{m_n}\right] \tag{A.4}$$

The most rigorous definition of stationarity is the definition in the strict sense: A process is said to be *strictly* stationary if the stochastic properties of the time series are invariant under time shift. That is, for any finite collection of times $t_1 < t_2 < ... < t_n$ the process $\{X(t)\}$ can be defined by the condition, that the finite set $X(t_1)$,$X(t_2)$,...,$X(t_n)$ and $X(t_1+\tau)$,$X(t_2+\tau)$,...,$X(t_n+\tau)$ of random variables from the process have the same joint distribution for an arbitrary time shift τ [Box et al 2008], [Brockwell and Davis 2002], i.e.

$$F(x_1, x_2, \ldots, x_n; t_1+\tau, t_2+\tau, \ldots, t_n+\tau) = F(x_1, x_2, \ldots, x_n; t_1, t_2, \ldots, t_n) \tag{A.5}$$

That is, it must be kept in mind, that the knowledge of the time-invariance of the second order moments does not provide any information on the finite dimensional distribution defined (A.5), and thus, a stationary process in the wide sense may not be stationary in the strict sense.

A.1.3 Ergodicity

A process is said to be mean ergodic, if it is mean-value stationary and the time average of any realization j of the process converges to the expected value $\mu(t) = E[X(t)]$ as $T \to \infty$, i.e.

$$\mu(t) = \lim_{T\to\infty} \frac{1}{T} \int_{-T/2}^{T/2} X^j(t)dt = E[X(t)] \tag{A.6a}$$

Similarly a process is said to be ergodic in the second moment if it is second-moment stationary and the following identity holds

$$R(\tau) = \lim_{T\to\infty} \frac{1}{T} \int_{-T/2}^{T/2} X^j(t+\tau)X^j(t)dt = E[X^j(t+\tau)X^j(t)] \tag{A.6b}$$

It must be stressed that it is difficult to prove that a physical process is ergodic as there will be never an infinite time series available in order to calculate the required cumulative distribution function. For a detailed discussion on ergodicity see for instance [Lutes and Sarkani 2004, p. 132ff].

A.1.4 Selected processes

A.1.4.1 Gaussian vector process

If a process is characterized by a set of random variables $X(t_1), X(t_2),...,X(t_n)$ which belong to the same probability space, then the sequence $\mathbf{x} = [X(t_1), X(t_2, \ldots, X(t_n)]$ is a n-dimensional random vector process with the following joint multidimensional normal distribution

$$f(\mathbf{x},\mathbf{t}) = (2\pi)^{-n/2}|\mathbf{C}_X|^{-1} \exp\left((\mathbf{x}-\mu)^T\mathbf{C}_X^{-1}(\mathbf{x}-\mu)^T\right) \tag{A.7a}$$

where $\mu \in \mathbb{R}^n$, $\mathbf{C}_X \in \mathbb{R}^{n\times n}$ denote the mean vector and covariance matrix of the sequence $X(t_1), X(t_2),...,X(t_n)$ which are given by

$$\mu = \begin{bmatrix} \mu(t_1) \\ \mu(t_2) \\ \cdots \\ \mu(t_n) \end{bmatrix}; \qquad \mathbf{C}_X = \begin{bmatrix} C_x(t_1,t_1) & C_x(t_1,t_2) & \ldots & C_x(t_1,t_n) \\ C_x(t_2,t_1) & C_x(t_2,t_2) & \ldots & C_x(t_2,t_n) \\ \cdots & \cdots & \cdots & \cdots \\ C_x(t_n,t_1) & C_x(t_n,t_2) & \ldots & C_x(t_n,t_n) \end{bmatrix} \tag{A.7b}$$

where the mean values $\mu(t_k)$ and covariances $C_x(t_k,t_j)$ are calculated by Eq. (2.5) and Eq. (2.6), Thus, Gaussian processes are completely characterized by the statistics up to the second order. Hence, the existence of a time invariant mean $\mu(t)$ and autocorrelation function $R_X(\tau)$ defined in Eq. (2.6) ensures the stationarity of the Gaussian process. That is, in the Gaussian case, weak stationarity of the process also implies strict stationarity.

A.1.4.2 Gaussian random fields

This section is based on the definitions given in [Di Paola 1998]. This paper gives an excellent review on digital simulation techniques with application to wind velocity fields and is recommended for further reading. A process which vary in space and in time can be modeled as random field. Assume for instance a wind velocity field acting on a building. Then the velocity at a certain point depends on the time t as well as on the coordinates $(\mathrm{x}, \mathrm{y}, \mathrm{z})$ describing the location of the point P in space. Thus, the stochastic field velocity $V(x, y, z; t)$ can be expressed as one-variate four-dimensional ($1V$-$4D$) random field. Let P, P' denote two locations in space, then the cross correlation (XC) function of the processes $V(x,y,z;t)$ and $V(x',y',z';t)$ is given by

$$R_V(x, y, z,x', y', z'; t,t') = E[V(x, y, z; t)V(x', y', z'; t, t')] \tag{A.8a}$$

where $E[\cdot]$ denotes the expectation operator. In case the process is stationary and homogeneous, then the XC function depends solely on the time shift $\tau = t - t'$ and the spatial distance $\xi = x - x'$, $\eta = y - y'$ and $\zeta = z - z'$, yielding

$$R_V(\xi, \eta, \zeta; \tau) = E[V(x, y, z, ; t)V(x + \xi, y + \eta, z + \zeta; t + \tau)] \tag{A.8b}$$

Alternatively, the process can be characterized in the frequency domain by the cross power spectral density (XPSD) function obtained by a four folded Fourier Transform, i.e.

$$S_Y(k_1,k_2,k_3;\omega) = \frac{1}{(2\pi)^4} \int_{-\infty}^{\infty} .. \int_{-\infty}^{\infty} R_V(\xi, \eta, \zeta; \tau) e^{-i(\xi k_1 + \eta k_2 + \zeta k_3 + \omega\tau)} d\xi d\eta d\zeta d\tau \tag{A.8c}$$

where k_1, k_2 and k_3 are wave numbers. If the random field depends only on the absolute value of the distance between ξ, η and ζ, then the field is said to be isotropic. It must be stressed, that a wind velocity field is in general dependent on the height z and thus not homogeneous.

Alternatively, the velocity field can be discretized and characterized by the field velocities in a finite number of n points. In this case the field reduces to a discretized n-variate *one*-dimensional (nV-$1D$) stochastic vector process where the components of the n-dimensional zero-mean vector $\{\mathbf{V}(t)\} = [V_1(t), V_2(t), \ldots, V_n(t)]$ describe the along wind processes acting on n locations of the structure at time t. The zero-mean stationary Gaussian nV-$1D$ stochastic vector field is completely characterized by the XC and corresponding XPSD matrices of

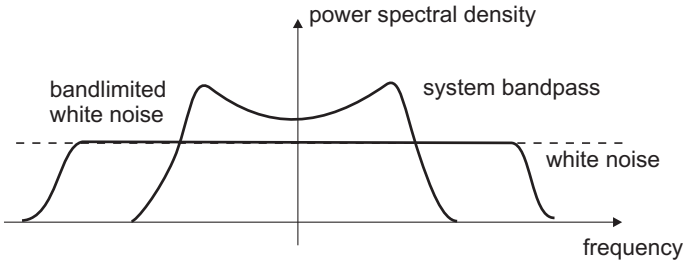

Figure A.1: System's bandpass and band-limited white noise [Maybeck 1979]

the components given by

$$\mathbf{R}_V(\tau) = \begin{bmatrix} R_{11}(\tau) & R_{12}(\tau) & \dots & R_{1n}(\tau) \\ R_{21}(\tau) & R_{22}(\tau) & \dots & R_{2n}(\tau) \\ \dots & \dots & \dots & \dots \\ R_{n1}(\tau) & R_{n2}(\tau) & \dots & R_{nn}(\tau) \end{bmatrix}; \quad \mathbf{S}_V(\omega) = \begin{bmatrix} S_{11}(\omega) & S_{12}(\omega) & \dots & S_{1n}(\omega) \\ S_{21}(\omega) & S_{22}(\omega) & \dots & S_{2n}(\omega) \\ \dots & \dots & \dots & \dots \\ S_{n1}(\omega) & S_{n2}(\omega) & \dots & S_{nn}(\omega) \end{bmatrix} \tag{A.9a}$$

where $S_{ij}(\omega)$ is the Fourier Transform of the cross correlation function $R_{ij}(\tau)$. They are given by

$$R_{ij}(\tau) = \int_{-\infty}^{\infty} V_i(t+\tau)V_j(t)d\tau \tag{A.9b}$$

$$S_{ij}(\omega) = \frac{1}{2\pi}\int_{-\infty}^{\infty} R_{ij}(\tau)e^{-i\omega\tau}d\tau \tag{A.9c}$$

A.1.4.3 White noise process

A stationary random process with constant PSD function $S_W(\omega)$ is defined as white noise process $\{W(t)\}$. Its name originated from optics where light with constant power spectral density over all visible frequencies is denoted as white light. Whiteness implies that the process is uncorrelated, i.e. its autocorrelation function (AC) is described by the dirac delta function $\delta(t)$, being infinite at time lag $\tau = 0$ and zero elsewhere. Consequently, the white noise signal is unpredictable as the information about values at past instants of time does not provide any information on the values of the process at future time steps. If the random variables $W(t_j)$, $W(t_k)$ are not only uncorrelated for every time instant t_j and $t_j \neq t_k$ but additionally independent, then $\{W(t)\}$ is called a strictly white noise process.
From a physical point of view, in nature the white noise process does not exist as the constant PSD leads to a process with infinite variance corresponding to an unbounded, infinite fast varying signal. However, the white noise assumption is often justified for two reasons: Firstly, each system is characterized by its frequency bandpass, that is the frequency range in which the system is excitable. Outside this frequency band the system response is insignificant in

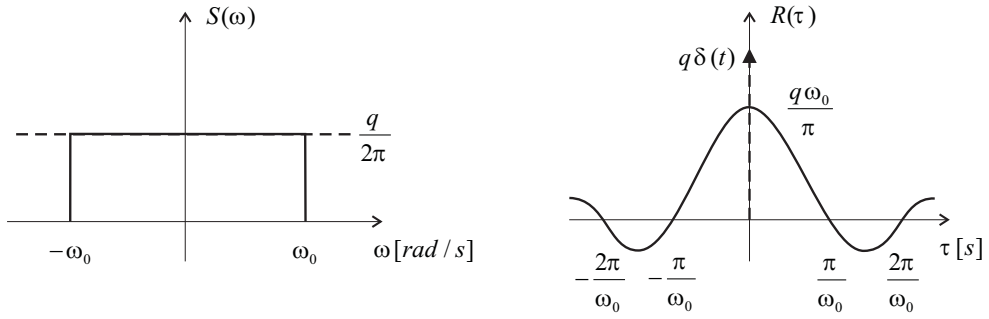

Figure A.2: PSD and AC function of the white noise process (dashed) and band-limited counterpart (line)

the overall system response. Secondly, many input processes can be characterized as band-limited white noise, e.g. the PSD is flat within the system bandpass and vanishes above a certain frequency ω_0 as illustrated in Fig. A.1 [Maybeck 1979, p. 7ff.]. The PSD and AC function of the white noise is depicted in Fig. A.2. It must be noted that $R_{Wb}(\tau)$ is zero for $\tau = k\pi/\omega_0$ and $k \in \mathbb{N}_{>0}$. Consequently, if the underlying process is discretized choosing $t_s = \pi/\omega_0$ an uncorrelated set of random variables is obtained. In order to make use of this simplification, band-limited input processes are often approximated as white band-limited and assumed to be uncorrelated [Brown and Hwang 1997, p. 92ff.].
The so-called white noise sequence refers to a discretized white noise process with zero mean and AC function $R_W(\tau) = E[W_k W_j] = qt_s\delta_{kj}$. The elements of the sequence are mutually uncorrelated and can be generated as Gaussian random numbers with zero mean and standard deviation $\sigma^2 = qt_s$ There exists other non-Gaussian white noise processes, such as the Poisson or the Lévy white noise process, but which won't be treated throughout the thesis.

A.1.4.4 Brownian motion

Brownian motion is a physical phenomenon, first observed experimentally by Robert Brown in 1827, describing the random movement of microscopic particles suspended in a liquid or gas caused e.g. by other particles hitting it or by an external force. Assuming that the particle position at time $t = 0$ is Y_0, then its position at time n is given as $Y_n = Y_0 + \sum_{i=1}^{n} X_i$, where the displacements $X_1, X_2, X_3, \ldots$ are modeled as independent and identical distributed random variables. Such a process is also known as random walk process which approaches a Brownian motion in distribution as the time step $\tau \to 0$. Wiener proofed that the path of Brownian particle is almost everywhere continuous but nowhere differentiable is almost everywhere continuous but nowhere differentiable. That is the Brownian motion $\{B(t)\}$ describes the macroscopic characteristics of a random walk with sufficiently small jumps to become

negligible in the macroscopic picture, such that the sample path is continuous. It has the following properties [Mörters and Peres 2010, p. 1-2]

- for all times $0 \leq t_1 \leq t_2 \leq \ldots \leq t_n$ the increments $B(t_n) - B(t_{n-1})$, $B(t_{n-1}) - B(t_{n-2})$, etc. are independent,
- the increments are stationary, that is, the probability distribution of the increment $\Delta B = B(t+\tau) - B(t)$ is time-invariant, e.g. independent from t
- the process $\{B(t)\}$, $t \geq 0$ has almost surely[1] continuous paths.

Consequently, using the central limit theorem it can be shown that these properties imply that for every $t \geq 0$ and $\tau \geq 0$ the increment process $\Delta B(t)$ is normally distributed with

$$E[\Delta B(t)] = \mu\tau \tag{A.10a}$$
$$E[\Delta B(t)^2] = \sigma^2\tau \tag{A.10b}$$

The process is characterized by three values, the drift μ, the diffusion σ and the initial probability distribution of $B(0)$ and thus is denoted as *Brownian motion with drift μ and diffusion σ*. The standard *Brownian motion* process refers to the special case where $\mu = 0$ and $\sigma^2 = 1$ and which starts from zero, i.e. $B(0) = 0$. Introducing $t = 0$ and $\tau = t$ in the definitions Eq. (A.10), it follows that not only the increments are Gaussian distributed but also the Brownian motion process is Gaussian with

$$E[B(t)] = \mu t \tag{A.11a}$$
$$E[B(t)^2] = \sigma^2 t \tag{A.11b}$$

Moreover suppose that $s < t$ and using that the increment $B(t) - B(s)$ is of zero mean and is independent of $B(s)$, and $B(s)$ has variance $\sigma^2 s$, then the correlation of $B(t)$ and $B(s)$ is given by

$$R_B(t,s) = E[B(t)B(s)] = E[(B(t) - B(s))\,B(s)] + E[B(s)^2] = \sigma^2 s$$

In the general case for any t and s, the autocorrelation can be expressed as

$$R_B(t,s) = \frac{\sigma^2}{2}\left(|t| + |s| - |t-s|\right) = \sigma^2 \min(t,s) \tag{A.11c}$$

These properties lead to the following recursive generation procedure

[1] that is, with probability 1

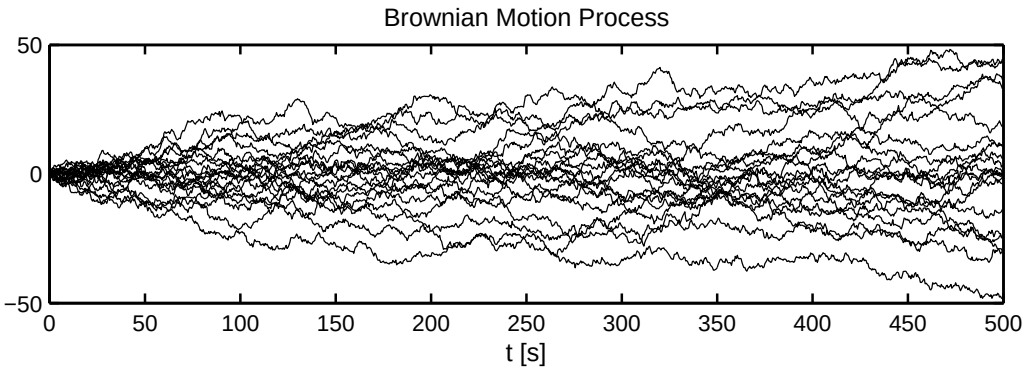

Figure A.3: 20 samples of the Brownian motion process $B(t)$ for $B(0) = 0$, $\mu = 0$, $\tau = 0.05$ [s]

$$B(t+1) = B(t) + \Delta B(t) = B(t) + \sqrt{\tau}G(t) \tag{A.12}$$

where $G(t)$ is a realization of the Gaussian white noise process $WN(0,1)$. Fig. (A.3) depicts 20 samples of the process choosing $\tau = 0.05$ and $\mu = 0$. In agreement with Eq. (A.11) the process is non-stationary with linearly increasing variance. A process $\{X(t)\}$ is said to be mean square differentiable if the limit $\dot{X}(t) \approx \lim_{\tau\to 0}(X(t+\tau) - X(t))/\tau$ used to describe the mean square of the approximated derivative $\{\dot{X}\}$ exists.
In case of the Brownian motion $B(t)$

$$E\left[\frac{B(t+\tau) - B(t)}{\tau}\right] = 0 \tag{A.13a}$$

$$E\left[\left(\frac{B(t+\tau) - B(t)}{\tau}\right)^2\right] = \frac{\sigma^2}{\tau} \tag{A.13b}$$

the mean value (A.13a) of the difference approximation approaches zero as $\tau \to 0$ and the mean square derivative (A.13b) becomes infinite, proofing that the Brownian motion is non-differential almost surely. However, interpreting the time derivative of the Brownian motion in a distributional sense, such that $\lim_{\tau\to 0} 1/\tau = \delta(t)$, it can be thought of as a δ-correlated stationary, Gaussian process with zero mean zero and covariance

$$E[\dot{B}(t)\dot{B}(s)] = \sigma^2\delta(t-s) \tag{A.13c}$$

which are exactly the characteristics of a Gaussian white noise process. This leads to the formal definition

$$B(t) - B(0) \stackrel{\text{def}}{=} \int_0^t W(s)ds; \qquad \text{or equivalently} \qquad W(t) \stackrel{\text{def}}{=} \frac{d}{dt}B(t) \tag{A.14}$$

relating the Brownian motion and the Gaussian white noise process which is of great importance for the solution of stochastic differential equations. A mathematical derivation can be found for instance in [Maybeck 1979, p. 147ff].

B.1 Digital Simulation of Ambient Loads

B.1.1 Iterative derivation of the ARMA coefficients

A weakly univariate stationary process $\{F_t\}$ with given AC function $R_F(\tau)$ is said to be an ARMA(p,q) series with autoregressive order $p \geq 0$ and moving-average order $q \geq 0$, if it is the solution of the following discrete difference equation[1]

$$F_k - a_1 F_{k-1} - \ldots - a_p F_{t-p} = W_k - b_1 W_{k-1} - \ldots - b_q W_{k-q} \tag{B.1}$$

where $\{W_t\}$ is a sample of a zero mean Gaussian white noise sequence with variance σ_W^2 (compare Eq. (2.11)). The coefficients of the ARMA(p,q) model can be estimated on basis of Eq. (3.13) from the empirical covariances known from measurements of the load process. Assuming that $n = 0,1,\ldots,N-1$ samples of the process $F_t = [F_0, F_1, \ldots, F_{N-1}]$ are known, the AC function is estimated by

$$\hat{R}_F(k) = \frac{1}{N} \sum_{n=0}^{N-1-|k|} F_n F_{n+|k|} \tag{B.2}$$

and introduced in Eq. (3.16), leading to

$$\sum_{n=0}^{p} a_n \hat{R}_F(k-n) = \epsilon(n), \qquad k > q \tag{B.3}$$

where $\epsilon(n)$ refers to the error introduced by the estimation of the AC function. Rewriting this result in the linear least square problem

$$\hat{R}_F(k) = \sum_{n=1}^{p} a_n \hat{R}_F(k-n) = \epsilon(n), \qquad k > q \tag{B.4}$$

Estimating the AC functions for lags $n = 0,1,\ldots,M$ (and $M \leq N-1$), then the linear least square estimate (LSE) of the p AR coefficients of the ARMA model are obtained by

[1] It must be noted that in literature, e.g. [Box et al 2008], the ARMA series is sometimes defined using negative signs before the moving-average coefficients

minimizing [Kay 1993, p. 266ff.]

$$J = \sum_{n=q+1}^{M} \left[\hat{R}_F(n) - \left(\sum_{n=1}^{p} a_n \hat{R}_F(k-n) \right) \right]^2 = (\mathbf{x} - \mathbf{H}\mathbf{a})^T (\mathbf{x} - \mathbf{H}\mathbf{a}) \tag{B.5}$$

where

$$\mathbf{x} = \begin{bmatrix} \hat{R}_F(q+1) \\ \hat{R}_F(q+2) \\ \dots \\ \hat{R}_F(M) \end{bmatrix}, \quad \mathbf{a} = \begin{bmatrix} a_1 \\ a_2 \\ \dots \\ a_p \end{bmatrix}, \quad \mathbf{H} = \begin{bmatrix} \hat{R}_F(q) & \hat{R}_F(q-1) & \dots & \hat{R}_F(q-p+1) \\ \hat{R}_F(q+1) & \hat{R}_F(q) & \dots & \hat{R}_F(q-p+2) \\ \dots & \dots & \dots & \dots \\ \hat{R}_F(M-1) & \hat{R}_F(M-2) & \dots & \hat{R}_F(M-p) \end{bmatrix} \tag{B.6}$$

Here M should not be chosen too high, as for higher lags the number of averages considered in the estimation of the AC function, reduces to $N-k$ (compare Eq. B.2). Consequently, the AC estimate is less reliable with increasing lag k. The estimated autoregressive parameters $a_1, a_2, \dots, a_p$ can now be used for the estimation of the moving average coefficients $b_1, b_2, \dots, b_q$ and the variance of the white noise sequence σ_W^2 following an approach given in [Box et al 2008, p, 226ff.]. Unlike the modified Yule-Walker equations which are linear in the AR coefficients, the estimation of the MA parameters leads to an nonlinear problem which must be solved iteratively as shown in the following.
The ARMA(p,q) process in Eq. (3.9) might be thought of as pth order AR process

$$a(L)F_t = e_t \tag{B.7}$$

where the disturbance e_t follows a q order MA process

$$e_t = b(L)w_t \tag{B.8}$$

The latter can be expressed in terms of the estimated AR coefficients as

$$e_t = F_t - a_1 F_{t-1} - a_2 F_{t-2} - \dots - a_p F_{t-p} \tag{B.9}$$

The autocorrelation function $R_e(k) = E[e_{t-k} e_t]$ of the series Eq. (B.9) satisfies

$$R_e(k) = \sum_{j=0}^{p} a_j^2 R_F(k) + \sum_{j=1}^{p} (a_0 a_j + a_1 a_{j+1} + \dots + a_{p-j} a_p)(R_F(k+j) + R_F(k-j)) \tag{B.10}$$

for $j = 0,1,\ldots,q$, $a_0 = -1$ and $R_F(k)$ approximated by Eq. (B.4). Similarly, the autocorrelation can be expressed using Eq. (B.8) by

$$R_e(k) = E[b(L)a_{t-k}b(L)a_t] = (-b_k + b_1 b_{k+1} + b_2 b_{k+2} + \ldots + b_{q-k}b_q)\sigma_W^2, \qquad k = 1,2,\ldots,q \quad \text{(B.11)}$$

where $b_0 = 1$ and $R_e(k) = 0$ for $n > q$. Equalizing of the two equations yields the estimates of the parameters σ_W^2 and the coefficients b_q, b_{q-1}, ..., b_1 using the iteration

$$\sigma_W^2 = \frac{R_e(0)}{1 + b_1^2 + \ldots + b_q^2} \quad \text{(B.12)}$$

$$b_k = -\left(\frac{R_e(k)}{\sigma_W^2} - b_1 b_{k+1} - b_2 b_{k+2} - \ldots - b_{q-k}b_q\right) \quad \text{(B.13)}$$

For instance, in case $q = 2$, this leads to

$$\sigma_W^{2\,(i)} = \frac{R_e(0)}{1 + b_1^{2(i-1)} + b_2^{2(i-1)}}; \qquad b_2^{(i)} = -\frac{R_e(2)}{\sigma_W^{2\,(i)}}; \qquad b_1^{(i)} = -\left(\frac{R_e(1)}{\sigma_W^{2\,(i)}} - b_1^{(i-1)} b_2^{(i)}\right) \quad \text{(B.14)}$$

where $^{(i)}$ denotes the iteration step. The procedure is initialized, setting $b_1^0 = b_2^0 = \ldots = b_q^0 = 0$. The parameters are calculated iteratively starting with the variance $\sigma_W^{(i)}$ and the qth coefficient $b_q^{(i)}$. The remaining parameters $b_{q-1}, b_{q-2}, \ldots, b_1$ are calculated subsequently in decreasing order, using the most up to date values available. It can be shown, that the method converges linearly to the model parameters. To improve the rate of convergence, the Newton-Raphson method, which has quadratic convergence, can be used, as shown in [Box et al 2008, p. 226ff.].

B.1.2 Fractional spectral moments

B.1.2.1 Wind velocity spectra

In the following the FSMs $\Lambda(\gamma)$ (5.5) of the model wind velocity PSD functions $S_u(\omega) = 1/2G_u(\omega)$ discussed in section 2.2.2.4 are listed which can be used to reconstruct the PSD and AC function by the relation (5.11). Furthermore, the H-FSMs (5.14) of the transfer function are given which can be used for the reconstruction of the latter and the corresponding non-causal unit response function defined in Eq. (5.16) as well as the simulation of a realization of the velocity fluctuations by means of Eq. (5.31).

B.1.2.1.1 Kaimal (2.30)

$$\Lambda(\gamma) = \frac{aL(bL)^{-2-\gamma}\bar{U}_z^{1+\gamma}\sigma^2\Gamma\left(-\frac{1}{3}-\gamma\right)\Gamma(2+\gamma)}{\Gamma\left(\frac{5}{3}\right)}; \qquad -2 < Re\gamma < -\frac{1}{3} \tag{B.15a}$$

$$\Pi_H(\gamma) = \frac{2\sqrt{\pi}\left(\frac{bL}{\bar{U}_z}\right)^{-\frac{3}{2}-\gamma}\sqrt{\frac{aL\sigma^2}{q\bar{U}_z}}\Gamma\left(-\frac{2}{3}-\gamma\right)\Gamma\left(\frac{3}{2}+\gamma\right)}{\Gamma\left(\frac{5}{6}\right)}; \qquad -\frac{3}{2} < Re\gamma < -\frac{2}{3} \tag{B.15b}$$

B.1.2.1.2 Simiu (2.32)

$$\Lambda(\gamma) = \frac{2\bar{U}_z^{1+\gamma}z\lambda(z\lambda)^{-2-\gamma}\sigma^2\Gamma\left(-\frac{1}{3}-\gamma\right)\Gamma(2+\gamma)}{3\Gamma\left(\frac{5}{3}\right)} \qquad -2 < Re\gamma < -\frac{1}{3} \tag{B.16a}$$

$$\Pi_H(\gamma) = \frac{2\sqrt{\frac{2\pi}{3}}\left(\frac{\bar{U}_z}{z\lambda}\right)^{\frac{3}{2}+\gamma}\sqrt{\frac{z\lambda\sigma^2}{q\bar{U}_z}}\Gamma\left(-\frac{2}{3}-\gamma\right)\Gamma\left(\frac{3}{2}+\gamma\right)}{\Gamma\left(\frac{5}{6}\right)}; \qquad -\frac{3}{2} < Re\gamma < -\frac{2}{3} \tag{B.16b}$$

B.1.2.1.3 Davenport (2.36)

$$\tilde{\Lambda}(\gamma) = \frac{\bar{U}_{10}^{1+\gamma}\sigma^2\Gamma\left(-\frac{1}{6}-\frac{\gamma}{2}\right)\Gamma\left(\frac{3+\gamma}{2}\right)}{3L^{1+\gamma}\Gamma\left(\frac{4}{3}\right)}; \qquad -3 < Re\gamma < -\frac{1}{3} \tag{B.17a}$$

$$\tilde{\Pi}_H(\gamma) = -\frac{\sqrt{\frac{2}{3}}\pi^{3/2}\sqrt{\frac{1}{q}}\left(\frac{\bar{U}_{10}}{L}\right)^{1+\gamma}\sigma\Gamma\left(1+\frac{\gamma}{2}\right)}{\Gamma\left(\frac{2}{3}\right)\Gamma\left(\frac{4}{3}+\frac{\gamma}{2}\right)\sin\left(\frac{1}{6}\pi(2+3\gamma)\right)}; \qquad -2 < Re\gamma < -\frac{2}{3} \tag{B.17b}$$

B.1.2.1.4 Harris (2.37)

$$\tilde{\Lambda}(\gamma) = \frac{2^{\frac{1}{6}+\frac{\gamma}{2}}L\left(\frac{L}{\bar{U}_{10}}\right)^{-2-\gamma}\sigma^2\Gamma\left(-\frac{1}{6}-\frac{\gamma}{2}\right)\Gamma\left(1+\frac{\gamma}{2}\right)}{3\bar{U}_{10}\Gamma\left(\frac{5}{6}\right)}; \qquad -2Re\gamma < -\frac{1}{3} \tag{B.18a}$$

$$\tilde{\Pi}_H(\gamma) = \frac{2^{\frac{5}{6}+\frac{\gamma}{2}}\sqrt{\frac{\pi}{3}}\left(\frac{L}{\bar{U}_{10}}\right)^{-\frac{3}{2}-\gamma}\sqrt{\frac{L}{q\bar{U}_{10}}}\sigma\Gamma\left(-\frac{1}{3}-\frac{\gamma}{2}\right)\Gamma\left(\frac{3}{4}+\frac{\gamma}{2}\right)}{\Gamma\left(\frac{5}{12}\right)}; \qquad -\frac{3}{2} < Re\gamma < -\frac{2}{3} \tag{B.18b}$$

B.1.2.1.5 Kareem (2.38)

$$\Lambda(\gamma) = \frac{Bz\left(\frac{Cz}{\bar{U}_z}\right)^{-2-\gamma}\sigma^2\Gamma\left(-\frac{1}{3}-\gamma\right)\Gamma(2+\gamma)}{\bar{U}_z\Gamma\left(\frac{5}{3}\right)}; \qquad -2 < Re\gamma < -\frac{1}{3} \tag{B.19a}$$

$$\Pi_H(\gamma) = \frac{2\sqrt{\pi}\bar{U}_z^{1+\gamma}(Cz)^{-\frac{3}{2}-\gamma}\sqrt{\frac{Bz}{q}}\sigma\Gamma\left(-\frac{2}{3}-\gamma\right)\Gamma\left(\frac{3}{2}+\gamma\right)}{\Gamma\left(\frac{5}{6}\right)}; \qquad -\frac{3}{2} < Re\gamma < -\frac{2}{3} \tag{B.19b}$$

B.1.2.2 Wind load spectra

The PSD function $S_F(f)$ of the wind load is determined by means of the aerodynamic admittance function $\chi_a^2(z,f)$ given here for a rectangular structure with surface A and the two-sided model wind velocity PSD function $S_u(f) = 1/2G_u(f)$ discussed in section 2.2.2.4, yielding

$$S_F(f) = D|\chi_a(z;f)|^2 S_u(f); \qquad \chi_a(z;f) = \frac{1}{1+\left(\frac{2f\sqrt{A}}{\bar{U}_z}\right)^{4/3}}$$

where $D = (\rho_a A C_d \bar{U}_z)^2$. The following H-FSMs (5.14) of the transfer function can be used for the reconstruction of the latter and the corresponding non-causal unit response function defined in Eq. (5.16) as well as the simulation of a realization of the wind load fluctuations by means of Eq. (5.31).

B.1.2.2.1 Kaimal (2.30)

$$\Pi_H(\gamma) = \sum_{k=1}^{3} a_{1,k} C_{1,k}(\gamma) + \sum_{k=1}^{2} a_{2,k} C_{2,k}(\gamma) + \sum_{k=1}^{2} a_{3,k} C_{3,k}(\gamma); \qquad -\frac{3}{2} < Re\gamma \tag{B.20a}$$

where

$$\begin{aligned}
c_k &= \frac{8k-6\gamma}{24}; \qquad b_k = \frac{11+6k}{24} \\
a_{1,k} &= \frac{(-1)^{k-1}\bar{U}_z^{\gamma} K}{2^{\frac{4k}{3}-\frac{1}{2}} A^{\frac{2k}{3}} (bL)^{\frac{3}{2}-\frac{4k}{3}+\gamma}} \\
C_{1,k}(\gamma) &= \frac{{}_5F_4\left[\left\{1, c_k-\frac{1}{6}, c_k+\frac{1}{12}, c_k+\frac{1}{3}, c_k+\frac{7}{12}\right\}, \left\{c_k-\frac{1}{8}, c_k+\frac{1}{8}, c_k+\frac{3}{8}, c_k+\frac{5}{8}\right\}, -\left(\frac{bL}{2\sqrt{A}}\right)^4\right)}{\Gamma\left(\frac{5}{6}\right)\left(\Gamma(-\frac{2}{3}+4c_k)\Gamma(\frac{3}{2}-4c_k)\right)^{-1}}; \\
a_{2,k} &= \frac{55\pi\bar{U}_z^{\gamma}(bL)^{1+k}K}{2^{8+2k+\gamma}3^{2k-1}17^{1-k}A^{\frac{1}{4}(5+2k+2\gamma)}} \\
C_{2,k}(\gamma) &= \frac{{}_4F_3\left[\left\{b_k, b_k+\frac{1}{4}, b_k+\frac{1}{2}, b_k+\frac{3}{4}\right\}, \left\{2b_k-\frac{2}{3}, b_k+\frac{13}{24}, b_k+\frac{19}{24}\right\}, -\left(\frac{bL}{2\sqrt{A}}\right)^4\right]}{\sin\left(\frac{\pi(1+2\gamma(-1)^k)}{8}\right)\sin\left(\frac{\pi(5-6\gamma(-1)^k)}{24}\right)\cos\left(\frac{\pi(1-6\gamma(-1)^k)}{24}\right)}; \\
a_{3,k} &= \frac{-3^{2-k}5^{k-1}K(-bL)^{k-1}\pi\bar{U}_z^{\gamma}}{2^{3+2k+\gamma}A^{\frac{1}{4}(1+2k+2\gamma)}} \\
C_{3,k}(\gamma) &= \frac{{}_4F_3\left[\left\{b_k-\frac{1}{2}, 2b_k-\frac{23}{24}, \frac{17}{24}, b_k+\frac{1}{4}\right\}, \left\{b_k-\frac{11}{24}, b_k-\frac{5}{24}, 2b_k-\frac{2}{3}\right\}, -\left(\frac{bL}{2\sqrt{A}}\right)^4\right]}{\sin\left(\frac{\pi(1-6\gamma(-1)^k)}{24}\right)\cos\left(\frac{\pi(1+2\gamma(-1)^k)}{8}\right)\cos\left(\frac{\pi(5-6\gamma(-1)^k)}{24}\right)}
\end{aligned} \tag{B.20b}$$

where ${}_pF_q[a_1,...a_p;b_1,...b_q;z]$ is the generalized hypergeometric function and where $a = 6.8$, $b = 10.2$, $K = \bar{U}_z\sigma\sqrt{2\pi aDL/q_W}$ and where $z < 200$ [m].

B.1.2.2.2 Simiu (2.32)

Introducing $a = b = z$, $L = \lambda = 50$ [m], $K = \bar{U}_z\sigma\sqrt{\frac{4\pi zD\lambda}{3q}}$ in Eq. (B.20b), provides the H-FSMs of the wind loads with Kaimal velocity spectrum in the form

$$\Pi_H(\gamma) = \sum_{k=1}^{3} a_{1,k}C_{1,k}(\gamma) + \sum_{k=1}^{2} a_{2,k}C_{2,k}(\gamma) + \sum_{k=1}^{2} a_{3,k}C_{3,k}(\gamma); \qquad -\frac{3}{2} < Re\gamma < \frac{2}{3} \tag{B.21}$$

where $z < 50$ [m].

B.1.2.2.3 Davenport (2.36)

$$\Pi_H(\gamma) = K\left(C_1(\gamma) + C_2(\gamma)\right); \qquad -2 < Re\gamma \tag{B.22a}$$

where

$$\begin{aligned}
a_k &= \frac{k}{3} - \frac{\gamma}{4};\\
C_1(\gamma) &= \sum_{k=1}^{3} \frac{\Gamma\left(\frac{6a_k-1}{3}\right)\Gamma(1-2a_k)\,{}_3F_2\left[\left\{1, -\frac{1}{6}+a_k, \frac{1}{3}+a_k\right\}, \left\{a_k, \frac{1}{2}+a_k\right\}, -\left(\frac{\bar{U}_zL}{2\sqrt{A}\bar{U}_{10}}\right)^4\right]}{(-1)^{1-k}\bar{U}_z^{-\gamma}\left(\frac{L\bar{U}_z}{\bar{U}_{10}}\right)^{1-4a_k}(4A)^{\frac{2k}{3}}\Gamma\left(\frac{2}{3}\right)}\\
C_2(\gamma) &= \frac{-3\pi L\bar{U}_z^{1+\gamma}\sin\left(\frac{3\pi\gamma}{4} - \frac{2}{3}\mathrm{arccot}\left(\left(\frac{2\sqrt{A}\bar{U}_{10}}{L\bar{U}_z}\right)^2\right)\right)}{2^{\frac{2}{3}+\gamma}\bar{U}_{10}\left(16 + \left(\frac{\bar{U}_zL}{\sqrt{A}\bar{U}_{10}}\right)^4\right)^{\frac{1}{3}}A^{1+\frac{\gamma}{2}}\sin\left(\frac{3\pi\gamma}{2}\right)}
\end{aligned} \tag{B.22b}$$

where $L \approx 1200$ [m] and $K = u\sigma\sqrt{\frac{2\pi D}{3q_W}}$.

B.1.2.2.4 Harris (2.37)

$$\Pi_H(\gamma) = K_1\left(C_1(\gamma) + C_2(\gamma)\right); \qquad -\frac{3}{2} < Re\gamma \tag{B.23a}$$

where

$$a_k = \frac{k}{3} - \frac{\gamma}{4};$$

$$C_1(\gamma) = \sum_{k=1}^{3} \frac{\Gamma\left[2a_k - \frac{1}{3}\right]\Gamma\left[\frac{3}{4} - 2a_k\right]{}_3F_2\left[\left\{1, a_k - \frac{1}{6}, a_k + \frac{1}{3}\right\}, \left\{a_k + \frac{1}{8}, a_k + \frac{5}{8}\right\}, -\left(\frac{L\bar{U}_z}{\sqrt{8A}\bar{U}_{10}}\right)^4\right]}{(-1)^{1-k}\bar{U}_z^{-\gamma}2^{2k-\frac{1}{3}-\frac{\gamma}{2}}\left(\frac{L\bar{U}_z}{\bar{U}_{10}}\right)^{1-4a_k}A^{\frac{2k}{3}}\Gamma\left[\frac{5}{12}\right]}$$

$$C_2(\gamma) = \sqrt{\frac{L}{\bar{U}_{10}}}\frac{3\pi\bar{U}_z^{\frac{1}{2}+\gamma}(1+i)(-1)^{7/8}e^{\frac{3i\pi\gamma}{4}}\left((1+i)e^{\frac{3i\pi\gamma}{2}}K_2^{5/12} + \sqrt{2}(K_2^*)^{5/12}\right)}{2^{\frac{5}{3}+\gamma}A^{\frac{3}{4}+\frac{\gamma}{2}}\left(64 + \left(\frac{L\bar{U}_z}{\sqrt{A}\bar{U}_{10}}\right)^4\right)^{5/24}(i + e^{3i\pi\gamma})\left(K_2K_2^*\right)^{5/24}}$$

$$K_2 = -i(Lu)^2 + 8A\bar{U}_{10}^2 \tag{B.23b}$$

where * denotes conjugate complex, $L \approx 1800$ [m] and $K_1 = u\sigma\sqrt{\frac{2\pi D}{3q_W}}$.

B.1.2.2.5 Kareem (2.38)

Introducing $a = B$, $b = C$, $L = z$ in Eq. (B.20b), provides the H-FSMs of the wind loads with Kareem velocity spectrum in the form

$$\Pi_H(\gamma) = \sum_{k=1}^{3} a_{1,k}C_{1,k}(\gamma) + \sum_{k=1}^{2} a_{2,k}C_{2,k}(\gamma) + \sum_{k=1}^{2} a_{3,k}C_{3,k}(\gamma); \qquad -\frac{3}{2} < Re\gamma \tag{B.24}$$

B.1.2.3 Wind wave spectra

In the following the FSMs $\Lambda(\gamma)$ (5.5) of the model wave PSD functions $S_u(\omega) = 1/2G_u(\omega)$ discussed in section 2.3.5 are listed which can be used to reconstruct the PSD and AC function by the relation (5.11). Furthermore, the H-FSMs (5.14) of the transfer function are given which can be used for the reconstruction of the latter and the corresponding non-causal unit response function defined in Eq. (5.16) as well as the simulation of a realization of the velocity fluctuations by means of Eq. (5.31).

B.1.2.3.1 Generic PSD function (2.47)

$$\Lambda(\gamma) = \frac{AB^{\frac{1-p+\gamma}{q}}\Gamma\left(\frac{-1+p-\gamma}{q}\right)}{q}; \qquad p > 1 + Re\gamma \tag{B.25a}$$

$$\Pi_H(\gamma) = \frac{2^{\frac{-2+p+2q-2\gamma}{2q}}B^{\frac{2-p+2\gamma}{2q}}\sqrt{\pi}\sqrt{\frac{A}{q_W}}\Gamma\left(\frac{p-2(1+\gamma)}{2q}\right)}{q}; \qquad Re\gamma < 2 \cap p > 2 + 2Re\gamma \tag{B.25b}$$

Finally the FSMs of the discussed model spectra are obtained by introducing the following parameters:

$$\begin{aligned}
&\text{Neumann:} && p=6;\ q=2;\ A=\frac{C\pi}{2}; && B=\frac{2g^2}{\bar{U}_{7.5}^2}\\
&\text{Bretschneider:} && p=5;\ q=4;\ A=0.1687H_s^2\omega_s^4; && B=0.675\omega_s^4\\
&\text{Pierson-Moskowitz:} && p=5;\ q=4;\ A=0.0081g^2; && B=0.74\left(\frac{g}{\bar{U}_{19.5}}\right)^4
\end{aligned} \tag{B.26}$$

B.1.2.4 Wind-wave load spectra

The PSD function $S_F(f)$ of the wind wave load acting on a vertical pile is obtained from the following relation (2.65b)

$$S_F(z;\omega)=1/2\left(K_1+K_m^2\omega^2\right)|H(\omega,z)|^2\,G(\omega) \tag{B.27a}$$

using the one-sided model spectra $G(\omega)$ of the surface evaluation discussed in section 2.3.6. The transfer function $H(\omega,z)$ and the coefficients K_1 are given by

$$H(\omega,z)=\begin{cases}\dfrac{\omega\cosh[k(z+h)]}{\sinh[kh]}; & \dfrac{h}{\lambda}\geq\dfrac{1}{2}\ \text{(finite depth)}\\ \omega\exp(kz); & \dfrac{h}{\lambda}\leq\dfrac{1}{20}\ \text{(deep water)}\end{cases} \tag{B.27b}$$

$$K_1=\frac{8}{\pi}K_d^2\sigma_u^2; \qquad K_2=K_m^2 \tag{B.27c}$$

The following H-FSMs (5.14) of the transfer function can be used for the reconstruction of the latter and the corresponding non-causal unit response function defined in Eq. (5.16) as well as the simulation of a realization of the wind wave load fluctuations by means of Eq. (5.31).

B.1.2.4.1 Neumann (2.48)

$$\begin{aligned}\Pi_H(\gamma)=C(\gamma)\Bigg(&-\sqrt{4\pi}B^{\frac{(\gamma-1)}{2}}\Gamma\left(\frac{1-\gamma}{2}\right){}_1F_1\left[-\frac{1}{2},\frac{1+\gamma}{2},\frac{BK_m^2}{2K_1}\right]+\\&+\left(\frac{2K_1}{K_m^2}\right)^{\frac{\gamma-1}{2}}\Gamma\left(\frac{\gamma-1}{2}\right)\Gamma\left(-\frac{\gamma}{2}\right){}_1F_1\left[-\frac{\gamma}{2},\frac{3}{2}-\frac{\gamma}{2},\frac{BK_m^2}{2K_1}\right]\Bigg); \qquad Re\gamma<0\end{aligned}$$

where

$$C(\gamma) = \begin{cases} -2^{-\frac{\gamma}{2}}\sqrt{\dfrac{AK_1}{2q_w}}\dfrac{\cosh(k(h+z))}{\sinh(hk)}; & \dfrac{h}{\lambda} \geq \dfrac{1}{2} \text{ (finite depth)} \\ -2^{-\frac{\gamma}{2}}\sqrt{\dfrac{AK_1}{2q_w}}\exp(kz); & \dfrac{h}{\lambda} \leq \dfrac{1}{20} \text{ (deep water)} \end{cases} \tag{B.28a}$$

B.1.2.4.2 Brettschneider (2.49) and Pierson Moskowitz (2.50)

$$\begin{aligned} \Pi_H(\gamma) = C(\gamma)\Bigg(&\frac{\sqrt{16\pi}\Gamma(c)}{B^c}{}_2F_2\left[\left\{-\frac{1}{4},\frac{1}{4}\right\},\left\{\frac{1}{2},1-c\right\},-\frac{BK_m^4}{2K_1^2}\right] + \\ &+\frac{K_m^2 B^{\frac{1}{2}-c}\sqrt{2\pi}\Gamma\left(c-\frac{1}{2}\right)}{K_1}{}_2F_2\left[\left\{\frac{1}{4},\frac{3}{4}\right\},\left\{\frac{3}{2},\frac{3}{2}-c\right\},-\frac{BK_m^4}{2K_1^2}\right] - \\ &-\frac{\Gamma\left(2c-\frac{1}{2}\right)\Gamma[-2c]}{2^{c-2}\left(\frac{K_1}{K_m^2}\right)^{2c}}{}_2F_2\left[\left\{c-\frac{1}{4},\frac{1}{4}+c\right\},\left\{\frac{1}{2}+c,1+c\right\},-\frac{BK_m^4}{2K_1^2}\right]\Bigg) \end{aligned}$$

where $Re\gamma < -1/2$, $c = 1/8 + \gamma/4$ and

$$C_1(\gamma) = \begin{cases} \dfrac{\sqrt{\frac{AK1}{q_W}}\cosh(k(h+z))}{2^{3-c}\sinh(hk)}; & \dfrac{h}{\lambda} \geq \dfrac{1}{2} \text{ (finite depth)} \\ \dfrac{\sqrt{\frac{AK1}{q_W}}\exp(kz)}{2^{3-c}}; & \dfrac{h}{\lambda} \leq \dfrac{1}{20} \text{ (deep water)} \end{cases} \tag{B.29a}$$

The coefficients A, B are summarized in Eq. (B.26).

C.1 Kalman Filter

In the following an alternative derivation of the Kalman filter equations is summarized which is based on a least square approach.

C.1.1 Least square approach to the Kalman filter

The algorithm is characterized by an iterative prediction-correction structure as shown in Fig. (6.2). In the *prediction step* (6.3) a time update of the current state and error covariance matrix $\mathbf{x}_k$, $\mathbf{\Sigma}_{xx,k}$ based on the observation data $\mathbf{Z}_k = [\mathbf{z}_k, \mathbf{z}_{k-1}, \ldots, \mathbf{z}_1]$ up to time k is taken in order to obtain a prior estimate of the process state and its associated error covariance matrix $\hat{\mathbf{x}}_{k+1|k}$, $\mathbf{\Sigma}_{xx,k+1|k}$ at the next time step. The prior state estimate is denoted as prediction and is defined by the expectation of the state at time $k+1$ conditioned on the observations up to time k, yielding

$$\begin{aligned}\hat{\mathbf{x}}_{k+1|k} &= E[\mathbf{x}_{k+1}|\mathbf{Z}_k] \\ &= E[\mathbf{A}_k\mathbf{x}_k + \mathbf{B}_k\mathbf{u}_k + \mathbf{G}_k\mathbf{w}_k|\mathbf{Z}_k] \\ &= \mathbf{A}_k E[\mathbf{x}_k|\mathbf{Z}_k] + \mathbf{B}_k[\mathbf{u}_k|\mathbf{Z}_k] + \mathbf{G}_k[\mathbf{w}_k|\mathbf{Z}_k] \qquad \text{(C.1a)}\end{aligned}$$

Using the fact, that the process noise is of zero mean and the input is independent of the past observations, finally the prediction is given by an undisturbed system equation

$$= \mathbf{A}_k\hat{\mathbf{x}}_{k,k} + \mathbf{B}_k\mathbf{u}_k \qquad \text{(C.1b)}$$

where $\hat{\mathbf{x}}_{k,k}$ is the posterior estimate known from the previous time step. The corresponding covariance results from the prediction error

$$\mathbf{e}_{x,k+1|k} = \tilde{\mathbf{x}}_{k+1|k} - \hat{\mathbf{x}}_{k+1} = \mathbf{A}_k(\tilde{\mathbf{x}}_k - \hat{\mathbf{x}}_{k|k}) + \mathbf{B}_k(\tilde{\mathbf{u}}_k - \mathbf{u}_k) + \mathbf{G}_k(\tilde{\mathbf{w}}_k - \mathbf{w}_k) \qquad \text{(C.2)}$$

$$\mathbf{\Sigma}_{xx,k+1|k} = E\left[\mathbf{e}_{x,k+1|k}\mathbf{e}_{x,k+1|k}^T\right] = \mathbf{A}_k\mathbf{\Sigma}_{xx,k|k}\mathbf{A}_k^T + \mathbf{B}_k\mathbf{\Sigma}_{uu,k}\mathbf{B}_k^T + \mathbf{G}_k\mathbf{Q}_k\mathbf{G}_k^T \qquad \text{(C.3)}$$

where the tilde indicates the true, undisturbed state.
In the *correction step* (6.4-6.5) the new measurement $\mathbf{z}_{k+1}$ is used to correct the predicted state and covariance dependent on all available information up to time k in order to find the posterior (optimal) state estimate and covariance $\hat{\mathbf{x}}_{k+1|k+1}$, $\mathbf{\Sigma}_{xx,k+1|k+1}$ at time $k+1$. Assuming that the posterior estimate can be expressed as linear weighted sum of the prediction and

the new observation, then it holds

$$\hat{\mathbf{x}}_{k+1|k+1} = \mathbf{K}'_{k+1}\hat{\mathbf{x}}_{k+1|k} + \mathbf{K}_{k+1}\mathbf{z}_{k+1} \tag{C.4}$$

where $\mathbf{K}'_{k+1}$, $\mathbf{K}_{k+1}$ are weighting matrices, sometimes also denoted as gain matrices and which are determined in the following. The estimation error between the posterior estimate and the true value $\tilde{\mathbf{x}}_{k+1|k+1}$

$$\mathbf{e}_{x,k+1|k+1} = \tilde{\mathbf{x}}_{k+1|k+1} - \hat{\mathbf{x}}_{k+1|k+1} \tag{C.5a}$$

is a measure for the quality of the estimation. Furthermore, in order to obtain an unbiased estimate, the conditional expectation of the estimation error must vanish, i.e.

$$E[\mathbf{e}_{x,k+1|k+1}] = E[\mathbf{e}_{x,k+1}|\mathbf{Z}_{k+1}] = E[\tilde{\mathbf{x}}_{k+1}|\mathbf{Z}_{k+1}] - E[\hat{\mathbf{x}}_{k+1}|\mathbf{Z}_{k+1}] \equiv \mathbf{0} \tag{C.5b}$$

and consequently, the identity $E[\tilde{\mathbf{x}}_{k+1}|\mathbf{Z}_{k+1}] = E[\hat{\mathbf{x}}_{k+1}|\mathbf{Z}_{k+1}]$ must hold. Introducing Eq. (6.1b) in Eq. (C.4) and taking the expectation, yields

$$\begin{aligned} E[\hat{\mathbf{x}}_{k+1}|\mathbf{Z}_{k+1}] &= E[\mathbf{K}'_{k+1}\hat{\mathbf{x}}_{k+1|k} + \mathbf{K}_{k+1}\mathbf{C}_k\tilde{\mathbf{x}}_{k+1} + \mathbf{K}_{k+1}\mathbf{v}_k]|\mathbf{Z}_{k+1}] \\ &= \mathbf{K}'_{k+1}E[\hat{\mathbf{x}}_{k+1|k}|\mathbf{Z}_{k+1}] + \mathbf{K}_{k+1}\mathbf{C}_k E[\tilde{\mathbf{x}}_{k+1}|\mathbf{Z}_{k+1}] \end{aligned} \tag{C.6a}$$

Using the assumption that the estimate of the previous $\hat{\mathbf{x}}_{k|k}$ time step is unbiased, i.e. $E[\tilde{\mathbf{x}}_k|\mathbf{Z}_k] = E[\hat{\mathbf{x}}_k|\mathbf{Z}_k]$, it follows

$$\begin{aligned} E[\hat{\mathbf{x}}_{k+1|k}|\mathbf{Z}_{k+1}] &= E[\mathbf{A}_k\hat{\mathbf{x}}_{k|k} + \mathbf{B}_k\mathbf{u}_k + \mathbf{G}_k\mathbf{w}_k|\mathbf{Z}_{k+1}] \\ &= E[\mathbf{A}_k\tilde{\mathbf{x}}_k + \mathbf{B}_k\mathbf{u}_k + \mathbf{G}_k\mathbf{w}_k|\mathbf{Z}_{k+1}] \\ &= E[\tilde{\mathbf{x}}_{k+1}|\mathbf{Z}_{k+1}] \end{aligned} \tag{C.6b}$$

and Eq. (C.6a) reduces to

$$E[\hat{\mathbf{x}}_{k+1}|\mathbf{Z}_{k+1}] = (\mathbf{K}'_{k+1} + \mathbf{K}_{k+1}\mathbf{C}_k)E[\tilde{\mathbf{x}}_{k+1}|\mathbf{Z}_{k+1}] \tag{C.6c}$$

The condition C.5b that the optimal estimate is unbiased, i.e. $E[\hat{\mathbf{x}}_{k+1}|\mathbf{Z}_{k+1}] = E[\tilde{\mathbf{x}}_{k+1}|\mathbf{Z}_{k+1}]$, requires that the following relation holds

$$\mathbf{K}'_{k+1} = (\mathbf{I} - \mathbf{K}_{k+1}\mathbf{C}_k) \tag{C.6d}$$

Introducing this relation in Eq. (C.4) finally yields the sought optimal posterior state estimate in the form

$$\begin{aligned}\hat{\mathbf{x}}_{k+1|k+1} &= (\mathbf{I} - \mathbf{K}_{k+1}\mathbf{C}_k)\hat{\mathbf{x}}_{k+1|k} + \mathbf{K}_{k+1}\mathbf{z}_{k+1} \\ &= \hat{\mathbf{x}}_{k+1|k} + \mathbf{K}_{k+1}\underbrace{(\mathbf{z}_{k+1} - \mathbf{C}_k\hat{\mathbf{x}}_{k+1|k})}_{innovation}\end{aligned} \tag{C.7}$$

where $\mathbf{K}_{k+1}$ is the so-called Kalman gain matrix. The term in brackets is called residual as it describes the difference between the actual measurement $\mathbf{z}_{k+1}$ and the predicted measurement $\mathbf{C}_k\hat{\mathbf{x}}_{k+1|k}$, which is the likeliest observation for the given prior state estimate. In the correction step, the residual is weighted by the Kalman gain matrix and used to correct the prior state estimate. Thus, the residual is often denoted as innovation as the difference can be interpreted as the part of the measurement that contains new information about the state.

The quality of the posterior estimate is reflected in the corresponding posterior error covariance $\mathbf{\Sigma}_{xx,k+1|k+1}$ of the prediction error $\mathbf{e}_{x,k+1|k+1}$, which describes the discrepancy between the true state $\tilde{\mathbf{x}}_{k+1|k+1}$ and the posterior estimate $\hat{\mathbf{x}}_{k+1|k+1}$. Substituting $\hat{\mathbf{x}}_{k+1|k+1}$ by the relation (C.7) and the measurement $\mathbf{z}_{k+1}$ by the Eq. (6.1b), the posterior estimation error defined in Eq. (C.5a) can be rewritten in the form

$$\mathbf{e}_{x,k+1|k+1} = (\mathbf{I} - \mathbf{K}_{k+1}\mathbf{C}_k)(\tilde{\mathbf{x}}_{k+1|k+1} - \hat{\mathbf{x}}_{k+1|k}) + \mathbf{K}_{k+1}\mathbf{v}_{k+1} \tag{C.8a}$$

Noting that the term in the second bracket corresponds to the prior prediction error $\mathbf{e}_{x,k+1|k}$ defined in Eq. (C.2), the posterior error covariance matrix finally follows from

$$\begin{aligned}\mathbf{\Sigma}_{xx,k+1|k+1} &= E\left[\mathbf{e}_{x,k+1|k+1}\mathbf{e}_{x,k+1|k+1}^T\right] \\ &= (\mathbf{I} - \mathbf{K}_{k+1}\mathbf{C}_k)\mathbf{\Sigma}_{xx,k+1|k}(\mathbf{I} - \mathbf{K}_{k+1}\mathbf{C}_k)^T + \mathbf{K}_{k+1}\mathbf{R}_k\mathbf{K}_{k+1}^T\end{aligned} \tag{C.8b}$$

where for the last equality the following identities were used

$$\begin{aligned}E\left[\mathbf{e}_{x,k+1|k}\mathbf{e}_{x,k+1|k}^T\right] &= \mathbf{\Sigma}_{xx,k+1|k} \\ E\left[\mathbf{v}_{k+1}^T\mathbf{v}_{k+1}\right] &= \mathbf{R}_{k+1} \\ E\left[\mathbf{e}_{x,k+1|k}^T\mathbf{v}_{k+1}\right] &= \mathbf{0}\end{aligned}$$

The last step in the derivation of the Kalman filter equations is the determination of the Kalman gain matrix. It will be chosen in such a way, that the obtained posterior estimate is optimal in the mean least squared sense, that is the Kalman filter leads to a minimum

variance estimate. This is archived by minimizing the conditional mean-squared estimation error $\mathbf{e}_{x,k+1|k} = \tilde{\mathbf{x}}_{k+1|k+1} - \hat{\mathbf{x}}_{k+1|k+1}$. Using the fact that the trace of the posteriori estimate covariance matrix is the sum of the mean-square errors in the estimates of all the elements of the state vector, this is equivalent to minimizing $tr\left(\mathbf{\Sigma}_{xx,k+1|k+1}\right)$. Thus the minimization problem can be state as follows

$$\mathbf{K}_{k+1} = \underset{\mathbf{K}\in\mathbb{R}^{n\times m}}{\arg\min}\ E\left[\mathbf{e}_{x,k+1|k+1}^T\mathbf{e}_{x,k+1|k+1}\right] \equiv \underset{\mathbf{K}\in\mathbb{R}^{n\times m}}{\arg\min}\ tr\left(\mathbf{\Sigma}_{xx,k+1|k+1}\right) \tag{C.9a}$$

and the Kalman gain matrix which produces the optimal estimate can be easily calculated by first, setting the partial derivative of the trace of the posterior covariance matrix zero and secondly, by solving the resulting equation for $\mathbf{K}_{k+1}$. In order to calculate the partial derivative, the following property, valid for any matrix $\mathbf{A}$ and a symmetric matrix $\mathbf{B}$, is used

$$\frac{\partial}{\partial\mathbf{B}}\ tr\left(\mathbf{ABA}^T\right) = 2\mathbf{AB} \tag{C.9b}$$

Applying this property to Eq. (C.8b) and differencing with respect to the gain matrix, leads to

$$\frac{\partial}{\partial\mathbf{K}_{k+1}}\ tr\left(\mathbf{\Sigma}_{xx,k+1|k+1}\right) = -2(\mathbf{I}-\mathbf{K}_{k+1}\mathbf{C}_k)\mathbf{\Sigma}_{xx,k+1|k}\mathbf{C}_k^T + 2\mathbf{K}_{k+1}\mathbf{R}_k \tag{C.9c}$$

Then, setting the result equal to zero and solving for the optimal gain $\mathbf{K}_{k+1}$, finally yields

$$\mathbf{K}_{k+1} = \mathbf{\Sigma}_{xx,k+1|k}\mathbf{C}_k^T(\mathbf{R}_k + \mathbf{C}_k\mathbf{\Sigma}_{xx,k+1|k}\mathbf{C}_k^T)^{-1} \tag{C.9d}$$

Substituting the optimal gain in Eq. (C.8b) leads to various possible implementations of the posterior error covariance matrix. They lead to identical results if the optimal gain C.9d is used and perfect arithmetic is assumed. Due to the in general numerical implementation of the Kalman filter the latter assumption of course cannot be preserved and thus they vary significantly with respect to accuracy and computational cost.
The main advantage of the implementation defined in Eq. (C.8b), the so-called Joseph form, results from the fact that the symmetry as well as the positive semidefiniteness of the error covariance is ensured also in the presence of roundoff errors. Thus, it is often used for actual software implementation of the filter [Lewis et al 2008, p. 73].
In many engineering applications, the system's order is significantly higher than the dimension of the measurement vector, i.e. $n >> m$. In this case a computational more efficient

implementation is given by

$$\begin{aligned}\boldsymbol{\Sigma}_{xx,k+1|k+1} &= \boldsymbol{\Sigma}_{xx,k+1|k} - \boldsymbol{\Sigma}_{xx,k+1|k}\mathbf{C}_k^T\left(\mathbf{C}_k\boldsymbol{\Sigma}_{xx,k+1|k}\mathbf{C}_k^T + \mathbf{R}_k\right)^{-1}\mathbf{C}_k\boldsymbol{\Sigma}_{xx,k+1|k} \\ &= \boldsymbol{\Sigma}_{xx,k+1|k} - \mathbf{K}_k\mathbf{C}_k\boldsymbol{\Sigma}_{xx,k+1|k} \end{aligned} \tag{C.10a}$$

which is widely used as it requires a significant lower number of computations (multiplications and additions) than the Jordan form. As it involves m-by-m inversions, computational efficiency increases with decreasing numbers of measurement locations. The form ensures the symmetry of the covariance matrix, but the positive semidefiniteness of the covariance is not necessarily preserved. Further numerical problems can arise if the accuracy of the measurements is very high and thus a small difference of large numbers must be calculated. Moreover, the following simplification should be avoided

$$\boldsymbol{\Sigma}_{xx,k+1|k+1} = \left(\mathbf{I} - \mathbf{K}_k\mathbf{C}_k\right)\boldsymbol{\Sigma}_{xx,k+1|k} \tag{C.10b}$$

Although algebraically equivalent to the implementation Eq. (C.9a) the factorized form suffers additionally from the lack of symmetry as instead of subtracting two symmetric matrices as in the previous form, a product of a antisymmetric and a symmetric matrix is calculated. Thus it is a less desirable form and should be avoided [Maybeck 1979, p. 236-237]. In [Maybeck 1982, Ch. 5.6, 7.8] the property of diverse implementations are discussed in detail and which is recommended for further reading.
Fig. (6.2) summarizes the implementation of the Kalman filter as it is used throughout this work.

C.1.2 Partial derivative matrices

Introducing the mass stiffness and damping matrix defined in Eqs. (6.31b-6.32a) in the state space representation 6.36b leads to the following nonlinear function

$$f\left(\mathbf{x}'(t),\mathbf{w}'(t)\right) = \begin{bmatrix} \dot{y}_1 \\ \dot{y}_2 \\ \dot{y}_3 \\ -\frac{(c_1+c_2)\dot{y}_1}{m_1} + \frac{c_2\dot{y}_2}{m_1} - \frac{(k_1+k_2)y_1}{m_1} + \frac{k_2y_2}{m_1} + \frac{w_1}{m_1} \\ \frac{c_2\dot{y}_1}{m_3} - \frac{(c_2+c_3)\dot{y}_2}{m_3} + \frac{c_3\dot{y}_3}{m_3} + \frac{k_2y_1}{m_3} - \frac{(k_2+k_3)y_2}{m_3} + \frac{k_3y_3}{m_3} + \frac{w_2}{m_3} \\ \frac{c_3\dot{y}_2}{m_3} - \frac{c_3\dot{y}_3}{m_3} + \frac{k_3y_2}{m_3} - \frac{k_3y_3}{m_3} + \frac{w_3}{m_3} \\ w_{k_1} \\ w_{k_2} \\ w_{k_3} \\ w_{c_1} \\ w_{c_2} \\ w_{c_3} \end{bmatrix} \tag{C.11}$$

The linearization of is performed by a Taylor series with respect to the previous state estimate $\mathbf{x}'(t)$ and noise term $\mathbf{w}'(t)$, that is around

$$\mathbf{x}'(t) = \begin{bmatrix} \mathbf{x}(t) \\ \mathbf{p}(t) \end{bmatrix} = \begin{bmatrix} \hat{\mathbf{x}}(t) \\ \hat{\mathbf{p}}(t) \end{bmatrix}; \qquad \mathbf{w}'(t) = \begin{bmatrix} \mathbf{w}(t) \\ \mathbf{w}_p(t) \end{bmatrix} = \begin{bmatrix} \mathbf{0} \\ \mathbf{0} \end{bmatrix} \tag{C.12}$$

where the last equality results from the assumptions that the model disturbances are of zero mean. The linearized state transition matrix is then given by the partial derivative matrix

$$\mathbf{A}_{c,L} = \left.\frac{\partial f}{\partial \mathbf{x}'(t)}\right|_{\mathbf{x}'=\hat{\mathbf{x}}'} = \begin{bmatrix} \left.\frac{\partial \mathbf{x}(t)}{\partial \mathbf{x}(t)}\right|_{\mathbf{x}=\hat{\mathbf{x}}} & \left.\frac{\partial \mathbf{x}(t)}{\partial \mathbf{p}(t)}\right|_{\mathbf{p}=\hat{\mathbf{p}}} \\ \left.\frac{\partial \mathbf{p}(t)}{\partial \mathbf{x}(t)}\right|_{\mathbf{x}=\hat{\mathbf{x}}} & \left.\frac{\partial \mathbf{p}(t)}{\partial \mathbf{p}(t)}\right|_{\mathbf{p}=\hat{\mathbf{p}}} \end{bmatrix} = \begin{bmatrix} \mathbf{A}_c & \left.\frac{\partial \mathbf{x}(t)}{\partial \mathbf{p}(t)}\right|_{\mathbf{p}=\hat{\mathbf{p}}} \\ \mathbf{0}_{5\times 6} & \mathbf{I}_{5\times 5} \end{bmatrix} \tag{C.13a}$$

where the matrix

$$\left.\frac{\partial \mathbf{x}(t)}{\partial \mathbf{p}(t)}\right|_{\mathbf{p}=\hat{\mathbf{p}}} = \begin{bmatrix} \left.\frac{\partial y_1(t)}{\partial k_1}\right|_{k_1=\hat{k}_1} & \left.\frac{\partial y_1(t)}{\partial k_2}\right|_{k_2=\hat{k}_2} & \cdots & \left.\frac{\partial y_1(t)}{\partial c_3}\right|_{c_3=\hat{c}_3} \\ \left.\frac{\partial y_2(t)}{\partial k_1}\right|_{k_1=\hat{k}_1} & \left.\frac{\partial y_2(t)}{\partial k_2}\right|_{k_2=\hat{k}_2} & \cdots & \left.\frac{\partial y_2(t)}{\partial c_3}\right|_{c_3=\hat{c}_3} \\ \vdots & \vdots & \ddots & \vdots \\ \left.\frac{\partial \dot{y}_3(t)}{\partial k_1}\right|_{k_1=\hat{k}_1} & \left.\frac{\partial \dot{y}_3(t)}{\partial k_2}\right|_{k_2=\hat{k}_2} & \cdots & \left.\frac{\partial \dot{y}_3(t)}{\partial c_3}\right|_{c_3=\hat{c}_3} \end{bmatrix}$$

$$= \begin{bmatrix} 0 & 0 & 0 & 0 & 0 & 0 \\ 0 & 0 & 0 & 0 & 0 & 0 \\ 0 & 0 & 0 & 0 & 0 & 0 \\ -\frac{y_1}{m_1} & \frac{-y_1+y_2}{m_1} & 0 & -\frac{\dot{y}_1}{m_1} & \frac{-\dot{y}_1+\dot{y}_2}{m_1} & 0 \\ 0 & \frac{y_1-y_2}{m_3} & \frac{-y_2+y_3}{m_3} & 0 & \frac{\dot{y}_1-\dot{y}_2}{m_3} & \frac{-\dot{y}_2+\dot{y}_3}{m_3} \\ 0 & 0 & \frac{y_2-y_3}{m_3} & 0 & 0 & \frac{\dot{y}_2-\dot{y}_3}{m_3} \end{bmatrix} \tag{C.13b}$$

relates the unknown parameters to the system's states. Similarly the noise transition matrix $\mathbf{G}_{c,L}$ follows from

$$\mathbf{G}_{c,Lin} = \left.\frac{\partial \mathbf{x}(t)}{\partial \mathbf{w}'(t)}\right|_{\hat{\mathbf{w}}'=\mathbf{0}} = \begin{bmatrix} \left.\frac{\partial \mathbf{x}(t)}{\partial \mathbf{w}(t)}\right|_{\mathbf{w}=\mathbf{0}} & \left.\frac{\partial \mathbf{x}(t)}{\partial \mathbf{w}_p(t)}\right|_{\mathbf{w}_p=\mathbf{0}} \\ \left.\frac{\partial \mathbf{p}}{\partial \mathbf{w}(t)}\right|_{\mathbf{w}=\mathbf{0}} & \left.\frac{\partial \mathbf{p}(t)}{\partial \mathbf{w}_p(t)}\right|_{\mathbf{w}_p=\mathbf{0}} \end{bmatrix} = \begin{bmatrix} \mathbf{G}_c & \left.\frac{\partial \mathbf{x}(t)}{\partial \mathbf{w}_p}\right|_{\mathbf{w}_p=\mathbf{0}} \\ \mathbf{0}_{6\times 6} & \mathbf{I}_{6\times 6} \end{bmatrix} \tag{C.14a}$$

where the partial derivative matrix is given by

$$\left.\frac{\partial f}{\partial \mathbf{w}_p(t)}\right|_{\mathbf{w}_p=\mathbf{0}} = \begin{bmatrix} \left.\frac{\partial y_1(t)}{\partial w_{k_1}}\right|_{w_{k_1}=0} & \left.\frac{\partial y_1(t)}{\partial w_{k_2}}\right|_{w_{k_2}=0} & \cdots & \left.\frac{\partial y_1(t)}{\partial w_{c_3}}\right|_{w_{c_3}=0} \\ \left.\frac{\partial y_2(t)}{\partial w_{k_1}}\right|_{w_{k_1}=0} & \left.\frac{\partial y_2(t)}{\partial w_{k_2}}\right|_{w_{k_2}=0} & \cdots & \left.\frac{\partial y_2(t)}{\partial w_{c_3}}\right|_{w_{c_3}=0} \\ \vdots & \vdots & \ddots & \vdots \\ \left.\frac{\partial \dot{y}_3(t)}{\partial w_{k_1}}\right|_{w_{k_1}=0} & \left.\frac{\partial \dot{y}_3(t)}{\partial w_{k_2}}\right|_{w_{k_2}=0} & \cdots & \left.\frac{\partial \dot{y}_3(t)}{\partial w_{c_3}}\right|_{w_{c_3}=0} \end{bmatrix} = \mathbf{0}_{6\times 6} \tag{C.14b}$$

D.1 State-of-the-art on System Identification Techniques for Operational Modal Analysis

Experimental modal analysis (EMA) has been extensively used in the aerospace, automotive, railway and maritime industries in order to study the dynamic behavior of structures under dynamic excitation. In the last decades the EMA has gained great attention in civil engineering where the development towards constantly lighter and slender structures leads to a higher susceptibility of the structures to vibrations. Consequently the experimental verification of design parameters such as eigenfrequencies, damping rations and modeshapes, characterizing the dynamic behavior, is crucial for design and model validation in order to comply with the increased demands for higher levels of safety, serviceability and durability [Reynders 2012]. The classical EMA is based on input-output measurements, i.e. the measurements of the loads exciting the structure and the system's response in order to obtain frequency and impulse response functions, respectively [Zhang et al 2005]. Such forced vibrations test are in general costly and time consuming as they require a specific excitation by impact hammers, drop weights or heavy electrodynamic shakers in order to excite the modes of interest with sufficient energy.

In contrast to applications of the EMA in other fields of engineering, where smaller components of the structure can be tested under laboratory conditions, in civil engineering the measurements on the typically large structures must be conducted under operational conditions due to the constantly present and in general non-negligible operational loads as wind or traffic [Reynders 2012]. Hence, in recent years so-called operational modal analysis (OMA) techniques, also known as output-only, natural excitation or ambient modal analysis methods, have been developed. They are based on ambient vibration tests (AvTs), i.e. output-only measurements of the system subjected to the natural excitation and/or service loads as wind, seismic ground motion, traffic or humans. Most natural loads applied to civil engineering structures are caused by the superposition of multiple inputs and thus lead to a broad-band excitation of a significant number of vibration modes [Yuen and Katafygiotis 2001; Cunha and Caetano 2006]. Due to their inherent random nature, the unmeasured ambient forces are modeled in the OMA as stochastic processes with unknown parameters but with known behavior, e.g. as zero-mean white noise process with unknown covariance [Reynders 2012].

A literature review on the use of AvTs can be found for instance in [Ivanovic et al 2000]. The first use of AvTs for the dynamic characterization of full-scale structures is reported in the '70s. Since then, the technique is extensively used in engineering in the scope of parameter identification (eigenfrequencies, damping ratios and mode shapes) [James et al 1993; Peeters

et al 1995, 1998; De Roeck et al 2000; Brownjohn 2003; Ren and Zong 2004; Gentile and Saisi 2007], model updating [Jaishi and Ren 2005; Gentile and Saisi 2007] as well as damage detection and health monitoring [Doebling and Farrar 1996; Peeters et al 2001; Lee et al 2002] of slender structures such as pedestrian bridges, chimneys, long-span frame structures or high-rise buildings. While forced vibration tests in general require a temporary out of service state of the structure, ambient vibration tests are based on the natural and/or service loads permitting to continuously measure the structural response without interruption of its use during large time intervals.
System identification techniques can be classified as parametric and non-parametric approaches. In the former case the functional form of the system model is known, thus the identification problem reduces to the identification of a finite number of model parameters like the matrix entries of a state-space model or the coefficients of a time series model. Non-parametric identification techniques do not require any information about the mathematical model of the system and are based e.g. on the measured frequency response, transfer, covariance or spectral densities functions from which the modal parameters can be determined by modal decomposition of the identified system model [Reynders 2012; Luk and Damper 2006; Åström 1970].

In this chapter a literature review of different time-domain operation modal identification techniques is provided, following the structure given in [Zhang et al 2005] which is recommended for further reading. To this aim the fundamentals of the methods are briefly summarize without intending to give an exhaustive derivation. In each section a great number of publications describing both theory and applications are critically discussed with respect to computational efficiency, applicability and restrictions.

D.1.1 NExT-type methods

The Natural Excitation Technique (NExT) belongs to the nonparametric time domain identification methods and was first proposed in [Lauffer et al 1985] for the modal identification of vertical wind turbines subjected to wind loads using output-only measurements James et al [1993]. A literature review on the first developments and applications of NExT to wind turbines, trucks, highway bridges and offshore structures under operational conditions is given in [James et al 1996]. The technique is based on the assumptions that the system behaves linearly and the unmeasured forces are stationary and uncorrelated with the system's response [Caicedo 2011]. The method uses auto- and cross-correlation functions instead of impulse response functions (IRF) generated between the system's response and a reference

sensor X_{ref}. The latter must be chosen carefully as it provides the reference for the whole set of measurements. Assuming that the unmeasured force exciting the system can be modeled as stationary, broad-banded noise process, the system can be described by the equation of motion of a multi-degree of freedom (MDOF), linear time-invariant system

$$\mathbf{M}\ddot{\mathbf{X}}(t) + \mathbf{C}\dot{\mathbf{X}}(t) + \mathbf{K}\mathbf{X}(t) = \mathbf{W}(t) \tag{D.1}$$

where $\mathbf{M}$, $\mathbf{C}$, $\mathbf{K} \in \mathbb{R}^{n\times n}$ is the deterministic mass, damping and stiffness matrix, $\{\mathbf{X}(t)\}$, $\{\dot{\mathbf{X}}(t)\}$, $\{\ddot{\mathbf{X}}(t)\} \in \mathbb{R}^n$ is the stationary stochastic vector process of the system's displacement, velocity and acceleration, respectively, and $\{\mathbf{W}(t)\}$ is the unmeasured input modeled as Gaussian white noise process. Multiplying Eq. (D.1) by the scalar reference response process $X_{ref}(s)$ and taking the expected value, denoted as $E[\cdot]$, yields

$$\mathbf{M}E[\ddot{\mathbf{X}}(t)X_{ref}(s)] + \mathbf{C}E[\dot{\mathbf{X}}(t)X_{ref}(s)] + \mathbf{K}E[\mathbf{X}(t)X_{ref}(s)] = E[\mathbf{W}(t)X_{ref}(s)] \tag{D.2}$$

which leads to a differential equations in terms of the vector of correlation functions $\mathbf{R}(t,s)$ given by

$$\mathbf{M}\mathbf{R}_{\ddot{\mathbf{X}}X_{ref}}(\tau) + \mathbf{C}\mathbf{R}_{\dot{\mathbf{X}}X_{ref}}(\tau) + \mathbf{K}\mathbf{R}_{\mathbf{X}X_{ref}}(\tau) = \mathbf{R}_{\mathbf{W}X_{ref}}(\tau) \tag{D.3}$$

where $\tau = t - s$. In [Bendat and Piersol 2010, p. 151 ff] it is shown that for (wide sense) stationary processes, the derivative $\dot{R}_{XX}(\tau)$ of the autocorrelation function with respect to the time shift τ is the same as the cross-correlation function between the processes $\{X(\tau)\}$ and $\{\dot{X}(\tau)\}$. This relation can be extended to the general case $R_{X^{(m)}X}(\tau) = R^{(m)}_{XX}(\tau)$ where the superscript (m) denotes the mth derivative with respect to τ. Assuming that the system's responses are uncorrelated to the external disturbances $\{\mathbf{W}(t)\}$ for $\tau > 0$ one obtains the following homogeneous differential equation [Caicedo et al 2004]

$$\mathbf{M}\ddot{\mathbf{R}}_{\mathbf{X}X_{ref}}(\tau) + \mathbf{C}\dot{\mathbf{R}}_{\mathbf{X}X_{ref}}(\tau) + \mathbf{K}\mathbf{R}_{\mathbf{X}X_{ref}}(\tau) = \mathbf{0}, \qquad \tau > 0 \tag{D.4}$$

which strongly resembles the homogeneous differential equation of a MDOFs. Hence, its solution leads to a series of decaying sinusoids where each sinusoid is characterized by a damped eigenfrequency, damping ration and mode shape coefficient corresponding to the modal parameters of the system James et al [1993]. The free response data obtained by the NExT can be processed as the impulse responses function of the system in order to extract modal parameters using standard modal parameter identification techniques, such as the Eigensystem Realization Algorithm (ERA) [Juang and Pappa 1985; Brownjohn 2003; Caicedo et al 2004; Siringoringo and Fujino 2008; Caicedo 2011; Chang and Pakzad 2012]

or the Ibrahim Time Domain (ITD) method [Siringoringo and Fujino 2008]. The main weakness in the implementation of the NExT is related to the fact that one sensor is selected as reference for the whole set of measurements. The location of the sensor must be selected in such a way that all modes contribute to the measured response. If the sensor is for instance placed close to a modal node or if the vibrations of the structure are orthogonal to the measurement direction of the sensor, then little or no information about the respective mode are contained in the estimated free response. Therefore in general the measurements have to be conducted repeatedly with different reference sensors [Giraldo et al 2009]. Furthermore long-time series of response data are required to allow significant averaging of the data under relative stationary operating conditions [Shen et al 2003]. If the assumption of the whiteness of the input is violated, the parameter estimation can have significant errors leading to estimation errors of about 0.5 % in the frequency and 50 % in the damping estimates [Barney and Carne 1999]. A benchmark study based on a four-story laboratory scale-model building on the influence of the number of sensors, the model order (12/ 120 DOFs), the mass distribution (symmetric, asymmetric) and different damage pattern on the damage detection can be found in Caicedo et al [2004]. In [Siringoringo and Fujino 2008] the NExT-ERA algorithm is applied to the Hakucho Suspension Bridge and compared with the Random Decrement technique which was combined with the Ibrahim Time Domain (RD-ITD) used for the identification of the modal parameters. A further comparative study of the NExT-ERA algorithm with the frequency-domain decomposition and the Random Decrement Method applied in the scope of damage detection to the L'Aquila City Hall (Margherita Palac, Italy) can be found in [Cimellaro et al 2012].

D.1.2 ARMA-type methods

Output-only parametric time-domain identification of dynamic systems refers to the fitting of a finite, parametrized mathematical time-domain model to the measured response signals of the vibrating structure. While non-parametric identification techniques lead to a representation in terms of frequency, correlation or impulse response functions, parametric identification algorithms result in parameterized models such as difference/differential equation or state space representations [Kadakal and Yüzügüllü 1996]. Non-parametric models have the advantage that they do not require any knowledge about the model order, whereas parametric representation are mainly relevant in optimal prediction and control [Isermann 1988b, p. 193]. In the last two decades parametric time-domain identification based on time series models, such as autoregressive (AR) or autoregressive moving average (ARMA) models gained great attention in engineering as they allow modeling structures with ambient

vibration records as single-output models which have widely been used in the literature to identify systems excited by random white noise [Kadakal and Yüzügüllü 1996]. The most general description of a linear time-invariant system excited by white disturbances is the n-dimensional vector ARMA model of order (p,q) denoted as ARMAV(n,p,q)

$$\mathbf{y}(t) + \mathbf{A}_1\mathbf{y}(t-1) + \ldots + \mathbf{A}_p\mathbf{y}(t-p) = \mathbf{w}(t) + \mathbf{B}_1\mathbf{w}(t-1) + \ldots + \mathbf{B}_q\mathbf{w}(t-q) \tag{D.5}$$

where $\{\mathbf{y}(t)\} \in \mathbb{R}^n$, $\mathbf{A}_k$, $\mathbf{B}_k \in \mathbb{R}^{n\times n}$ are vectors of constants and $\{\mathbf{w}(t)\} \in \mathbb{R}^n \sim \mathrm{WN}(\mathbf{0},\mathbf{\Sigma}\delta_{ts})$ is a zero-mean white noise process. The autoregressive part on the left hand side ARV(n,p) of Eq. (D.5) corresponds to the measured system's response $\{\mathbf{y}(t)\}$ and the moving average term MAV(n,q) on the right hand side is related to the process noise $\{\mathbf{w}(t)\}$. The unknown coefficients can be solved from measurements of the system's response by minimizing the error between the predicted output of the model and the measured output signal. Such methods known as prediction error methods [Caines 1988, p. 482 ff] were introduced by [Ljung 1974] and contain under certain conditions the maximum likelihood method as a special case. They allow taking into account the noise characteristics of the signals and are extensions of the so-called output error or equation error methods, originally designed for noiseless data and deterministic systems [Mehra and Lainiotis 1976, p. 122 ff]. However, the prediction error method leads to a highly non-linear minimization problem which is computational demanding, especially in the multivariate case. Moreover due to local minima the convergence is not necessarily guaranteed and the results might strongly depend on the initial estimates. The nonlinearity is caused be the moving average (MA) part of the ARMA model and hence one possible solution is to omit the ARMA part leading to an autoregressive model whose coefficient can be estimated directly by a linear least-square algorithm. Since this model is less general, the main disadvantage of this procedure requires an over-specification of the model order resulting in a number of spurious numerical modes as will be shown in the following [Peeters and De Roeck 1999].
The difference equation given in Eq. (D.5) can be expressed using the backward shift operator L (also called lag operator) with the property $L^k\mathbf{y}(t) = \mathbf{y}(t-k)$ in the form

$$\mathbf{y}(t) = \frac{\mathbf{I}_n + \mathbf{B}_1L^{-1} + \ldots + \mathbf{B}_qL^{-q}}{\mathbf{I}_n + \mathbf{A}_1L^{-1} + \ldots + \mathbf{A}_pL^{-p}}\mathbf{w}(t) = \frac{B(L)}{A(L)}\mathbf{w}(t) = C(L)\mathbf{w}(t) \tag{D.6}$$

where $\mathbf{I}_n$ denotes the $n \times n$ identity matrix. Hence, the finite ARMAV(n,p,q) model can be transformed into a infinite MAV(n,∞) model

$$\mathbf{y}(t) = \mathbf{w}(t) + \mathbf{C}_1\mathbf{w}(t-1) + \mathbf{C}_2\mathbf{w}(t-2) + \ldots = \sum_{j=0}^{\infty}\mathbf{C}_j\mathbf{w}(t-j) \tag{D.7}$$

where $\mathbf{C}_0 = \mathbf{I}_n$ or an infinite ARV(n,∞) model

$$\mathbf{y}(t) = \mathbf{w}(t) - \mathbf{D}_1\mathbf{y}(t-1) - \mathbf{D}_2\mathbf{y}(t-2) - \ldots = \mathbf{w}(t) - \sum_{j=1}^{\infty}\mathbf{D}_j\mathbf{y}(t-j) \tag{D.8}$$

where $D(L) = C^{-1}(L)$ is used. From a physical point of view, an infinite order process does not exist which allows approximating the ARMAV(n,p,q) model by a high order, but finite ARV(n,l), MAV(n,l) model, respectively Vu et al [2007]. When no information about the input is available, the ARV process is appropriate as the n^2l unknown coefficients can be determined from the measured system response data by solving a linear least square problem: Multiplying both sides of Eq. (D.8) by $\mathbf{y}^T(t-k)$ and taking the expected value yields

$$\mathbf{r}(k) = -\sum_{j=1}^{l}\mathbf{D}_j\mathbf{r}(k-j) \tag{D.9}$$

where $\mathbf{r}(k) = E[\mathbf{y}(t)\mathbf{y}^T(t-k)]$. Furthermore the relation $E[\mathbf{w}(t)\mathbf{y}^T(t-k)] = \mathbf{0}_n$ for $k > 0$ was used as the system response can be considered uncorrelated with future inputs [Huang 2001]. Eq. (D.9) can be expressed in matrix form

$$\mathbf{R} = \hat{\mathbf{R}}\,\theta \tag{D.10}$$

where $\mathbf{R} = [\mathbf{r}(1)\,\mathbf{r}(2)\,\ldots\,\mathbf{r}(m)]^T \in \mathbb{R}^{mn\times n}$, $\theta = [-\mathbf{D}_1\,-\mathbf{D}_2\,\ldots\,-\mathbf{D}_l]^T \in \mathbb{R}^{ln\times n}$ and $\hat{\mathbf{R}} \in \mathbb{R}^{mn\times ln}$ is a matrix with Toeplitz form whose elements are obtained by $\hat{R}_{ij} = \mathbf{r}(i-j)$ and $i = 1..m$, $j = 1..l$ leading to

$$\hat{\mathbf{R}} = \begin{bmatrix} \mathbf{r}(0) & \mathbf{r}(-1) & \mathbf{r}(-2) & \ldots & \mathbf{r}(1-l) \\ \mathbf{r}(1) & \mathbf{r}(0) & \mathbf{r}(-1) & \ldots & \mathbf{r}(2-l) \\ \ldots & \ldots & \ldots & \ldots & \ldots \\ \mathbf{r}(m) & \mathbf{r}(m-1) & \mathbf{r}(m-2) & \ldots & \mathbf{r}(m-l) \end{bmatrix} \tag{D.11}$$

In general the system of equations is solvable if the number of equations m is equal to the number of unknowns l. However due to the measurement error, this would lead to a high estimation error. Therefore the value of m is always set much larger than that of l and a least square approach is used in order to determine the coefficient matrices Best [1991]; Huang [2001].

With the knowledge of the coefficient matrices, the model parameters of the structure including natural frequencies, damping ratios and mode shapes can be obtained by truncating

the infinite sum Eq. (D.8) for the chosen model order l, yielding

$$(\mathbf{I}_n + \mathbf{D}_1 L^{-1} + \mathbf{D}_2 L^{-2} + \ldots + \mathbf{D}_l L^{-l}) y(t) = \mathbf{0}_n \tag{D.12}$$

and solving the eigenproblem

$$det(\mathbf{I}_n + \mathbf{D}_1 L^{-1} + \mathbf{D}_2 L^{-2} + \ldots + \mathbf{D}_l L^{-l}) = \mathbf{0}_n \tag{D.13}$$

which can be expressed in matrix form by

$$\mathbf{\Phi} = \begin{bmatrix} -\mathbf{D}_1 & -\mathbf{D}_2 & \ldots & \ldots & -\mathbf{D}_l \\ \mathbf{I}_n & \mathbf{0}_n & \mathbf{0}_n & \ldots & \mathbf{0}_n \\ \mathbf{0}_n & \mathbf{I}_n & \mathbf{0}_n & \ldots & \mathbf{0}_n \\ \ldots & \ldots & \ldots & \ldots & \ldots \\ \mathbf{0}_n & \mathbf{0}_n & \ldots & \mathbf{I}_n & \mathbf{0}_n \end{bmatrix} \tag{D.14}$$

Solving the characteristic equation $det\,(\mathbf{I}_{l \cdot n}\lambda - \mathbf{\Phi}) = \mathbf{0}$ of a VAR(n,l)-model describing a system with n-channels and l-order, leads to $l \cdot n$ discrete, complex eigenvalues λ_1, λ_2, …, $\lambda_{l \cdot n}$ [He and De Roeck 1997]. If the measured data of a structure contains j vibration modes, it will have j-pairs of conjugate system eigenvalues. In order to identify all modes, the model order must be selected in such a way that $l \geq 2j/n$ holds. In general $l \cdot n$ is chosen much higher than $2n$ in order to get a good correlation between the fitted model and the measured data leading to $l \cdot n - 2n$ artificial modes. In [Abdel Wahab and De Roeck 1999] different techniques for extracting the physical modes from the artificial ones are proposed. In [Hung and Ko 2002] a backward ARV model is introduced, for which can be shown, that the first $2j$ eigenvalues located outside or on the unit circle can be directly attributed to the system modes while the remaining eigenvalues belongs to the computational modes.
The continuous eigenvalues μ_k of the original vibrating system are acquired by the transformation

$$\lambda_k = \exp(\mu_k \Delta t) \tag{D.15}$$

where Δt denotes the sampling interval. The modal frequencies and damping ratios are calculated from the complex eigenvalue $\mu_k = \alpha_k + i\beta_k$ using the relation

$$\omega_k = \sqrt{\alpha_k^2 + \beta_k^2} \qquad \text{and} \qquad D = \frac{\alpha_k}{\omega_k} \tag{D.16}$$

The kth mode shape $\mathbf{\Psi}_k$ is determined from the following equation

$$\left[\mathbf{I}_{2j}\lambda_k^l + \mathbf{D}_1\lambda_k^{l-1} + \mathbf{D}_2\lambda_k^{l-2} + \ldots + \mathbf{D}_{l-1}\lambda_k + \mathbf{D}_l\right]\mathbf{\Psi}_k = \mathbf{0} \tag{D.17}$$

Comparative studies of parametric time-domain identification methods based on ARV models and nonparametric frequency domain methods can be found in [Kadakal and Yüzügüllü 1996]. It is shown, that nonparametric frequency domain methods allow estimating modal frequencies with a certain accuracy, but modal damping estimates are highly biased and vary strongly if the calculations are repeated for different sensor locations, leading to the estimation of a range of possible modal damping values rather than a single value.
In [Vu et al 2007; He and De Roeck 1997] a high order ARV model is used to approximate an ARMAV model. In the first cased the effect of the noise level and characteristics of the input (random excitation, impulsive excitation, harmonic components), of closely separated frequency modes, of low or high damping ratios as well as the dependency of the accuracy of the parameter identification on the chosen model order are investigated. In [He and De Roeck 1997] the method is applied for the modal parameter identification of a water transmission tower subjected to wind excitation using in situ vibration measurements. The comparison with a classical frequency domain identification approach shows that the method is superior as problems such as leakage or a low frequency resolution, caused by the restriction of the observation window and sampling rate, can be avoided.
In [Huang 2001] a modification of LS approach used for the parameter identification of an ARV model is proposed which uses the equivalence between the correlation function matrix for the responses of a linear system subjected to white-noise input and the deterministic free vibration responses of the system as shown in the previous section D.1.1. The influence of the signal-type (velocity or acceleration responses), the signal to noise ratio, the number of measured DOFs, and non-white-noise input (band-limited white noise) on the identifiability of the modal parameters is studied.
In [Bodeux and Golinval 2003] the modal identification and damage detection on the Steel-Quake structure using the ARMAV and the data-driven stochastic subspace (DSS) methods are studied. For the identification of the ARMAV(n,p,q) model given in Eq. (D.5) from measurements of the system response only, the prediction error method (PEM) [Caines 1988, p. 482 ff] is used leading to a non-linear, iterative estimation procedure: The model parameters θ are estimated by minimizing a criterion function, e.g.

$$C_N(\theta) = det\left(\frac{1}{N}\sum_{k=1}^{N}\mathbf{e}(k|\theta)\mathbf{e}(k|\theta)^T\right) \tag{D.18}$$

where N is the number of samples and $\mathbf{e}(k|\theta) = \mathbf{y}(k) - \hat{\mathbf{y}}(k|\theta)$ describes the error at time $t = k\Delta t$ between the predicted response $\hat{\mathbf{y}}(t|\theta)$ and the measurements $\mathbf{y}(t)$. As the predictor $\hat{\mathbf{y}}(t|\theta)$ depend nonlinearly on the unknown model parameters, the minimization of the criterion function is applied in an iterative manner.

In order to select an appropriate model order method such as the Akaike's Final Prediction Error Criterion (FPE) or Akaike's Information Theoretic Criterion (AIC) can be applied [Ljung 1998, p. 219 ff, p. 503 ff]. These criteria are based on monitoring the decrease in the criterion function $C_N(\theta)$ as the order p,q increases [Giraldo et al 2009]. In the special case of Gaussian distributes prediction errors the ARMAV/PEM algorithm yields efficiently asymptotically unbiased model parameter estimates where the estimation errors as well as the uncertainties in the modal parameter estimation can be calculated. The case study showed that the ARMAV/PEM as well as the data-driven stochastic subspace method lead to comparable identification results. However, the subspace method converges quickly while the PEM required a long computation time.

In [Giraldo et al 2009] a comparative study of three output-only time domain identification techniques of the modal parameters, namely the eigensystem realization algorithm with data correlations (ERA/DC), the prediction error method through least squares (PEM/LS), and the stochastic subspace identification (SSI) is performed. Here, an ARMAV-based two-stage least squares approach combining the prediction error method and the standard least square algorithm is used. First, a high order ARV model is fitted to the measurement data. Then, a pseudo-ARX model (AR model with exogenous input) is estimated using the prediction error of the AR model as the pseudoinput. The resulting ARX model is given

$$\hat{\mathbf{y}}(t) = -\mathbf{D}_1\mathbf{y}(t-1) - \mathbf{D}_2\mathbf{y}(t-2) - \ldots - \mathbf{D}_p\mathbf{y}(t-p) + \mathbf{B}_1\mathbf{e}(t-1) + \mathbf{B}_2\mathbf{e}(t-2) + \ldots + \mathbf{B}_q\mathbf{e}(t-q) \quad \text{(D.19)}$$

from which the p autoregressive $\mathbf{A}_i$ and q moving average $\mathbf{B}_i$ coefficient matrices can be calculated by a least square approach solving

$$\begin{bmatrix} \mathbf{y}(p+1) \\ \mathbf{y}(p+2) \\ \cdots \\ \mathbf{y}(j) \end{bmatrix} = \begin{bmatrix} \mathbf{y}(p) & \ldots & \mathbf{y}(1) & \mathbf{e}(p) & \ldots & \mathbf{e}(p-q+1) \\ \mathbf{y}(p+1) & \ldots & \mathbf{y}(2) & \mathbf{e}(p+1) & \ldots & \mathbf{e}(p-q+2) \\ \cdots & \cdots & \cdots & \cdots & \cdots & \cdots \\ \mathbf{y}(j-1) & \ldots & \mathbf{y}(j-p) & \mathbf{e}(j-1) & \ldots & \mathbf{e}(j-q) \end{bmatrix} \cdot \begin{bmatrix} \mathbf{A}_1^T \\ \ldots \\ \mathbf{A}_p^T \\ \mathbf{B}_1^T \\ \ldots \\ \mathbf{B}_q^T \end{bmatrix} \quad \text{(D.20)}$$

Finally, the modal parameters can be extracted from the obtained AR matrix coefficients following the approach described before. The comparative study showed that SSI and PEM/LS lead to much better results than the ERA algorithm. The identification result of the fre-

quencies and damping parameters is in all three methods robust to sensor noise. The signal-to-noise-ratio mainly affects the identification of the mode shapes, where SSI is clearly more robust than ERA/DC and PEM/LS. While the errors in the frequency estimation is below 1 %, damping ratios are often estimated with an error of about 20 % and even reach 50 % in case of the ERA algorithm.

D.1.3 Stochastic realization-based methods

The realization problem of identifying a linear dynamic system from its nonparametric impulse response sequence was first defined in [Kálmán 1963] and solved by [Ho and Kálmán 1966] using a finite-dimensional block Hankel matrix composed of noise-free impulse responses from which the system matrices of a deterministic state-space model were derived. In the 1970's the method was modified by [Zeiger and McEwen 1974] to consider noise corrupted impulse response functions by introducing a singular value decomposition of the Hankel matrix. [Akaike 1974] extended the realization theory for stochastic systems leading to a stochastic interpretation of the Ho-Kalman algorithm. In [Benveniste and Fuchs 1985] the method was first applied to modal identification [Reynders 2012].
The stochastic realization-based parameter identification procedures which where developed in the last two decades in the scope of operational modal analysis [Peeters and De Roeck 1999; Lardies and Larbi 2001; Magalhães et al 2009a] are often called Covariance-driven Stochastic Subspace Identification (SSI-COV) methods [Zhang et al 2005] as the system model is obtained for a random process on the basis of covariance data. The stochastic realization problem address the question of finding a minimal stochastic state space representation in the form

$$\mathbf{x}_{t+1} = \mathbf{A}\mathbf{x}_t + \mathbf{w}_t \tag{D.21}$$

$$\mathbf{y}_t = \mathbf{C}\mathbf{x}_t + \mathbf{v}_t \tag{D.22}$$

from the knowledge of the measured system output. The system response is modeled as zero-mean Gaussian stochastic process defined by

$$E[\mathbf{y}_k] = 0, \qquad E[\mathbf{y}_{t+k}\mathbf{y}_t^T] = \mathbf{\Lambda}_k \tag{D.23}$$

which implies that the additive process and measurement noises $\{\mathbf{w}_k\}$, $\{\mathbf{v}_k\}$ are as well of zero mean and normal and complete characterized by their covariance matrix

$$\mathbf{W} = E\left[\begin{pmatrix}\mathbf{w}_k\\ \mathbf{v}_k\end{pmatrix}\begin{pmatrix}\mathbf{w}_k^T & \mathbf{v}_k^T\end{pmatrix}\right] = \begin{pmatrix}\mathbf{Q} & \mathbf{S}\\ \mathbf{S}^T & \mathbf{R}\end{pmatrix}\delta(t) \tag{D.24}$$

The stochastic realization problems consists of two parts, namely finding the state space matrices $\mathbf{A}, \mathbf{C}$ under the constraint of a minimal dimension of the system matrix $\mathbf{A}$ from measurements of the zero mean stochastic vector process $\{\mathbf{y}_t\}$ describing the system output and secondly, determining the covariance matrices $\mathbf{Q}$, $\mathbf{S}$, $\mathbf{R}$ so that the second order statistics of the output of the model and of the given output with covariance sequence $\mathbf{\Lambda}_k$ are equal. The former is archived by expressing y_{k+m} repetitively in terms of $\mathbf{x}_k$ using Eq. (D.21), (D.22) and taking into account that $E[\mathbf{x}_k\mathbf{v}_k^T] = E[\mathbf{w}_k\mathbf{x}_k^T] = E[\mathbf{v}_{k+1}\mathbf{v}_k^T] = E[\mathbf{v}_{k+1}\mathbf{x}_k^T] = \mathbf{0}$ which allows determining the covariance of the output in the form

$$\mathbf{\Lambda}_k = \mathbf{C}\mathbf{A}^{k-1}\mathbf{\Sigma} \qquad \text{for} \quad k \geq 0 \tag{D.25}$$

$$\mathbf{\Lambda}_0 = \mathbf{C}\mathbf{\Sigma}\mathbf{C}^T + \mathbf{R} \qquad \text{for} \quad k = 0 \tag{D.26}$$

with $\mathbf{\Sigma} = E[\mathbf{x}_{k+1}\mathbf{y}_k^T] = \mathbf{A}\mathbf{\Sigma}_{xx}\mathbf{C}^T + \mathbf{S}$ and where $\mathbf{\Sigma}_{xx} = E[\mathbf{x}_k\mathbf{x}_k^T]$ denotes the state covariance matrix [Gevers 2006]. Using Eq. (D.25) the Hankel matrix $\mathcal{H}_{p,q} = \mathcal{O}_p\mathcal{C}_q$, consisting of p block rows and q block columns of the correlation matrix $\mathbf{R}(k)$, can be factored into the product of a so-called observability block matrix $\mathcal{O}_p$ of order p and a controllability $\mathcal{C}_q$ block matrix of order q, respectively, given by

$$\mathcal{H}_{p,q} = \begin{bmatrix}\mathbf{R}(1) & \mathbf{R}(2) & \mathbf{R}(3) & \dots & \mathbf{R}(q)\\ \mathbf{R}(2) & \mathbf{R}(3) & \mathbf{R}(4) & \dots & \mathbf{R}(q+1)\\ \dots & \dots & \dots & \dots & \dots\\ \mathbf{R}(p) & \mathbf{R}(p+1) & \mathbf{R}(p+2) & \dots & \mathbf{R}(q+p)\end{bmatrix} = \begin{bmatrix}\mathbf{C}\\ \mathbf{C}\mathbf{A}\\ \dots\\ \mathbf{C}\mathbf{A}^{p-1}\end{bmatrix}\cdot\begin{bmatrix}\mathbf{\Sigma} & \mathbf{A}\mathbf{\Sigma} & \dots & \mathbf{A}^{q-1}\mathbf{\Sigma}\end{bmatrix} \tag{D.27}$$

The name observability matrix implies that the matrices $\mathbf{A}$, $\mathbf{C}$ are observable, i.e. it is assumed that all the dynamical modes of the system can be observed in the output. Similarly, the name controllability matrix refers to the assumption, that the matrix pair $\mathbf{A}$, $\mathbf{\Sigma}$ is controllable, which implies that all the dynamical modes of the system can be excited by the stochastic input [Peeters and De Roeck 1999]. Assuming that the system is described by N eigenmodes, the rank of the observability matrix and controllability matrix is $2N$. Hence, multiplying Eq. (D.27) from right and left by user defined weighting matrices $\mathbf{W}_1$, $\mathbf{W}_2$ [Arun and Kung 1990; Van Overschee and De Moor 1996; Zhang et al 2005] and performing

a singular value decomposition of $\mathcal{H}_{p,q}$ yields

$$\mathbf{W}_1\mathcal{H}_{p,q}\mathbf{W}_2^T = (\mathbf{W}_1\mathcal{O}_p)(\mathcal{C}_q\mathbf{W}_2^T) = \begin{bmatrix}\mathbf{U}_1 & \mathbf{U}_2\end{bmatrix}\begin{bmatrix}\mathbf{S}_1 & \mathbf{0}\\ \mathbf{0} & \mathbf{0}\end{bmatrix}\begin{bmatrix}\mathbf{V}_1\\ \mathbf{V}_2\end{bmatrix} = \mathbf{U}_1\mathbf{S}_1\mathbf{V}_1^T \tag{D.28}$$

where $\mathbf{S}_1$ contains $2N$ non-zero singular values in decreasing order and where the $2N$ columns of $\mathbf{U}_1$, $\mathbf{V}_1$ corresponds to left, right singular vectors, respectively. Using Eq. (D.28) the observability matrix, controllability matrix, respectively, can be derived immediately

$$\mathcal{O}_p = \mathbf{W}_1^{-1}\mathbf{U}_1\mathbf{S}_1^{1/2} \tag{D.29}$$

$$\mathcal{C}_c = \mathbf{S}_1^{1/2}\mathbf{V}_1^T\mathbf{W}_2^{-1} \tag{D.30}$$

and the system matrices $\mathbf{A}$, $\mathbf{C}$ can be extracted from the first two block rows of $\mathcal{O}_p$. Different choices of weighting matrices $\mathbf{W}_1$ and $\mathbf{W}_2$ will lead to different stochastic subspace identification methods [Hermans and Van der Auweraer 1999]. There are three mayor methods, namely the *Principal Component* (PC) method, the *Canonical Correlation* or *Canonical Variant Analysis* (CVA) method and the *Balanced Realization* (BR) method. The latter is also called *Un-weighted Principal Component* (UPC) method as the singular value decomposition (SVD) is directly applied to the Hankel matrix, i.e. the weights are identity matrices. The method is mainly used if the modes are of equal strength and in presence of a good signal-to-noise ratio in the data. It is the stochastic counterpart of the deterministic realization/identification algorithm, e.g. ERA [Zhang et al 2005]. In case of the CVA all sensors are used as reference channels and the weights are set in such a way that the system modes are balanced in terms of energy leading to a better identification of the less excited modes in operational conditions and when dealing with noisy data. The PC method can be regarded as compromise between UPC and CVA [Hermans and Van der Auweraer 1999; Rainieri 2008].

It must be noted that the covariances used for the construction of the Hankel matrix are calculated from a finite number of measurements and thus are just estimates. Hence the result Eq. (D.28) only hold for infinite block-Hankel matrices and for a finite order system. In practice, the dynamic system is of infinite order (due to an infinite number of eigenvalues) and due to modeling inaccuracies, measurement noise and computational noise, the higher singular values are not exactly zero [Peeters and De Roeck 1999]. Hence, the SVD decomposition yields

$$\mathbf{W}_1\mathcal{H}_{p,q}\mathbf{W}_2^T = \begin{bmatrix}\mathbf{U}_1 & \mathbf{U}_2\end{bmatrix}\begin{bmatrix}\mathbf{S}_1 & \mathbf{0}\\ \mathbf{0} & \mathbf{S}_2\end{bmatrix}\begin{bmatrix}\mathbf{V}_1\\ \mathbf{V}_2\end{bmatrix} = \mathbf{U}_1\mathbf{S}_1\mathbf{V}_1 + \mathbf{U}_2\mathbf{S}_2\mathbf{V}_2 \approx \mathbf{U}_1\mathbf{S}_1\mathbf{V}_1 \tag{D.31}$$

where the second summand contains non-physical eigenvalues. An estimation of the observability matrix $\hat{\mathcal{O}}_p$ is then obtained by neglecting the second term leading again to the result given in Eq. (D.29). The system's order is in general unknown, but might be identified from the maximal gap between two successive singular values. However, for large, real structures there is generally no significant drop in the singular values and other techniques such as stabilization diagrams are required in order to estimate the model order [Hermans and Van der Auweraer 1999; Peeters and De Roeck 1999].

The dynamics of the system are completely characterized by the eigenvalues and corresponding eigenvectors of the system matrix $\mathbf{A}$. Hence, the modal parameters are obtained from the eigenvalue decomposition of $\mathbf{A}$ given by

$$\mathbf{A} = \mathbf{\Phi}\mathbf{\Lambda}\mathbf{\Phi}^{-1} \tag{D.32}$$

solving the characteristic equation $det\,(\mathbf{A} - \mathbf{I}_{2N}\lambda) = \mathbf{0}$. The diagonal matrix contains the discrete complex eigenvalues λ_k which can be transformed into system poles μ_k using Eq. (D.15) and the modal parameters are extracted applying Eq. (D.16). The elements of the kth mode shape $\psi_k = \mathbf{C}\phi_k$ at the sensor locations, are the observed components of the system eigenvectors ϕ_k of $\mathbf{\Phi}$. As the input force is not measured, the extracted mode shapes cannot be mass-normalized [Hermans and Van der Auweraer 1999].

In [Benveniste and Fuchs 1985] the problem of identifying the modal parameters of a Gauss-Markov process subjected to non-stationary noises using only a single record of the process is addressed. Different realization methods including the Ho-Kalman algorithm and the balanced realization algorithm are compared with ARMA-based methods. In contrast to the nonlinear identification problem in case of the latter class of algorithms, the estimates in the realization based methods are solutions of equations which are linear in the estimated covariances of the single sample of the process.

A referenced-based SSI-COV method is proposed in [Peeters and De Roeck 1999] which only requires the computation of the covariances between the outputs and a limited set of reference channels instead of the covariances between all outputs as in the classical approach. The method is applied for the modal analysis of a steel mast excited by wind loads. It is shown that it is considerably faster than the classical SSI-COV, requires a lower model order which is faster and leads to more accurate results.

In [Lardies and Larbi 2001] different methods such as the ordinary least squares, total least squares, partial least squares algorithms and a new iterative procedure are used in order to estimate the system matrix from the variance based Hankel matrix.

An application of the SSI-COV to the Humber Suspension Bridge (UK) for modal analysis is described in Magalhães et al [2009a]. It is based on an automatic algorithm for the inter-

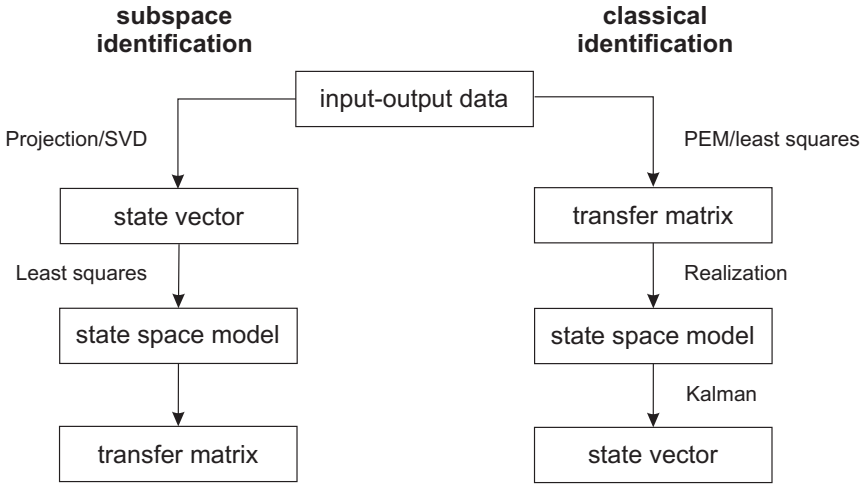

Figure D.1: Subspace and classical system identification methods [Katayama 2005]

pretation of stabilization diagrams in order to distinguish between the physical modes and artificial ones, recently introduced in [Magalhães et al 2009b].

D.1.4 Stochastic subspace-based methods

Subspace identification algorithms can be considered as an extension of the system realization theory. While the stochastic realization methods described in the previous section is covariance driven, the stochastic subspace identification (SSI) is data driven. Hence, it does not require the calculation of the covariance matrix but starts directly from the measured response data [Kirkegaard and Andersen 1997]. The method is widely used in engineering since the publication of the book [Van Overschee and De Moor 1996] which gives a detailed insight into the theory. As previously discussed the most general model of a linear time-invariant systems excited by white noise is the so-called ARMA model. The classical system identification is based on the prediction error methods which leads to a highly nonlinear minimization problem where convergence is not guaranteed and which is computational demanding. Thus the ARMAV model is often approximated by a high order ARV method which can be identified by a linear least square algorithm, but which requires a over-specification of the model order leading to non-physical modes. The SSI combines the advantages of both methods, i.e. it allows a general description of the system while the identification problem is linear. Consequently the SSI is much faster and more robust than the classical prediction error method [Peeters and De Roeck 1999]. In Fig. D.1 a comparison of the subspace and classical system identification methods is illustrated [Katayama 2005]. Both system identification techniques aim at finding a state space representation from input-output data (or just output data as

described before). In the classical methods first a transfer function is estimated from which the system matrices of the state space model can be derived. Finally the system states can be estimated applying the Kalman filter algorithm. In contrast, the subspace identification method starts with the estimation of a Kalman filter state sequence directly from the output data and allows identifying the system matrices without knowledge of the underlying mathematical model by applying projection techniques and numerical methods such as the singular value decomposition. The projection can be interpreted as conditional mean of the future outputs retaining all information on the past outputs. Once the Kalman states are known the identification of the system matrices of the state space model reduces to a linear least square problem. Hence the subspace idenification technique can be interpreted as a conditional linearization of the nonlinear prediction error problem [Van Overschee and De Moor 1996; Katayama 2005].

The SSI is based on the general assumptions, that the underlying physical system model is time-invariant and behaves linearly. Similar to the stochastic realization problem, it addresses the question of finding a stochastic state space representation in the form

$$\mathbf{x}_{t+1} = \mathbf{A}\mathbf{x}_t + \mathbf{w}_t \tag{D.33}$$

$$\mathbf{y}_t = \mathbf{C}\mathbf{x}_t + \mathbf{v}_t \tag{D.34}$$

as already defined in Eq. (D.21-D.26) from output only measurements. In contrast to the stochastic realization method which is based on a Hankel matrix constructed from the (cross)-covariances of the system outputs, the SSI algorithm starts directly from a Hankel matrix of the measured response data: the available N data points are grouped in the response matrix $\mathbf{Y}_{0:N-1} = [\mathbf{y}_0, \mathbf{y}_1, \ldots, \mathbf{y}_{N-1}]$ where each of the vectors $\mathbf{y}_j \in \mathbb{R}^m$ collects the system response at m sensor locations at time $t = j\Delta t$. The first row of the Hankel matrix is then created from the first $N - 2s$ data points $\mathbf{y}_1, \mathbf{y}_2, \ldots, \mathbf{y}_{N-2s}$ of the system's response. The following rows are obtained by shifting the data matrix successively by one position leading to

$$\mathcal{H}_{2s,N-2s-1} = \left[\begin{array}{ccccc} \mathbf{y}_0 & \mathbf{y}_1 & \mathbf{y}_2 & \cdots & \mathbf{y}_{N-2s-1} \\ \mathbf{y}_1 & \mathbf{y}_2 & \mathbf{y}_3 & \cdots & \mathbf{y}_{N-2s} \\ \cdots & \cdots & \cdots & \cdots & \cdots \\ \mathbf{y}_{s-1} & \mathbf{y}_s & \mathbf{y}_{s+1} & \cdots & \mathbf{y}_{N-s-1} \\ \hline \mathbf{y}_s & \mathbf{y}_{s+1} & \mathbf{y}_{s+2} & \cdots & \mathbf{y}_{N-s} \\ \mathbf{y}_{s+1} & \mathbf{y}_{s+2} & \mathbf{y}_{s+3} & \cdots & \mathbf{y}_{N-s+1} \\ \cdots & \cdots & \cdots & \cdots & \cdots \\ \mathbf{y}_{2s-1} & \mathbf{y}_{2s} & \mathbf{y}_{2s+1} & \cdots & \mathbf{y}_{N-1} \end{array}\right] = \left[\begin{array}{c} \mathbf{Y}_p \\ \hline \mathbf{Y}_f \end{array}\right] \tag{D.35}$$

and the matrix is spitted into s block rows of past outputs $\mathbf{Y}_p \in \mathbb{R}^{sm \times N-2s-1}$ and future outputs $\mathbf{Y}_f \in \mathbb{R}^{sm \times N-2s-1}$, respectively. The number of block rows is user defined and should be selected in such a way that sm is larger than the number of system modes. The number of columns is $N-2s-1$ if all available N data samples are used. For statistical reasons it is in general assumed that $s, N \to \infty$ [De Cock et al 2002]. The next step is the optimal prediction of the future outputs at time k given all information about the past output up to time $k-1$. An optimal predictor results in a minimum square error between the predicted $\hat{\mathbf{y}}_k$ and measured system response $\mathbf{y}_k$ and allows estimating the underlying model in an optimal sense. In the Gaussian case the optimal prediction is given by the conditional expectation [Brincker and Andersen 2006] of the system state $\mathbf{x}_k$ vector describing the system's dynamics at time k given the past outputs up to time $k-1$

$$\hat{\mathbf{x}}_k = E[\mathbf{x}_k|\mathbf{Y}_{1:k-1}] \tag{D.36}$$

The state prediction error $\mathbf{e}_{x,k} = \mathbf{x}_k - \hat{\mathbf{x}}_k$ between the true and estimated state is the part of $\mathbf{x}_k$ which is unpredictable. Similarly to Eq. (D.36) the optimal prediction can be formulated in terms of the measured system response, leading to [Andersen and Brincker 2001]

$$\hat{\mathbf{y}}_k = E[\mathbf{y}_k|\mathbf{Y}_{1:k-1}] = E[\mathbf{C}\mathbf{x}_k + \mathbf{v}_k|\mathbf{Y}_{1:k-1}] = \mathbf{C}\hat{\mathbf{x}}_k \tag{D.37}$$

Assuming a zero mean Gaussian process $\mathbf{y}_k$, the conditional mean $\hat{\mathbf{y}}_k$ given in Eq. (D.37) can be calculated directly by

$$\hat{\mathbf{y}}_k = E[\mathbf{y}_k \mathbf{Y}_{0:k-1}^T] \cdot E[\mathbf{Y}_{0:k-1}\mathbf{Y}_{0:k-1}^T]^{-1} \cdot \mathbf{Y}_{0:k-1} \tag{D.38}$$

The Hankel matrix in Eq. (D.35) can be used to calculate the optimal predictions of the system response efficiently in matrix form

$$\hat{\mathcal{H}}_{sm,sm} = E[\mathbf{Y}_f|\mathbf{Y}_p] \approx \frac{1}{s}\mathbf{Y}_f\mathbf{Y}_p^T(\mathbf{Y}_p\mathbf{Y}_p^T)^{-1}\mathbf{Y}_p, \qquad \mathcal{O} \in \mathbb{R}^{sm \times sm} \tag{D.39}$$

where

$$\hat{\mathcal{H}}_{sm,sm} = \begin{bmatrix} \hat{\mathbf{y}}_s & \hat{\mathbf{y}}_{s+1} & \cdots & \hat{\mathbf{y}}_{N-s} \\ \hat{\mathbf{y}}_{s+1} & \hat{\mathbf{y}}_{s+2} & \cdots & \hat{\mathbf{y}}_{N-s+1} \\ \hat{\mathbf{y}}_{s+2} & \hat{\mathbf{y}}_{s+3} & \cdots & \hat{\mathbf{y}}_{N-s+2} \\ \cdots & \cdots & \cdots & \\ \hat{\mathbf{y}}_{2s-1} & \hat{\mathbf{y}}_{2s+1} & \cdots & \hat{\mathbf{y}}_{N-1} \end{bmatrix} \tag{D.40}$$

The last matrix in this product defines the conditions, while the first four matrices in the product introduces the covariances between sensors at different time lags [Brincker and Andersen 2006]. The matrix $\hat{\mathcal{H}}_{sm,sm}$ is again of Hankel form and plays a key roll in the stochastic subspace identification method as will be shown in the following.
The relation between the two predictors given in Eq. (D.36) and Eq. (D.37) is defined by the Kalman filter for linear and time-invariant systems. As shown in section C.1.1, the Kalman filter equations are obtained by minimization of the mean square prediction error $\mathbf{e}_{x,k}$ taking into account the uncertainties in the model and the measurements. Assuming that the system matrices are known, the optimal state estimate in the mean square sense is given by

$$\hat{\mathbf{x}}_{k+1} = \mathbf{A}\hat{\mathbf{x}}_k + \mathbf{K}_k\mathbf{e}_{y,k} \tag{D.41}$$

$$\mathbf{K}_k = (\mathbf{A}\mathbf{P}_k\mathbf{C}^T + \mathbf{S})(\mathbf{C}\mathbf{P}_k\mathbf{C}^T + \mathbf{R})^{-1} \tag{D.42}$$

$$\begin{aligned}\mathbf{P}_{k+1} &= E[(\mathbf{x}_k - \hat{\mathbf{x}}_k)(\mathbf{x}_k - \hat{\mathbf{x}}_k)^T] = \\ &= \mathbf{A}\mathbf{P}_k\mathbf{A}^T + \mathbf{Q} + (\mathbf{A}\mathbf{P}_k\mathbf{C}^T + \mathbf{S})(\mathbf{C}\mathbf{P}_k\mathbf{C}^T + \mathbf{R})^{-1}(\mathbf{A}\mathbf{P}_k\mathbf{C}^T + \mathbf{S})^T\end{aligned} \tag{D.43}$$

$$\mathbf{e}_{y,k} = \mathbf{y}_k - \mathbf{C}\hat{\mathbf{x}}_k \tag{D.44}$$

where $\mathbf{K}_k$ denotes the Kalman gain. The innovation $\mathbf{e}_{y,k} = \mathbf{y}_k - \hat{\mathbf{y}}_k$ is a zero mean Gaussian process and describes the error between the measured and predicted output. Hence, it is the part of the measurement that contains new information about the state. Rearranging Eq. (D.44) yields the so-called innovation form of the state space representation in Eq. (D.33)

$$\hat{\mathbf{x}}_{k+1} = \mathbf{A}\hat{\mathbf{x}}_k + \mathbf{K}_k\mathbf{e}_{y,k} \tag{D.45}$$

$$\mathbf{y}_k = \mathbf{C}\hat{\mathbf{x}}_k + \mathbf{e}_{y,k} \tag{D.46}$$

which is widely used in output only modal analysis and where

$$\mathbf{K}_k = (\mathbf{G} - \mathbf{A}\mathbf{P}_k\mathbf{C}^T)(\mathbf{\Lambda}_0 - \mathbf{C}\mathbf{P}_k\mathbf{C}^T)^{-1} \tag{D.47}$$

$$\mathbf{P}_{k+1} = \mathbf{A}\mathbf{P}_k\mathbf{A}^T + (\mathbf{G} - \mathbf{A}\mathbf{P}_k\mathbf{C}^T)(\mathbf{\Lambda}_0 - \mathbf{C}\mathbf{P}_k\mathbf{C}^T)^{-1}(\mathbf{G} - \mathbf{A}\mathbf{P}_k\mathbf{C}^T)^T \tag{D.48}$$

The classical and the innovation Kalman filter look different, but they lead to the same state estimate $\hat{\mathbf{x}}_{k+1}$ as shown in [Van Overschee and De Moor 1996, p. 205f]. In the innovation form the state vector is replaced by its optimal prediction and the measurement and process noise are converted into a single input process, namely the innovation [Andersen and Brincker 2001]. Defining $\mathbf{P}_k = E[\hat{\mathbf{x}}_k\hat{\mathbf{x}}_k^T]$ the state covariance matrix of the predicted state vector and $\mathbf{\Sigma}_{ee} = E[\mathbf{e}_{y,k}\mathbf{e}_{y,k}^T]$ the covariance matrix of the innovation, the unknown quantities $\mathbf{P}_{k+1}$, $\mathbf{K}_k$

are calculated from the following three constrains characterizing the innovation model in Eq. (D.33), (D.34)

$$\mathbf{P}_{k+1} = E[\hat{\mathbf{x}}_k \hat{\mathbf{x}}_k^T] = \mathbf{A}\mathbf{P}_k\mathbf{A}^T + \mathbf{K}_k\boldsymbol{\Sigma}_{ee}\mathbf{K}_k^T \tag{D.49}$$

$$\mathbf{G} = E[\mathbf{y}_k \hat{\mathbf{x}}_k^T] = \mathbf{A}\mathbf{P}_k\mathbf{C}^T + \mathbf{K}_k\boldsymbol{\Sigma}_{ee} \tag{D.50}$$

$$\boldsymbol{\Lambda}_0 = E[\mathbf{y}_k \mathbf{y}_k^T] = \mathbf{C}\mathbf{P}_k\mathbf{C}^T + \boldsymbol{\Sigma}_{ee} \tag{D.51}$$

Solving Eq. (D.50) for the covariance $\boldsymbol{\Sigma}_{ee}$ and introducing it in Eq. (D.51) yields the time-variant (i.e. non-steady) Kalman gain $\mathbf{K}_k$ defined in Eq. (D.47). Introducing both matrices in Eq. (D.49) finally leads to the state covariance matrix $\mathbf{P}_{k+1}$ given in Eq. (D.48) [Gevers 2006].

Assuming that a sufficient number of states $\hat{\mathbf{X}}_{s:s+i} = [\hat{\mathbf{x}}_s, \hat{\mathbf{x}}_{s+1}, \ldots, \hat{\mathbf{x}}_{s+i-1}]$ and $\hat{\mathbf{X}}_{s+1:s+i+1} = [\hat{\mathbf{x}}_{s+1}, \hat{\mathbf{x}}_{s+2}, \ldots, \hat{\mathbf{x}}_{s+i}]$ can be predicted then the identification of the system matrices $\mathbf{A}, \mathbf{C}$ reduces to a the least square regression problem defined by

$$\begin{bmatrix} \hat{\mathbf{X}}_{s+1:s+i} \\ \mathbf{Y}_{s:s+j-1} \end{bmatrix} = \begin{bmatrix} \mathbf{A} \\ \mathbf{C} \end{bmatrix} \hat{\mathbf{X}}_{s:s+i-1} + \begin{bmatrix} \rho_w \\ \rho_v \end{bmatrix} \tag{D.52}$$

where the innovations or Kalman residuals $\rho_w = [\rho_{w_s}, \rho_{w_{s+1}}, \ldots, \rho_{w_{s+i-1}}]$, $\rho_v = [\rho_{v_s}, \rho_{v_{s+1}}, \ldots, \rho_{v_{s+i-1}}]$ are defined by

$$\rho_{w_k} = \hat{\mathbf{x}}_{k+1} - \hat{\mathbf{A}}\hat{\mathbf{x}}_k \qquad \rho_{v_k} = \mathbf{y}_k - \hat{\mathbf{C}}\hat{\mathbf{x}}_k \tag{D.53}$$

As the innovations are uncorrelated with the Kalman states $\hat{\mathbf{X}}_{s:s+i-1}$, the system of equations given in Eq. (D.52) can be solved for the system matrices by

$$\begin{bmatrix} \hat{\mathbf{A}} \\ \hat{\mathbf{C}} \end{bmatrix} = \begin{bmatrix} \hat{\mathbf{X}}_{s+1:s+i} \\ \mathbf{Y}_{s:s+j-1} \end{bmatrix} \hat{\mathbf{X}}_{s:s+i-1}^{-1} \tag{D.54}$$

The covariance matrices are calculated by the least square error

$$\begin{pmatrix} \hat{\mathbf{Q}} & \hat{\mathbf{S}} \\ \hat{\mathbf{S}}^T & \hat{\mathbf{R}} \end{pmatrix} = \frac{1}{i} \begin{pmatrix} \rho_w \\ \rho_v \end{pmatrix} \begin{pmatrix} \rho_w^T & \rho_v^T \end{pmatrix} \tag{D.55}$$

In order to calculate the system and covariance matrices according to Eq. (D.54, D.55) it was assumed that the Kalman states are known beforehand. Now the question arises how to extract these states directly from the output data when the system matrices are still unknown. Recalling that the optimal predictors are defined by the conditional mean with respect to past observations, the state space model is transfered from an input-output relation

given in Eq. (D.33), (D.34) in a 'Kalman state'-output relation by applying the expectation operator on both sides of Eq. (D.33), (D.34) which yields

$$E[\mathbf{x}_{k+1}|\mathbf{Y}_{0:k}] = \mathbf{A}E[\mathbf{x}_k|\mathbf{Y}_{0:k-1}] + E[\mathbf{w}_k|\mathbf{Y}_{0:k-1}] \quad \Rightarrow \quad \hat{\mathbf{x}}_{k+1} = \mathbf{A}\hat{\mathbf{x}}_k \tag{D.56}$$

$$E[\mathbf{y}_k|\mathbf{Y}_{0:k-1}] = \mathbf{C}E[\mathbf{x}_k|\mathbf{Y}_{0:k-1}] + E[\mathbf{v}_k|\mathbf{Y}_{0:k-1}] \quad \Rightarrow \quad \hat{\mathbf{y}}_k = \mathbf{C}\hat{\mathbf{x}}_k \tag{D.57}$$

and where $\hat{\mathbf{x}}_k$ denotes the optimal Kalman state estimate. Assuming that a recursion is started at time step s by inserting Eq. D.56 recursively into itself i times yields the following formulation

$$\hat{\mathcal{H}}_{sm,1} = \begin{bmatrix} \hat{\mathbf{y}}_s \\ \hat{\mathbf{y}}_{s+1} \\ \hat{\mathbf{y}}_{s+2} \\ \dots \\ \hat{\mathbf{y}}_{s+i-1} \end{bmatrix} = \begin{bmatrix} \mathbf{C} \\ \mathbf{CA} \\ \mathbf{CA}^2 \\ \dots \\ \mathbf{CA}^{s-1} \end{bmatrix} \hat{\mathbf{x}}_s = \mathbf{\Gamma}_s \hat{\mathbf{x}}_s \tag{D.58}$$

where $\hat{\mathcal{H}}_{sm,1}$ corresponds to the first column of the matrix $\hat{\mathcal{H}}_{sm,sm}$ defined in Eq. (D.40) if $i = s$ is chosen. Defining $\hat{\mathbf{X}}_{s:s+i-1} = [\hat{\mathbf{x}}_s, \hat{\mathbf{x}}_{s+1}, \dots, \hat{\mathbf{x}}_{s+i-1}]$ one obtains finally

$$\hat{\mathcal{H}}_{sm,sm} = \mathbf{\Gamma}_s \hat{\mathbf{X}}_{s:s+i-1} \tag{D.59}$$

which strongly resembles the result of the stochastic realization method given in Eq. (D.27). Following the steps Eq. (D.28), (D.29), the singular value decomposition of $\hat{\mathcal{H}}_{sm,sm}$ yields

$$\mathbf{\Gamma}_s = \mathbf{W}_1 \mathbf{U}_1 \mathbf{S}_1^{1/2} \tag{D.60}$$

$$\hat{\mathbf{X}}_{s:s+i-1} = \mathbf{S}_1^{1/2} \mathbf{V}_1^T \mathbf{W}_2^{-1} \tag{D.61}$$

In a similar manner an estimate of the state sequence $\hat{\mathbf{X}}_{s+1:s+i}$ can be derived. Having determined the state sequences $\hat{\mathbf{X}}_{s:s+i-1}$, $\hat{\mathbf{X}}_{s+1:s+i}$ the system matrices and corresponding error covariances can be derived solving the linear least square problem defined in Eq. (D.52)-(D.55). Once the system matrices are obtained, the modal parameters are identified solving an eigenvalue problem using Eq. (D.15), (D.16) and Eq. (D.32).

In [Peeters and De Roeck 1999] a modified implementation of the SSI method was proposed where instead of all past outputs, just the past reference outputs are considered in order to predict the future outputs. Consequently, the dimensions of the matrices are reduced which makes the SSI/ref algorithm much faster than the standard SSI algorithm. The new technique is applied to a vibration test on a steel transmitter mast and compared with the standard SSI algorithm.

A comparative study of various identification techniques for the modal analysis of the bridge dynamics of the Z24-Bridge, a three-span reinforced concrete bridge in Switzerland subjected to ambient loads such as traffic, wind and micro-earthquakes, to a drop weight and to a periodic excitation by shakers is presented in [Peeters and Ventura 2003]. The identification results of two frequency domain techniques, namely the peak picking and frequency decomposition method, as well as of four time domain methods, among them the Ibrahim time domain method, the stochastic Realization method, the stochastic subspace method and an ARMAV-based technique are discussed. It is shown that the SSI method yields in all load cases the most complete and consistent modal parameter estimates. Another comparative study of the SSI technique and the peak-picking method used for ambient vibration testing and experimental modal analysis on large civil engineering structures can be found in [Ren and Zong 2004]. The methods are applied to a 15 story reinforced concrete shear core building as well as to a concrete filled steel tubular arch bridge. Also in these case studies the SSI technique outperforms the peak picking method which is computational efficient but fails to identify the complete set of eigenfrequencies and yields inaccurate mode shape estimates.
In [Bodeux and Golinval 2003] modal analysis and damage detection of a steel-frame structure is performed using an ARMAV-based algorithm and the SSI method. The accuracy of the modal analysis and damage detection of both methods is comparable. However, the SSI technique requires a shorter computation time in order to obtain good results while at the same time the mean uncertainties of the estimates are smaller.

Bibliography

[Abdel Wahab and De Roeck 1999] Abdel Wahab, M. M. ; De Roeck, Guido: An effective method for selecting physical modes by vector autoregressive models. In: *Mechanical Systems and Signal Processing* 13 (1999), Nr. 3, p. 449 –474

[Akaike 1974] Akaike, Hirotugo: Stochastic theory of minimal realization. In: *Automatic Control, IEEE Transactions on* 19 (1974), dec, Nr. 6, p. 667 – 674

[Andersen and Brincker 2001] Andersen, Palle ; Brincker, Rune: *The Stochastic Subspace Identification Techniques.www.svibs.com.* 2001

[Andersen and Enmark 2011] Andersen, Torben ; Enmark, Anita: *Integrated Modeling of Telescopes.* Springer, 2011 (Astrophysics and Space Science Library)

[Andrews 2004] Andrews, Larry C.: *Field Guide to Atmospheric Optics.* SPIE Press, 2004 (Spie Field Guides)

[Arun and Kung 1990] Arun, K. S. ; Kung, S. Y.: Balanced Approximation of Stochastic Systems. In: *SIAM Journal on Matrix Analysis and Applications* 11 (1990), Nr. 1, p. 42–68

[Åström 1970] Åström, Karl J.: *Introduction to stochastic control theory.* Academic Press, New York, 1970. – 98 ff p

[Bagchi 2003] Bagchi, Arunabha: Rational Approximations of the power spectral density of atmospheric turbulence arising in adaptive optics / University of Twente. 2003. – Research Report

[Bai 2003] Bai, Yong: *Marine Structural Design.* Elsevier, 2003 (Referex Engineering)

[Balendra 1993] Balendra, Thambirajah: *Vibration of buildings to wind and earthquake loads.* Springer-Verlag, 1993

[Barney and Carne 1999] Barney, P. ; Carne, T.: Modal Parameter Extraction Using Natural Excitation Response Data. In: *Proceedings of the 17th International Modal Analysis Conference*, 1999, p. 49–55

[Barpi and Valente 2002] Barpi, Fabrizio ; Valente, Silvio: Creep and fracture in concrete: a fractional order rate approach. In: *Engineering Fracture Mechanics* 70 (2002), march, Nr. 5, p. 611–623. – ISSN 0013-7944

[Bendat and Piersol 1993] Bendat, Julius S. ; Piersol, Allan G.: *Engineering Applications of Correlation and Spectral Analysis*. John Wiley & Sons, 1993 (Wiley Series in Probability and Statistics). – 196–203 p

[Bendat and Piersol 2010] Bendat, Julius S. ; Piersol, Allan G.: *Random Data - Analysis and Measurement Procedures*. John Wiley & Sons, 2010 (Wiley Series in Probability and Statistics)

[Benveniste and Fuchs 1985] Benveniste, Albert ; Fuchs, Jean-Jacques: Single sample modal identification of a nonstationary stochastic process. In: *Automatic Control, IEEE Transactions on* 30 (1985), jan, Nr. 1, p. 66 – 74

[Beran 1994] Beran, John: *Statistics for Long-Memory Processes*. Chapman & Hall, 1994 (Chapman and Hall/CRC Monographs on Statistics and Applied Probability Series)

[Best 1991] Best, Roland: *Digitale Meßwertverarbeitung*. R. Oldenbourg Verlag, 1991

[Bodeux and Golinval 2003] Bodeux, J.-B. ; Golinval, J.-C.: Modal identification and damage detection using the data-driven stochastic subspace and ARMAV methods. In: *Mechanical Systems and Signal Processing* 17 (2003), Nr. 1, p. 83 – 89

[Borgman 1969] Borgman, Leon E.: Ocean wave simulation for engineering design. In: *Journal of the Waterways and Harbors Division* 95 (1969), Nr. 4, p. 557–583

[Box et al 2008] Box, George E. P. ; Jenkins, Gwilym M. ; Reinsel, Gregory C. ; Sons, John Wiley (Editor.): *Wiley Series in Probability and*. Volume 3: *Time Series Analysis: Forecasting and Control*. John Wiley & Sons, 2008

[Bretschneider 1959] Bretschneider, C.L.: *Wave Variability and Wave Spectra for Wind Generated Gravity Waves*. A. & M. College of Texas., 1959 (Technical memorandum)

[Brigham 1988] Brigham, E. O.: *The fast Fourier transform and its applications*. Upper Saddle River, NJ, USA : Prentice-Hall, Inc., 1988

[Brincker and Andersen 2006] Brincker, Rune ; Andersen, Palle: Understanding Stochastic Subspace Identification. In: *Proceedings of the 24th International Modal Analysis Conference (IMAC), St. Louis, Missouri*, 2006

[Brockwell and Davis 2002] Brockwell, Peter J. ; Davis, Richard A.: *Spectral Analysis and Time Series*. Volume 2. Springer Verlag, 2002

[Broersen and De Waele 2003] Broersen, Piet M. T. ; De Waele, Stijn: Generating data with prescribed power spectral density. In: *IEEE Transactions on Instrumentation and Measurement* 52 (2003), Nr. 4, p. 1061–1067

[Brown and Hwang 1997] Brown, R.G. ; Hwang, P.Y.C.: *Introduction to random signals and applied Kalman filtering: with MATLAB exercises and solutions*. Wiley, 1997

[Brownjohn 2003] Brownjohn, J. M. W.: Ambient vibration studies for system identification of tall buildings. In: *Earthquake Engineering and Structural Dynamics* 32 (2003), p. 71–95

[Burton et al 2001] Burton, Tony ; Jenkins, Nick ; Sharpe, David ; Bossanyi, Ervin: *Wind Energy Handbook*. Wiley, 2001

[Busch and Panofsky 1968] Busch, N. E. ; Panofsky, H. A.: Recent spectra of atmospheric turbulence. In: *Quarterly Journal of the Royal Meteorological Society* 94 (1968), Nr. 400, p. 132–148

[Caicedo 2011] Caicedo, J. M.: Practical Guidelines for the Natural Excitation Technique (NExT) and the Eigensystem Realization Algorithm (ERA) for Modal Identification Using Ambient Vibration. In: *Experimental Techniques* 35 (2011), p. 52–58

[Caicedo et al 2004] Caicedo, Juan M. ; Dyke, Shirley J. ; Johnson, Erik A.: Natural Excitation Technique and Eigensystem Realization Algorithm for Phase I of the IASC-ASCE Benchmark Problem: Simulated Data. In: *Journal of Engineering Mechanics* 130 (2004), Nr. 1, p. 49–60

[Caines 1988] Caines, Peter E.: *Linear stochastic systems*. J. Wiley, 1988 (Wiley series in probability and mathematical statistics: Probability and mathematical statistics)

[Ceravolo 2004] Ceravolo, R.: Use of instantaneous estimators for the evaluation of structural damping. In: *Journal of Sound and Vibration* 274 (2004), p. 385–401

[Chakrabarti 2005] Chakrabarti, Subrata K.: *Handbook of Offshore Engineering*. Elsevier, 2005 (Handbook of Offshore Engineering Bd. 1)

[Chan 1999] Chan, Grace: An effective method for simulating Gaussian random fields. In: *Proceedings of the statistical Computing Section* Citeseer (Veranst.), 1999, p. 133–138

[Chang and Pakzad 2012] Chang, Minwoo ; Pakzad, Shamim N.: Modified Natural Excitation Technique for Stochastic Modal Identification. In: *Journal of Structural Engineering* 1 (2012), Nr. 1, p. 419–454

[Chen and Kareem 2001] Chen, X. ; Kareem, A.: Aeroelastic analysis of bridges under multicorrelated winds: Integrated state-space approach. In: *Journal of Engineering Mechanics* 127 (2001), Nr. 11, p. 1124–1134

[Chen 2003] Chen, Zhe: Bayesian filtering: From Kalman filters to particle filters, and beyond / McMaster University, Hamilton, ON, Canada. 2003. – Research Report

[Cimellaro et al 2012] Cimellaro, G. P. ; Piantá, S. ; De Stefano, A.: Output-Only Modal Identification of Ancient L'Aquila City Hall and Civic Tower. In: *Journal of structural engineering* 138 (2012), p. 481–491

[Coleridge 1845] Coleridge, Samuel T. ; Smedley, Eward (Editor.) ; Rose, Hugh J. (Editor.) ; Rose, Henry J. (Editor.): *Encyclopaedia Metropolitana: Differm- Falter*. B. Fellowes, 1845 (Encyclopaedia Metropolitana: Or, Universal Dictionary of Knowledge, Comprising the Twofold Advantage of a Philosophical and an Alphabetical Arrangement, with Appropriate Engravings)

[Cottone et al 2011] Cottone, Giulio ; Barone, Giorgio ; Tamura, Yukio: Wind loads spectrum generation by the 'H-fractional spectral moments' decomposition. In: *Proceedings of the 13th International Conference on Wind Engineering*, July 2011

[Cottone and Di Paola 2010c] Cottone, Giulio ; Di Paola, M.: A new representation of power spectral density and correlation function by means of fractional spectral moments. In: *Probabilistic Engineering Mechanics* 25 (2010c), Nr. 3, p. 348–353. – ISSN 0266-8920

[Cottone and Di Paola 2010] Cottone, Giulio ; Di Paola, Mario: On the use of fractional calculus for the probabilistic characterization of random variables. In: *Probabilistic Engineering Mechanics* 24 (2010), p. 321–330

[Cottone and Di Paola 2011] Cottone, Giulio ; Di Paola, Mario: Fractional spectral moments for digital simulation of multivariate wind velocity fields. In: *Journal of Wind Engineering and Industrial Aerodynamics* 99 (2011), Nr. 6-7, p. 741–747

[Cottone et al 2010b] Cottone, Giulio ; Di Paola, Mario ; Metzler, Ralf: Fractional calculus approach to the statistical characterization of random variables and vectors. In: *Physica A* 389 (2010b), p. 909–920

[Cottone et al 2010d] Cottone, Giulio ; Di Paola, Mario ; Santoro, Roberta: A novel exact representation of stationary colored Gaussian processes (fractional differential approach). In: *Journal of Physics A: Mathematical and Theoretical* 43 (2010d), Nr. 085002, p. 16–32

[Counihan 1975] Counihan, J.: Adiabatic atmospheric boundary layers: A review and analysis of data from the period 1880–1972. In: *Atmospheric Environment (1967)* 9 (1975), Nr. 10, p. 871 – 905

[Cunha and Caetano 2006] Cunha, Álvaro ; Caetano, Elsa: Experimental Modal Analysis. In: *Sound and Vibrations* 40 (2006), Nr. 6, p. 12–20

[Davenport 1961] Davenport, A.G.: The spectrum of horizontal gustiness near the ground in high winds. In: *Quarterly Journal of the Royal Meteorological Society* 87 (1961), Nr. 372, p. 194–211

[De Cock et al 2002] De Cock, Katrien ; Peeters, Bart ; Vecchio, Antontio ; Van der Auweraer, Herman ; De Moor, Bart: Subspacesystem identification for mechanical engineering. In: *In Proceedings of the 25th International Seminar on Modal Analysis, Leuven, Belgium*, 2002

[De Roeck et al 2000] De Roeck, Guido ; Peeters, Bart ; Ren, Wei-Xin: Benchmark study on system identification through ambient vibration measurements. In: *Proceedings 18th Int. Modal Analysis Conference, San Antonio*, 2000, p. 1106–1112

[Deodatis 1996a] Deodatis, George: Non-stationary stochastic vector processes: seismic ground motion applications. In: *Probabilistic Engineering Mechanic* 11 (1996), Nr. 3, p. 149–167

[Deodatis 1996b] Deodatis, George: Simulation of ergodic multi-variate stochastic processes. In: *Journal of Engineering Mechanics* 122 (1996), Nr. 8, p. 778–787

[Deodatis and Shinozuka 1989] Deodatis, George ; Shinozuka, Ma: Simulation of Seismic Ground Motion Using Stochastic Waves. In: *Journal of Engineering Mechanics* 115 (1989), Nr. 12, p. 2723– 2737

[Deodatis et al 1990] Deodatis, George ; Shinozuka, Masanobu ; Papageorgiou, Apostolos: Stochastic Wave Representation of Seismic Ground Motion. II: Simulation. In: *Journal of Engineering Mechanics* 116 (1990), Nr. 11, p. 2381–2399

[Det Norske Veritas 2010] Det Norske Veritas (Veranst.): *Recommended practice DNV-RP-C205: Environmental Conditions and Environmental Loads*. 2010

[Di Paola 1998] Di Paola, Mario: Digital simulation of wind field velocity. In: *Journal of Wind Engineering and Industrial Aerodynamics* 74-76 (1998), p. 91–109

[Di Paola et al 2012] Di Paola, Mario ; Failla, Giuseppe ; Pirrotta, Antonina: Stationary and non-stationary stochastic response of linear fractional viscoelastic systems. In: *Probabilistic Engineering Mechanics* 28 (2012), Nr. 0, p. 85 – 90. – ISSN 0266-8920

[Di Paola and Zingales 2008] Di Paola, Mario ; Zingales, M.: Stochastic differential calculus for wind-exposed structures with autoregressive continuous (ARC) filters. In: *Journal of Wind Engineering and Industrial Aerodynamics* 96 (2008), Nr. 12, p. 2403 – 2417

[Dietrich and Newsam 1997] Dietrich, C. R. ; Newsam, Garry N.: Fast and exact simulation of stationary Gaussian processes through circulant embedding of the covariance matrix. In: *SIAM Journal on Scientific Computing* 18 (1997), Nr. 4, p. 1088–1107

[Doebling and Farrar 1996] Doebling, Scott W. ; Farrar, Charles R.: Computation of structural flexibility for bridge health moitoring using ambient modal data. In: *Proceedings of the 11th ASCE Engineering Mechanics Conference*, 1996, p. 1114–1117

[Dolenc et al 2005] Dolenc, David ; Romanowicz, Barbara ; Stakes, Debra ; McGill, Paul ; Neuhauser, Doug: Observations of infragravity waves at the Monterey ocean bottom broadband station (MOBB). In: *Geochemistry, Geophysics, Geosystems* 6 (2005), september, Nr. 9

[Du Plessis 1997] Du Plessis, R.: *Poor man's explanation of Kalman Filtering: Or how I stopped worrying and learned to love matrix inversion*. Taygeta Scientific Inc, 1997

[Dullerud and Paganini 2000] Dullerud, Gier E. ; Paganini, Fernando G.: *A Course in Robust Control Theory: A Convex Approach*. Springer, 2000 (Texts in Applied Mathematics)

[Dyrbye and Hansen 1997] Dyrbye, C. ; Hansen, S.O.: *Wind Loads on Structures*. John Wiley & Sons, 1997

[EN 1991-1-4:2005 2010] : *Eurocode 1: Actions on structures - Part 1-4: General actions - Wind actions;*. december 2010

[ESDU-85020 1985] ESDU-85020: Characteristics of atmospheric turbulence near the ground Part II: single point data for strong winds (neutral atmosphere) / Engineering Sciences Data Unit (ESDU). 1985. – Research Report

[Ferdi et al 2008] Ferdi, Youcef ; Taleb-Ahmed, Abdelmalik ; Lakehal, Mohamed R.: Efficient generation of $1/f^{\beta}$ noise using signal modeling techniques. In: *IEEE Transactions on circuits and systems - 1: Regular papers* 55 (2008), Nr. 6, p. 1704–1710

[Gavriluta et al 2012] Gavriluta, C. ; Spataru, S. ; Mosincat, I. ; Citro, C. ; Candela, I. ; Rodriguez, P.: Complete methodology on generating realistic wind speed profiles based on measurements. In: *International Conference on Renewable Energies and Power Quality (ICREPQ)*, 2012

[Gentile and Saisi 2007] Gentile, C. ; Saisi, A.: Ambient vibration testing of historic masonry towers for structural identification and damage assessment. In: *Construction and Building Materials* 21 (2007), p. 1311–1321

[Gevers 2006] Gevers, Michel: A personal view of the development of system identification. In: *IEEE Control Systems Magazine* 26 (2006), Nr. 6, p. 93–105

[Giraldo et al 2009] Giraldo, Diego F. ; Song, Wei ; Dyke, Shirley J. ; Caicedo, Juan M.: Modal Identification through Ambient Vibration: Comparative Study. In: *Journal of Engineering Mechanics* 135 (2009), Nr. 8, p. 759–770

[Granger and Joyeux 1980] Granger, C. W. J. ; Joyeux, Roselyne: An introduction to long-memory time series models and fractional differencing. In: *Journal of Time Series Analysis* 1 (1980), Nr. 1, p. 15–29. – ISSN 1467-9892

[Grewal and Andrews 2008] Grewal, Mohinder S. ; Andrews, Angus P.: *Kalman Filtering: Theory and Practice Using MATLAB*. John Wiley & Sons, 2008

[Gurley and Kareem 1993] Gurley, Kurtis ; Kareem, Ahsan: Gust loading factors for tension leg platforms. In: *Applied Ocean Research* 15 (1993), Nr. 3, p. 137 – 154

[Gustafsson and Isaksson 1996] Gustafsson, Fredrik ; Isaksson, Alf. J.: Best choice of coordinate system for tracking coordinated turns. In: *Proceedings of the 35th IEEE Conference on Decision and Control* Volume 3, 1996, p. 3145–3150

[Harris 1968] Harris, R. I.: *On the Spectrum and Auto-correlation Function of Gustiness in High Winds*. Electrical Research Association, 1968 (ERA report)

[Harris 1970] Harris, R. I. ; Construction Industry Research & Information, London (Editor.): *The nature of the wind, Seminar on Modern Design of Wind-Sensitive Structures*. Construction Industry Research and Information Association, 1970 (CIRIA publication)

[Harris 1990] Harris, R. I.: Some further thoughts on the spectrum of gustiness in strong winds. In: *Journal of Wind Engineering and Industrial Aerodynamics* 33 (1990), Nr. 3, p. 461 – 477

[Hasselmann et al 1973] Hasselmann, K. ; Barnett, TP ; Bouws, E. ; Carlson, H. ; Cartwright, DE ; Enke, K. ; Ewing, JA ; Gienapp, H. ; Hasselmann, DE ; Kruseman, P. et al: Measurements of wind-wave growth and swell decay during the Joint North Sea Wave Project (JONSWAP). In: *Ergänzungsheft zur Deutschen Hydrographischen Zeitschrift* Reihe A, 8 (1973), Nr. 12, p. 1–95

[He and De Roeck 1997] He, Xia ; De Roeck, G.: System identification of mechanical structures by a high-order multivariate autoregressive model. In: *Computers & Structures* 64 (1997), Nr. 1–4, p. 341 – 351

[Hedrih 2006] Hedrih, Katica S.: The transversal creeping vibrations of a fractional derivative order constitutive relation of nonhomogeneous beam. In: *Mathematical Problems in Engineering* (2006)

[Hermans and Van der Auweraer 1999] Hermans, L. ; Van der Auweraer, H.: Modal testing and analysis of structures under operational conditions: Industrial applications. In: *Mechanical Systems and Signal Processing* 13 (1999), Nr. 2, p. 193 – 216

[Ho and Kálmán 1966] Ho, B. ; Kálmán, Rudolf E.: Effective reconstruction of linear state-variable models from input/output functions. In: *Regelungstechnik* 14 (1966), Nr. 12, p. 545–548

[Holan et al 2010] Holan, Scott H. ; Lund, Robert ; Davis, Ginger: The ARMA alphabet soup: A tour of ARMA model variants. In: *Statistical Surveys* 4 (2010), p. 232–274

[Holm 2005] Holm, D. D.: Taylor′s hypothesis, Hamilton′s principle and the LANS-alpha model for computing turbulence. In: *Los Alamos Science* 29 (2005), p. 172–180

[Holmes 2007] Holmes, John D.: *Wind Loading of Structures*. Taylor & Francis, 2007

[Hoshiya and Maruyama 1987] Hoshiya, Masaru ; Maruyama, Osamu: Identification of running load and beam systems. In: *Journal of Engineering Mechanics* 113 (1987), Nr. 6, p. 813–824

[Hoshiya and Saito 1984] Hoshiya, Masaru ; Saito, Etsuro: Structural Identification by Extended Kalman Filter. In: *Journal of Engineering Mechanics* 110 (1984), Nr. 12, p. 1757–1770

[Hoshiya and Sutoh 1993] Hoshiya, Masaru ; Sutoh, Atsushi: Kalman filter – Finite Element Method in Identification. In: *Journal of Engineering Mechanics* 119 (1993), Nr. 2, p. 197–2010

[Hosking 1981] Hosking, Jonathan R. M.: Fractional differencing. In: *Biometrika* 68 (1981), Nr. 1, p. 165–176

[Hu et al 1991] Hu, Sau-Lon J. ; Tsiatas, George ; McGrath, James E.: Optimal Linearization of Morison-Type Wave Loading. In: *Journal of Engineering Mechanics* 117 (1991), Nr. 7, p. 1537–1553

[Huang 2001] Huang, C. S.: Structural identification from ambient vibration measurement using the multivariate AR model. In: *Journal of Sound and Vibration* 241 (2001), Nr. 3, p. 337 – 359

[Hung and Ko 2002] Hung, C. F. ; Ko, W. J.: Identification of modal parameters from measured output data using vector backward autoregressive model. In: *Journal of Sound and Vibration* 256 (2002), Nr. 2, p. 249 – 270

[Hurst 1950] Hurst, Harold E.: *Long-term Storage Capacity of Reservoirs.* American Society of Civil Engineers, Hydraulics Division, 1950

[Isermann 1988a] Isermann, Rolf: *Identifikation dynamischer Systeme.* Springer-Verlag Berlin, Heidelberg, 1988 (Band 2)

[Isermann 1988b] Isermann, Rolf: *Identifikation dynamischer Systeme.* Springer, 1988 (Band 1)

[Ivanovic et al 2000] Ivanovic, Sanja S. ; Trifunac, Mihailo D. ; I., Todorovska M.: Ambient vibration tests of structures: A review. In: *ISET Journal of Earthquake Technology* 37 (2000), December, Nr. 4, p. 165–197

[Jaishi and Ren 2005] Jaishi, Bijaya ; Ren, Wei-Xin: Structural finite element model updating using ambient vibration test results. In: *Journal of Structural Engineering* ASCE 131 (2005), Nr. 4, p. 617–628

[James et al 1993] James, George H. ; Carne, Thomas G. ; Lauffer, James P.: The natural excitation technique (NExT) for modal parameter extraction from operating wind turbines / Sandia National Laboratories. 1993. – Research Report

[James et al 1996] James, George H. ; Carne, Thomas G. ; Mayes, Randy L.: Modal parameter extraction from large operating structures using ambient excitation. In: *Proceedings in the 14th International Modal Analysis Conference (IMAC).* Dearborn, Michigan, 1996

[Juang and Pappa 1985] Juang, Jer-Nan ; Pappa, Richard S.: An Eigensystem Realization Algorithm for Modal Parameter Identification and Model Reduction. In: *Journal of Guidance, Control and Dynamics* 8 (1985), Nr. 5, p. 620–627

[Kadakal and Yüzügüllü 1996] Kadakal, U. ; Yüzügüllü, Ö.: A comparative study on the identification methods for the autoregressive modelling from the ambient vibration records. In: *Soil Dynamics and Earthquake Engineering* 15 (1996), Nr. 1, p. 45 – 49

[Kaimal et al 1972] Kaimal, J. C. ; Wyngaard, J.C. ; Izumi, Y. ; Cote, O. R.: Spectral characteristics of surface-layer turbulence. In: *Quarterly Journal of the Royal Meteorological Society* 98 (1972), Nr. 417, p. 563–589

[Kálmán 1960] Kálmán, Rudolf E.: A new approach to linear filtering and prediction problems. In: *Journal of Basic Engineering* (1960), p. 35–45

[Kálmán 1963] Kálmán, Rudolf E.: Mathematical description of linear dynamical systems. In: *SIAM J Control* 1 (1963), Nr. 2, p. 152–192

[Kantz and Schreiber 2008] Kantz, Holdger ; Schreiber, Thomas: *Nonlinear Time Series Analysis*. Cambridge University Press, 2008. – 396–397 p

[Kareem 1985] Kareem, Ahsan: Wind-induced Response Analysis of Tension Leg Platforms. In: *Journal of Structural Engineering* 111 (1985), Nr. 1, p. 37–55

[Kareem 2008] Kareem, Ahsan: Numerical simulation of wind effects: A probabilistic perspective. In: *Journal of Wind engineering and Industrial Aerodynamics* 96 (2008), p. 1472–1497

[Kareem and Dalton 1982] Kareem, Ahsan ; Dalton, Charles: Dynamic effects of wind on tension leg platforms. In: *Offshore Technology Conference*, 1982

[Kasdin 1995] Kasdin, N. J.: Discrete simulation of colored noise and stochastic processes and $1/f^{\alpha}$ - Power law noise generation. In: *Proceedings of the IEEE* 83 (1995), may, Nr. 5, p. 802 –827

[Katayama 2005] Katayama, T.: *Subspace Methods for System Identification*. Springer, 2005 (Communications and Control Engineering)

[Kay 1993] Kay, Steven M.: *Fundamentals of Statistical Signal Processing: Estimation Theory*. Prentice-Hall PTR, 1993 (Prentice Hall Signal Processing Series Volume 1)

[Kijewski and Kareem 2000] Kijewski, Tracy ; Kareem, Ahsan: *Estimation and Modeling of Damping and Engineering Auxiliary Damping Systems in Civil Engineering Structures: An Overview*. NatHaz Modeling Laboratory Report, University of Notre Dame. 2000

[Kilbas et al 2006] Kilbas, A. Anatolii A. ; Srivastava, Hari M. ; Trujillo, Juan J.: *Theory And Applications of Fractional Differential Equations*. Elsevier Science & Tech, 2006 (North-Holland Mathematics Studies)

[Kinsman 2002] Kinsman, Blair: *Wind Waves: Their Generation and Propagation on the Ocean Surface*. Dover Publications, 2002 (Phoenix Edition Series)

[Kirkegaard and Andersen 1997] Kirkegaard, P. H. ; Andersen, P.: State space identification of civil engineering structures from output measurments. In: *Proceedings of the 15th International Modal Analysis Conference, Orlando, Florida*, 1997

[Koh and Kelly 1990] Koh, Chan G. ; Kelly, James M.: Application of fractional derivatives to seismic analysis of base-isolated models. In: *Earthquake Engineering & Structural Dynamics* 19 (1990), Nr. 2, p. 229–241

[Kolmogorov 1933] Kolmogorov, Andrei N.: *Grundbegriffe der Wahrscheinlichkeitsrechnung - Ergebnisse der Mathematik und ihrer Grenzgebiete*. Springer, 1933

[Kolmogorov 1941] Kolmogorov, Andrei N.: Interpolation and Extrapolation. In: *Bulletin de l'Académie des Sciences de U.S.S.R., Series Mathematics* 5 (1941), p. 3–14

[Kopp and Orford 1963] Kopp, Richard E. ; Orford, Richard J.: Linear Regression applied to System Identification for adaptive Control Systems. In: *AIAA Journal* 1 (1963), Nr. 10, p. 2300–2306

[Lardies and Larbi 2001] Lardies, Joseph ; Larbi, Noureddine: Dynamic System Parameter Identification by Stochastic Realization Methods. In: *Journal of Vibration and Control* 7 (2001), Nr. 5, p. 711–728

[Lauffer et al 1985] Lauffer, J. P. ; Carne, T. G. ; Nord, A. R.: Mini-Modal Testing of Wind Turbines using novel Excitation. In: *Proceedings of the 3rd International Modal Analysis Conference*. Orlando, 1985, p. 28–31

[Lee et al 2002] Lee, J. W. ; Kim, J. D. ; Yun, C. B. ; Shim, J. M.: Health-monitoring method for bridges under ordinary traffic loadings. In: *Journal of Sound and Vibration* 257 (2002), Nr. 2, p. 247–264

[Lewis et al 2008] Lewis, Frank L. ; Xie, Lihua ; Popa, Dan: *Optimal and Robust Estimation: With an Introduction to Stochastic Control Theory*. Taylor &Francis Group, 2008

[Li and Chen 2009] Li, Jie ; Chen, Jianbing: *Stochastic dynamics of structures*. Wiley, 2009. – ISBN 9780470824245

[Li and Kareem 1990] Li, Yousun ; Kareem, Ahsan: ARMA representation of wind field. In: *Journal of Wind Engineering and Industrial Aerodynamics* 36, Part 1 (1990), Nr. 0, p. 415 – 427. – The Sixth U.S. National Conference on Wind Engineering

[Liang et al 2007] Liang, Jianwen ; Chaudhuri, Samit R. ; Shinozuka, Masanobu: Simulation of Nonstationary Stochastic Processes by Spectral Representation. In: *Journal of Engineering Mechanics* 133 (2007), Nr. 6, p. 616–627

[Lin and Liu 2007] Lin, R. ; Liu, Fawang: Fractional high order methods for the nonlinear fractional ordinary differential equation. In: *Nonlinear Analysis: Theory, Methods & Applications* 66 (2007), Nr. 4, p. 856 – 869

[Ljung 1974] Ljung, Lennart ; 7405, Report (Editor.): *On Consistency for Prediction Error Identification Methods*. Lund Institute of Technology, 1974 (Report // Division of Automatic Control, Lund Institute of Technology)

[Ljung 1998] Ljung, Lennart: *System Identification: Theory for the User*. Pearson Education, 1998

[Longuet-Higgins 1952] Longuet-Higgins, Michael S.: On the Statistical Distribution of the Heights of Sea Waves. In: *Journal of Marine Research* 11 (1952), Nr. 3, p. 245–266

[Lubich 1986] Lubich, Christian: Discretized fractional calculus. In: *SIAM Journal on Mathematical Analysis* 17 (1986), july, Nr. 3, p. 704–719

[Luk and Damper 2006] Luk, Robert W.-P. ; Damper, Robert I.: Non-parametric Linear Time-invariant System Identification by Discrete Wavelet Transforms. In: *Digital Signal Processing* 16 (2006), p. 303–319

[Lungu and van Gelder 1997] Lungu, Dan ; van Gelder, Pieter: Characteristics of wind turbulence with applications to wind codes. In: *Proceedings of the 2nd European & African Conference on Wind Engineering*, 1997, p. 1271–1277

[Lutes and Sarkani 2004] Lutes, Loren D. ; Sarkani, Shahram: *Random Vibrations: Analysis of Structural and Mechanical Systems*. Elsevier Science, 2004

[Magalhães et al 2009a] Magalhães, Filipe ; Brownjohn, M. W. ; Cunha, Álvaro ; Caetano, Elsa: Challenges in Identification of the Humber Bridge Modal Parameters based on an Ambient Vibration Test. In: *Proceedings in 3rd International Operational Modal Analysis Conference (IOMAC)*, 2009

[Magalhães et al 2009b] Magalhães, Filipe ; Cunha, Álvaro ; Caetano, Elsa: Online automatic identification of the modal parameters of a long span arch bridge. In: *Mechanical Systems and Signal Processing* 23 (2009), Nr. 2, p. 316 – 329

[Makris and Constantinou 1991] Makris, Nicos ; Constantinou, M. C.: Fractional-Derivative Maxwell Model for Viscous Dampers. In: *Journal of Structural Engineering* 117 (1991), Nr. 9, p. 2708–2724

[Mandelbrot and Van Ness 1968] Mandelbrot, Benoit B. ; Van Ness, John W.: Fractional Brownian motions, fractional noises and applications. In: *SIAM review* 10 (1968), Nr. 4, p. 422–437

[Mathieu and Scott 2000] Mathieu, Jean ; Scott, Julian: *An Introduction to Turbulent Flow*. Cambridge University Press, 2000

[Maybeck 1979] Maybeck, Peter S.: *Stochastic models, Estimation and Control*. Academic Press, 1979 (Mathematics in Science and Engineering Volume 1)

[Maybeck 1982] Maybeck, Peter S.: *Stochastic Models, Estimation and Control*. Academic Press, 1982 (Mathematics in Science and Engineering Volume 2)

[McCormick 2009] McCormick, Michael E.: *Ocean Engineering Mechanics: With Applications*. Cambridge University Press, 2009

[McGee and Schmidt 1985] McGee, Leonard A. ; Schmidt, Stanley F.: Discovery of the Kalman Filter as a Practical Tool for Aerospace and / NASA Technical Memo 86847. 1985. – Research Report

[Mehra and Lainiotis 1976] Mehra, Raman K. ; Lainiotis, Dimitri G.: *System Identification: Advances and Case Studies*. Academic Press, 1976 (Mathematics in Science and Engineering)

[Meinhold and Singpurwalla 1983] Meinhold, R. J. ; Singpurwalla, N. D.: Understanding the Kalman filter. In: *The American Statisticia* 37 (1983), Nr. 2, p. 123–127

[Mendis et al 2007] Mendis, P. ; Ngo, T. ; Haritos, N. ; Hira, A. ; Samali, B. ; Cheung, J.: Wind loading on tall buildings. In: *EJSE Special Issue: Loading on Structures* 3 (2007), p. 41–54

[Mignolet and Spanos 1991] Mignolet, Marc P. ; Spanos, Pol D.: Autoregressive spectral modeling: Difficulties and remedies. In: *International Journal of Non-Linear Mechanics* 26 (1991), Nr. 6, p. 911 – 930

[Mignolet and Spanos 1987] Mignolet, Marcus P. ; Spanos, Pol D.: Recursive Simulation of Stationary Multivariate Random Processes - Part 1. In: *Journal of Applied Mechanics, ASME* 109 (1987), p. 674–680

[Moreau et al 2002] Moreau, Xavier ; Ramus-Serment, Caroline ; Oustaloup, Alain: Fractional Differentiation in Passive Vibration Control. In: *Nonlinear Dynamics* 29 (2002), p. 343–362

[Mörters and Peres 2010] Mörters, Peter. ; Peres, Yuval: *Brownian Motion*. Cambridge University Press, 2010 (Cambridge Series in Statistical and Probabilistic Mathematics)

[Moskowitz 1964] Moskowitz, Lionel: Estimates of the power spectrums for fully developed seas for wind speeds of 20 to 40 knots. In: *Journal of geophysical research* 69 (1964), Nr. 24, p. 5161–5179

[Munk 1950] Munk, Walter H.: Origin and generation of waves. In: *Proceedings of the 1st Coastal Engineering Conference, Long Beach, California* Office of Naval Research and United States (Veranst.), Scripps Institution of Oceanography, 1950

[Mur Amada 2009] Mur Amada, Joaquín: *Wind power variability in the grid*, Universidad de Zaragoza, Ph.D. thesis, 2009

[Neumann 1953] Neumann, Gerhard ; Technical Memo No. 43, U.S. Army Corps of E. (Editor.): *On Ocean Wave Spectra and a New Method of Forecasting Wind-generated Sea*. Defense Technical Information Center, 1953 (Technical memorandum // Department of Army, Corps of Engineers, Beach Erosion Board)

[Norton and Quarton 2003] Norton, E. J. ; Quarton, D. C.: Recommendations for design of offshore wind tubines (RECOFF) / Garrad Hassan and Partners Ltd. 2003. – Research Report

[Ortigueira 2006] Ortigueira, Manuel D.: RIESZ POTENTIAL OPERATORS AND INVERSES VIA FRACTIONAL CENTRED DERIVATIVES. In: *International Journal of Mathematics and Mathematical Sciences* (2006), p. 1–12

[Ortigueira 2008] Ortigueira, Manuel D.: Fractional Central Differences and Derivatives. In: *Journal of Vibration and Control* 14 (2008), Nr. 9-10, p. 1255–1266

[Padé 1892] Padé, Henri: Sur la représentation approchée d'une fonction par des fractions rationnelles. In: *Annales scientifiques de l'É.N.S., 3e série, Théses de la Faculté des sciences de Paris,* tome 9 (1892), p. 3–93 (Supplément)

[Peeters and De Roeck 1999] Peeters, Bart ; De Roeck, Guido: Reference-based stochastic subspace identification for output-only modal analysis. In: *Mechanical Systems and Signal Processing* 13 (1999), Nr. 6, p. 855–878

[Peeters et al 1998] Peeters, Bart ; De Roeck, Guido ; Hermans, Luc ; Wauters, Tom ; Krämer, Christoph ; De Smet, Camiel: Comparison of system identification methods using operational data of a bridge test. In: *Proceedings of ISMA 23, International Conference on Noise and Vibration Engineering.* Leuven, Belgium, 1998, p. 923–930

[Peeters et al 1995] Peeters, Bart ; De Roeck, Guido ; Pollet, T. ; Schueremans, L.: Stochastic subspace techniques applied to parameter identification of civil engineering structures. In: *Proceedings of New Advances in Modal Synthesis of Large Structures: Nonlinear, Damped and Nondeterministic Cases*, September 1995, p. 151–162

[Peeters et al 2001] Peeters, Bart ; Maeck, Johan ; De Roeck, Guido: Vibration-based damage detection in civil engineering: excitation sources and temperature effects. In: *Smart Materials and Structures* 10 (2001), p. 518–527

[Peeters and Ventura 2003] Peeters, Bart ; Ventura, C. E.: Comparative study of modal analysis techniques for bridge dynamic characteristics. In: *Mechanical Systems and Signal Processing* 17 (2003), Nr. 5, p. 965 – 988

[Petersen 2000] Petersen, Christian: *Dynamik der Baukonstruktionen.* Vieweg & Teubner Verlag, 2000

[Phillips 1958] Phillips, Oliver M.: The equilibrium range in the spectrum of wind-generated waves. In: *Journal of Fluid Mechanics* 4 (1958), Nr. 04, p. 426–434

[Pierson and Moskowitz 1963] Pierson, Willard J. ; Moskowitz, Lionel: A proposed spectral form for fully developed wind seas based on the similarity theory of S. A. Kitaigorodskii / Department of Meteorology and Oceanography, U. S. Naval Oceanographic Office under contract N62306 -1042. 1963. – Research Report

[Pierson et al 1955] Pierson, Willard J. ; Neumann, Gerhard ; James, Richard W. ; 603, H.O. P. (Editor.): *Practical Methods for Observing and Forecasting Ocean Waves by Means of Wave Spectra and Statistics.* U.S. Naval Oceanographic Office, 1955

[Podlubny 1999] Podlubny, Igor: *Fractional Differential Equations: An Introduction to Fractional Derivatives, Fractional Differential Equations, to Methods of Their Solution and Some of Their Applications*. Elsevier Science, 1999 (Mathematics in Science and Engineering)

[Priestley 1965] Priestley, Maurice B.: Evolutionary Spectra and Non-Stationary Processes. In: *Journal of the Royal Statistical Society. Series B (Methodological)* 27 (1965), Nr. 2, p. pp. 204–237

[Priestley 1981] Priestley, Maurice B.: *Introduction to Time Series and Forecasting: Univariate Series*. Volume 1. Academic Press, 1981

[Rainieri 2008] Rainieri, Carlo: *Operational Modal Analysis for Seismic Protection of Structures*, University of Naples "Federico II", Ph.D. thesis, 2008

[Rao 2008] Rao, Suhasini S.: *A course in time series analysis (lecture notes)*. Department of Statistics, Texas A&M University. 2008

[Reid 2003] Reid, Ian: *Estimation (lecture notes)*. Department of Engineering Science, University of Oxford. 2003

[Ren and Zong 2004] Ren, Wei-Xin ; Zong, Zhou-Hong: Output-only modal parameter identification of civil engineering structures. In: *Structural Engineering and Mechanics* 17 (2004), Nr. 3-4, p. 429–444

[Reynders 2012] Reynders, Edwin: System Identification Methods for (Operational) Modal Analysis: Review and Comparison. In: *Archives of Computational Methods in Engineering* 19 (2012), p. 51–124. – ISSN 1134-3060

[Ross 1975] Ross, Bertram: *A brief history and exposition of the fundamental theory of frational calculus*. Volume 457. Springer Lectrue Notes in Mathematics, Vol. 57, 1975. – 1–36 p

[Roweis and Ghahramani 1999] Roweis, Sam ; Ghahramani, Zoubin: A Unifying Review of Linear Gaussian Models. In: *Neural Computation* 11 (1999), p. 305–345

[Runtemund et al 2013] Runtemund, Katrin ; Cottone, Giulio ; Müller, Gerhard: Treatment of arbitrarily autocorrelated load functions in the scope of parameter identification. In: *Computers & Structures* (2013), Nr. 0, p. –

[Ruscheweyh 1982a] Ruscheweyh, Hans: *Dynamische Windwirkung an Bauwerken - Band 1: Grundlagen*. Bauverlag, 1982. – 53–61 p

[Ruscheweyh 1982b] Ruscheweyh, Hans: *Dynamische Windwirkung an Bauwerken - Band 2: Praktische Anwendungen*. Bauverlag, 1982. – 53–61 p

[Sabatier et al 2007] Sabatier, Jocelyn ; Agrawal, Om P. ; Machado, J. A. T.: *Advances in Fractional Calculus: Theoretical Developments and Applications in Physics and Engineering*. Springer, 2007

[Sadabadi et al 2009] Sadabadi, Mahdiye S. ; Shafiee, Masoud ; Karrari, Mehdi: Two-dimensional ARMA model order determination. In: *ISA Transactions* 48 (2009), Nr. 3, p. 247 – 253

[Salzmann 1988] Salzmann, Martin A.: Some aspects of Kalman filtering / Department of Geodesy and Geomatics Engineering, University of New Brunswick, Canada. 1988. – Research Report

[Samaras et al 1985] Samaras, Elias ; Shinzuka, Masanobu ; Tsurui, Akira: ARMA Representation of Random Processes. In: *Journal of Engineering Mechanics* 111 (1985), Nr. 3, p. 449–461

[Samko et al 1993] Samko, S.G. ; Kilbas, A.A. ; Marichev, O.I.: *Fractional integrals and derivatives: theory and applications*. Gordon and Breach Science Publishers, 1993. – 385–388 p. – ISBN 9782881248641

[Sayed and Kailath 2001] Sayed, Ali H. ; Kailath, Thomas: A survey of spectral factorization methods. In: *Numerical Linear Algebra with Applications* 8 (2001), Nr. 6-7, p. 467–496

[Schuëller 1997] Schuëller, Gerhart I.: A State-of-the-Art Report on Computational Stochastic Mechanics. In: *Probabilistic Engineering Mechanics* 12 (1997), Nr. 4, p. 197–321

[Shen et al 2003] Shen, F. ; Zheng, M. ; Feng Shi, D. ; Xu, F.: Using the cross-correlation technique to extract modal parameters on response-only data. In: *Journal of Sound and Vibration* 259 (2003), Nr. 5, p. 1163–1179

[Shinozuka 1971] Shinozuka, Masanobu: Simulation of Multivariate and Multidimensional Random Processes. In: *The Journal of the Acoustical Society of America* 49 (1971), Nr. 1B, p. 357–368

[Shinozuka 1974] Shinozuka, Masanobu: Digital simulation of random processes in engineering mechanics with the aid of FFT technique. In: Ariaratnam, S. T. (Editor.) ; Leipholz, H. H. E. (Editor.): *Stochastic problems in mechanics: Proceedings of the Symposium on Stochastic Problems in Mechanics held at the University of Waterloo* Volume ., Solid Mechanics Division, University of Waterloo, 1974, p. 277–286

[Shinozuka and Deodatis 1991] Shinozuka, Masanobu ; Deodatis, George: Simulation of stochastic processes by spectral representation. In: *Applied Mechanics Reviews* 44 (1991), Nr. 4, p. 191–204

[Shinozuka and Deodatis 1996] Shinozuka, Masanobu ; Deodatis, George: Simulation of multi-dimensional Gaussian stochastic fields by spectral representation. In: *Applied Mechanics Reviews* 49 (1996), Nr. 1, p. 29–53

[Shinozuka and Jan 1972] Shinozuka, Masanobu ; Jan, C.-M.: Digital simulation of random processes and its applications. In: *Journal of Sound and Vibration* 25 (1972), Nr. 1, p. 111 – 128. – ISSN 0022-460X

[Simiu 1974] Simiu, Emil: Wind Spectra and Dynamic Alongwind Response. In: *Journal of the Structural Division* 100 (1974), Nr. 9, p. 1897–1910

[Simiu and Scanlan 1996] Simiu, Emil ; Scanlan, Robert H.: *Winds Effects on Structures: Fundamentals and Applications to Design.* John Wiley & Sons, 1996 (A Wiley-Interscience publication)

[Simon 2006] Simon, Dan: *Optimal State Estimation: Kalman, H_∞, and Nonlinear Approaches.* Wiley, 2006

[Siringoringo and Fujino 2008] Siringoringo, Dionysius M. ; Fujino, Yozo: System identification of suspension bridge from ambient vibration response. In: *Engineering Structures* 30 (2008), Nr. 2, p. 462 – 477

[Sivaprasad et al 2009] Sivaprasad, R ; Venkatesha, S ; Manohar: Identification of dynamical systems with fractional derivative damping models using inverse sensitivity analysis. In: *Computers, Materials & Continua* 9 (2009), Nr. 3, p. 179–207

[Smith 1980] Smith, Stuart D.: Wind Stress and Heat Flux over the Ocean in Gale Force Winds. In: *Journal of Physical Oceanography* 10 (1980), Nr. 5, p. 709–726

[Sousa 2012] Sousa, Ercilia: HOW TO APPROXIMATE THE FRACTIONAL DERIVATIVE OF ORDER $1 < \alpha \leq 2$. In: *International Journal of Bifurcation and Chaos* 22 (2012), Nr. 04

[Spanos 1983] Spanos, Pol D.: ARMA Algorithms for Ocean Wave Modeling. In: *Journal of Energy Resources Technology* 105 (1983), Nr. 3, p. 300–309

[Spanos and Mignolet 1986] Spanos, Pol D. ; Mignolet, Marc P.: Z-Transform Modeling of P-Wave Spectrum. In: *Journal of Engineering Mechanics* 112 (1986), Nr. 8, p. 745–759

[Spanos and Mignolet 1990] Spanos, Pol D. ; Mignolet, Marc P.: Simulation of Stationary Random Processes: Two Stage MA to ARMA Approach. In: *Journal of Engineering Mechanics* 116 (1990), Nr. 3, p. 620–641

[Spanos and Mignolet 1987] Spanos, Pol D. ; Mignolet, Marcus P.: Recursive Simulation of Stationary Multivariate Random Processes - Part 2. In: *Journal of Applied Mechanics, ASME* 54 (1987), p. 681–687

[Spanos and Zeldin 1996] Spanos, Pol D. ; Zeldin, B. A.: Efficient iterative ARMA approximation of multivariate random processes for structural dynamics applications. In: *Earthquake Engineering & Structural Dynamics* 25 (1996), Nr. 5, p. 497–507

[Sprouse et al 2010] Sprouse, Brian P. ; MacDonald, Christopher L. ; Silva, Gabriel A.: Computational efficiency of fractional diffusion using adaptive time step memory. In: *Department of Bioengineering, University of California, San Diego* (2010)

[Särkkä 2012] Särkkä, Simo: *Bayesian Estimation of Time-Varying Systems: Discrete-Time Systems, Lectures notes of course S-114.4610*. Alto University, Department of Biomedical Engineering and Computational Science, Finland. Spring 2012. – Planned to be published as book by Cambridge University Press in 2013

[Stathopoulos and Baniotopoulos 2007] Stathopoulos, Ted ; Baniotopoulos, Charalambos C.: *Wind Effects on Buildings and Design of Wind-Sensitive Structures*. Springer, 2007 (International Centre for Mechanical Sciences, Courses and Lectures)

[Stoica and Selen 2004] Stoica, Petre ; Selen, Yngve: Model-order selection: a review of information criterion rules. In: *Signal Processing Magazine, IEEE* 21 (2004), july, Nr. 4, p. 36 – 47

[Van der Hoven 1957] Van der Hoven, Isaac: Power spectrum of horizontal wind speed in the frequency range from 0,0007 to 900 cycles per hour. In: *Journal of Meteorology* 14 (1957), p. 160–164

[Van Overschee and De Moor 1996] Van Overschee, Peter ; De Moor, Bart ; Katholieke Universiteit Leuven, Belgium (Editor.): *Subspace idetnification for linear systems: Theory - Implementation - Applications*. Kluwer Academic Publishers, Boston/London/Dordrecht, 1996

[Vanmarcke 2010] Vanmarcke, Erik: *Random fields: analysis and synthesis*. World Scientific, 2010. – ISBN 9789812562975

[Von Kármán 1948] Von Kármán, Theodore: Progress in the statistical theory of turbulence. In: *Proceedings of the National Academy of Sciences of the United States of America* 34 (1948), Nr. 11, p. 530—539

[Vu et al 2007] Vu, V. H. ; Thomas, M. ; Lakis, A. A. ; Marcouiller, L.: Multi-autoregressive model for structural output-only modal analysis. In: *Proceedings of the 25th Seminar on machinery vibration, Canadian Machinery Vibration Association, Canada*, 2007

[Wiener 1949] Wiener, Norbert: *Extrapolation, Interpolation, and Smoothing of stationary Time Series with Engineering Applications*. New York : MIT Press Cambridge, Massachusetts and John Wiley & Sons, 1949

[World Meteorological Organization 1988] World Meteorological Organization: *Guide to wave analysis and forecasting*. Secretariat of the World Meteorological Organization, 1988 (WMO (Series))

[Yamazaki and Shinozuka 1988] Yamazaki, Fumio ; Shinozuka, Masanobu: Digital generation of non-Gaussian stochastic Fields. In: *Journal of Engineering Mechanics* 114 (1988), Nr. 7, p. 1183–1197

[Yang 1972] Yang: Simulation of random envelope processes. In: *Journal of Sound and Vibration* 21 (1972), Nr. 1, p. 73 – 85

[Yuen and Katafygiotis 2001] Yuen, Ka-Veng ; Katafygiotis, Lambos S.: Bayesian time-domain approach for modal updating using ambient data. In: *Probabilistic Engineering Mechanics* 16 (2001), Nr. 3, p. 219–231

[Yura and Hanson 2011] Yura, Harold T. ; Hanson, Steen G.: Digital simulation of an arbitrary stationary stochastic process by spectral representation. In: *Journal of the Optical Society of America A* 28 (2011), Apr, Nr. 4, p. 675–685

[Zeiger and McEwen 1974] Zeiger, H. ; McEwen, A.: Approximate linear realizations of given dimension via Ho's algorithm. In: *Automatic Control, IEEE Transactions on* 19 (1974), Nr. 2, p. 153

[Zhang et al 2005] Zhang, Lingmi ; Brincker, Rune ; Andersen, Palle: An Overview of Operational Modal Analysis: Major Development and Issues. In: *Proceedings of 1st International Operational Modal Analysis Conference*. Copenhagen, Denmark, 2005